Interfacial behavior of hybrid SHCC-Concrete beams with a joint at midspan

Othman Harrass

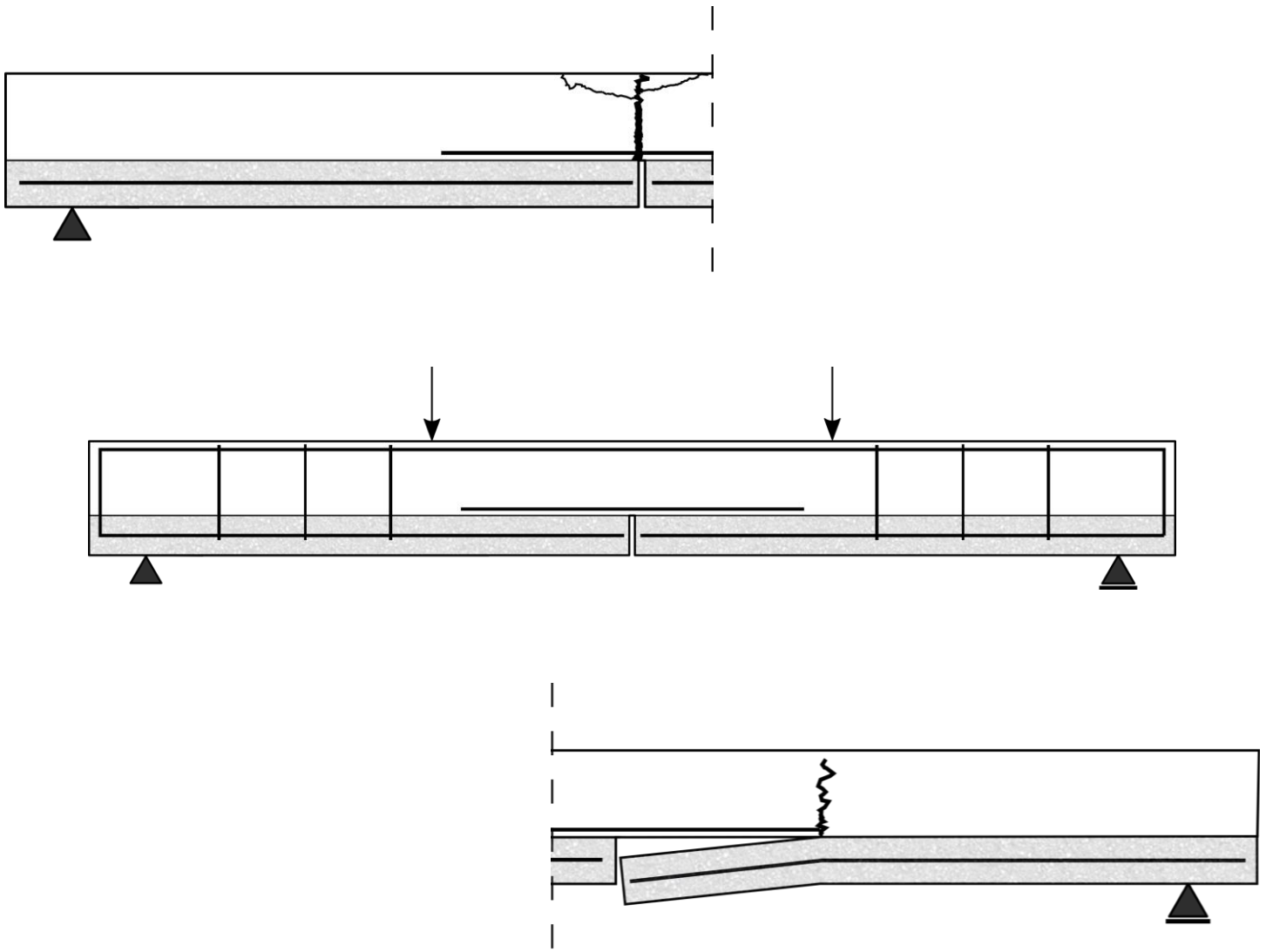

TU Delft

DELFT UNIVERISTY OF TECHNOLOGY

MASTER'S THESIS

Interfacial behavior of hybrid SHCC-Concrete beams with a joint at midspan

Author:
Othman Harrass

Thesis Committee:
Dr. ir. M. Luković (Chair and Daily supervisor)
Prof. Dr.ir. E. Schlangen
Dr. ir. B. Šavija
Dr. ir. C.B.M. Blom
Ir. S. Mustafa

A thesis submitted in partial fulfillment of the requirements for the degree

Master of Science

In Structural Engineering

January 19, 2020

Preface

In this Master thesis, I present the results of my research on the interfacial behavior of hybrid SHCC-concrete beams. Strain Hardening Cementitious Composite (SHCC) is an innovative material that possesses strain-hardening behavior as a result of the multiple cracking behavior. Therefore, this new type of material is an interesting alternative to conventional concrete. This research has led to an enjoyable journey the past year from which I've learned a lot.

First and foremost, I would like to thank Mladena Luković for introducing me to this interesting topic and for her support throughout my research. Furthermore, I would like to thank her for the passion and knowledge she shared during our meetings about this topic.

I would also like to thank Erik Schlangen, Branko Šavija, Kees Blom and Shozab Mustafa for their feedback during the progress meetings. Their critical remarks during these meetings have helped me massively in providing this report. Additionally, I would like to thank Shozab Mustafa for his support with DIANA FEA and for the many discussions we had on this topic.

Furthermore, I want to thank Ton and Albert for their help during the casting and testing sessions. Their flexibility while scheduling for the experimental campaign made it also a lot more easier to plan my research.

Last but not least, I want to thank my family for their support and understanding throughout this project.

Othman Harrass,

Utrecht, January 2020

Delft University of Technology

Abstract

Master of Science

Interfacial behavior of hybrid SHCC-Concrete beams with a joint at midspan

By Othman Harrass

Strain Hardening Cementitious Composite (SHCC) is a new type of concrete that is able to control the crack-width in concrete structures. The application of this material in the tension zone of hybrid concrete structures is thus of interest in practice. The interfacial behavior for these hybrid structures is something that is of importance for the composite action. Therefore, a study is performed to investigate the behavior of the interface in hybrid SHCC-concrete beams. This is done by performing an experimental study on beams with a joint at midspan. Several parameters such as the interface roughness, coupling reinforcement cover, curing method and protruding reinforcement have been investigated. The hybrid SHCC-concrete beams are tested in a four-point bending configuration to obtain a constant-bending moment region along the interface. The crack propagation along the interface and through the SHCC/concrete has been evaluated with the use of Digital Image Correlation (DIC). Furthermore, also a numerical analysis has been performed using DIANA FEA based. The numerical analysis was used to help to determine the experimental campaign. Furthermore, also several experimental samples have been modelled to study the behavior of the beam in more detail and to make recommendations for future modelling of the interface.

Based on the experimental results, the influence of the interface roughness resulted in an increased bond at the interface. This is both seen in an increased bearing capacity and a reduction of the interface and joint opening at equal loads. The profiled interface and holed interface resulted in an increased capacity due to the mechanical interlocking at the interface. The bearing capacity of these samples increased by 78.4% and 54.7% respectively compared to the reference sample (13.9 kN). In case of the profiled sample, no delamination of the interface occurred as the sample failed due to a horizontal crack at the level of the coupling reinforcement. This can be attributed to the localized tensile stresses at the reinforcement level. The last sample with a different interface roughness consisted of epoxy and sand (1-2 mm). For this sample, the bearing capacity increased by 51.8%. The failure of this sample was a combination of interface delamination (initially at the joint) and a horizontal crack through the coupling reinforcement. For all the samples with a different interface roughness, no yielding of the coupling reinforcement occurred.

Several beams with a smooth interface have also been tested by adjusting the reinforcement cover, curing method and applying protruding reinforcement. The influence of the reinforcement cover didn't have an effect on the bearing capacity. However, the interface and joint opening reduced significantly as the eccentricity of the reinforcement bars also reduced. Furthermore, also the effective height increased resulting in lower reinforcement stresses. The influence of a different curing method was investigated by placing the sample in a humidity-controlled (50 %) room to investigate the effect of shrinkage. The results

showed that the bearing capacity remained similar to the reference samples. This can be attributed to the fact that the bond internally was still good, caused by the restraint of the reinforcement bars. However, the deflection of the beam increased as a result of the reduced stiffness by the shrinkage induced cracks.

Finally, one sample consisted of stirrups at a distance of 50 mm from the joint to take up the tensile stresses at the interface (e.g. due to reinforcement eccentricity). The results showed an increase in bearing capacity by 102.7% compared to the reference sample. However, also in this case, no yielding of the coupling reinforcement occurred. The failure of the sample is also caused by the delamination of the interface. Furthermore, as a result of this delamination, fracture of the top part of the SHCC occurred at the location of the protruding reinforcement due to the rotational restraint of the stirrup.

The 2nd part of the study consisted of a numerical analysis. A Coulomb-friction model with an interface tensile strength cut-off is used to model the interface. Based on this, a good correspondence between the experimental results and FE results is found in terms of the bearing capacity and failure mode for the sample with a smooth interface(delamination). However, the crack propagation of the flexural cracks through the concrete and SHCC was substantially different.

The sample with a profiled interface has also been modelled in Diana FEA. This is done by implementing the profiled interface manually in the FE model. The model showed a good correspondence with the experimental results in terms of bearing capacity and interface and joint opening. The crack propagation in the concrete is also similar to the experimental results. The model however doesn't show any flexural cracking in the SHCC layer as a result of the limitation of DIANA FEA. Also, an additional study is done to replicate the behavior of this beam using a smooth interface. Based on this model, it is recommended to use a perfect bond at the interface.

For both these models, the FE model wasn't able to replicate the strain hardening behavior of SHCC. This is due to the limiting material models in DIANA.

Contents

1 Introduction

1.1 Background

Over the last decades, new types of concrete have been developed to improve the limitation of conventional concrete such as the tensile capacity and brittleness. One of those types of concrete is Strain Hardening Cementitious Composites (SHCC) which is a class of fiber reinforced concrete with a high strain hardening capacity due to the fibers being able to bridge the micro-cracks. As a result of this, SHCC leads to a controlled crack situation in reinforced concrete beams which has been investigated in 2017 by Zhekang Huang [1].

In his master thesis, he tested several reinforced concrete samples with and without SHCC in order to investigate the cracking behavior of the hybrid concrete beams (Figure 1-1). The main goal was to find out if the SHCC layer in the tension zone would be able to reduce the crack width to negate the serviceability limit state being decisive for the amount of longitudinal reinforcement. The results showed that the crack width decreased significantly for the hybrid SHCC-concrete beam with a 70 mm layer of SHCC. The beams with a 30 mm SHCC layer in the tension zone had barely any effect on the crack width due to the fact that with a small cover, the cracks are controlled by the longitudinal reinforcement bars. Furthermore, also the bending moment capacity of the beams increased due to the inclusion of the SHCC layer, the 70 mm SHCC layer showed a larger increase of bending capacity compared to the thin layer of SHCC. In practice, where the heights of the beams are larger, this effect becomes less prominent.

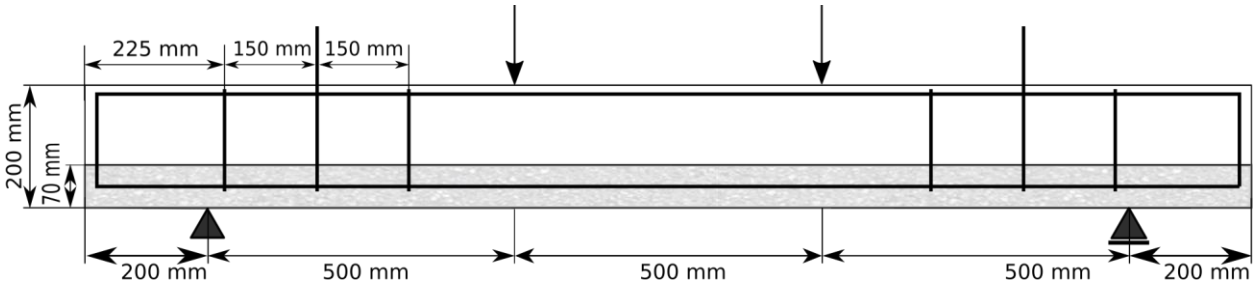

Figure 1-1: Experimental set-up of Zhekang's study

Based on Huang's promising study a follow-up study will be done to investigate the behavior of the interface at a joint. The interface between SHCC and concrete is detrimental to the behavior of these hybrid SHCC-concrete beams. These interface properties can be obtained by direct tensile and shear tests. However, this might lead to localized failure in one of the materials while interface failure is of interest in this study. Therefore, global testing of a structural system will be done to investigate the interface behavior in transferring forces between adjacent SHCC layers at the joint (see Figure 1-2). Inverse modelling will then be done afterwards to obtain the characteristics of the interface in terms of interface tensile and shear strength.

A similar case which can be related to this problem is the Eindhoven parking garage which collapsed in May 2017. The parking garage consisted of a plank floor system ('breedplaatvloeren in Dutch'). These floor systems are made of a prefabricated plate with a lattice girder on which an in-situ concrete topping is cast. Research has shown that the bending moment capacity at the connection of the joint between two prefabricated plates was insufficient to carry the positive bending moment during the construction

stage [2]. The tensile forces which have to be taken by the reinforcement in the prefabricated plate are disturbed at the location of the joint. Therefore, coupling reinforcement is placed at the bottom side of the in-situ concrete layer to transfer the forces to the adjacent plates.

The detailing of this connection between two adjacent plates is an important aspect which depends on different factors such as the anchorage length of the coupling reinforcement bars, protruding reinforcement though the interface, surface roughness at the interface, reinforcement cover, reinforcement diameter and detailing of the reinforcement at the joint. Other factors which influence the behavior of these systems to a lesser extent are the concrete compressive strength, amount of coupling reinforcement and whether the reinforcement is bundled or spaced.

The main differences between the Eindhoven case and the research of this thesis are a higher tensile reinforcement percentage, no plastic spheres, prefabricated panel will be made of SHCC and beam elements will be investigated instead of slab elements. The interaction between the SHCC plate and the cast in-situ concrete is something which has to be taken into account, especially at the joint between adjacent plates. This interface has to ensure composite action by transferring the tensile force due to the positive bending moment. This transfer of forces happens through the coupling reinforcement which enables the interaction of forces between the adjacent SHCC panels. Therefore, it is of interest to study this interface to understand which factors influence this interaction and how it could be improved.

1.2 Problem statement and Thesis objective

In order to benefit from the strain hardening behavior of SHCC to limit the crack-width, the interface between the SHCC and concrete is a crucial factor. Research regarding this interface so far mainly focusses on the interface between SHCC and concrete for concrete repairs. The interface for hybrid concrete structures is something that has not been investigated thoroughly. This interfacial behavior is of importance as delamination of the interface negates the positive effects of SHCC.

Therefore, the objective of this thesis is to investigate the influence of governing parameters on the concrete interface for hybrid SHCC-concrete structures. This is done in a four-point bending configuration with a joint at midspan in order to investigate the interface both in shear and tension. It would be too complicated to investigate all the parameters which influence this joint behavior. Therefore, the main goal is to investigate the interaction at the contact layer and how the bending moment capacity at this joint can be improved by taking into account the anchorage of the coupling reinforcement, interface roughness, reinforcement cover, curing method and the inclusion of stirrups. First, an experimental study will be executed to determine the influence of governing factors. Furthermore, also inverse modelling will be applied to determine the interface tensile and shear strength for future modelling purposes.

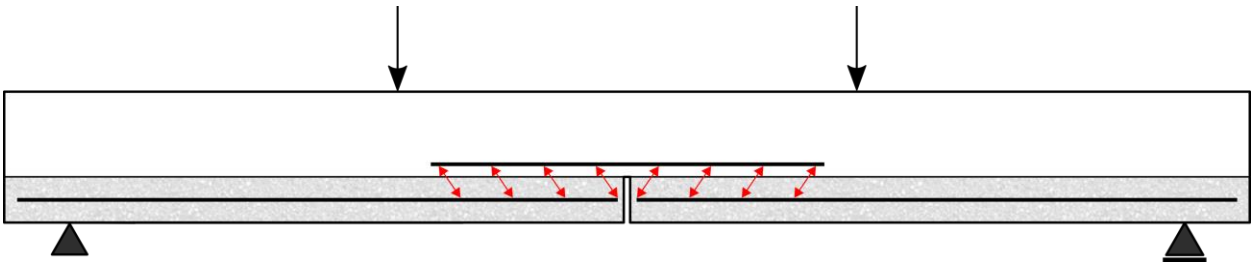

Figure 1-2: Force transfer (compression diagonals) at the interface of a reinforced concrete beam with a middle joint

1.3 Research question

Main question

- *What are the governing parameters for the interfacial behavior of hybrid SHCC-concrete beams and how do they influence the global behavior of these beams?*

Sub-questions

- *How does the profile at the contact area influence the interface behavior and how is this reflected in the cracking pattern?*
- *What is the influence of the curing method on the interfacial behavior?*
- *How does the cover of the coupling reinforcement influence the interfacial behavior?*
- *How do stirrups at the joint influence the interfacial behavior?*
- *What are the tensile and shear capacity of the concrete-to-concrete interface based on inverse modelling?*

1.4 Thesis outline

The outline of this report can be divided into four parts shown in Figure 1-3. The first chapter consists of the thesis background and objectives of this study. In chapter 2 a literature study will be done. First, a literature review on the material SHCC will be done to understand the behavior compared to conventional concrete. The effect of drying shrinkage and hybrid systems will be briefly discussed in the second subchapter. The third subchapter covers the concrete-to-concrete interface. This is done by first taking a look at the codes in the Eurocode. After this, the influence of important factors on the interfacial behavior will be looked at based on researches. Finally, previously done researches which are related to this subject will be elaborated. These researches can be divided into regular hybrid SHCC-Concrete beam (e.g. Zhekang's study) and Hybrid SHCC-Concrete beams with a joint (e.g. Eindhoven case).

In the 2nd part of this study, the experiment will be thoroughly explained. This includes the preparation of the samples, testing method and measuring devices. Detailed drawings of the different samples will be shown. Furthermore, also the experimental results of the hybrid SHCC-concrete beams will be included in this chapter.

The third part elaborates the model which is used to model the beams. The finite element program DIANA will be used for the simulation. A non-linear 2D model is created to simulate the non-linear effect of concrete and steel and their interaction. Important aspects are the concrete-to-concrete interface and the implementation of the reinforcement in the concrete.

In chapter 5, the numerical results of the model are shown. Inverse modelling is executed with the obtained experimental results in the 2nd part of the study. Chapter 6 consists of the conclusion and recommendations which are made based on the results and observations of this study.

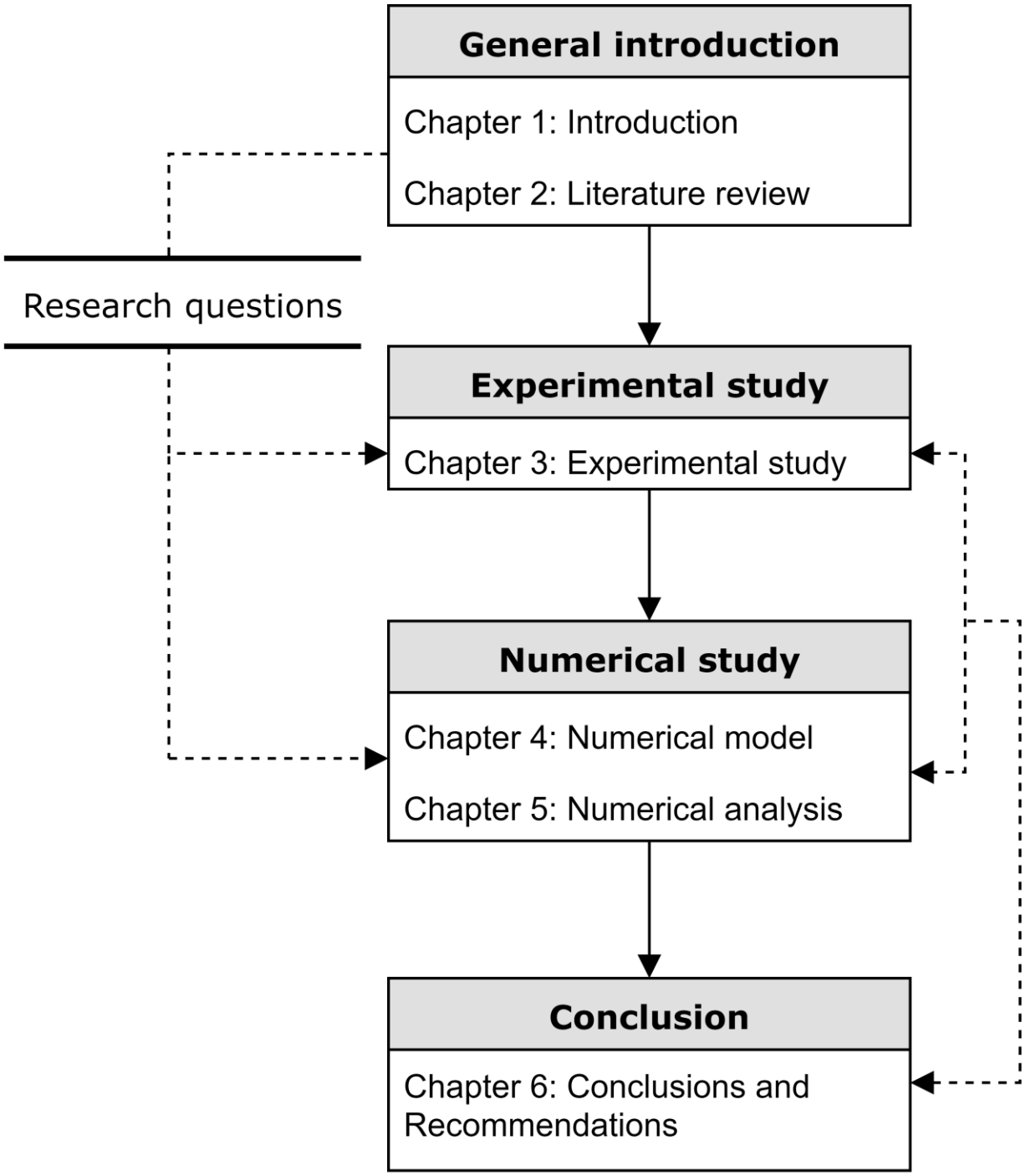

Figure 1-3: Thesis outline

2 Literature review

2.1 Strain Hardening Cementitious Composite

Strain Hardening Cementitious Composites (SHCC) is a type of fiber reinforced concrete which is also known as Engineered Cementitious Composites (ECC). This type of concrete has strain-hardening behavior and multiple cracking properties. These properties can be reached with low fiber content ranging from 1% to 3%. As the first crack appears, the fibers in SHCC bridge this crack by taking up the tensile forces. Due to the tensile pull-out resistance of these fibers, the tensile stress has to increase. As a result of this, a new crack appears at a different location which limits the widening of existing cracks. Because of this crack bridging mechanism, high tensile strain and tensile stresses can be achieved. During the strain hardening, multiple cracks appear as is shown in Figure 2-1. In this figure also the behavior of conventional concrete is shown which exhibits no strain hardening capacity and fails due to the localization of cracks at the weakest area (strain softening behavior).

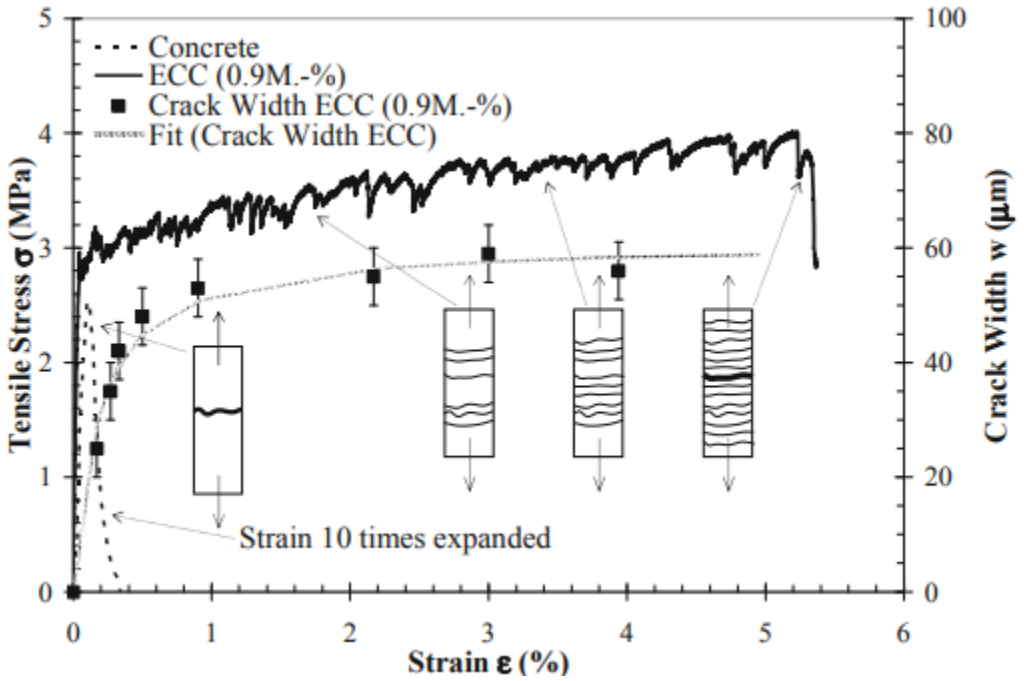

Figure 2-1:Strain-stress diagram of SHCC (Weimann and Li, 2003)

2.1.1 Mechanical properties

Tensile, compressive and flexural tests have been conducted by Victor C. Li [3] to determine the strength of the SHCC samples with a fiber content of 2% (Table 2-1).

Property		Value	Unit
Tensile strength	σ_{fc}	2.5	MPa
Tensile strain	ε_{fc}	0.021	%
Ultimate tensile strength	σ_{cu}	4.6	MPa
Ultimate tensile strain	ε_{cu}	5.6	%
Compressive strength	f_c	68.5	MPa
Compressive strain	ε_c	0.67	%
Stiffness	E	22	GPa
Flexural strength	$\sigma_{f,MOR}$	25	MPa

Table 2-1: Properties of SHCC with fiber content of 2% (Victor C. Li,1997)

The results shown in Table 2-1 clearly demonstrate the strain hardening capacity of SHCC, reaching strain values up to 5.6% which is significantly more than the strain capacity of conventional concrete ($\varepsilon_{cu} = 0.02\%$).

The mechanical properties of SHCC are however dependent on the composition of the SHCC sample. Wang and Li concluded based on tests that the inclusion of fly ash to replace a part of the cement reduced the strain hardening capacity of the SHCC sample while the ultimate strength remained the same [4].

2.2 Influence of SHCC and TRC in Hybrid systems

2.2.1 Drying shrinkage

SHCC has high drying shrinkage characteristics due to its high binder content in comparison with conventional concrete as the volume of coarse aggregates in conventional concrete reduces the amount shrinkage. Drying shrinkage occurs due to the difference in relative humidity between the environment and internal concrete. This relative difference will result in an internal pressure in the concrete which leads to a loss of volume. When SHCC and conventional concrete are placed on top of each other, differential shrinkage will occur at the interface between these two layers due to different casting times and different mix compositions. However, this shrinkage difference will be resisted at the interface resulting in differential shrinkage stresses.

Seok-Joon Jang et al. [5] investigated the shrinkage in SHCC. In his experiment, two SHCC samples and one conventional concrete sample were tested. One of the two SHCC mixes had shrinkage-compensation contents (CSA-based EXA). The shrinkage was measured with shrinkage gauges which were placed inside the samples (see Figure 2-2).

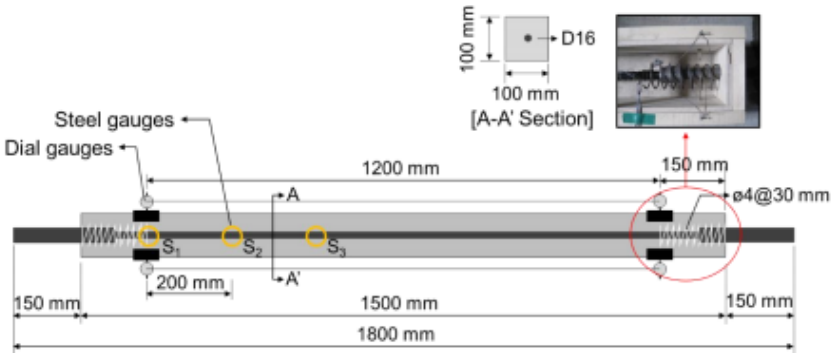

Figure 2-2: Experimental setup (Seok-Joon Jang et al.,2018)

The test results showed that the shrinkage of SHCC (SHCC30) is significantly more than conventional concrete (Figure 2-3). Also, the effect of the CSA-based EXA (SC-SHCC30) can be seen in the result as the sample first expanded (due to the formation of ettringite) before the shrinkage procedure started. Using this reducing shrinkage agent, the shrinkage reduced with 23.3%. However, the final shrinkage value is still considerably more than the shrinkage of conventional concrete.

As a result of these shrinkage differences, stresses at the interface occur before doing any experimental mechanical testing on samples. This might lead to cracking and debonding at the interface between two (different) concrete layers. Also, the different casting time should be considered for the differential shrinkage. Experiments have shown that the bond strength and profile of the interface plays a major role in the behavior at the interface caused by these differential shrinkage stresses. A rough interface profile

will lead to a decreased debonding length and to distributed cracking along the interface as a result of interlocking [6].

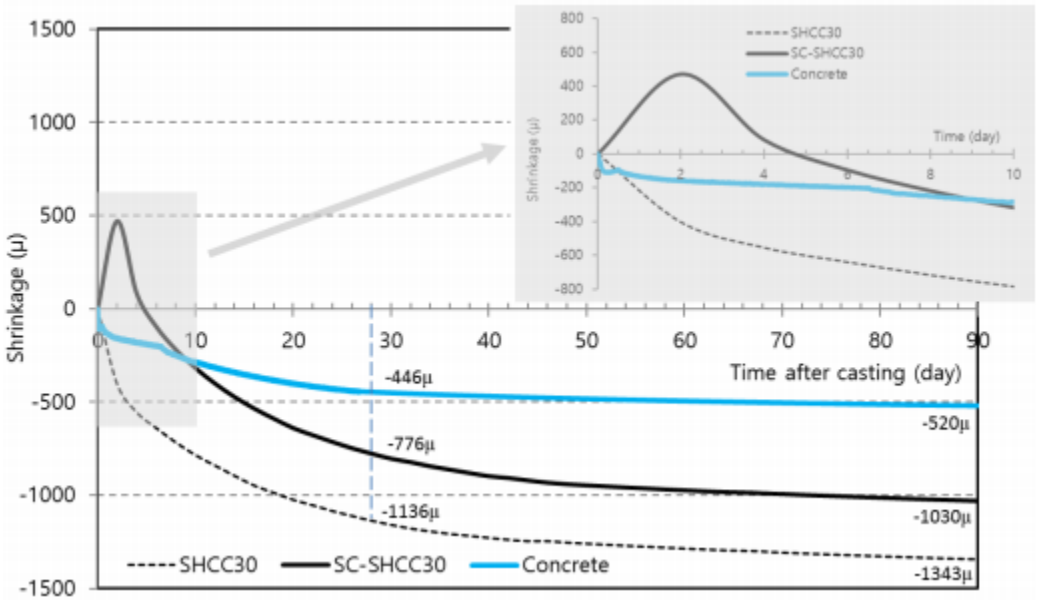

Figure 2-3: Experimental shrinkage results of the 3 samples (Seok-Joon Jang et al.,2018)

2.2.2 Textile-Reinforcement Concrete

Textile-Reinforced concrete (TRC) exhibits strain hardening behavior like SHCC and is therefore also suitable for controlling cracking behavior. This type of fiber-reinforced concrete is able to withstand even higher tensile forces, making it an attractive alternative for the tension zone of reinforced concrete beams.

S. Yin and S. Xu [7] investigated the flexural behavior of reinforced concrete beams with a thin layer of TRC in the tension zone. In total 15 reinforced concrete beams were tested with a 10 mm layer TRC in the tension zone. The surface treatment of the textile was varied between the samples. Samples were impregnated with epoxy or sand or a combination of both. Furthermore, the number of textile layers was varied between 0 and 3. The interface between the conventional concrete and TRC consisted of U-shaped hooks for several samples to check whether bond splitting could be prevented. Finally, also polypropylene fibers were put in the concrete mix for 7 samples. In total 15 beam samples were tested by subjecting them to a four-point bending test as is shown in Figure 2-4.

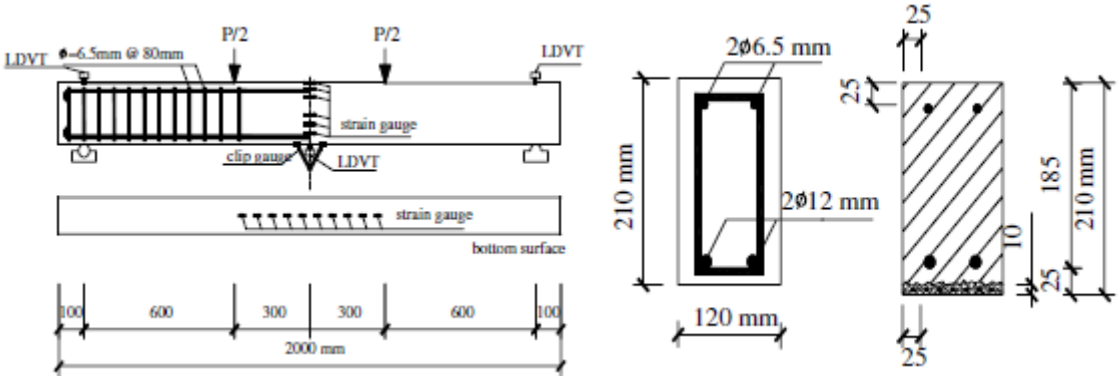

Figure 2-4: Testing configuration and cross-section of the beams (S. Yin and S. Xu,2014)

From the experimental results, the positive influence of the TRC on the flexural capacity of the reinforced concrete beams is shown. The increased capacity was the highest for the samples with three layers of textile and this capacity decreased for a lower amount of textile layers. Also, the crack width decreased for an increasing amount of textile layers (see Figure 2-5 and Figure 2-6). In Figure 2-7, the cracking pattern of two reinforced concrete beams is shown. The distribution of cracks in the TRC layer is better distributed compared to the conventional concrete which is due to the crack bridging mechanism. The samples with one layer of textile failed at the lowest load. All the beams eventually failed due to the textile rupture in the tension zone.

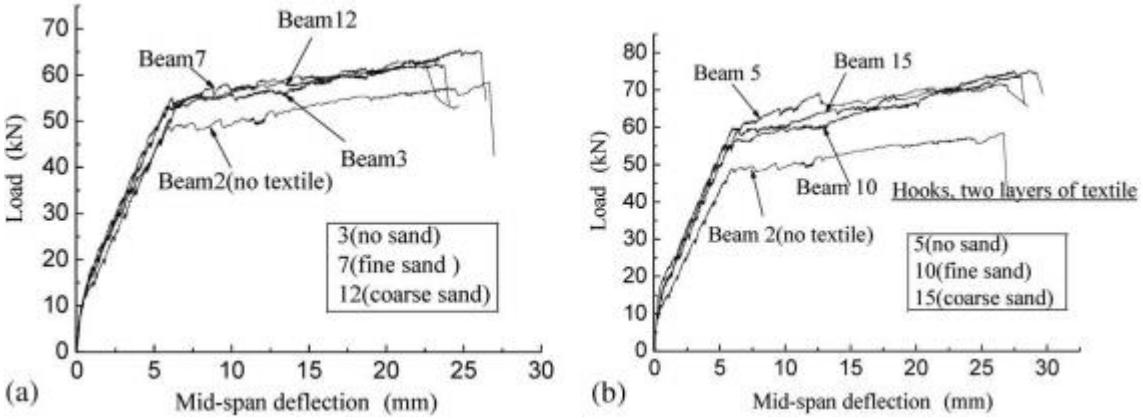

Figure 2-5: Load-displacement graph: (a) one textile layer;(b) two textile layers and hooks (S. Yin and S. Xu,2014)

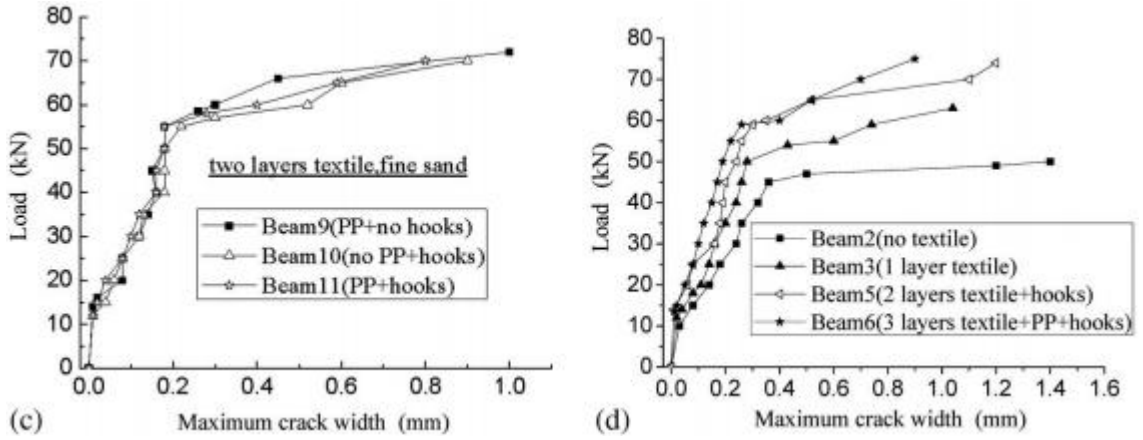

Figure 2-6: Crack width graph:(a) influence of hooks;(b) influence of amount of textile layers (S. Yin and S. Xu,2014)

Figure 2-7: Cracking pattern of the beams:(a) two textile layers;(b) one textile layer (S. Yin and S. Xu,2014)

The effect of the fine sand and coarse sand has no significant effect on the flexural capacity of the reinforced beams. However, these surface treatments did affect the crack width control of the beams. Treating the surface of the textile with coarse sand decreased the crack width significantly while the effect of fine sand improved the crack width to a lesser extent (Table 2-2). This table shows the loading capacity and crack width at the initial cracking (P_{cr} and w_{cr}), yielding (P_y and w_y) and ultimate load (P_u). D_y is the deflection at midspan at yielding of the reinforced concrete beam.

Specimen ID	Surface treatment of textile + number of textile layers	P_{cr} (kN)	%	w_{cr} (mm)	%	P_y (kN)	%	D_y (mm)	%	w_y (mm)	%	P_u (kN)	%	μ (ϕ_u/ϕ_y)	%
Beam 1	0	10.8	0	0.04	0	48.6	0	5.5	0	0.8	0	58.6	0	5.0	0
Beam 2	0	9.8		0.03		48.9		6.0		1.2		59.0		4.9	
Beam 3	Impregnated with epoxy + 1	11.4	11	0.02	43	53.8	10	6.6	15	0.43	57	64.5	10	4.7	5
Beam 4	Impregnated with epoxy + 1	11.8	15	0.01	71	54.0	11	6.5	13	0.42	58	65.6	12	5.1	3
Beam 5	Impregnated with epoxy + 2	12.0	17	0.01	71	59.5	22	6.2	8	0.32	68	74.7	27	5.0	1
Beam 6	Impregnated with epoxy + 3	13.5	31	0.01	71	59.0	21	6.5	13	0.26	74	85.0	45	4.6	7
Beam 7	Impregnated with epoxy +fine sand + 1	12.0	17	0.02	43	55.0	13	6.5	13	0.22	78	63.0	7	4.5	9
Beam 8	Impregnated with epoxy + fine sand + 1	12.2	18	0.01	71	56.0	15	6.3	10	0.24	76	65.8	12	4.6	7
Beam 9	Impregnated with epoxy + fine sand + 2	12.6	22	0.01	71	58.6	20	6.9	20	0.26	74	75.9	29	4.8	3
Beam 10	Impregnated with epoxy + fine sand + 2	12.3	19	0.01	71	57.0	17	6.5	13	0.30	70	75.0	28	4.6	7
Beam 11	Impregnated with epoxy + fine sand + 2	12.8	24	0.01	71	58.0	19	6.8	18	0.28	72	75.3	28	5.0	1
Beam 12	Impregnated with epoxy + coarse sand + 1	11.8	15	0.01	71	55.0	13	6.6	15	0.32	68	62.0	5	4.7	5
Beam 13	Impregnated with epoxy + coarse sand + 1	12.0	17	0.01	71	55.0	13	6.7	17	0.28	72	63.8	9	4.5	9
Beam 14	Impregnated with epoxy + coarse sand + 1	12.3	19	0.01	71	55.1	13	6.0	4	0.22	78	63.6	8	4.8	3
Beam 15	Impregnated with epoxy + coarse sand +2	12.2	18	0.01	71	58.9	21	6.5	13	0.24	76	71.8	22	4.5	9

Table 2-2:Crack width and load capacity for al samples (S. Yin and S. Xu,2014)

2.3 Interface

In practice concrete-to-concrete interfaces are present for applications like the rehabilitation and strengthening of existing concrete structures. However, the interface is also an important aspect for the construction of new structures. In these new concrete structures, composite concrete structures consist of in-situ and prefabricated concrete which have different casting ages. The bond strength of this interface is an important aspect for the force transfer between the different concrete layers. This bond strength is influenced by the moisture content, presence of cracks, protruding reinforcement and curing method [8].

This interface is of high important for the behavior of a reinforced concrete beam with a middle joint which hinders the transfer of forces. As a result of this, the tensile force in the reinforcement has to be diverted through the interface by a shear mechanism consisting of compressive struts and tensile ties. This force transfer mechanism for a beam with a joint depends besides on the earlier mentioned factors also on the anchorage length of the coupling reinforcement, the eccentricity of the two different reinforcement bars (see paragraph 3.1.4.2) and interface roughness.

2.3.1 Shear resistance at the interface according to Eurocode

In the Eurocode the shear stress between concrete cast at different times must satisfy the following requirement

$$\upsilon_{Edi} \leq \nu_{Rdi} \tag{2.1}$$

The resistance of the interface depends on several factors which are combined in one formula according to NEN-EN 1991 (art. 6.2.5(1))

$$\nu_{Rdi} = c * f_{ctd} + \mu * \sigma_n + \rho * f_{yd} * (\mu * \sin(\alpha) + \cos(\alpha)) \leq 0.5 * \upsilon * f_{cd} \tag{2.2}$$

- f_{ctd} is design value of the concrete tensile strength

- c and μ are factors which take into account the roughness of the interface. The factor c is the cohesion coefficient and μ is the friction of the interface
- σ_n is the normal force acting perpendicular to the interface, in case a tensile force is acting on the interface c should be taken as 0
- υ is a reduction factor which takes into account the cracks due to the shear force
- α is the angle of the anchorage (see Figure 2-8)

The factors c and μ depends on the roughness of the interface and can be classified as very smooth, smooth, rough and indented. As the roughness of the interface increases, also the factors c and μ increase.

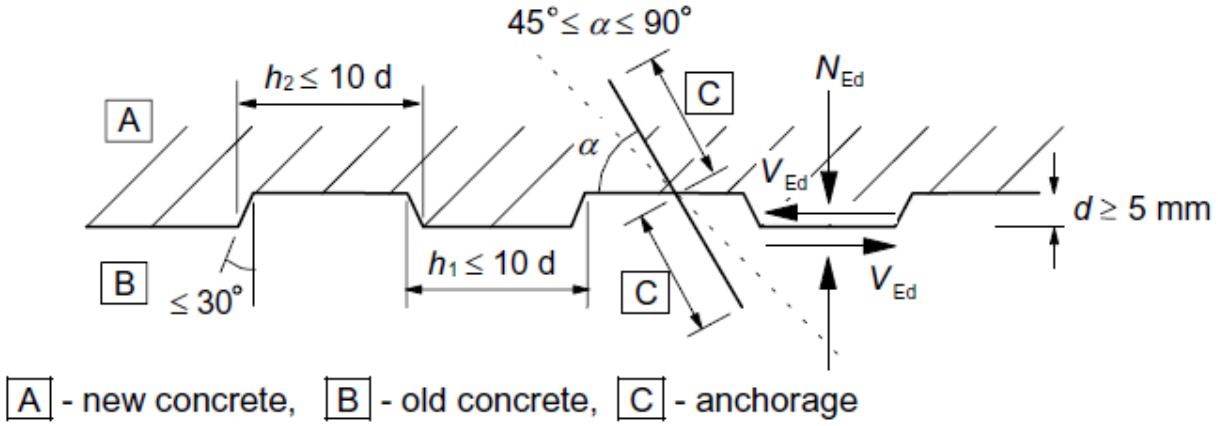

Figure 2-8: Example of a dented interface according to NEN-EN 1992

For a four-point bending test with a composite beam, the design shear stress at the interface results from the bending moment. This shear stress can be calculated using equation 2.3, with d defined as the effective depth of a concrete section.

$$V_{Ed,interface} = \frac{M_{Ed}}{0.9 * d} \tag{2.3}$$

This shear stress along the interface will be influenced by the perpendicular stresses on the interface which will occur at the interface due to the curvature of the hybrid beam. These tensile stresses occur because the SHCC layer and concrete top layer deform in the same manner but have different stiffnesses.

2.3.2 Influencing parameters

Interface roughness

The roughness of the interface is an important aspect for the transfer of the forces between two concrete layers. By increasing the roughness, the mechanical interlocking of this interface increases owing to an increased contact area. This will then result in a higher shear strength of the interface [9]. Different ways to roughen the interface are sandblasting, drilling, scraping and applying a dented profile.

G.A.P.G. van Zijl and H. Stander [10] investigated the effect of the interface roughness on the interfacial bond between SHCC and conventional concrete. This is done by investigating the shear and tensile characteristics of the interface. The testing set-ups are shown in Figure 2-9.

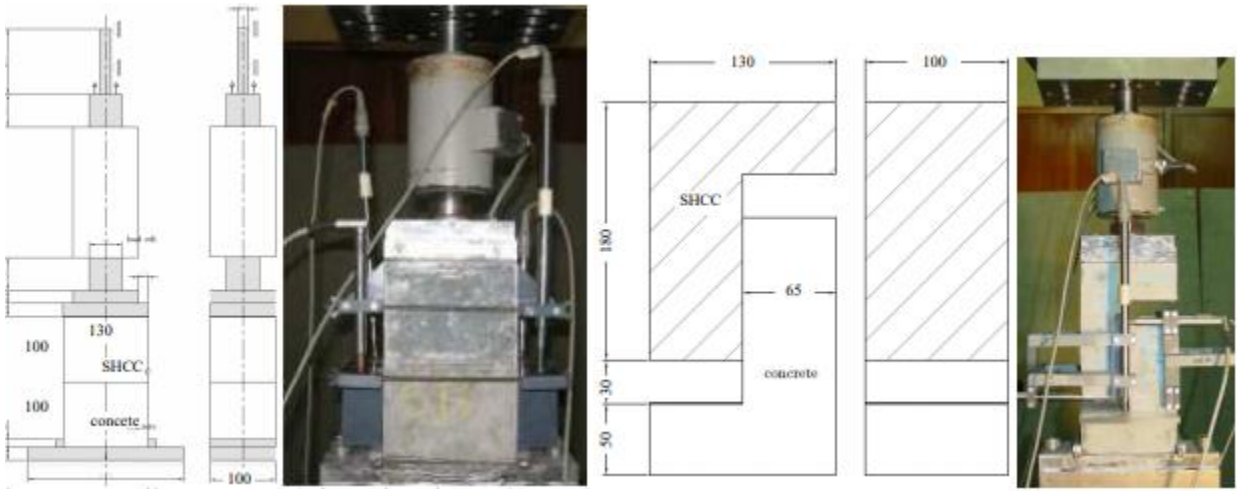

Figure 2-9: Tensile and shear test set-ups (G.P.A.G. van Zijl and H. Stander,2009)

The moistening method, testing age and mechanical preparation of the substrate have been taken into account while investigating the interfacial bond. The surface preparation included light scraping, sandblasting, drilled holes and cast grooves. The different concrete layers were cast in a Perspex mould at different casting times. The experimental results showed an increasing shear resistance for greater surface roughness. Sandblasting showed the best result both in tension as in shear while the interface with no surface treatment showed the worst results. The interface tensile strength of the interface is significantly lower than the tensile strength of the SHCC or conventional concrete as can be seen in Figure 2-10. For the sandblasted interface, localized failure occurred in the SHCC layer while for other surface preparations the interface delaminated.

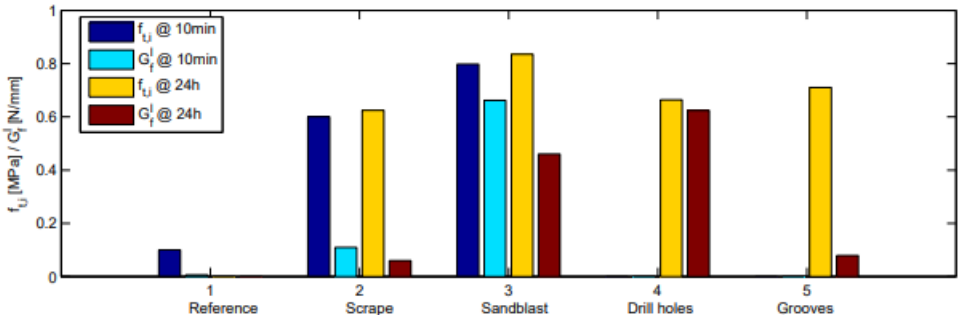

Figure 2-10: Maximum tensile strength for different surface preparations (H. Stander,2007)

Reinforcement diameter and concrete cover

The diameter of the reinforcement bar and concrete cover are important aspects for the interface behavior (SHCC-concrete behavior). These factors influence the splitting behavior and bond strength at the interface. T. Kanakubo [11] investigated the influence of size effect in ECC. He concluded that the bond strength reduced with increasing reinforcement bar diameter. Furthermore, he also concluded that the bond strength increased with increasing concrete cover/rebar diameter ($^{c}/_{d_b}$) ratio.

These results are based on a pullout test shown in Figure 2-11. Teflon sheets are added to prevent lateral movement of the SHCC specimen. Graphs showing the influence of the reinforcement diameter and concrete cover are shown in Figure 2-12.

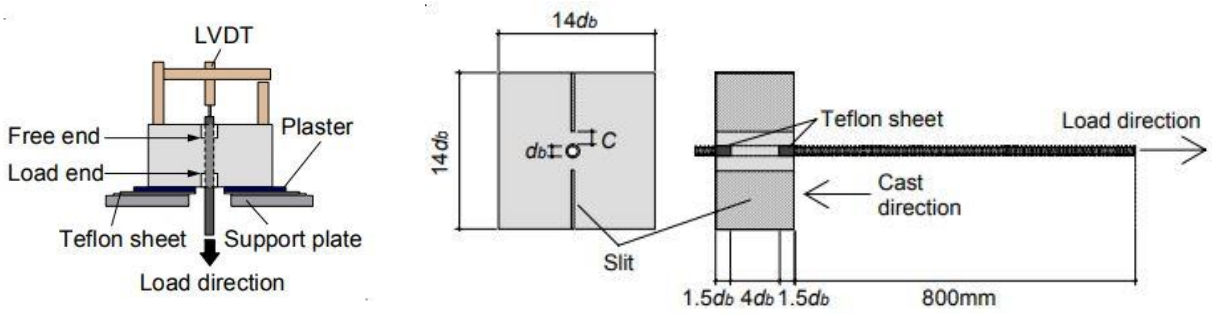

Figure 2-11:Test set-up (T. Kanakubo, 2012)

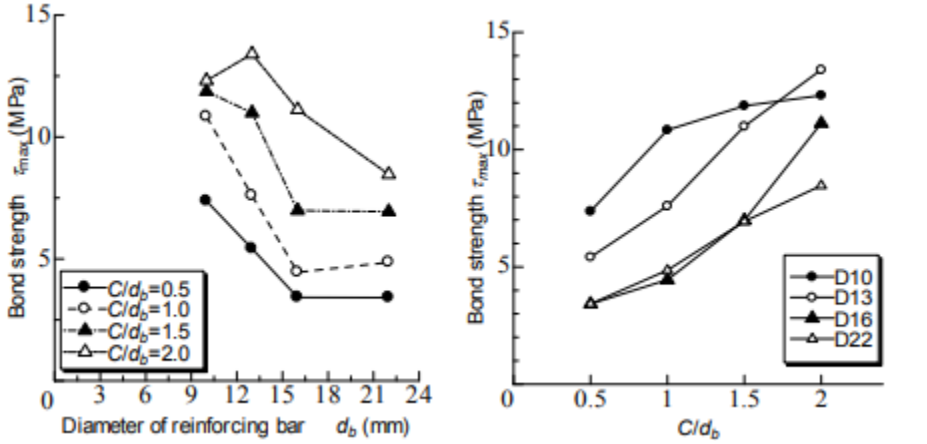

Figure 2-12: Influence of rebar diameter and concrete cover on bond strength (T. Kanakubo, 2012)

Friction

The shear friction at the interface is an important factor for the determination of the interface shear strength. The friction is expressed by the friction coefficient which can range from 0.3 – 0.8 [9]. This friction coefficient multiplied by the perpendicular normal stress gives the contribution to the interface shear strength. Compressive stresses (positive normal stress) will have a positive effect on the interface tensile strength while negative normal stresses can lead to the delamination of the interface which negates the effect of the interface friction. M.E. Mohamed et al. [12] determined the friction coefficient for different interface roughnesses. The lowest friction coefficient was found for the smooth surface while the transverse roughened interface had the highest friction coefficient. In Figure 2-13, the results for different roughnesses are shown. The friction coefficient can be determined by the slope of the experimental results.

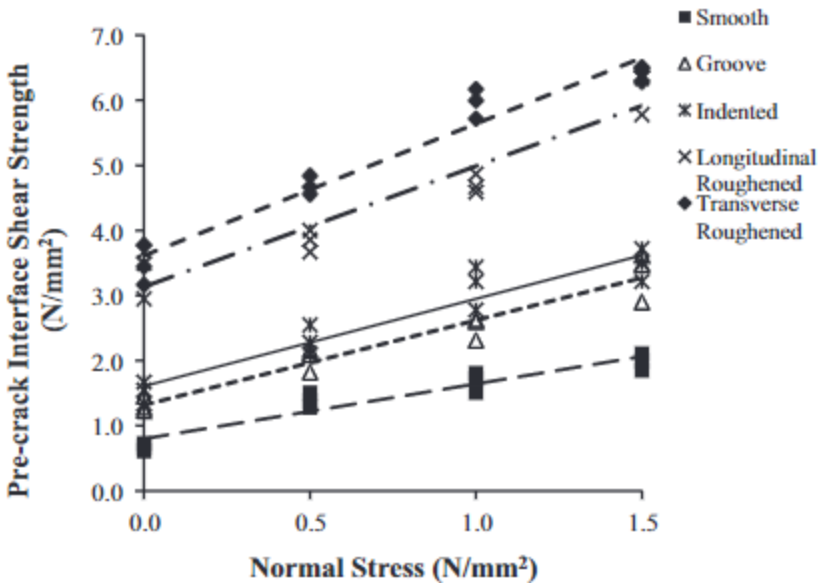

Figure 2-13: Determination of friction coefficient of different roughness (M.E. Mohamad et al., 2014)

Protruding reinforcement

The effect of protruding reinforcement through the interface has been investigated by M.E. Mohamad and I.S. Ibrahim [9]. The friction and cohesion parameters of the interface remained the same compared to the smooth interface (see Table 2-4). However, the interface shear strength of the beams increased significantly which can be explained by the clamping stress resulting from the dowel action of the reinforcement. The results of the experimental analysis are shown in Table 2-3.

Surface type	Specimen	Peak shear load (kN)	Average peak shear load (kN)	Interface slip at peak shear load (mm)	Interface shear strength (N/mm²)	Average interface shear strength (N/mm²)
Smooth or "left as-cast"	S1	55.10	60.30	1.62	0.61	0.67
	S2	65.40		1.50	0.73	
	S3	60.40		1.06	0.67	
Transverse roughened	T1	340.00	311.77	5.73	2.06	1.89
	T2	310.10		3.85	1.39	
	T3	285.20		3.97	2.22	
Projecting steel reinforcement	L1	185.00	170.10	3.50	3.78	3.46
	L2	125.30		1.57	3.45	
	L3	200.00		5.38	3.17	

Table 2-3: Effect of protruding reinforcement on the interface shear strength (M.E. Mohamad and I.S. Ibrahim, 2015)

Surface type	Normal stress, σ_n (N/mm²)	Clamping stress ($\rho . f_{yd}$) (N/mm²)	Splitting tensile strength, f_{ct} (N/mm²)	Friction coefficient, μ		Concrete cohesion, c	
				Experimental in Figure 5, μ_{exp} (from best fit line)	Cl. 6.2.5(2) Eurocode 2	Experimental in Figure 5, c_{exp} ($c = C/f_{ct}$) (from best fit line)	Cl. 6.2.5(2) Eurocode 2
Smooth or "left as-cast"	0	-	2.99	0.84	0.60	0.27	0.20
	0.5						
	1						
	1.5						
Transverse roughened	0			2.02	0.70	1.21	0.40
	0.5						
	1						
	1.5						
Projecting steel reinforcement	0	1.41		0.87	0.60	0.24	0.20
	0.5						
	1						
	1.5						

Table 2-4: Concrete cohesion and friction coefficient for different surface types (M.E. Mohamad and I.S. Ibrahim, 2015)

2.4 Hybrid SHCC-Concrete systems

2.4.1 Hybrid SHCC-Concrete beams

Changli Yu et al. [13] investigated the influence of SHCC in the tension zone by comparing a flat shaped and U-shaped SHCC layer. The SHCC mix consisted of fine silica sand as a replacement of the coarse aggregates. Furthermore, 80% of the cement was replaced with fly ash. PVA fibers were used with a total volume of 2%. The casting of SHCC was done in wooden moulds. Due to the high workability of the mix, no internal vibration was needed. A grooved profile was applied on the surface of the SHCC layer while it was still fresh to increase the bond at the interface. The U-shaped SHCC layer was also cast by using wooden moulds (see Figure 2-14). The formwork of the U-shaped SHCC layer consisted of 3 planks connected with 2 hinges. In order to prevent leaking of water during casting, the inner surface of the mould was sealed. First, the bottom part was cast with the use of two strips to be able to cast a higher thickness of SHCC in the middle part. The remaining 2 planks were then folded to cast the two outer sides of the U-shape after the bottom part reached the required stiffness.

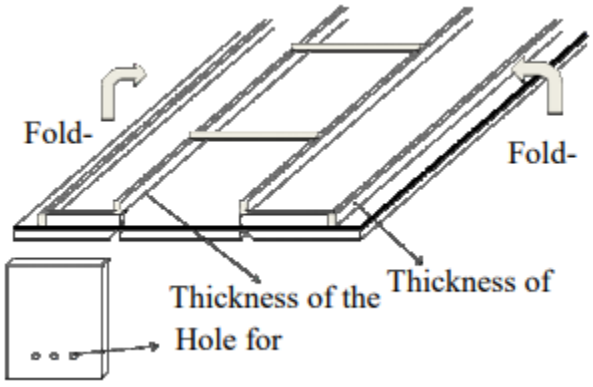

Figure 2-14: Formwork for the U-shaped SHCC Layer (Changli Yu et al., 2010)

Two beam samples were tested by doing a four-point bending best as is shown in Figure 2-15. Mild steel stirrups were also placed to prevent shear failure of the beams in the shear region.

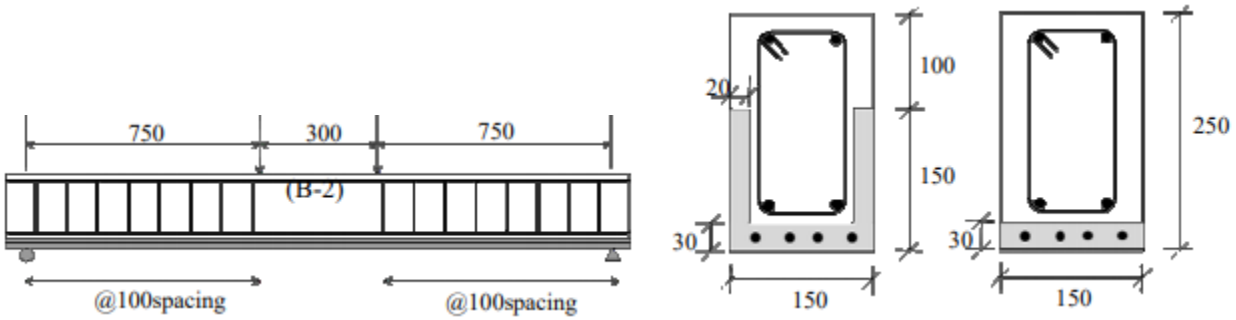

Figure 2-15: Experimental set-up (Changli Yu et al., 2010)

The U-shaped SHCC layer showed an increasing shear resistance at the interface area. Debonding failure didn't occur for this shape as all the samples had a flexural failure which resulted in concrete crushing. During testing, multiple fine cracks appeared at the tension zone which is a result of the strain hardening capacity of SHCC (Figure 2-16).

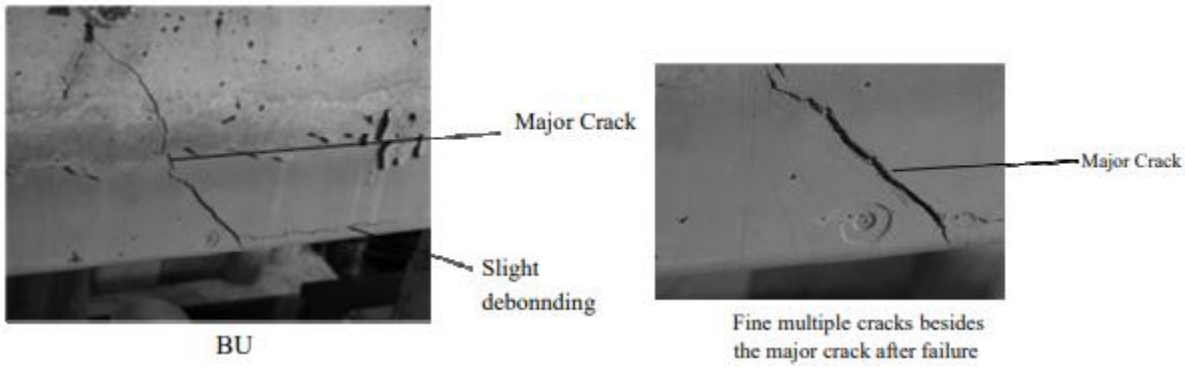

Figure 2-16:Failure of the U-shaped beam (Changli Yu et al., 2010)

The interface layer of the flat plate SHCC sample debonded during the application of the load. This interface debonding is due to the tensile stress exceeding the interface tensile strength of this interface area. During the experiments two different failure modes could be identified. The first failure, debonding failure, happened as the crack propagated along the interface between the SHCC and conventional concrete. The other failure mode which was identified during the experiment was flexural failure. Also, in this 2nd failure mode debonding occurred over a part of the contact area, however, it remained stable. As the load increased during the experiment, concrete crushing led to the eventual failure of the beam sample. This type of failure was expected based on the preliminary structural calculations. The experimental results showed an increase in capacity of 40% in case flexural failure occurred. Debonding failure showed a decrease of loading capacity compared to the theoretical design load (Figure 2-17). However, while in this research debonding failure was one of the major failure mechanisms for the flat SHCC layer, factors influencing this interface bond strength haven't been taken into account such as the roughness of the interface.

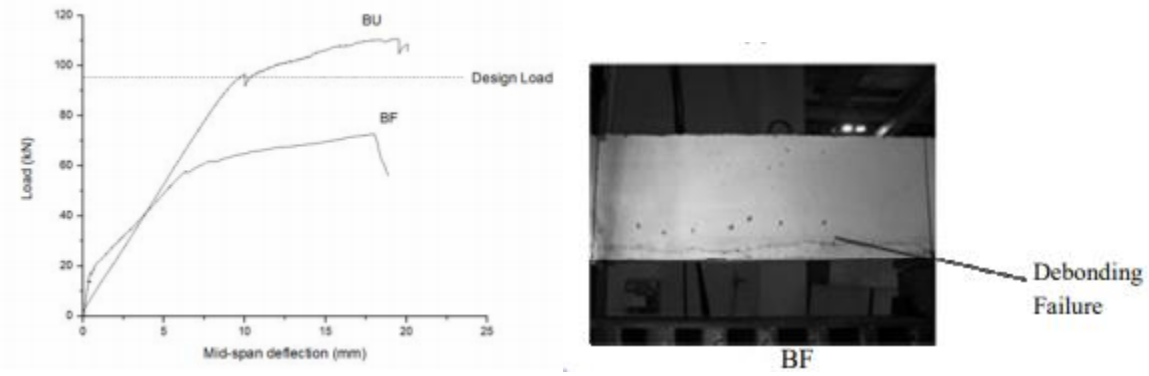

Figure 2-17: Debonding failure of flat SHCC sample (Changli Yu et al., 2010)

Hae Jun Yang et al. [14] investigated the flexural performance and cracking behavior of a reinforced concrete beam with a layer of expansive SHCC in the tension zone. The cement of the SHCC mix was partially replaced with calcium sulfoaluminate and expansive admixtures to control the shrinkage of SHCC. The drying shrinkage of SHCC is about 150% larger compared to the shrinkage of conventional concrete [15]. Furthermore, also water was sprinkled on the samples to maintain a wet condition to reduce the drying shrinkage. The thickness of the SHCC layers was 20 mm and 40 mm. All the beams were tested by doing a four-point bending test based on a displacement-controlled method (Figure 2-18).

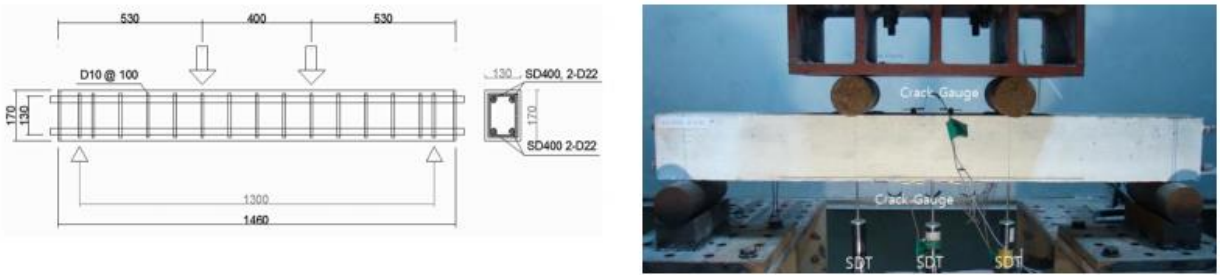

Figure 2-18: Experiment configuration (Hae Jun Yang et al., 2011)

The test results showed an increase of flexural capacity by 10% of the beam with an expansive SHCC layer of 20 mm (Figure 2-20). The 40 mm expansive layer showed a lower increase of capacity while the deformation capacity of the beam increased. The crack width of the mix with expansive admixtures had a decreasing crack width compared to the conventional concrete mix. Also, by increasing the thickness of the expansive SHCC layer a lower maximum crack width was achieved. The failure of the two expansive SHCC samples is shown in Figure 2-19. The sample with an expansive SHCC layer of 20mm showed debonding at the interface due to initial transverse bending cracks. These transverse cracks resulted in the ultimate failure of the beam. The sample with the 40mm layer showed better strain distribution. While interface cracks appeared, the ultimate failure was due to the diagonal cracks resulting in shear failure of the beam.

Figure 2-19: Failure of the strengthened samples with a 20mm SHCC layer (top) and 4 0mm SHCC layer (Hae Jun Yang et al., 2011)

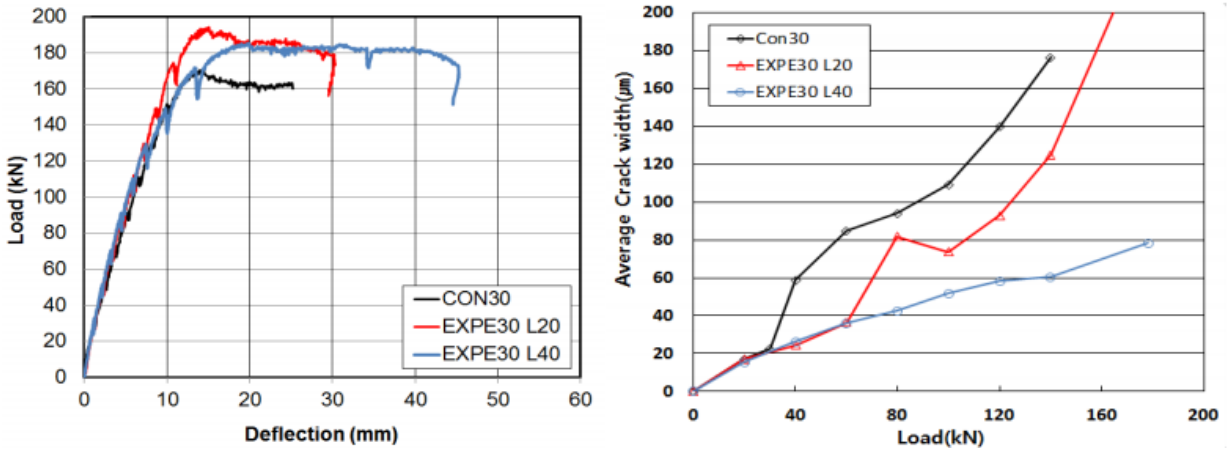

Figure 2-20: Load-displacement and crack width curve (Hae Jun Yang et al., 2011)

The shear failure of the 40mm expansive SHCC layer sample was due to the insufficient shear reinforcement. By preventing the shear failure, an increased bending moment capacity of the 40mm SHCC layer sample can be achieved compared to what is found in this study. Furthermore, as the results don't show a reference beam with a layer of SHCC without expansive admixtures, the effect of these expansive admixtures can't be linked to the decrease of crack width. A decrease in crack width was already expected due to the strain hardening capacity of SHCC.

Huang [1] did a similar experiment where he tested several reinforced concrete samples with different thicknesses of SHCC layers. The thickness of the SHCC layers was 30 mm and 70 mm. Two samples of each thickness were tested where one variant had a self-healing agent. To compare the result also two regular reinforced beams were cast to act as control beams. The cross-section of the samples with SHCC is shown in Figure 2-21. First, the SHCC was cast to the desired thickness. To obtain the required reinforcement cover, SHCC spacers were placed before the casting procedure started. After the SHCC was cast, a plastic sheet was placed on top of it to prevent evaporation. After 14 days, the plastic sheets were removed and the interface was roughened with a steel brush to improve the bond. The conventional concrete was then cast on the SHCC layers which were then left to harden for 33 days. The longitudinal reinforcement percentage in the samples was kept minimal to evaluate the cracking behavior of the samples during testing. Furthermore, to prevent shear failure, stirrups were placed in the shear region. Digital image correlation was used to visualize the crack propagation of the beams. Also, Linear Variable Data Transformers were placed on the reinforced concrete beam samples to measure the vertical displacements.

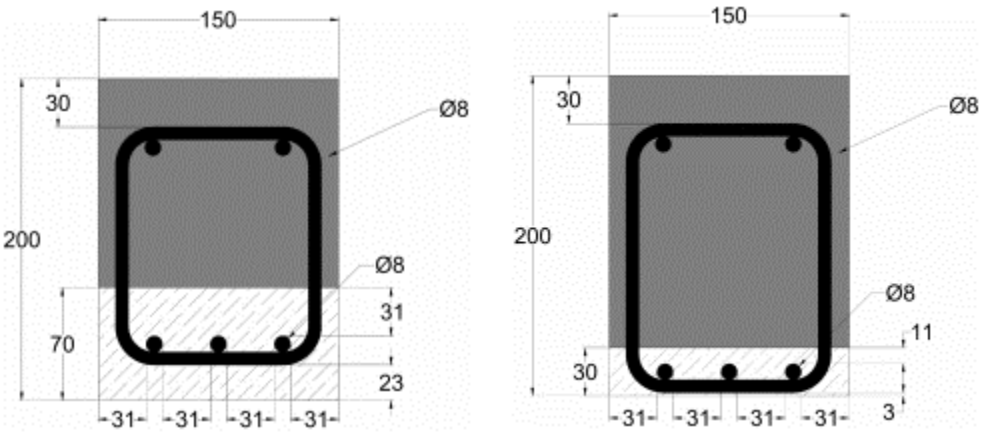

Figure 2-21:Cross-section of the two different SHCC samples (Huang, 2017)

The samples were tested by using a four-point bending configuration (see Figure 1-1). The results showed an increase in flexural capacity of the samples with a SHCC layer compared to the control beams. The cracking pattern of the beam is shown in Figure 2-22. The reinforced concrete sample with a 70 mm SHCC layer increased by 26% while the 30 mm SHCC layer sample increased by 17% (Figure 2-23 and Figure 2-24). This is contrary to the result of Hae Jun Yang et al. [14], which showed a lower increase of flexural capacity of the larger SHCC thickness layer. However, those results failed in shear which resulted in a lower capacity. The displacement in Huang's result was lower compared to Hae Jun Yang's result which is due to the different amount of reinforcement. The low displacement capacity of the 70 mm SHCC sample (Figure 2-23) is a result of the limitation of the measuring devices.

The effect of the SHCC layer on the crack width was only found in the samples with a SHCC layer of 70 mm (Figure 2-23). The samples with a 30 mm SHCC layer didn't have any effect on the crack width as the crack width was already small in the control beams.

The same results were also found by Hae Jun Yang where the higher SHCC layer exhibited a linear increase of crack width with a smaller slope (before the crack increases significantly due to failure) while for the thin layer of SHCC the decrease of crack width is minimal (or zero) with some irregular behavior.

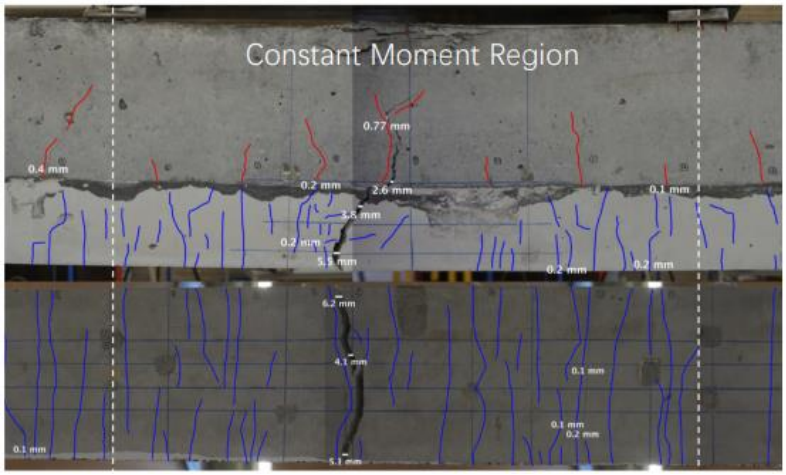

Figure 2-22: Cracking pattern during testing (side view and bottom view)

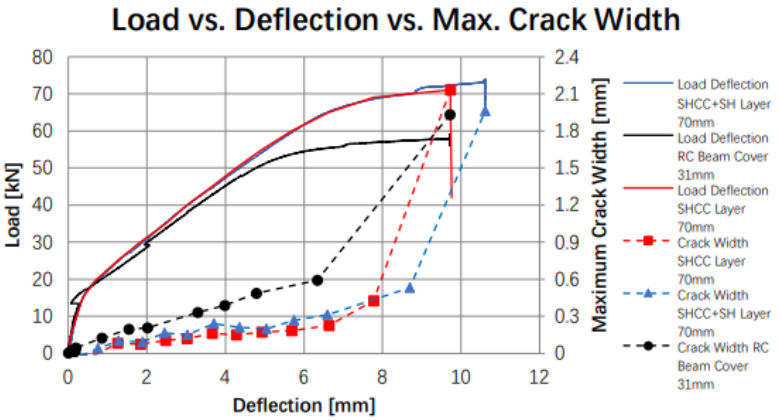

Figure 2-23: Load-deflection and crack width graph for 70 mm SHCC layer (Huang,2017)

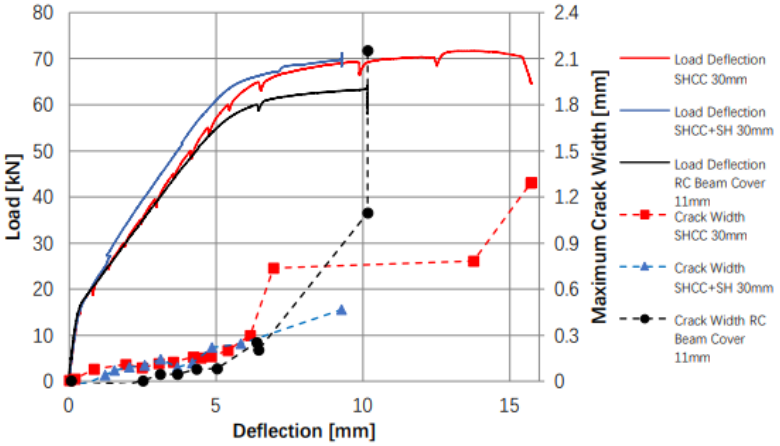

Figure 2-24:Load-deflection and crack width graph for 30 mm SHCC layer (Huang, 2017)

2.4.2 Hybrid systems with interface problem

In May 2017, the parking garage in Eindhoven collapsed. The collapse of this parking garage was investigated by two independent companies (TNO and Hageman Consultancy) to identify the failure mechanism. These studies have shown that the collapse of the parking garage started on the fourth storey due to the failure of the BubbleDeck floor at the joint between the adjacent plates. This failure occurred due to the positive bending moment on the floor system. As a result of this bending moment, tensile stresses occurred in the plate reinforcement while the upper part of the system was in compression (Figure 2-25). These tensile forces need to be transferred at the joint between the adjacent plates. Therefore, coupling reinforcement is placed at this joint to transfer these forces which results in shear stresses at the contact area.

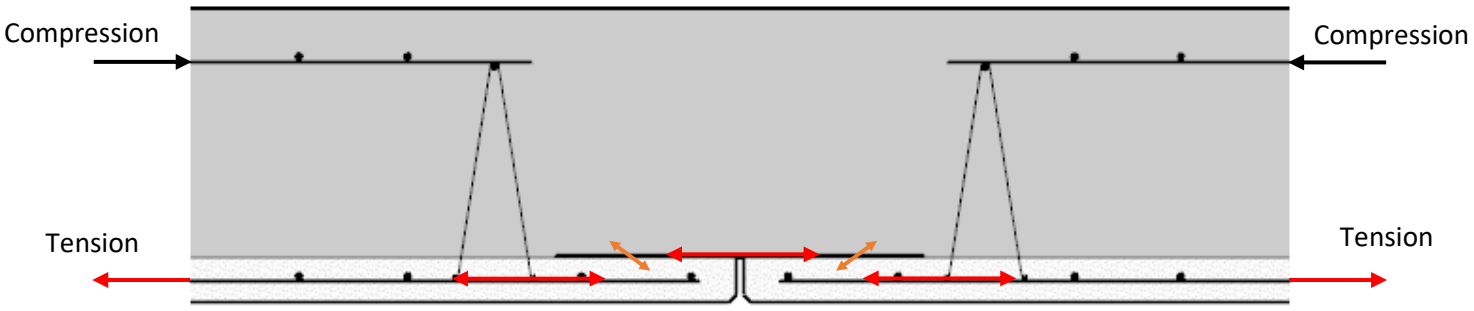

Figure 2-25: Forces due to the bending moment (note: weight reducing balls are left out)

To investigate this joint, Hageman consultancy has executed experiments to determine the bending moment capacity of the section at the joint. The samples were similar to the BubbleDeck system used at the parking garage in Eindhoven. Hageman consultancy [16] first tested 7 samples with the coupling reinforcement, compressive concrete strength and position of weight-reducing balls at the joint as variables (Figure 2-26). The compressive strength was varied between 22.6 and 37.8 MPa. The coupling reinforcement was varied by increasing the area and bundling the bars for several samples. The weight-reducing balls at the outer edges of the samples were removed to prevent shear failure. A four-point bending test was executed to achieve a constant bending moment at the joint.

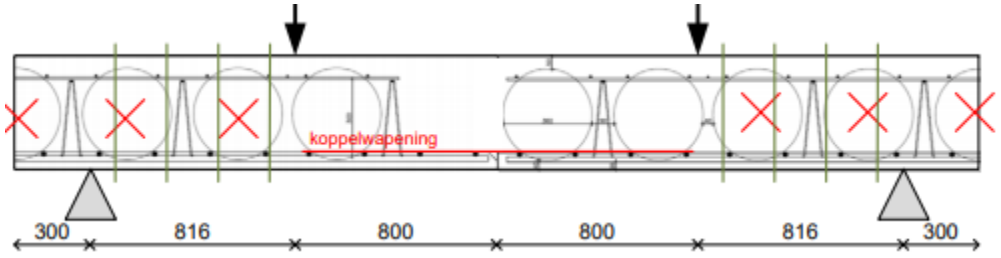

Figure 2-26:Experiment setup (Hageman consultancy, 2017)

All the samples failed due to the failure of the contact area caused by the pull-out of the lattice girder and delamination of the contact area. The maximum bending force ranged from 94 to 120 kNm. No correlation was found between the increase of bending moment with regard to the varying compressive concrete strength and amount of coupling reinforcement. Therefore, they concluded that the influence of the compressive concrete strength and amount of the coupling reinforcement had no significant influence on the capacity of these samples. A calculation was also made to determine the bending moment resistance by assuming yielding of the coupling reinforcement based on equation 2.4.

$$M_y = A_s * f_s * \left(d - 0.52 * \frac{A_s * f_s}{d - 0.8 * f_{cm.cube}}\right) \quad (2.4)$$

Based on these values, the bending moment capacity which was derived from experimental results (Figure 2-27) is 33% of the capacity compared to the analytical calculation.

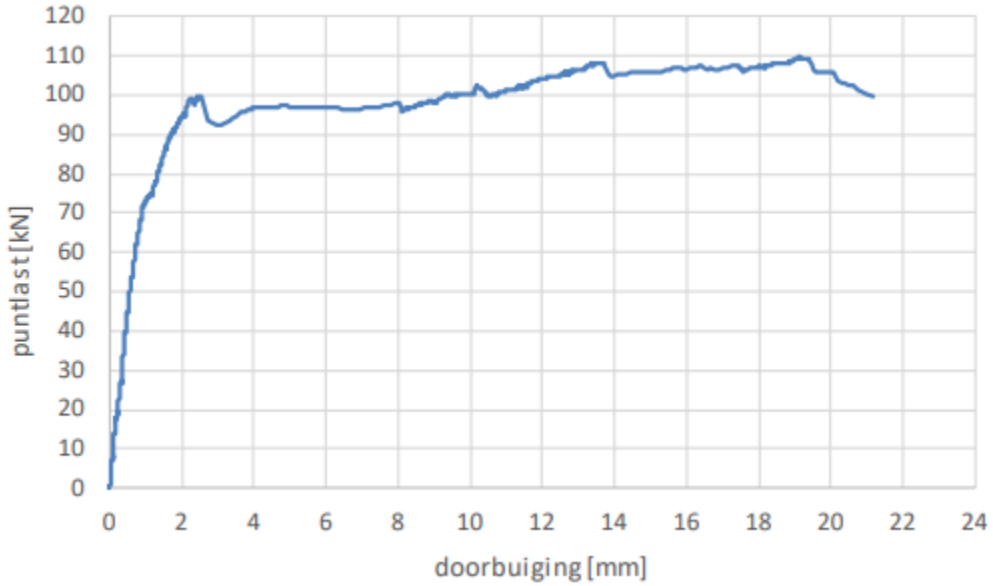

Figure 2-27: Load-displacement diagram of one of the samples (Hageman consultancy, 2017)

Another experiment was executed to determine the shear resistance of the contact area (Figure 2-14). Several samples have been tested with varying concrete compressive strength (22.7 and 37.5 MPa). Furthermore, also the lattice girder was removed from several samples to identify the interface behavior.

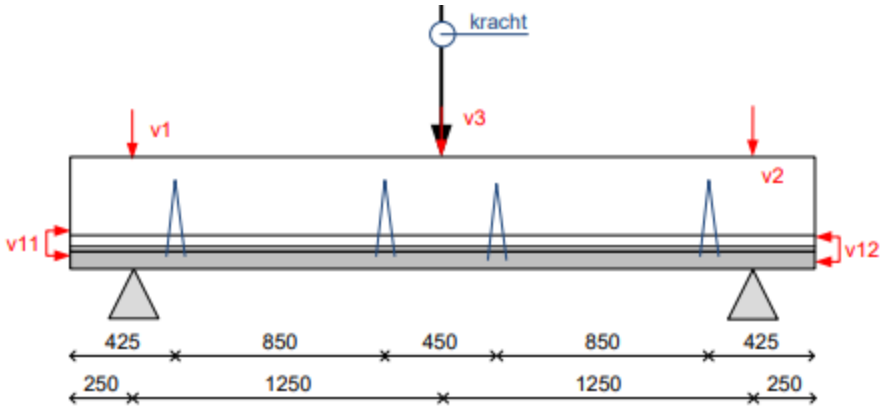

Figure 2-28: Interface test set-up for stirrups variant (Hageman consultancy, 2017)

The results showed that the shear capacity of the samples without the lattice girder was close to zero as the contact area delaminated before the experiment could be executed. The samples with a lattice girder had a shear capacity at the contact area ranging from 0.46 MPa to 0.64 MPa depending on the compressive concrete strength and roughness of the prefabricated plate.

However, this shear capacity is influenced by the lattice girder as the capacity of the interface without the stirrups was found to be zero. These shear values are however relatively low compared to values given in literature [17].

TNO [2] also looked at the anchorage of the coupling reinforcement. They concluded that the anchorage length of the coupling reinforcement at the parking garage in Eindhoven wasn't sufficient as they didn't take into account all the factors specified in NEN-EN 1992-1-1. These factors are related to the following

- As the coupling reinforcement was directly placed on the prefabricated plate, the anchorage length had to be increased with a factor ~1.4
- As the coupling reinforcement had a favorable concrete cover (the thickness of the plate), the anchorage length should have been reduced with a value of 0.85
- The reinforcement bars were bundled which requires an increase of anchorage length with a factor of 1.4-2
- At some places, the reinforcement was placed beside the weight-reducing balls which could lead to a reduced bonding which has to be taken into account with a factor of 1.05-1.1

The 2nd point suggests that the anchorage length should be reduced by 0.85 due to the favorable concrete cover. This concrete cover should however not take into account the thickness of the prefabricated plate and therefore no reduction of the anchorage length is allowed. Furthermore, the 3rd point takes into account the bundling of the reinforcement bars and suggests an increase with a factor of 1.4-2. However, based on the experimental result of Hageman consultancy [16], the anchorage length isn't influenced by the bundling of the coupling reinforcement bars. These results were found by comparing the load capacity of several beams with an identical amount of reinforcement but different reinforcement configuration (see Table 2-5).

Based on these studies, the governing parameters for the interfacial behavior are the interface roughness, protruding reinforcement and anchorage length of the coupling reinforcement. The concrete compressive strength and amount of coupling reinforcement doesn't seem that have a large effect on the interfacial behavior.

A lot of research has been done by Hageman on these hybrid SHCC-Concrete slabs with a joint to investigate the interfacial behavior. This research also consists of studies done by other researchers which are all shown in Table 2-5. In this table the dimension, coupling reinforcement configuration, interface preparation, load capacity and failure mode are shown for these hybrid concrete systems with a joint.

			Research											
			Stehle-3	Stehle-5	Stehle-6	TF450BR	TF280BG	ZG 1 – 3	ZR 1 – 3	R1 – R3	T1 – 3	T4 – 6	T10 – 12	Lundgren
Dimension	**Height**	(mm)	300	300	300	450	280	300	300	300	300	300	300	250
	Width	(mm)	500	500	500	800	800	1000	1000	1000	1000	1000	1000	500
	Height concrete top layer	(mm)	225	225	225	380	210	230	230	230	230	230	230	200
	Distance between loads	(mm)	1000	1000	1000	1600	1600	1600	1600	1600	1600	1600	1600	1300
Coupling reinforcement	**Length**	(mm)	1000	1000	600	1550	1550 1150	1400	1400	1700	1400	1700	1400	730
	Diameter	(mm)	10	10	10	16	16 10	12	12	16	12	16	16	8
	Area	(mm^2)	3Ø10	3Ø10	3Ø10	8Ø16	4Ø16 2Ø10	7Ø12	7Ø12	7Ø16	7Ø12	7Ø16	7Ø16	3Ø8
	Cover	(mm)	0	0	0	0	0	0	0	0	0	0	0	8
	Reinforcement percentage	*(%)*	0.21	0.21	0.21	0.53	0.57	0.34	0.34	0.64	0.34	0.61	0.61	0.1
Protruding reinforcement	**Distance to joint**	*(mm)*	95	–	95	425	300	400	400	400	400	400	400	365
	Depth in plank	*(mm)*	45	–	45	21	21	37	37	35	27	25	25	35
Interface	**Preparation**	—	–	–	–	–	–	–	Rough	–	–	–	–	–
Results	**Load capacity**	*(kN)*	159	127	154	244	128	216	240	436	214	302	225	40
	Failure mode	—	Yielding	Interface	Yielding	Interface	Interface	Yielding	Yielding	Yielding	Interface	Interface	Interface	Yielding

Table 2-5: Results of other researches for hybrid concrete beams with a joint

K. Lundgren et al. [18] analyzed the behavior of a lap splice in a lattice girder system using DIANA FEA. The model is shown in Figure 2-29. The interface between the precast and in-situ cast layers has been modelled using a friction model which is defined according to equation 2.5.

$$|\tau| + \mu * (\sigma_n - f_a) = 0 \tag{2.5}$$

Shear tests and wedge split tests were experimentally and numerically done to obtain the parameters for the friction model of the interface. The adhesive strength (f_a) was calibrated from the wedge split results. The friction coefficient (μ) was obtained using the results of the shear test which ranged from 1.33-3.7 depending on the roughness of the interface. These friction values are relatively large compared to the values found by other researchers [9].

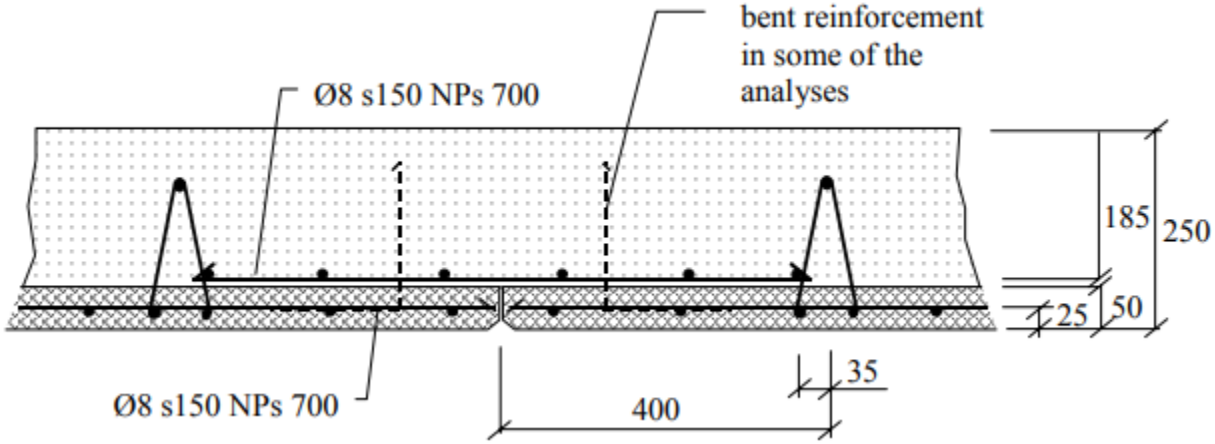

Figure 2-29: Modelled joint of the lattice girder system (K. Lundgren, 2003)

In the finite element model, the influence of bent reinforcement and the adhesive strength were investigated. In Figure 2-30 the FEA results are compared with the experimental results. The right diagram was based on a model without any adhesive strength at the interface. Due to having no adhesive strength at the interface, the interface failed before yielding of the coupling reinforcement occurred.

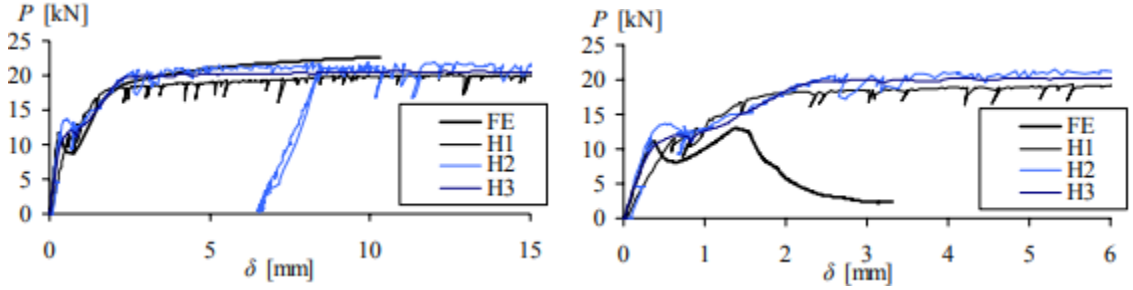

Figure 2-30: Experimental and FEA results with adhesion strength (L) and without adhesion strength (K. Lundgren, 2003)

In the model with bent reinforcement as shown in Figure 2-29, the girders showed a larger deformation capacity. However, the location of the bent reinforcement was crucial. Placing them nearby the middle joint resulted in instability as a result of the high stresses. Placing the bent reinforcement further away from the middle joint, resulted in a deformation capacity which is twice as large compared to other analyses.

Yielding of the specimen can be attributed to a low amount of reinforcement. This reinforcement percentage is calculated in equation 2.6.

$$\rho = \frac{A_s}{b * d} = \frac{3\text{Ø}8}{500 * 0.9 * 200} = 0.168\% \tag{2.6}$$

This low reinforcement percentage is close to the value of the minimum reinforcement ratio. As a result of this low reinforcement ratio, flexural failure happens at a low load capacity. Therefore, interface failure isn't analyzed as the sample might have had an interface failure for a larger amount of reinforcement.

J. Stehle et al. [19] investigated the performance of concrete slabs with a joint. These composite concrete slabs consist of a precast plank on which a top layer of in-situ concrete is cast with a compressive strength of 35 MPa (28-day cube strength). On top of the precast plank, coupling reinforcement with a length of 1000mm is placed to take up the tensile forces at the joint section. The reinforcement mesh of these samples is shown in Figure 2-31.

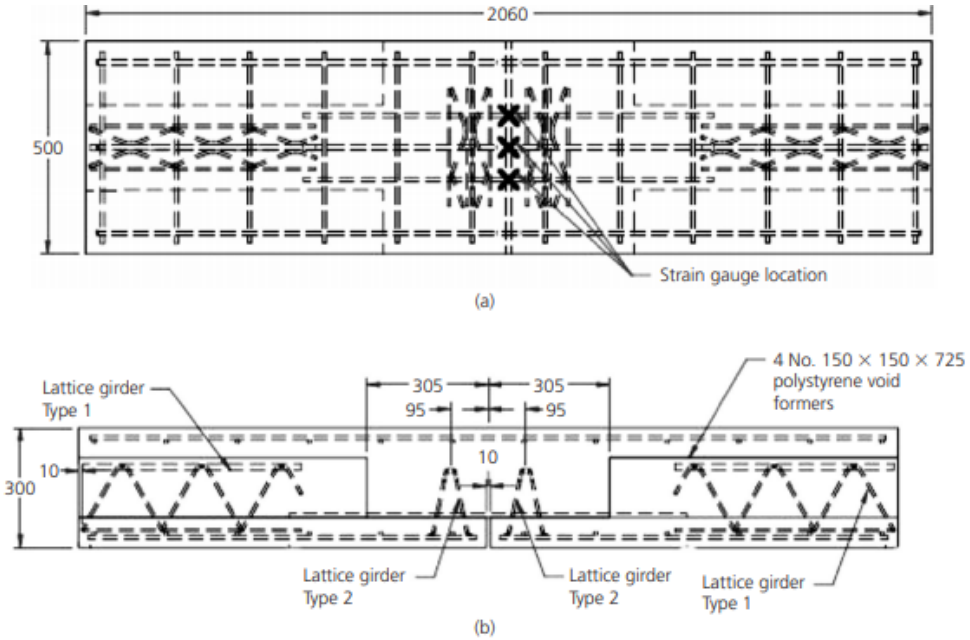

Figure 2-31: (a) top view of reinforcement mesh; (b) side view of reinforcement mesh (J. Stehle et al., 2010)

The samples were tested in a four-point bending configuration with the load being applied by a dynamic-static actuator in a load-controlled way (see Figure 2-32).

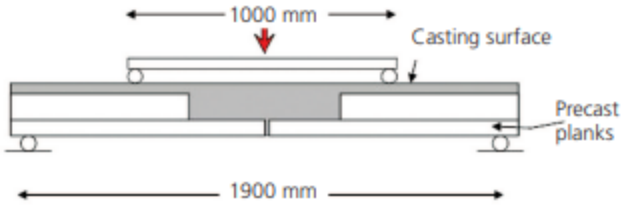

Figure 2-32: Experimental set-up (J. Stehle et al.,2010)

Strain gauges were used to measure the strain of the coupling reinforcement bars. The vertical displacement of the slabs was measured using Linear Variable Differential Transformers (LVDTs). In total 7 samples were tested with 5 of these samples being composite slabs. Only three of these 5 samples were tested by applying a constant positive bending moment on the beam. One of these three samples (specimen 3) consisted of a lattice girder close to the joint as is shown in Figure 2-31. Specimen 5 was cast without any lattice girder. The last sample (specimen 6) is identical to specimen 3 but with the coupling reinforcement reduced to 600 mm. Table 2-6 summarizes these samples.

Specimen	Type	Bending	Lattice girder	Lap length	
3	Composite	Positive	Yes	1000	mm
5	Composite	Positive	No	1000	mm
6	Composite	Positive	Yes	600	mm

Table 2-6: Test specimens (J. Stehle et al.,2010)

The experimental result showed that the lattice girder through the interface is of high importance for the failure of the samples. Specimen 3 failed due to the yielding of the reinforcement (see Figure 2-33) while specimen 5 failed due to the interface opening at a lower load capacity (see Figure 2-34). Specimen 6 with the decreased anchorage of the coupling reinforcement reached the same capacity as specimen 3 and also failed due to yielding of the reinforcement as is shown in Figure 2-35. However, this result cannot be used to conclude that the anchorage length of the coupling reinforcement doesn't have an influence on this interfacial behavior as in both cases the lattice girder prevented the opening of this interface.

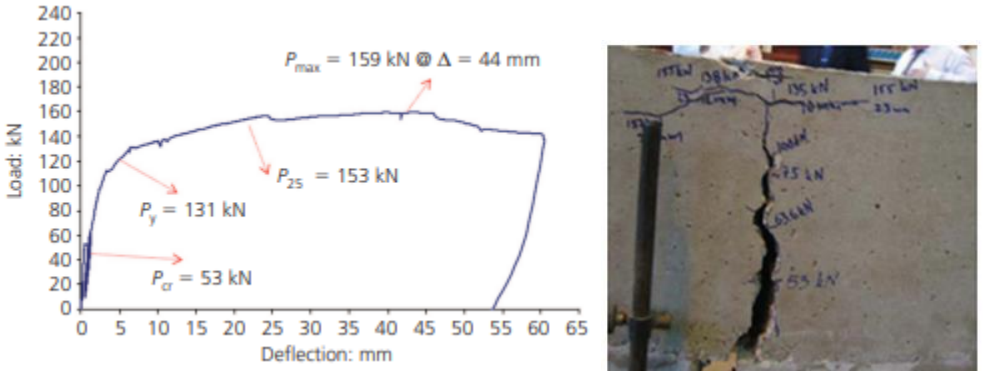

(a) (b)

Figure 2-33: (a) Load-displacement graph of specimen 3; (b) failure mode of specimen 3

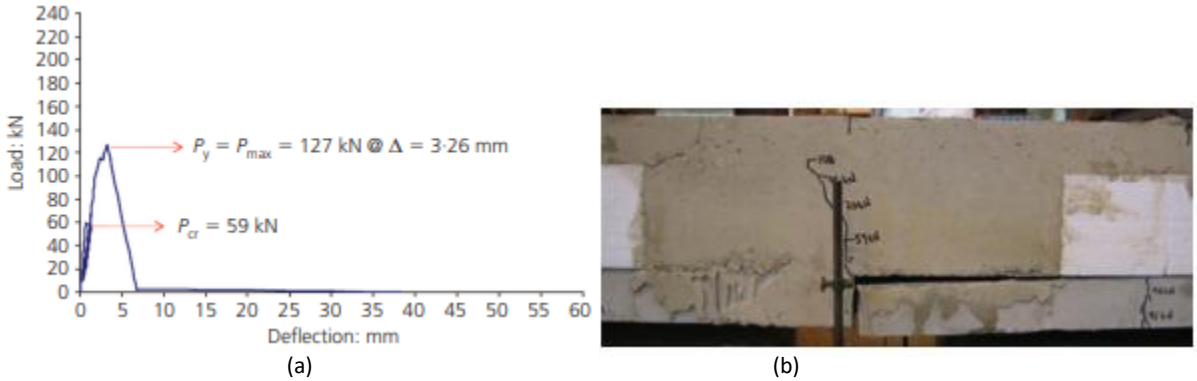

(a) (b)

Figure 2-34:(a) Load-displacement graph of specimen 5; (b) failure mode of specimen 5

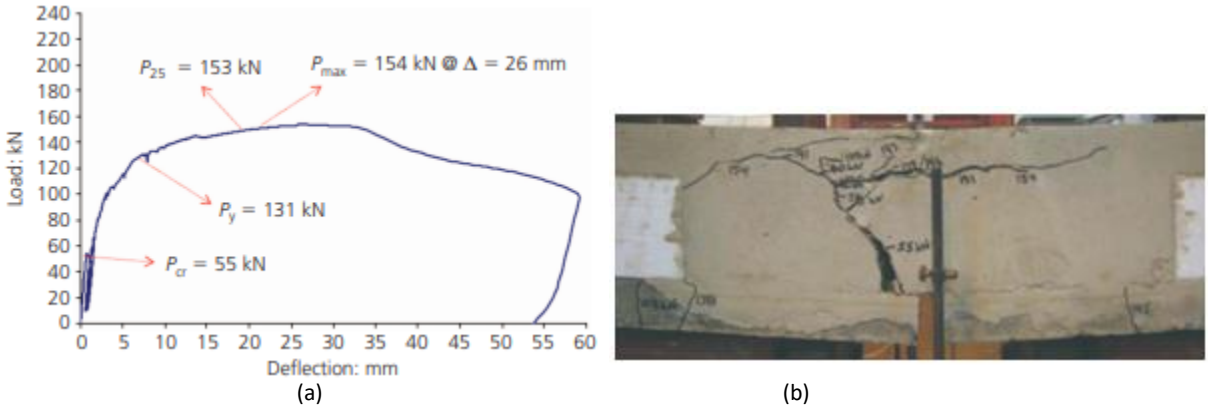

(a) (b)

Figure 2-35:(a) Load-displacement graph of specimen 6; (b) failure mode of specimen 6

2.5 Conclusion

Based on this literature study, the following conclusions can be drawn:

- The drying shrinkage of concrete and SHCC is investigated by Seok-Joon Jang et al. [5]. From these results, it can be concluded that the drying shrinkage is larger for SHCC. This is something that has an effect on the interfacial behavior as it will induce differential shrinkage stresses.
- The interface roughness is an essential parameter for the interface tensile and shear strength. H.Stander [10] investigated this by doing small scale tests for SHCC-concrete interfaces. From these results, the interface characteristics increased significantly by increasing the surface roughness. However, the influence of the interface roughness on the interfacial behavior for large scale tests of SHCC-concrete beams hasn't been researched.
- Based on the research from Hageman and TNO on the failure of the Eindhoven parking garage, several conclusions can be drawn:
    - Protruding reinforcement has a significant effect on the capacity of hybrid concrete beams as delamination of the interface can be prevented.
    - The anchorage length of the coupling reinforcement is an important factor for the behavior of these hybrid systems.
    - The configuration of the coupling reinforcement doesn't seem to have an effect (reinforcement area and bundled or non-bundled reinforcement bars).
    - The concrete compressive strength has barely any effect on the interfacial behavior

3 Experimental Study

3.1 Pre-study

Based on the literature study, the critical parameters for the behavior of the interface between the SHCC and conventional concrete are the interface roughness, curing method, protruding reinforcement and reinforcement cover. The dimension of the beams tested by Huang had a length of 1500 mm, height of 200 mm and thickness of 150 mm. The height of the beam was divided into a bottom SHCC layer with a thickness of 70 mm and a concrete top layer of 130 mm. As in this experiment the behavior at the middle joint is of importance, the influence of shear reinforcement should be investigated. Another important factor is the accommodation of the anchorage of the coupling reinforcement. The length between the loading points should be long enough in order not to anchor the coupling reinforcement.

An analytical study will be done to investigate whether removing the stirrups will still lead to flexural failure while taking into account the accommodation of the anchorage of the coupling reinforcement. The distances between the support and loading points are kept variable (see Figure 3-1) to determine the critical distance at which flexural failure happens prior to shear failure.

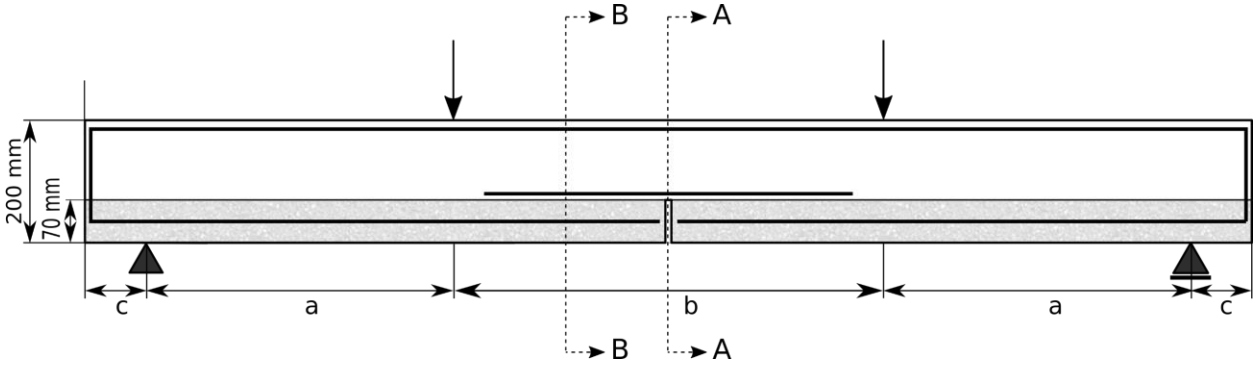

Figure 3-1: Experimental set-up

3.1.1 Analytical calculation

An analytical calculation will be made to predict the bending and shear capacity of the reinforced hybrid SHCC-concrete beam. The position of the point loads will be kept variable to determine the optimum position. The material properties used for the calculations are shown in Table 3-1 and Table 3-2.

	Young's modulus	Compressive strength	Tensile strength			Area
	E (MPa)	σ_c(MPa)	f_y(MP	σ_t(MPa)	σ_u(MPa)	$A(\mathrm{mm}^2)$
Reinforcement	200000	–	550	–	–	$3 * \pi * 4^2$
Concrete	32000	33	–	2.56	–	130 x 150
SHCC	18000	32	–	3	3.5	70 x 150

Table 3-1: Material properties

	Compressive strain		Tensile strain	
	$\epsilon_c(\%)$	$\epsilon_{cu}(\%)$	$\epsilon_t(\%)$	$\epsilon_{tu}(\%)$
Reinforcement	–	–	0.275	5
Concrete	0.175	0.35	–	–
SHCC	-	-	3	3.5

Table 3-2: Material properties continued

3.1.2 Bending moment capacity

The most critical cross-section for flexural failure is at midspan (see Figure 3-1, section A-A) due to the lower height as a result of the middle joint. The cross-section is shown in Figure 3-2. Three different stages will be taken into account which are the crack initiation, yielding and flexural failure stage.

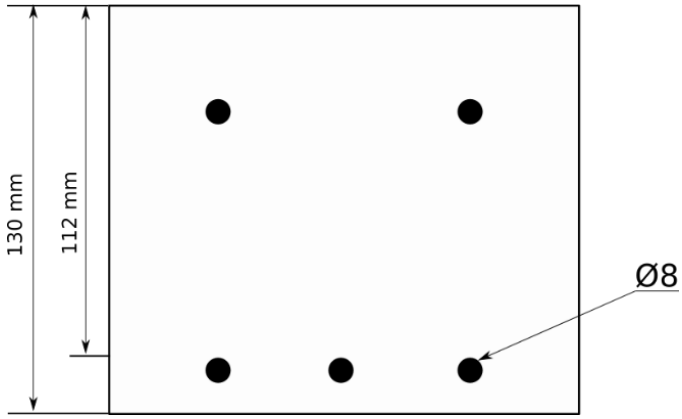

Figure 3-2: Cross-section of cut A-A

The following dimensions of this cross-section are used for the calculation

$h_c = 130$ mm	Height of the cross-section
$b = 150$ mm	Width of the beam
$\emptyset = 8$ mm	Reinforcement diameter
$c = 10$ mm	Concrete cover
$d_c = 116$ mm	Effective height of the cross-section

Section A-A – Crack initiation

The cracking stage starts when the tensile stress in the bottom fiber exceeds the tensile concrete strength. The bending moment in the beam at the initiation of cracking can therefore be calculated using the following equation

$$M_{cr} = W * \sigma_{fl,concrete}$$

$$W = \frac{1}{6} * b * {h_c}^2 = \frac{1}{6} * 150 * 130^2 = 4.225 * 10^5 \text{ mm}^3$$

$$\sigma_{fl,concrete} = 1.5 * \sigma_{t,concrete} = 3.84 \text{ MPa}$$

$$\rightarrow M_{cr} = 1.62 \text{ kNm}$$

In the calculation, the influence of the reinforcement steel on the elastic section modulus has been neglected. Furthermore, a factor of 1.5 between the tensile and flexural strength has been assumed. Based on the cracking moment, the total load capacity of the reinforced concrete beam for which cracking initiates can be obtained

$$F_{cr} = 2 * \frac{M_{cr}}{a}$$

Section A-A – Yielding stage

The yielding stage is reached when the stress in the reinforcement steel reaches the yield stress. To determine the compression zone height, horizontal equilibrium of the cross-section will be used

$$N_c = N_s$$
$$\frac{1}{2} * b * x * \sigma_{c,concrete} = A_s * f_y$$
$$\sigma_{c,concrete} = E_c * \frac{f_y}{E_s} * \frac{x}{d_c - x}$$
$$d_c = h_c - c - \frac{\emptyset}{2} = 116 \text{ mm}$$
$$\rightarrow x = 32.4 \text{ mm}$$

The equation for the horizontal equilibrium is only valid if the concrete strain hasn't exceeded a strain of 1.75 ‰. The compressive strain can be calculated based on the compression zone height and the yield strain of the reinforcement steel

$$\varepsilon_c = \varepsilon_s * \frac{x}{d_c - x} = 0.00275 * \frac{32.4}{83.6} = 0.00107 \ < 0.00175$$

The yielding moment can now be calculated based on the effective height between the tension and compression force

$$M_y = A_s * f_y * \left(d_c - \frac{1}{3}x\right) = 8.72 \text{ kNm}$$

The load capacity at the yielding point is calculated in the same way as in the cracked stage

$$F_y = 2 * \frac{M_y}{a}$$

Section A-A – Flexural failure

Flexural failure occurs at a compressive strain of $\varepsilon_{cu} = 3.5$ ‰. The compression zone height will decrease compared to the height in the yielding stage. This height can be obtained by making once again use of horizontal equilibrium. However, the compressive stress is now bilinear (assumption) which will be taken into account by the factor α

$$N_c = N_s$$
$$\alpha * b * x_u * f_{cm} = A_s * f_y$$
$$\alpha = \frac{\varepsilon_{cu} - \epsilon_c}{\varepsilon_{cu}} + \left(\frac{1 - \frac{\varepsilon_{cu} - \epsilon_c}{\varepsilon_{cu}}}{2}\right) = 0.75$$
$$\rightarrow \ x_u = 22.34 \text{ mm}$$

The bending moment at failure is therefore

$$M_u = A_s * f_y * (d_c - \beta * x_u) = 9 \text{ kNm}$$

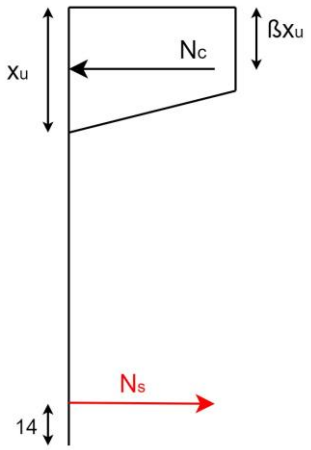

$$\beta = \frac{\frac{1}{2} * (\frac{\varepsilon_{cu} - \epsilon_c}{\varepsilon_{cu}})^2 + \frac{1}{2} * \left(1 - \frac{\varepsilon_{cu} - \epsilon_c}{2 * \varepsilon_{cu}}\right) * (\left(\frac{\varepsilon_{cu} - \epsilon_c}{\varepsilon_{cu}}\right) + \frac{1}{3} * \left(1 - \frac{\varepsilon_{cu} - \epsilon_c}{2 * \varepsilon_{cu}}\right))}{\alpha} = 0.39$$

The load at which the reinforced concrete beam will fail according to this calculation can now be determined (note that for the calculation the yield stress instead of the ultimate stress of the reinforcement has been assumed in order to be more conservative)

$$F_u = 2 * \frac{M_u}{a}$$

The bending moment capacity as a function of the distance a is shown in Figure 3-3 for the three different stages. The load increases as the value of the distance a decreases, as a higher force is needed to result in the same bending moment.

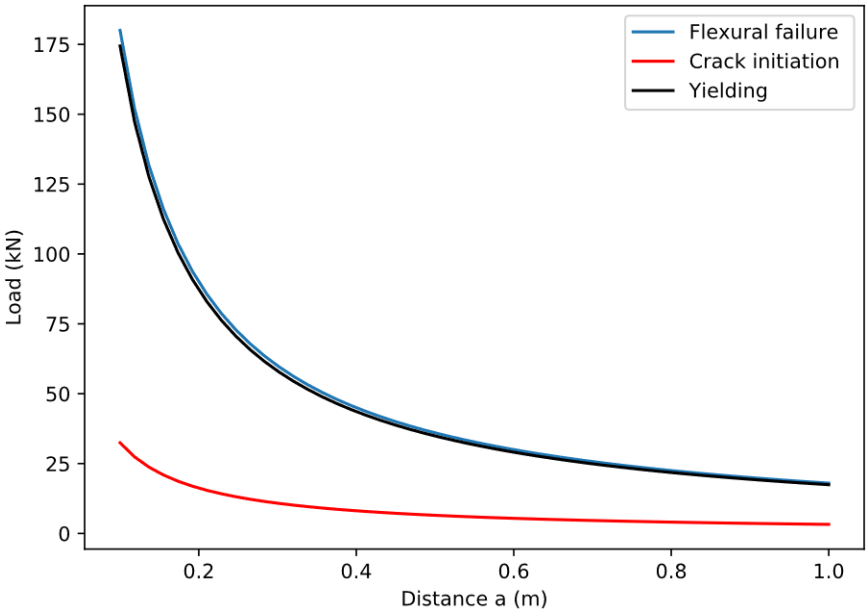

Figure 3-3: Load capacity for all three stages as a function of a at the critical section

The bending moment capacity will also be calculated at the location halfway along the lap splice. For this case, the whole height of the reinforced beam is contributing to the capacity in contrast with the calculation of the capacity at the critical location where the SHCC had no effect (see Figure 3-5). A linear relationship along the reinforcement bars is assumed as is shown in Figure 3-4. Using this assumption will result in the same stresses in the reinforcement bars and coupling reinforcement bars at the location halfway along the lap splice (only if the amount of reinforcement is the same). Only the crack initiation and yielding stage will be elaborated as the flexural failure won't happen at this section (midsection will fail before).

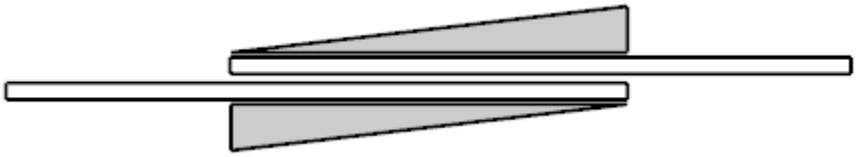

Figure 3-4: Assumption stresses at the lap splice for one half of the beam

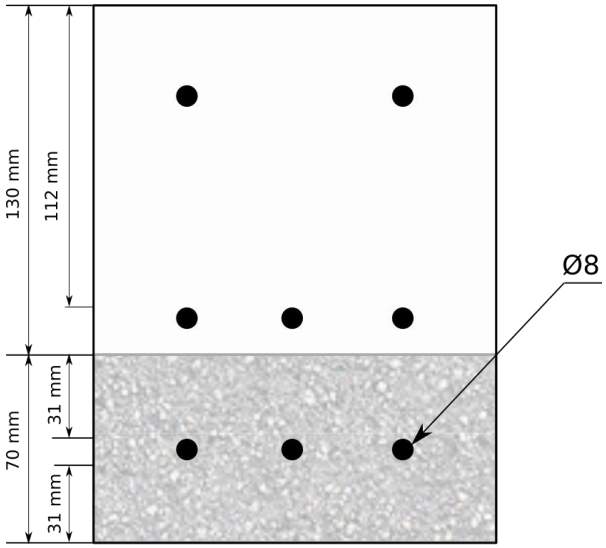

Figure 3-5: Cross-section of cut B-B

The following dimensions of this section B-B are used for the analytical calculation

$h = 200$ mm	Height of the cross-section
$h_{SHCC} = 70$ mm	Height of the SHCC layer
$b = 150$ mm	Width of the beam
$Ø = 8$ mm	Reinforcement diameter
$c = 31$ mm	Concrete cover
$d = 165$ mm	Effective height of the cross-section

Section B-B – Crack initiation

The cracked stage starts also in this case when the tensile stress in the bottom fiber exceeds the tensile concrete strength. However, there are two different material (neglecting the influence of the reinforcement steel) resulting in a shift of the neutral axis ($N.A$)

$$M_{cr} = W * \sigma_{fl,SHCC}$$

$$N.A = \frac{\left(E_c * (b * \frac{{h_c}^2}{2}) + E_{SHCC} * (b * h_{SHCC} * (h_c + \frac{h_{SHCC}}{2})\right)}{E_c * b * h_c + E_{SHCC} * b * h_{SHCC}} = 88.24 \text{ mm}$$

The inertia can be divided into two parts which are the inertia of the concrete (I_c) and inertia of the SHCC (I_{SHCC})

$$I_c = \frac{1}{12} * b * h_c^3 + b * h_c * (N.A - \frac{h_c}{2})^2$$

$$I_{SHCC} = \frac{1}{12} * b * h_{SHCC}^3 + b * h_{SHCC} * \left((h_c + \frac{h_{SHCC}}{2}) - N.A\right)^2$$

As we have a composite beam, first it will be determined whether the stress at the bottom fiber of the SHCC is larger than the stress at the bottom fiber of the concrete layer. The stress at the bottom fiber of the SHCC layer and the concrete layer as a function of the cracking moment is given as

$$\sigma_{SHCC,b} = \frac{M_{cr} * E_{SHCC} * (h - N.A)}{E_{SHCC} * I_{SHCC} + E_C * I_C} = 8.36 * 10^{-7} M_{cr}$$

$$\sigma_{Concrete,b} = \frac{M_{cr} * E_C * ((h - h_{SHCC}) - N.A)}{E_{SHCC} * I_{SHCC} + E_C * I_C} = 5.55 * 10^{-7} M_{cr}$$

Based on this result, the stress at the bottom fiber of the SHCC will reach the cracking stress before the bottom fiber of the concrete. The cracking moment at which cracking initiates can now be calculated

$$\sigma_{fl,SHCC} = 1.5 * \sigma_{t,SHCC} = 4.5 \text{ MPa}$$

$$\rightarrow M_{cr} = 5.38 \text{ kNm}$$

The force at which the cracking will start at this section will therefore be then

$$F_{cr} = 2 * \frac{M_{cr}}{a}$$

Section B-B – Yielding stage

The horizontal equilibrium for the yielding stage has an extra component compared to the calculation of the critical section as the SHCC layer is also able to take up tensile forces. Furthermore, the reinforcement tensile force has now two components instead of one (SHCC reinforcement and coupling reinforcement).

$$N_c = N_{s1} + N_{s2} + N_{SHCC}$$

$$\frac{1}{2} * b * x * \sigma_{c,concrete} = A_s * f_{y1} + A_s * f_{y2} + A_{SHCC} * \sigma_{SHCC,t}$$

$$f_{y1} = f_{y2} = \frac{f_y}{2} \text{ (only halfway along splice)}$$

$$\sigma_{c,concrete} = E_c * \frac{f_y}{E_s} * \frac{x}{d - x}$$

$$d = h - c - \frac{\emptyset}{2} = 165 \text{ mm}$$

$$\rightarrow x = 47.7 \text{ mm}$$

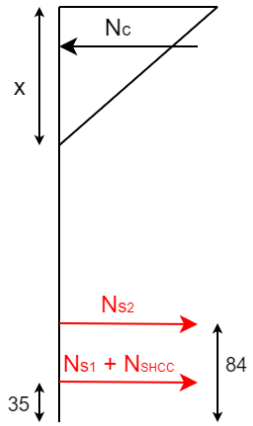

This equation for the horizontal equilibrium is only valid if the concrete strain hasn't exceeded a strain of 1.75 ‰. The compressive strain can be calculated based on the compression zone height and the yield strain of the reinforcement steel

$$\varepsilon_c = \varepsilon_s * \frac{x}{d - x} = 0.00275 * \frac{47.7}{117.3} = 0.0011 < 0.00175$$

The yielding moment can now be calculated based on the effective height between the tension and compression forces

$$M_y = A_s * f_{y1} * \left(d - \frac{1}{3}x\right) + A_s * f_{y2} * \left(d_c - \frac{1}{3}x\right) + A_{SHCC} * \sigma_{SHCC,t} * (h - \frac{h_{SHCC}}{2} - \frac{1}{3}x) = 15.6 \text{ kNm}$$

The loading capacity at the yield point is calculated in the same manner as in the cracked stage

$$F_y = 2 * \frac{M_y}{a}$$

Figure 3-6 depicts the loads at which halfway along the lap splice cracking and yielding start as a function of the distance a. Comparing these results with the result of Figure 3-4, a larger capacity is found at this lap splice location. This capacity will even increase more if a cut is made at the end of the lap splice as then all the steel stresses will be taken by the bottom reinforcement which has a larger effective height.

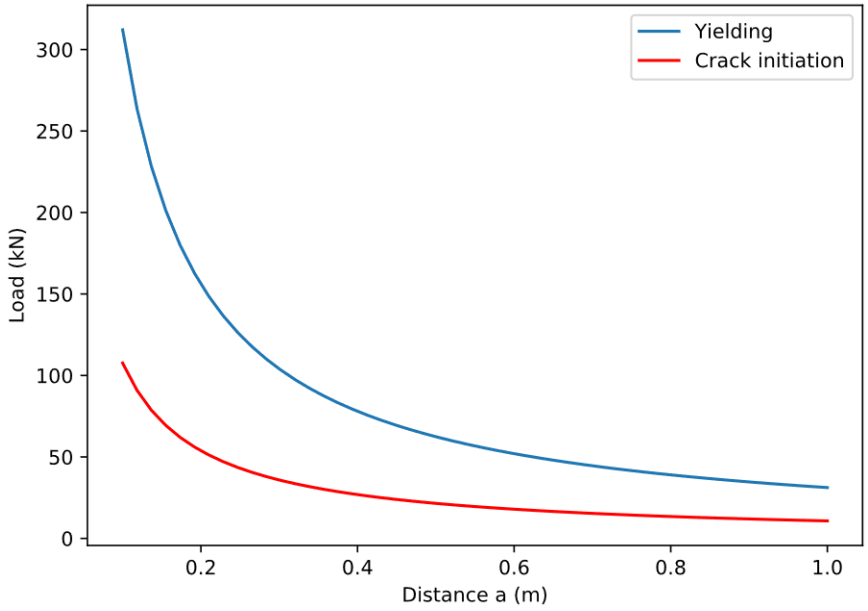

Figure 3-6: Load capacity for the two stages as a function of a at the lap splice

3.1.3 **Shear capacity**

The shear capacity of the reinforced concrete beam will be calculated in two different ways. The 1st method will be based on the Eurocode [20] while the 2nd method will make use of the critical shear displacement theory of Y. Yang [21].

3.1.3.1 Eurocode

According to the Eurocode the shear capacity of a reinforced concrete beam without shear reinforcement can be calculated using the following equation

$$v_{Rd,c} = 0.18 * k * (100 * \rho * f_{ck})^{\frac{1}{3}} \tag{3.1}$$

$$k = 1 + \sqrt{\frac{200}{d}} \leq 2.0 \tag{3.2}$$

$$\rightarrow v_{Rd,c} = 0.18 * 2 * \left(100 * \frac{A_s}{b * d} * 28\right)^{\frac{1}{3}} = 0.927 \text{ Mpa}$$

Therefore, the maximum allowable load on the reinforced concrete beam without shear reinforcement has to be limited to (the influence of the SHCC layer at the bottom has been neglected)

$$F_{max,EC} = 2 * \upsilon_{Rd,c} * b * d = 45.9 \text{ kN}$$

3.1.3.2 Critical shear displacement theory

The 2nd method is based on the critical shear displacement theory. This theory is based on the idea of an unstable development of a flexural crack in the shear region. This unstable development happens when the critical shear displacement value (Δ_{cr}) is exceeded. The crack profile model is simplified as bilinear with two branches which represent the major crack and a secondary crack in the compression zone as is shown in Figure 3-7.

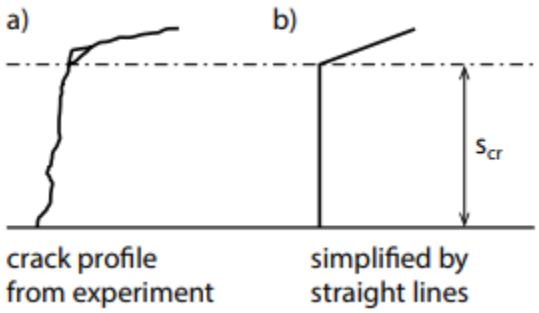

Figure 3-7: a) Crack according to experiment; b) Simplified crack profile used in theory (Y. Yang et al., 2016)

The height of the major crack shown in Figure 3-7 is calculated based on the following equation which is derived from the equilibrium of forces along the height of the beam.

$$s_{cr} = \left[1 + \rho * \alpha_e - \sqrt{2 * \rho * \alpha_e + (\rho * \alpha_e)^2}\right] * d \tag{3.3}$$

The shear capacity can be determined by three different load mechanisms which are the direct shear transfer, aggregate interlocking and dowel action

$$V = V_c + V_{ai} + V_d \tag{3.4}$$

These three different load-carrying mechanisms can be obtained using the following equations

$$V_c = \frac{d - s_{cr}}{d + 0.5 * s_{cr}} * V \tag{3.5}$$

$$V_d = 1.64 * b * \emptyset * f_c^{\frac{1}{3}} \tag{3.6}$$

$$V_{ai} = \frac{f_c^{0.56} * b * 0.03 * s_{cr}}{w_b - 0.01} * (-978 * \Delta^2 + 85 * \Delta - 0.27) \tag{3.7}$$

The crack width w_b at the level of the reinforcement is calculated using the following equation which is a function of the bending moment and crack spacing ($l_{cr,m}$):

$$w_b = \frac{M}{z * A_s * E_s} * l_{cr,m} \tag{3.8}$$

$$l_{cr,m} = \frac{s_{cr}}{1.28} \tag{3.9}$$

The critical shear displacement value can be obtained depending on whether the tensile reinforcement configuration is known. As in this case the amount of reinforcement is known the following expression can be used

$$\Delta_{cr} = \frac{25 * d}{30610 * \emptyset} + 0.0022 < 0.025\, mm \tag{3.10}$$

Based on the above-mentioned expressions, the shear capacity of an unreinforced beam can be calculated. This procedure is iterative and should be executed until the difference between the input and output is negligible. Based on a trial-and-error method, the following shear capacity is found

$$V_{Rd,csd} = 24.5 \text{ kN}$$

$$\rightarrow F_{max,csd} = 49 \text{ kN}$$

This result is roughly the same as the value found using the Eurocode. This result is however dependent on the distance a, while the result of the Eurocode is independent of the distance a (not taking into account the effect of direct shear transfer to the support). This critical displacement theory is however only tested for slender beams where the ratio a/d is larger than 3. Only the results for $a \geq 0.5$ m comply with this criterion. Nevertheless, also the result for $a = 0.4$ m is calculated and shown in Figure 3-8. Figure 3-8 shows the capacity of the beam for the flexural failure (critical section) and shear failure. In case the distance between the support and loading points becomes smaller than 0.5 m, shear failure will become critical. The shear capacity increases as the distance a decreases according to the critical shear displacement theory. This is due to the fact that a force closer to the support generates a smaller bending moment which will influence the flexural shear failure mechanism. Another influence could be that if the force is closer to the support a part of the force is directly (compression diagonal) transferred to the support. The results in Figure 3-8 are based on a reinforcement configuration of 3xØ8.

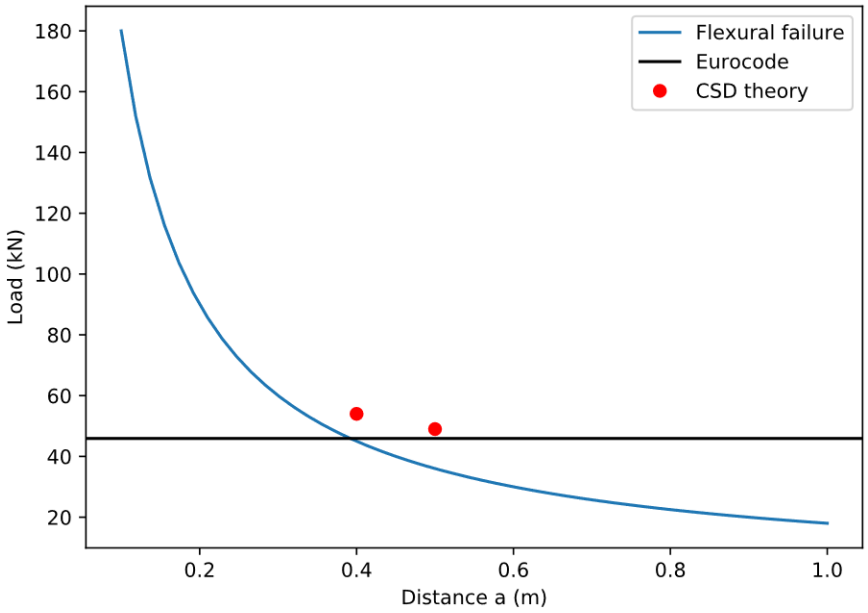

Figure 3-8: Load capacity comparison based on bending moment and shear capacity ($A_s = 3x\emptyset 8$)

In case the coupling reinforcement will be increased to $3x\emptyset 10$, the flexural failure curve shifts upwards resulting in a larger critical value of a. The results of the shear capacity remain the same as the amount of shear reinforcement is identical for each case. The graph is shown in Figure 3-9. For this increased amount of reinforcement, the point load can't be placed at a distance of 500 mm from the support as shear failure becomes critical. This is due to the increased bending moment capacity resulting in a higher load capacity. The only solution will be therefore to limit the diameter of the reinforcement to $\emptyset 8$ or to increase the length of the reinforced concrete beam.

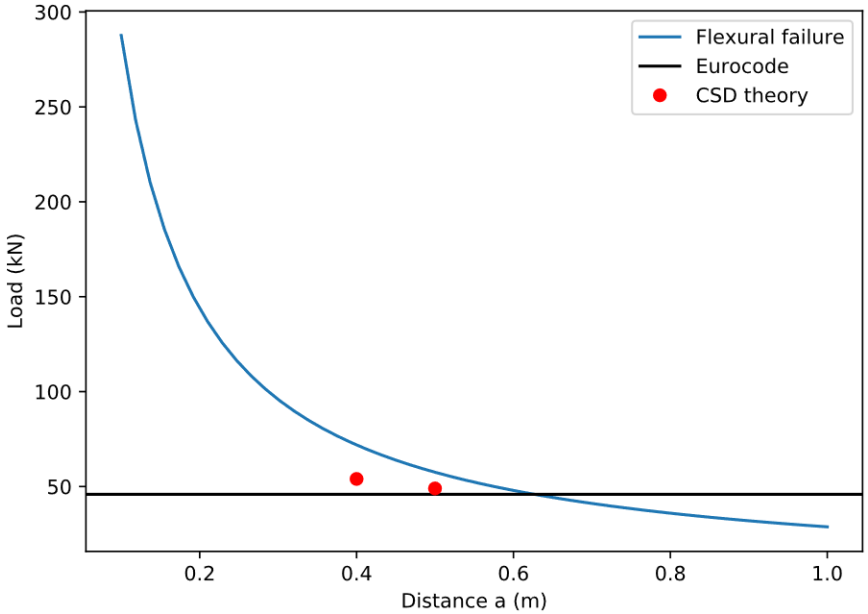

Figure 3-9: Load capacity comparison based on bending moment and shear capacity($A_s = 3x\emptyset 10$)

3.1.4 **Anchorage length**

The length of this coupling reinforcement is calculated according to Eurocode NEN-EN 1992 (see Paragraph 2.3.1) using mean values instead of design values. The concrete class is chosen according to Huang's concrete compressive tests which resulted in a concrete class of C25/30.

$$l_{b,rqd} = \frac{\emptyset}{4} * \frac{f_y}{2.25 * \eta_1 * \eta_2 * f_{ctm}} \tag{3.11}$$

- $\eta_1 = 1.0$ when the reinforcement has good bonding, if the coupling reinforcement is placed directly on the SHCC layer the factor should be taken as 0.7
- $\eta_2 = 1.0$ as the diameter of the coupling reinforcement is smaller than 32 mm

Furthermore, several factors have to be taken into account which are elaborated below:

$$l_0 = \alpha_1 * \alpha_2 * \alpha_3 * \alpha_4 * \alpha_5 * \alpha_6 * l_{b,rqd} \tag{3.12}$$

$$l_0 = 1.0 * 0.85 * 1.0 * 1.0 * 1.0 * 1.5 * l_{b,rqd} = 245 \text{ mm}$$

- $\alpha_1 = 1.0$ as the reinforcement bars are straight
- $\alpha_2 = 1.0$ if the reinforcement is directly placed on the SHCC layer else it is 0.85
- $\alpha_3 - \alpha_5 = 1.0$ as a result of no transverse reinforcement
- $\alpha_6 = 1.5$ due to 100% overlapping of the coupling reinforcement

The distance between the longitudinal reinforcement in the SHCC layer and coupling reinforcement also influences the length of the anchorage length. According to the Eurocode, this distance should not be larger than 50 mm in order to enable the transfer of forces between the reinforcement bars. Therefore, if the coupling reinforcement isn't directly placed on the SHCC layer, a spacing of 15 mm should be taken into account to not influence the anchorage length. The distance between the bars can be increased according to the Eurocode, but the length of the reinforcement should then also be increased accordingly. However, J.P. Grant did a study on the influence of the spacing between non-contact splice bars in dissimilar concretes. Based on his experiments, he concluded that the spacing between the bars in a lap splice can be placed at a distance of 100 mm while still reaching the required nominal strength of the beams [22].

The transfer length of the lap splice is also determined using a simple analytical model. The concrete tensile stress at a crack is zero. The reinforcement stress will as a result of this increase as it has to carry the concrete tensile force prior to cracking. The concrete will then reach its tensile strength again at a certain distance (transfer length) away from a crack due to bond stresses along the transfer length between the reinforcement and concrete.

$$A_c * f_{ctm} = \tau_{bm} * l_o * m * \pi * \emptyset$$

$$l_o = \frac{f_{ctm} * \emptyset}{4 * \tau_{bm} * \rho}$$

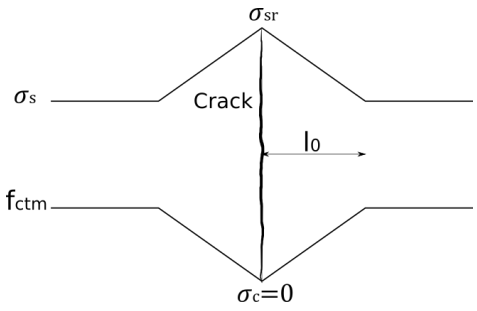

This bond along the reinforcement bars can be taken as $2 * f_{ctm}$ in case of a perfect bond between the two concrete layers. However, in this case the interface isn't perfectly bonded and therefore the bond will be taken as twice the cohesion of concrete to be conservative. The cohesion will be assumed as half the concrete tensile strength($C = 1.5$ MPa). The roughness of the interface strongly influences this value and therefore a higher roughness will increase the cohesion.

$$l_o = \frac{2.56 * 8}{4 * 2 * 1.5 * \frac{3 * \pi * 4^2}{165 * 150}} = 280 \text{ mm}$$

The required anchorage length according to the Eurocode results is smaller compared to the one found using the simple model. This is due to the fact that the Eurocode doesn't take into account the influence of the transfer of forces between reinforcement bars in two different concrete layers. As a result of this, the result of the simple model will be used for the experiments. The length of the lap splice at both halves of the beam will therefore be taken as 300 mm. If the diameter of the coupling reinforcement is increased to 10 mm, the anchorage length should be taken as 350 mm.

3.1.4.1 Force transfer mechanism

The force transfer between the reinforcement in the SHCC layer and coupling reinforcement is an important aspect. The transfer of this lap splice happens through the concrete as a result of diagonal compressive struts as can be seen in Figure 3-10. As a result of these forces on the bar, a radially outward pressure acts on the concrete. Consequently, tension stress rings will appear in order to balance these radial stresses.

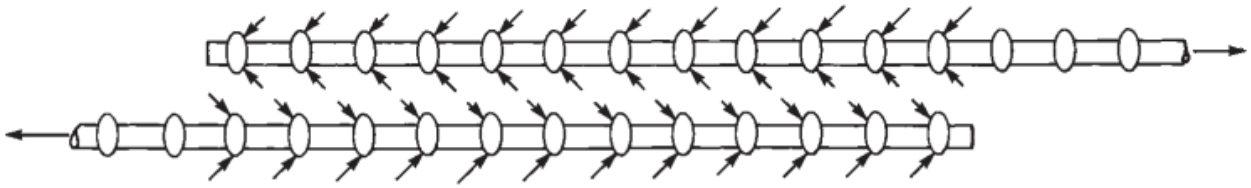

Figure 3-10: Force transfer at a lap splice (J.K Wight et al. 2012)

This splitting force can be related to the longitudinal force depending on the angle α of these diagonal forces.

$$F_{splitting} = F_{longitudinal} * \tan(\alpha) \tag{3.13}$$

The splitting force can be determined by the effective tension area of the reinforcement bar and the stresses of the splitting force (assuming uniformly distributed stresses along the effective tension area). The effective tension zone of the reinforcement bar depends on the concrete cover and reinforcement diameter [23]. This splitting force has to be balanced by the hoop stresses which will result in cracking if the hoop stress exceeds the concrete tensile strength.

$$F_{splitting} = F_{hoop} \tag{3.14}$$

$$Ø * l_o * \sigma_{sp} = A_{eff} * \sigma_{hoop} \tag{3.15}$$

$$A_{eff} = l_o * \left(2.5 * \left(c + \frac{Ø}{2}\right) - Ø\right) \tag{3.16}$$

The stress at which splitting cracks occur for one single bar can now be derived by using the concrete tensile strength for the hoop stress. This effective tension area is however limited to the distance between two reinforcement bars. If this distance is exceeded, the whole width of the reinforced concrete beam is effective.

$$\sigma_{sp} = \frac{f_{ctm} * \left(2.5 * \left(c + \frac{Ø}{2}\right) - Ø\right)}{Ø} \tag{3.16}$$

The longitudinal force is equal to the force in the reinforcement bar or the bond stress along the perimeter of the reinforcement bar.

$$F_{longitudinal} = f_y * A_s = \tau_b * \pi * Ø * l_o \tag{3.17}$$

Using the relation between the splitting force and longitudinal force, the longitudinal stress can be determined for which splitting occurs assuming a value of 45° for α.

$$\tau_b = \frac{\sigma_{sp}}{\pi * \tan(45)} \tag{3.18}$$

An important aspect is the splitting stresses at the coupling reinforcement. The concrete cover of the coupling reinforcement and the diameter of the reinforcement bars play a significant role. By having a low concrete cover for the coupling reinforcement relative to the interface, these splitting stresses will be localized in a smaller area. This is visualized in a plot shown in Figure 3-11 where along the x-axis the ratio of the concrete cover over the reinforcement diameter is shown and on the y-axis the ratio of the splitting stress and concrete tensile strength. In this figure, the stress for which splitting crack occurs increases for larger concrete cover.

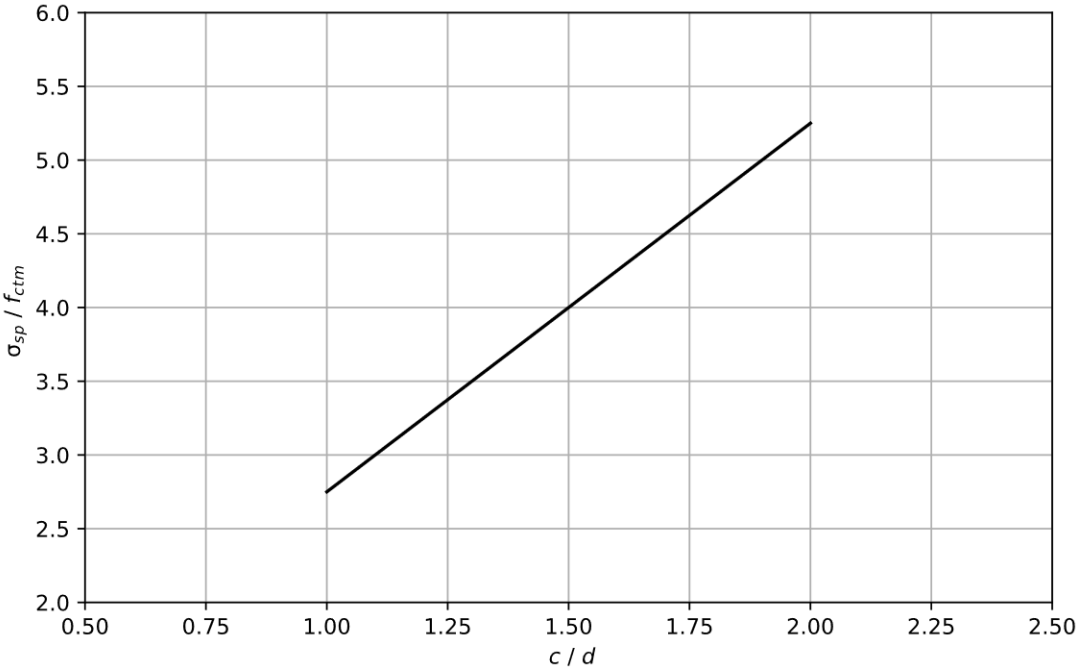

Figure 3-11: Influence concrete cover and bar diameter on splitting stresses

3.1.4.2 Eccentricity

The distance between the reinforcement in the SHCC layer and the coupling reinforcement will result in an internal bending moment. This will result in a tensile and compressive force at the interface as is shown in Figure 3-12. By increasing the distance between the reinforcement bars, this tensile force will also increase resulting in higher stresses at the interface. Consequently, the delamination of the interface can occur.

$$F_{internal} * L = F_{reinforcment} * e \tag{3.19}$$

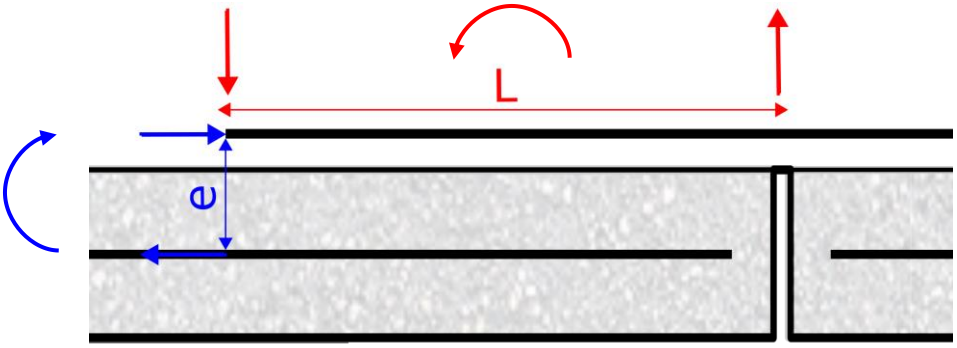

Figure 3-12: Tensile force due to eccentricity

The stress distribution along this interface will be nonlinear. The distance of the tensile and compressive force of the internal balancing moment is of high importance as it influences the magnitude of the tensile force. Next to this, also shear stresses are distributed along the interface as a result of the force transfer between the reinforcement bars. This makes the force distribution at the interface more complex as a combination of shear and tensile stresses occur.

3.1.5 Experimental set-up

The experimental set-up of the specimens will be based on the study of Zhekang [1]. However, the middle joint and length of the coupling reinforcement have to be taken into account. As the coupling reinforcement will have a length of 600 mm (see 3.1.4), the distance between the loading points will be increased to 700 mm to prevent anchorage of this reinforcement. The total length of the beam will remain however 1900 mm, which allows for two different options. The first option is to move the loading points by 100 mm to the support as is shown in Figure 3-13. This will ensure that the loading points won't be directly placed on the anchorage length. According to the analytical calculation, shear failure will then be critical as the bending moment capacity reduces as a result of the reduced distance of a.

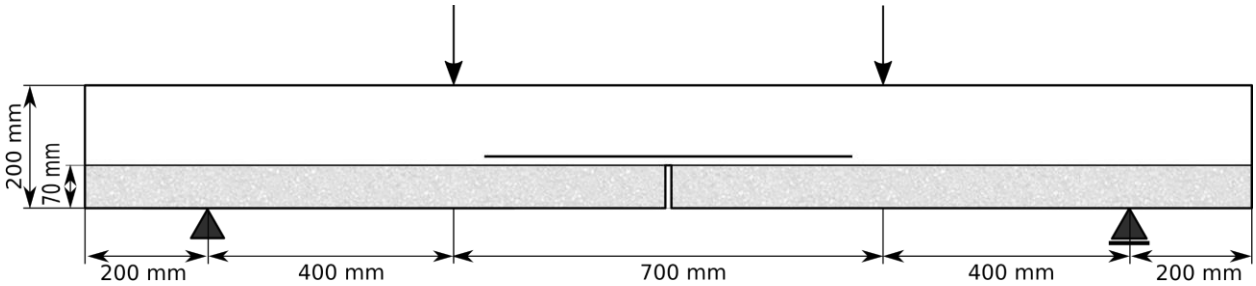

Figure 3-13: Experimental setup variant A

The 2nd option is to move the loading points by 100 mm while also moving the support points by 100 mm as can be seen in Figure 3-14 (reducing the length of the cantilever parts). This will ensure that the distance a will remain 500 mm. As can be seen in Figure 3-8, the bending moment capacity is in this case lower than the shear capacity. The reinforcement should however be limited to $3x\emptyset 8$, as increasing the coupling reinforcement to $3x\emptyset 10$ will result in shear failure (see Figure 3-9).

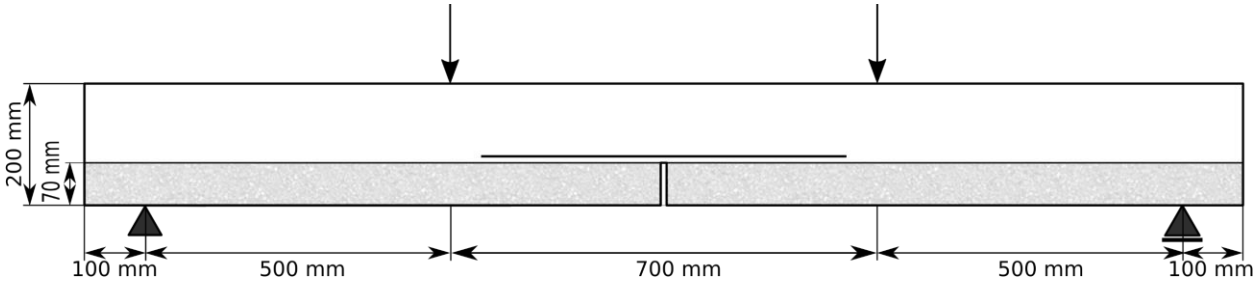

Figure 3-14: Experimental setup variant B

Thus, Variant B will be chosen as the constant bending moment region is long enough to accommodate for the coupling reinforcement and this set-up won't result in shear failure in case no shear reinforcement is provided. An extra numerical study is done to investigate the effect of having shear reinforcement on the interfacial behavior (see Appendix C). According to this study, the shear reinforcement has no effect on the interfacial behavior in the constant bending moment region. Therefore, it is also chosen to include the shear reinforcement. This will help with constructing the reinforcement mesh and lifting the beams.

3.2 Design

Two test series with in total seven beams are tested to investigate the interfacial behavior of the hybrid SHCC -concrete beam with a joint. The length of the beam is 1900, width 150 mm and height 200 mm. The height of the SHCC layer is 70 mm which is a result of the research of Zhekang [1]. In Figure 3-15, the geometry of the final beam is shown.

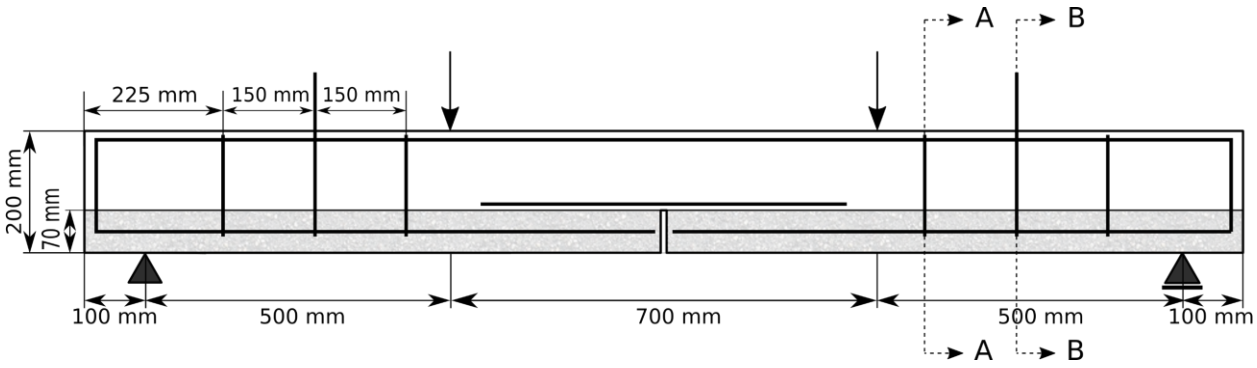

Figure 3-15: Geometry of hybrid SHCC-Concrete beam

The reinforcement mesh consists of three longitudinal tensile reinforcement bars in the SHCC layer ($\rho = 0.55\%$). The coupling reinforcement is similar to this reinforcement configuration. However, as the effective height at mid-span is lower, the reinforcement ratio at midspan is larger ($\rho = 0.86\%$). Shear reinforcement is also placed to prevent shear failure consisting of three 2-legged stirrups at each side of the beam (even though according to the calculation shear failure wouldn't be critical without shear reinforcement). The cross-sections of this hybrid beam are shown in Figure 3-16.

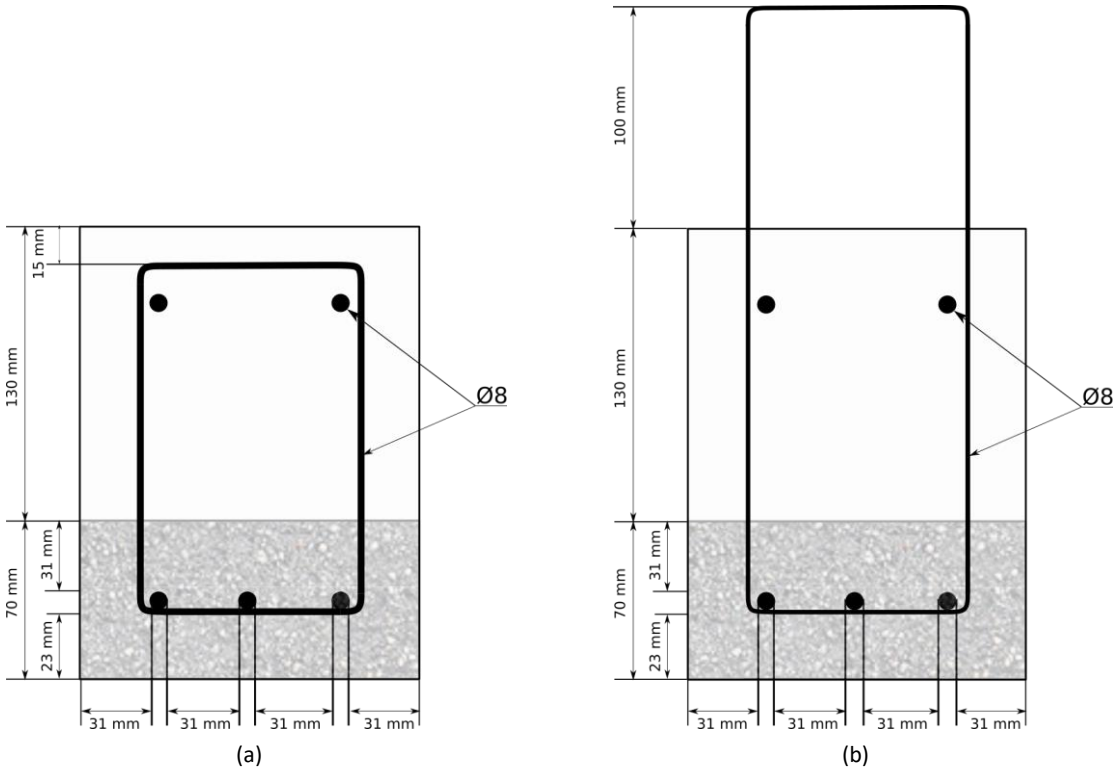

Figure 3-16: (a) Cross-section A-A; (b) Cross-section B-B

As mentioned before, in total seven beams are tested. The first sample will be the reference (control) beam with a smooth interface (Figure 3-17). Three samples will have a different interface roughness. These are the samples with a profiled interface (Figure 3-18), a holed interface (Figure 3-19) and an interface with epoxy and sand (Figure 3-20). The 5th beam is changed by placing the coupling reinforcement directly on top of the SHCC layer as is shown in Figure 3-21. The curing method will be investigated for one beam with a smooth interface. This beam will be taken from the mould to let it cure in a humidity-controlled room (Figure 3-17). Finally, one beam will have a smooth interface with one stirrup (diameter 6) placed on either side of the middle joint (Figure 3-22). This last sample is part of the 2nd series. In Table 3-3 the samples are shown including the parameters which have been changed.

	Interface roughness	Reinforcement configuration	Cover coupling reinforcement	Curing method	Stirrups at joint
	–	Ø (mm)	c (mm)	–	Ø (mm)
Sample 1	Smooth	3xØ8	10	–	–
Sample 2	Profiled interface	3xØ8	0 – 10	–	–
Sample 3	Holed interface	3xØ8	10	–	–
Sample 4	Epoxy + Sand	3xØ8	10	–	–
Sample 5	Smooth	3xØ8	10	Drying outside mould	–
Sample 6	Smooth	3xØ8	0	–	–
Sample 7*	Smooth	3xØ8	10	Drying outside mould	2xØ6

Table 3-3: Experimental plan, *part of 2nd series

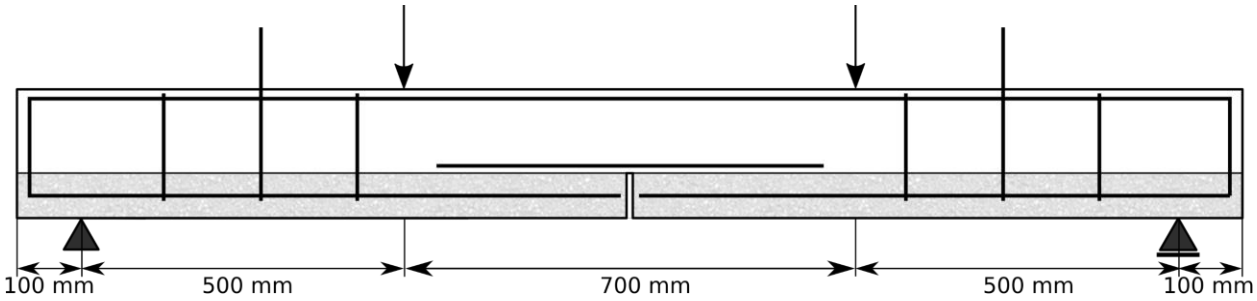

Figure 3-17: Sample 1 – Reference and Sample 5 – Curing

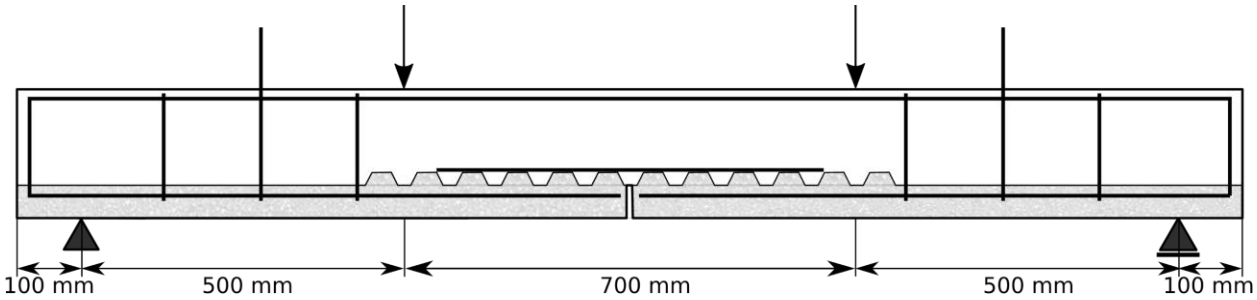

Figure 3-18: Sample 2 - Profiled interface

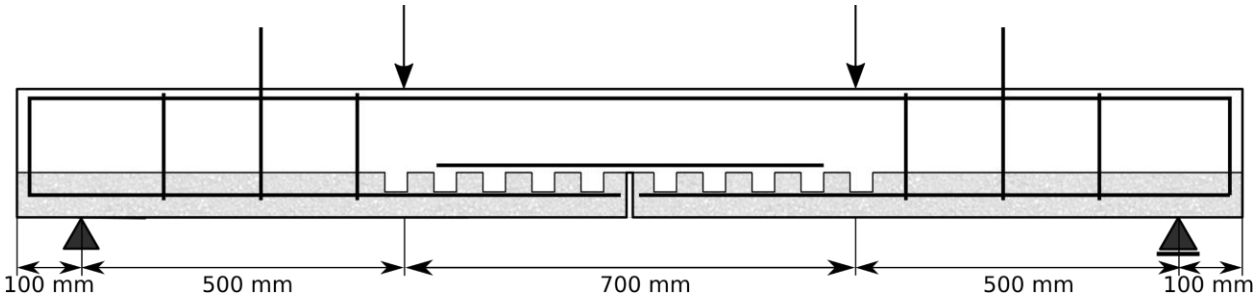

Figure 3-19: Sample 3 - Holed interface

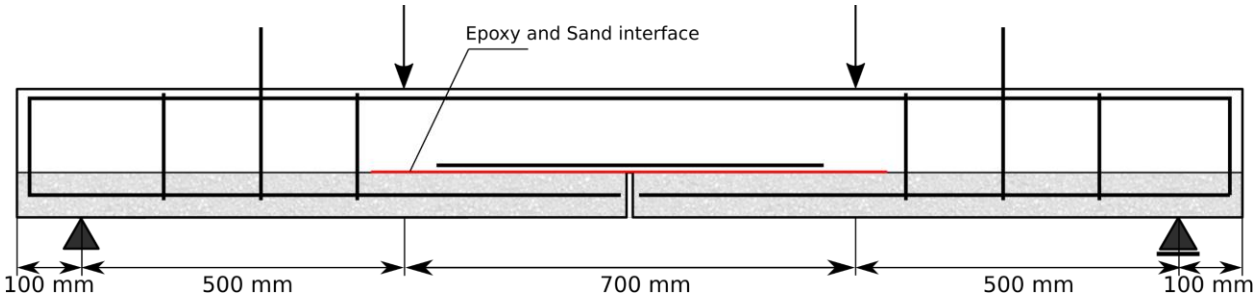

Figure 3-20: Sample 4 - Epoxy and Sand

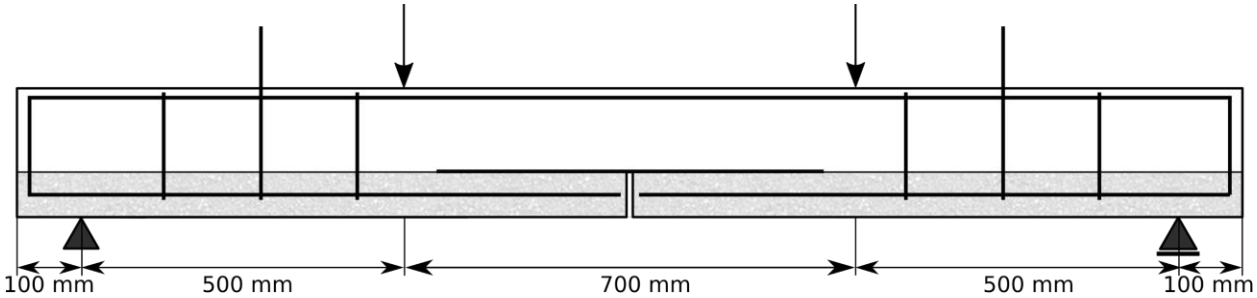

Figure 3-21: Sample 6 - No cover

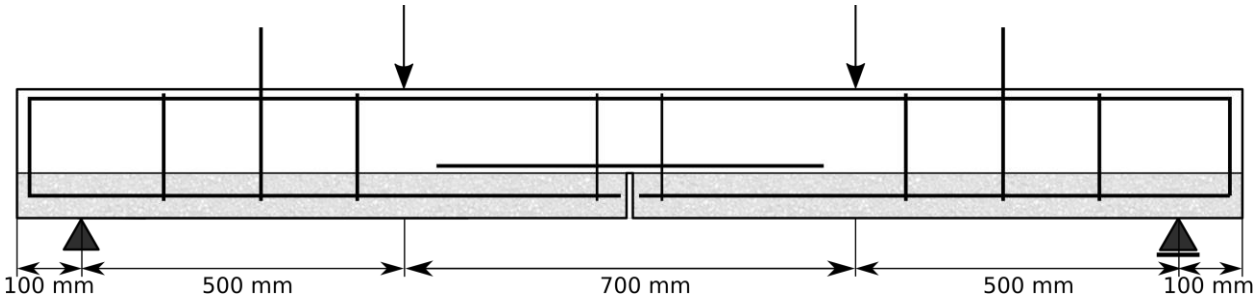

Figure 3-22: Sample 7 – Stirrups at joint

3.3 Casting

3.3.1 Joint

The joint in the middle of the beam is made by putting a plastic sheet in the mould with a thickness of 4 mm. This plastic sheet has a height of 70 mm and width of 150 mm according to the dimensions of the SHCC layer. The plastic part was fixed to the wooden mould using glue kit (see Figure 3-23).

3.3.2 Reinforcement

The reinforcement mesh consists of longitudinal reinforcement bars and stirrups. The cover of the reinforcement bars is set with plastic spacers. Furthermore, the separate reinforcement bars and stirrups have been fixed to one single reinforcement mesh using steel wires. The reinforcement mesh with the required cover is shown in Figure 3-24 – Figure 3-25.

Figure 3-23: Joint in the middle of the beam glued with kit

Figure 3-24: Reinforcement mesh

Figure 3-25: Top view with spacers for reinforcement mesh

One sample also consists of stirrups nearby the joint as is shown in Figure 3-26. Strain gauges are glued on the stirrup to measure the strain during testing. Each stirrup consists of 4 strain gauges (2 on each leg of the stirrup). The strain gauges are placed at the level of the interface and halfway along the height of the beam. As the interfacial behavior is important, the strain gauge at the interface is critical.

Figure 3-26: Stirrup at the joint

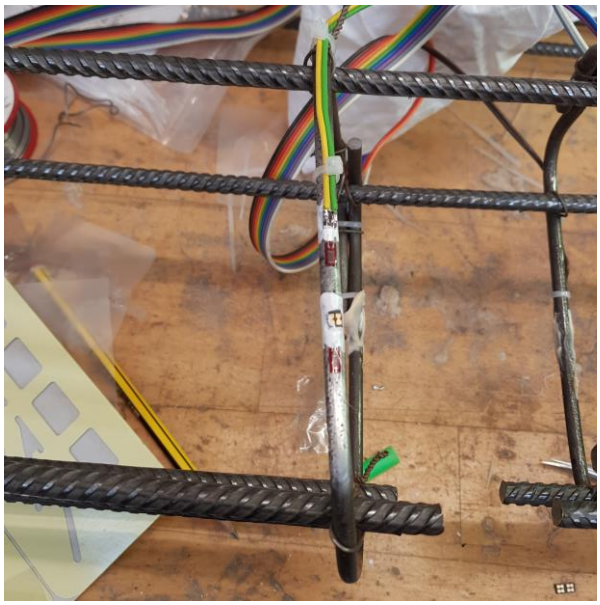

Figure 3-27: Strain gauges on the stirrup

3.3.3 SHCC

The composition of the SHCC used in the experiment consists of CEM III B, Limestone powder, PVA fibers, Superplasticizer and Water. In Table 3-4, the required amount of each component per cubic meter is presented. The PVA fibers have a length of 8 mm and a diameter of 0.04 mm. Before pouring the SHCC, the moulds are brushed with oil to ease the demoulding after the samples have hardened.

Material	Density	Unit
CEM III B	790	kg/m^3
Limestone powder	790	kg/m^3
PVA fibers	26	kg/m^3
Superplasticizer	2.13	kg/m^3
Water	410	kg/m^3

Table 3-4: Composition of the SHCC

The mixing procedure started with adding PVA fibers, limestone powder and CEM III B together which were mixed for 1 minute. After this, water and superplasticizer were added to the mix. This final mix was then mixed for 4 minutes to obtain SHCC. The SHCC mix was poured in the moulds (in several layers) to the required height of 70 mm using a levelling tool. The vibration of the SHCC was done on a vibration table to remove the air bubbles. Besides the 6 samples, also 3 cubes and 2 prisms were cast to determine the compressive strength and E-modulus of the SHCC.

3.3.4 Interface

The preparation of the interface was achieved by applying several techniques. These techniques were done either before or after the SHCC had hardened depending on the sample. The dented interface was achieved by applying a dented plastic sheet on top of the fresh SHCC. This sheet has a length of 800 mm consisting of dents which are 50 mm in width and 20 mm in height (see Figure 3-28). The interface with holes was achieved by penetrating several plastic tubes in the SHCC along a length of 800 mm. The tube diameter and penetration depth were 35 mm and 30 mm respectively (see Figure 3-29). After the SHCC had hardened, the plastic dented sheet and tubes were removed resulting in the interfaces shown in Figure 3-32.

One sample consists of an interface with epoxy and sand. After the SHCC had hardened (2 days curing), the interface was cleaned with ethanol. Subsequently, an epoxy layer was added on the interface for the adhesion of the sand with diameter 1-2 mm (see Figure 3-31). The remaining samples consist of a smooth interface which were cleaned with ethanol after two days of curing.

3.3.5 Coupling reinforcement

The coupling reinforcement is placed on top of the SHCC interface after two curing days. Spacers are used to get the required cover. For the dented interface, the elevation of the interface has been taken into account by a reduction of the cover to obtain the same effective height in all samples. The coupling reinforcement bars have been fixated to the top longitudinal bars with steel wires. The coupling reinforcement for the sample with holes is shown in Figure 3-30.

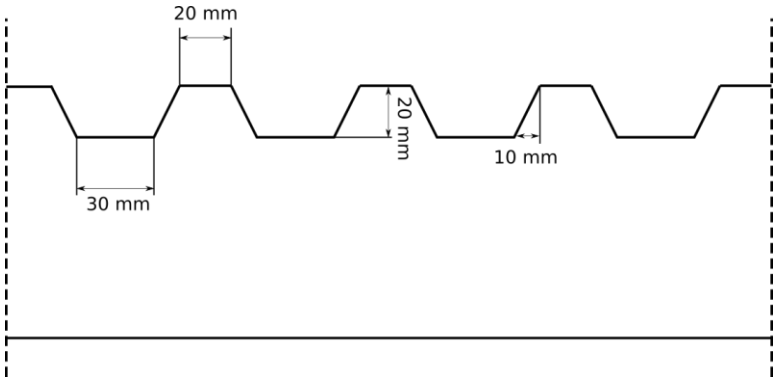

Figure 3-28: Dimension profiled interface

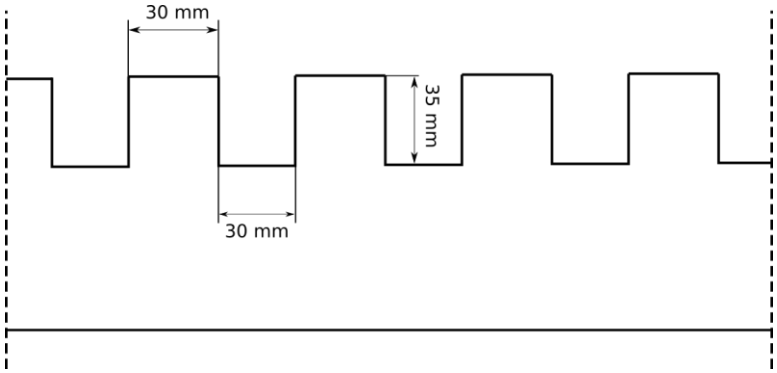

Figure 3-29: Dimension holed interface

Figure 3-30: Coupling reinforcement

Figure 3-31: Interface with Epoxy and Sand

Figure 3-32: Profiled and holed interface

3.3.6 **Concrete**

The recipe of the concrete top layer is presented in Table 3-5. This composition is based on a C20/25 concrete class of Blagojevic (2016). The mixing of the concrete started by adding fine aggregates in the mixer. After mixing for 1 minute, cement was added into the mixer which was then mixed for another minute. Subsequently, water and superplasticizer were added and mixed for 4 minutes with the cement and fine aggregates. During the mixing procedure, the materials fixed on the inner surface of the mixer were scraped off. Finally, coarse aggregates were added in the mixer and mixed for 3 more minutes.

Material	Density	Unit
CEM I 52.5R	260	kg/m^3
Sand 0.125-0.25 mm	78.83	kg/m^3
Sand 0.25-0.5 mm	256.199	kg/m^3
Sand 0.5-1 mm	256.199	kg/m^3
Sand 1-2 mm	157.661	kg/m^3
Sand 2-4 mm	98.538	kg/m^3
Gravel 4-8 mm	394.152	kg/m^3
Gravel 8-16 mm	729.181	kg/m^3
Superplasticizer	156	kg/m^3
Water	0.25	kg/m^3

Table 3-5: Composition of the concrete (Blagojevic, 2016)

The concrete paste was manually poured on top of the hardened SHCC layer (see Figure 3-33). The vibration of the concrete was done using a vibration poker (see Figure 3-34). After the moulds were fully filled with concrete to the required height of 200 mm, plastic sheets were put on top of the samples to prevent the evaporation of the water. Besides the beam samples, also 7 cubes were made to determine the compressive strength of the concrete mix.

Figure 3-33: Concrete material with spoons

Figure 3-34: Vibrating the concrete

3.4 Testing

All the Hybrid SHCC-Concrete beams have been tested in four-point bending configuration. A displacement-controlled method is chosen to apply the load at a rate of 0.002mm/sec. At one side of the beam, displacements are measured with LVDTs (Figure 3-35) while the other side of the beam is used to set-up for the Digital Image Correlation analysis (Figure 3-36).

Figure 3-35: Linear Variable Differential Transformers

Figure 3-36: Digital Image Correlation

3.4.1 Displacements

In order to measure the vertical displacement and opening of the interface and joint, Linear Variable Differential Transformers (LVDTs) have been used. These LVDTs are able to measure linear displacements with high accuracy. In total there are ten LVDTs, the first one is used to measure the vertical displacement of the Hybrid SHCC-Concrete beam (LVDT 1). The opening of the interface is measured with seven different LVDTs along the interface (LVDT 2 – 8). Finally, also two LVDTs are used to measure the opening of the middle joint at the bottom of the beam (LVDT 9 and 10). The placement of these LVDTs is shown in Figure 3-37 and Figure 3-38.

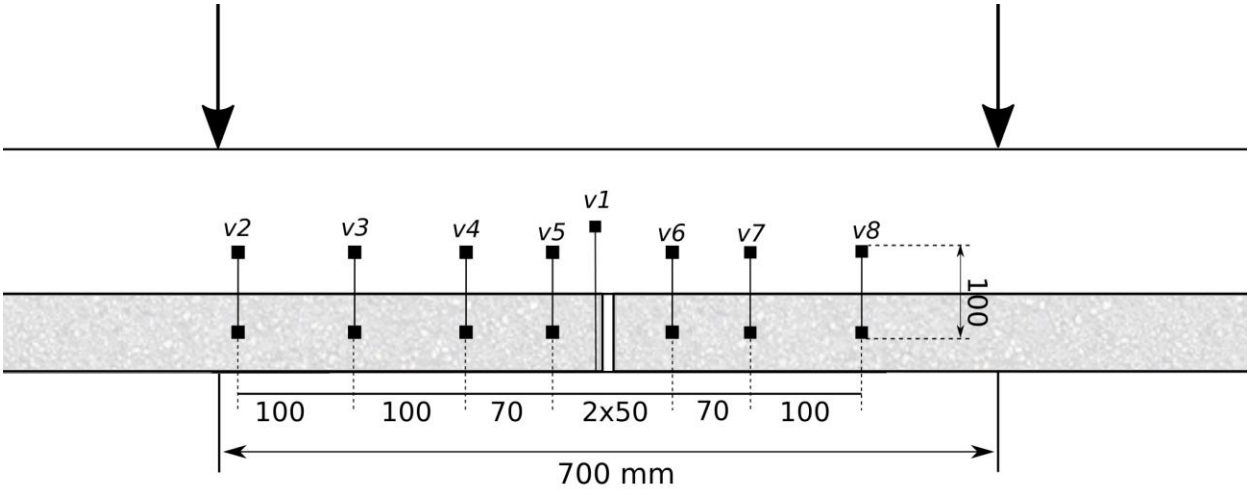

Figure 3-37: LVDTs placement on the side of the beam

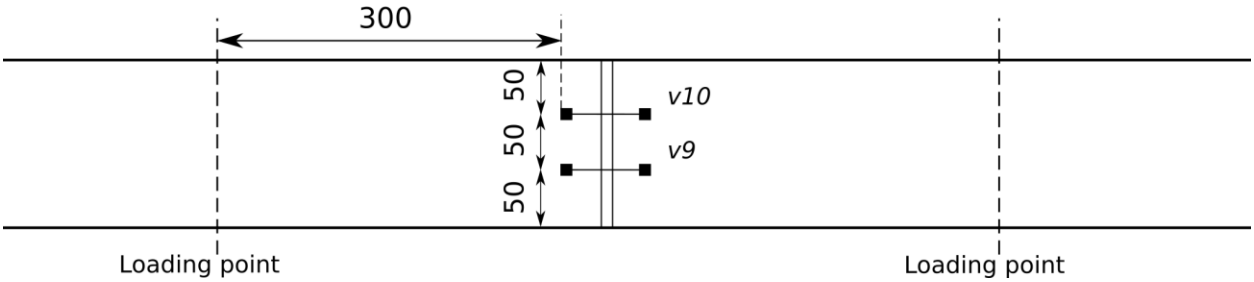

Figure 3-38: LVDTs placement on the bottom of the beam

3.4.2 **Digital Image Correlation**

Digital image correlation is used to determine the displacement field of the beam based on a series of images which were made during testing. Digital Image Correlation (DIC) is an optical non-contact method to determine the displacement field of a surface or object. This is done by correlation of two consecutive images which are divided into subsets as is shown in Figure 3-39 [24].

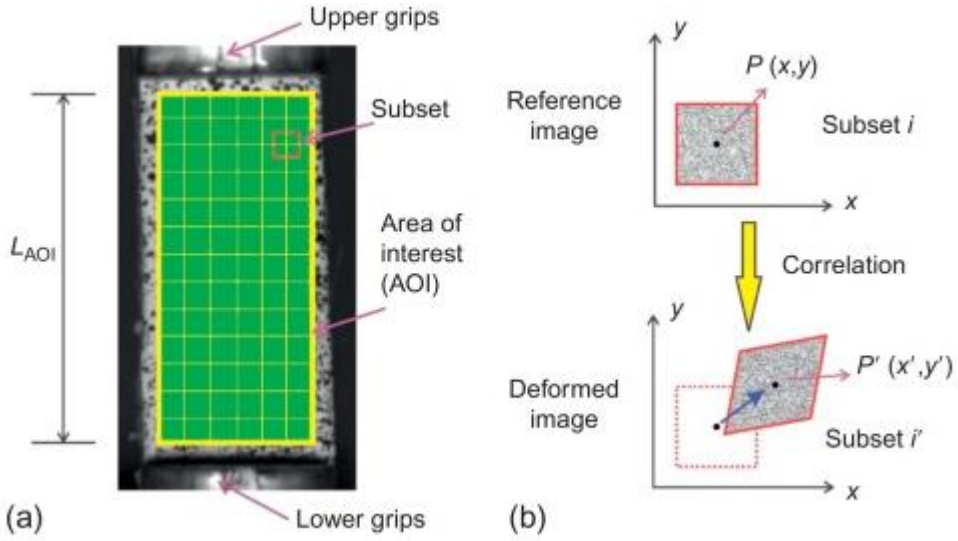

Figure 3-39: (a) Image divided into subsets; (b) correlation between two images (B. Mobasher, 2016)

The deformation between point $P(x,y)$ and $P'(x.y)$ of two consecutive images can be expressed as follows

$$x' = x + u(x,y) \tag{3.20}$$

$$y' = y + v(x,y) \tag{3.21}$$

In order to obtain the strain field use will be made of the Green-Lagrange strain tensor

$$E = \frac{1}{2} * [F^T * F - I] \tag{3.22}$$

In this expression F is the gradient displacement tensor, I is the identity matrix and $F^T * F$ is the stretch tensor. This Green-Lagrange strain tensor can be expressed as a function of the displacement field

$$E = \frac{1}{2} * \left(u_{i,j} + u_{j,i}\right) + \frac{1}{2} * \left(u_{k,i} * u_{k,j}\right) \tag{3.23}$$

In which $u_{i,j}$, $u_{j,i}$, $u_{k,i}$ and $u_{k,j}$ are the partial derivates of the displacement vectors with $i, j, k \in (x, y)$. The strain is obtained using the following expressions

$$\varepsilon_{xx} = \frac{\partial u_x}{\partial x} + \frac{1}{2}\left[\left(\frac{\partial u_x}{\partial x}\right)^2 + \left(\frac{\partial u_y}{\partial x}\right)^2\right] \tag{3.24}$$

$$\varepsilon_{yy} = \frac{\partial u_y}{\partial y} + \frac{1}{2}\left[\left(\frac{\partial u_x}{\partial y}\right)^2 + \left(\frac{\partial u_y}{\partial y}\right)^2\right] \tag{3.25}$$

$$\varepsilon_{xy} = \frac{1}{2}\left(\frac{\partial u_y}{\partial y} + \frac{\partial u_x}{\partial x}\right) + \frac{1}{2}\left[\frac{\partial u_x}{\partial x}\frac{\partial u_x}{\partial y} + \frac{\partial u_y}{\partial x}\frac{\partial u_y}{\partial y}\right] \tag{3.26}$$

The von Mises strain can finally be obtained as a combination of the major (ε_1) and minor (ε_3) principal stresses

$$\varepsilon_{vM} = \sqrt{\frac{2 * ((\varepsilon_1 - \varepsilon_3)^2 + {\varepsilon_1}^2 + {\varepsilon_3}^2)}{3}} \tag{3.27}$$

This same principle is used for the beams in this study. The beams have been painted white with a high density of black dots which will be used as the reference points for the subsets. These images are processed using the program GOM Correlate which is digital image correlation program for research of materials.

3.5 Experimental results

In this subchapter, the experimental results are presented. Furthermore, also Digital Image Correlation results are shown to visualize the crack propagation of each sample. First the reference sample will be discussed. After this, the samples with a different interface roughness will be discussed. Finally, the remaining samples with a smooth interface will elaborated. The following results are presented for each sample:

- Load-displacement curve and load versus maximum joint and interface opening of each sample.

- Figure presenting the damage of the sample at failure with a comparison of the Digital Image Correlation result. The Digital Image Correlation result has been mirrored to correspond to the image of the experimental result.

- Calculation of the yield stress for the coupling reinforcement at midspan based on the load-capacity of each sample and its effective height at midspan

- Table including the maximum load capacity, maximum interface opening, maximum joint opening and steel stress of the coupling reinforcement at midspan

- Digital Image Correlation results of the constant bending moment region for each load step. The load steps are shown in a separate load-displacement curve. Next to these images, also a bar chart is shown to compare the results of the interface and joint opening between the LVDTs and Digital Image Correlation.
    - *The Digital Image Correlation results are mirrored so that the location of the cracks corresponds to the results on the LVDT side of the beams.*
    - *The location of LVDT 5 and 6 is different for the Profiled interface sample as it was placed 20 mm away from the joint compared to the remaining samples where these are placed 50 mm from the joint.*
- The DIC analysis of sample 7 has been done differently using an improved DIC pattern. The photos are also made with a different camera using blue LED lights instead of a camera studio flashlight.

3.5.1 Sample 1 – Reference beam

Based on the results of the four-point bending test, the vertical displacement, maximum interface opening and maximum joint opening are plotted versus the load for the reference beam as is shown in Figure 3-40.

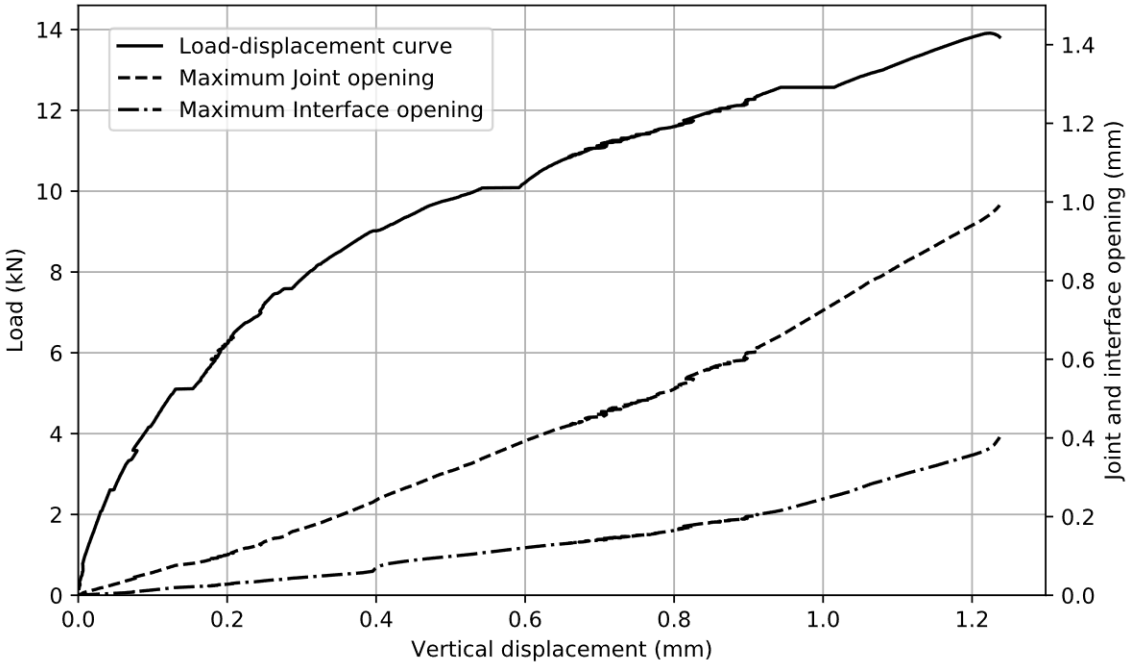

Figure 3-40: Sample 1 – Load-displacement graph with maximum interface and joint opening

The load capacity of the beam is roughly a third of the capacity which was calculated based on yielding of the coupling reinforcement (see Figure 3-3). This reduced capacity is a result of the opening of the interface similar to the case of Eindhoven. The maximum stress of the coupling reinforcement is calculated based on the load capacity of the sample

$$\sigma_s = \frac{M_{failure}}{A_s * \left(d - \frac{1}{3}x\right)} = 241MPa < f_y \tag{3.28}$$

In Table 3-6, the results at failure of this sample are shown.

Property	Value	Unit
Load capacity	13.9	kN
Maximum Displacement	1.24	mm
Maximum Interface opening	0.4	mm
Maximum Joint opening	0.99	mm
Maximum Steel stress	241	MPa

Table 3-6: Sample 1 - Test results at failure

Figure 3-41 shows the damage of the sample at failure at both sides of the beam. Based on these images, the interface opening is visible until the end of the coupling reinforcement. Furthermore, also several flexural cracks are visible along the length of the constant bending moment region. Barely any cracks are visible in the SHCC layer.

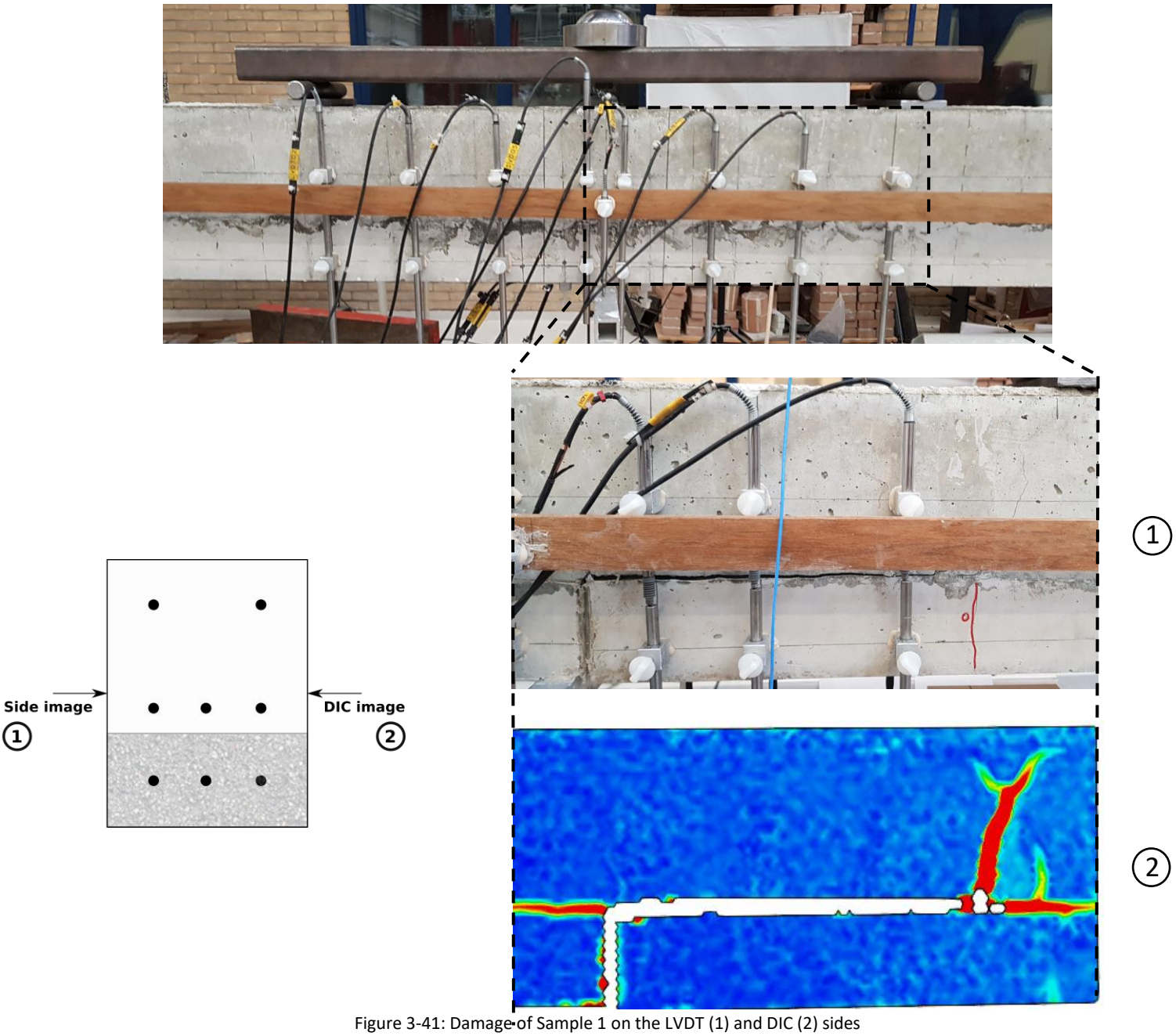

Figure 3-41: Damage of Sample 1 on the LVDT (1) and DIC (2) sides

The propagation of the cracks in the concrete and through the interface of the constant bending moment regions are shown Figure 3-43 – Figure 3-51. The corresponding load steps of these images are depicted in the load displacement graph shown in Figure 3-42.

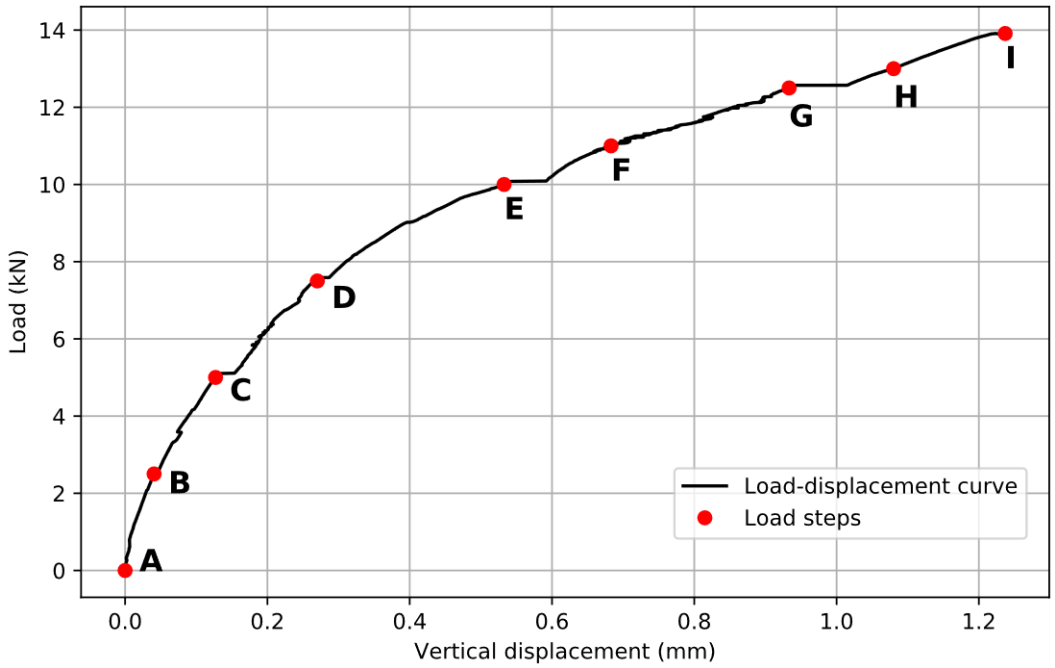

Figure 3-42: Sample 1 – Load-displacement graph with load steps for DIC images

In Figure 3-43 the surface component of the constant bending moment region is shown which is used to follow the crack propagation. Besides this, also a study is done to verify the DIC results of GOM Correlate by comparing the critical interface and joint opening to the obtained results from the LVDTs. These are shown in a bar chart in Figure 3-44 – Figure 3-51. These critical sections correspond to the locations of LVDT 5, LVDT 6 and LVDT 9 and are depicted in Figure 3-43 (note: no DIC images have been made of the bottom of the beam, therefore section LVDT 9 has been placed at the lowest possible points).

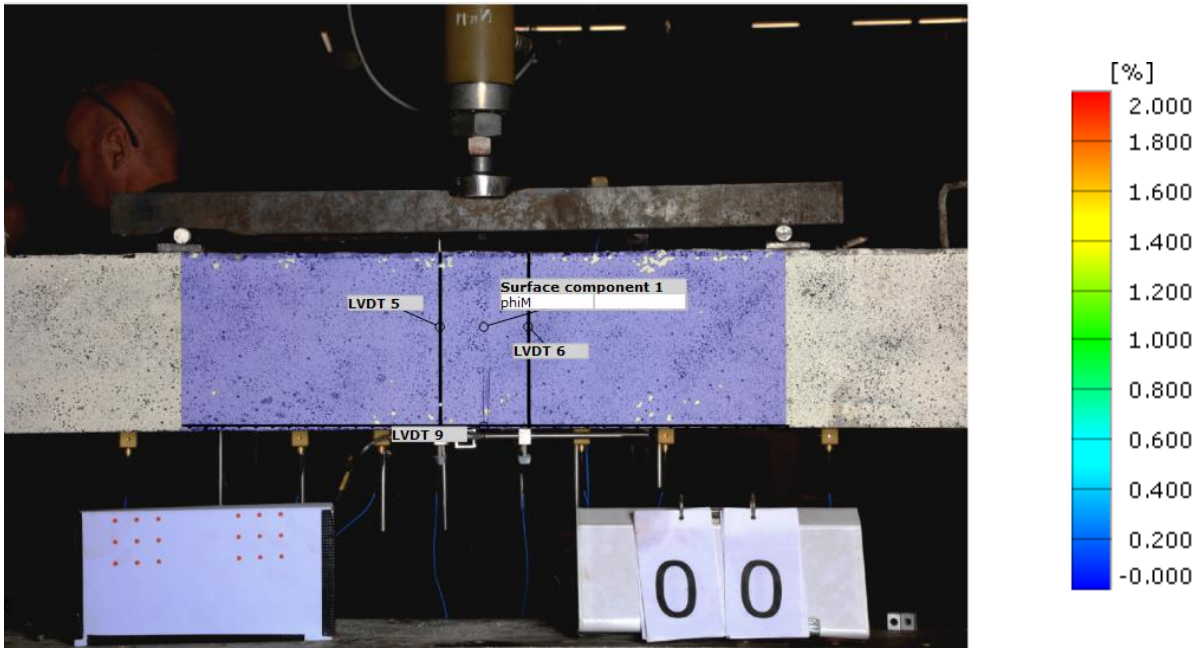

Figure 3-43: Load step A – 0 kN with surface component of constant bending moment region and LVDT sections

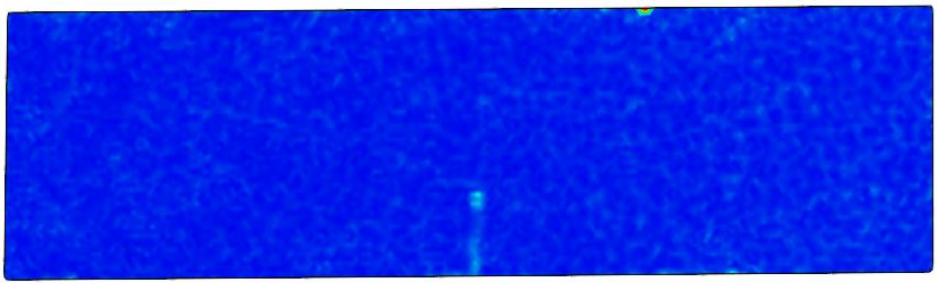

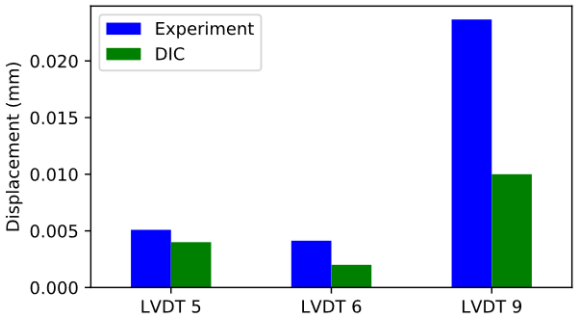

Figure 3-44: Load step B – 2.5 kN with comparison of DIC vs Experiments

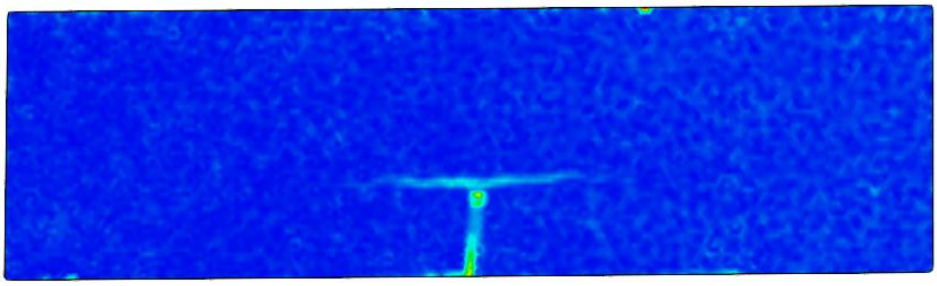

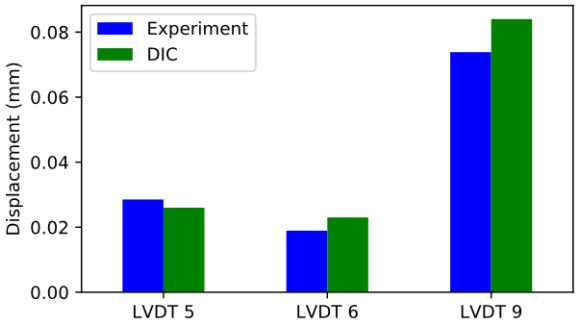

Figure 3-45: Load step C – 5kN with comparison of DIC vs Experiments

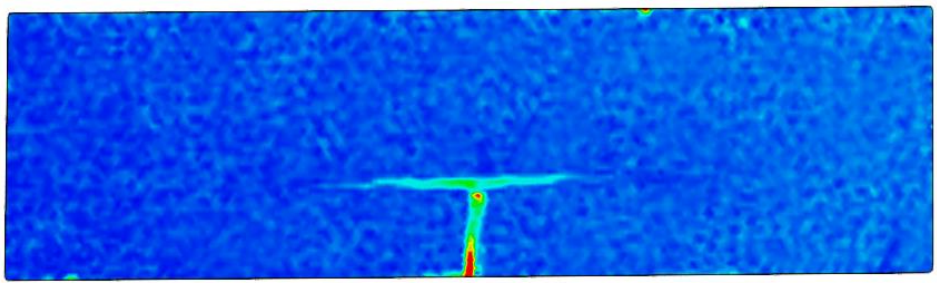

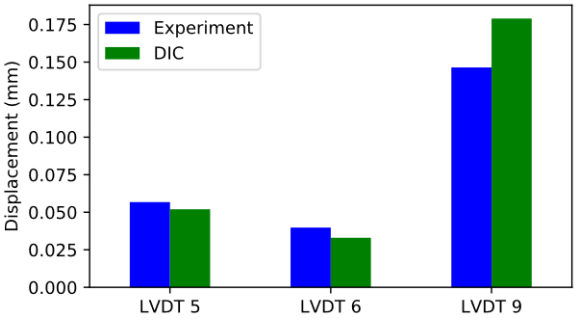

Figure 3-46: Load step D – 7.5 kN with comparison of DIC vs Experiments

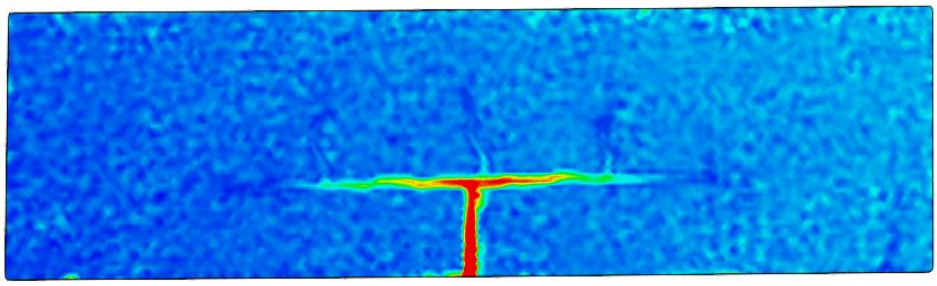

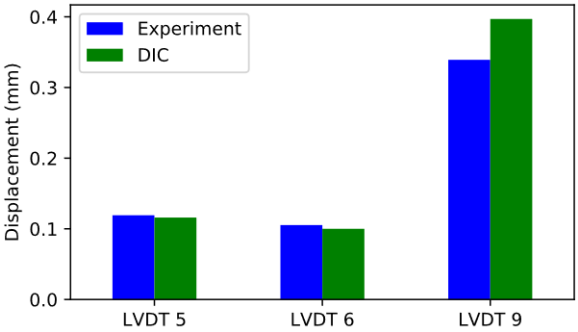

Figure 3-47: Load step E – 10 kN with comparison of DIC vs Experiments

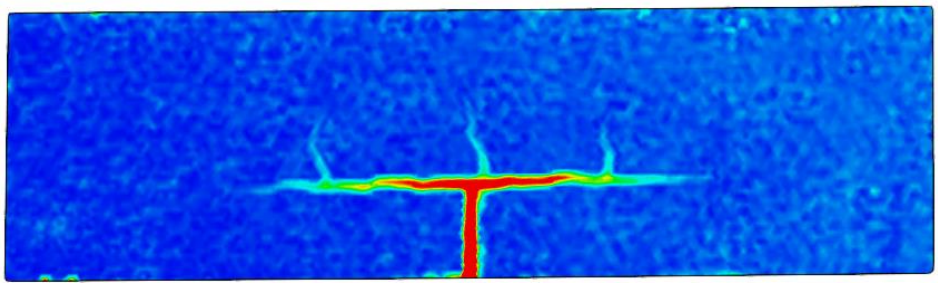

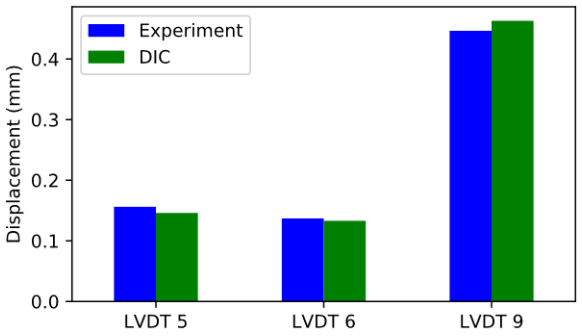

Figure 3-48: Load step F – 11 kN with comparison of DIC vs Experiments

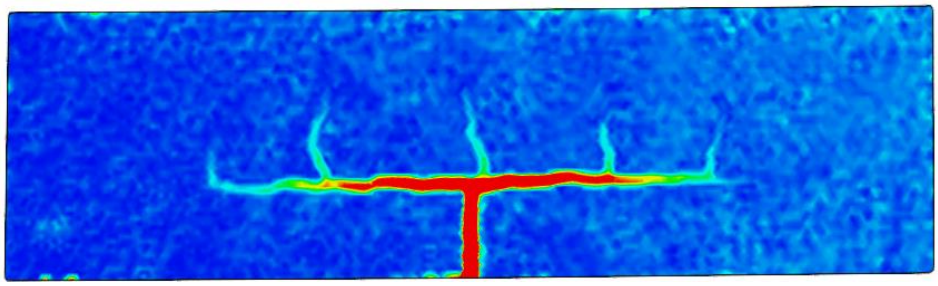

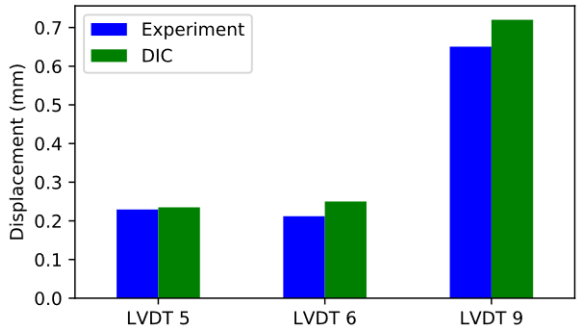

Figure 3-49: Load step G – 12.5 kN with comparison of DIC vs Experiments

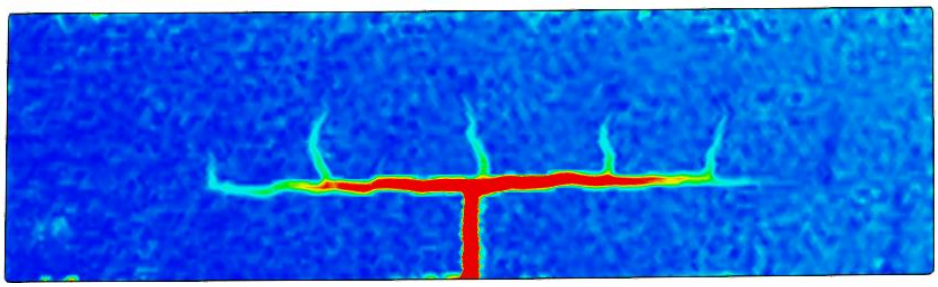

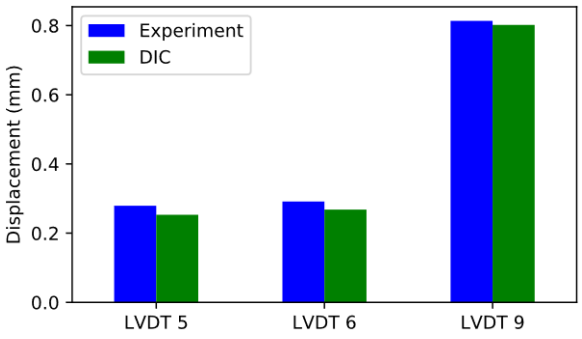

Figure 3-50: Load step H – 13 kN with comparison of DIC vs Experiments

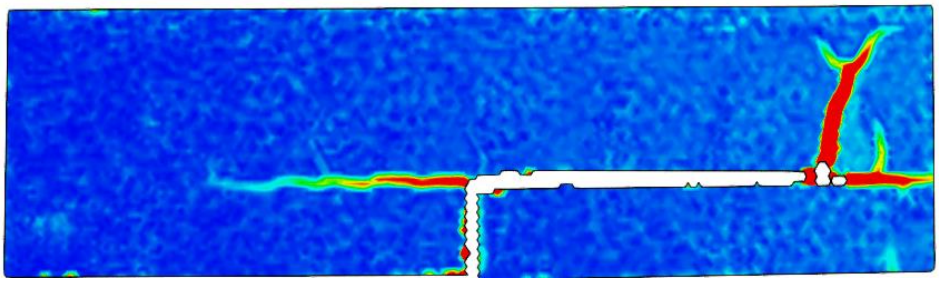

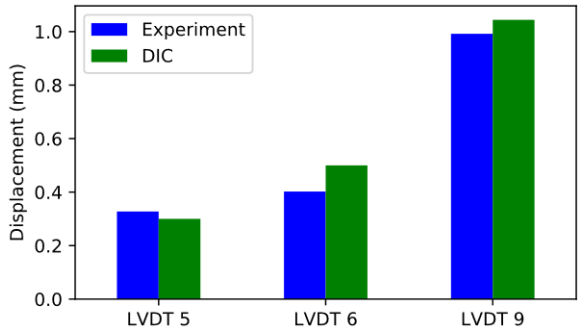

Figure 3-51: Load step I – Failure load with comparison of DIC vs Experiments at failure load

3.5.2 **Sample 2 – Profiled interface**

The vertical displacement, maximum interface opening and maximum joint opening is plotted against the load for the sample with a profiled interface. Furthermore, also the refence sample is shown as a comparison. This is depicted in Figure 3-52. The deviation of the load-displacement curve of the profiled interface sample at roughly 0.25 mm is because the LVDT was disturbed during the experiment.

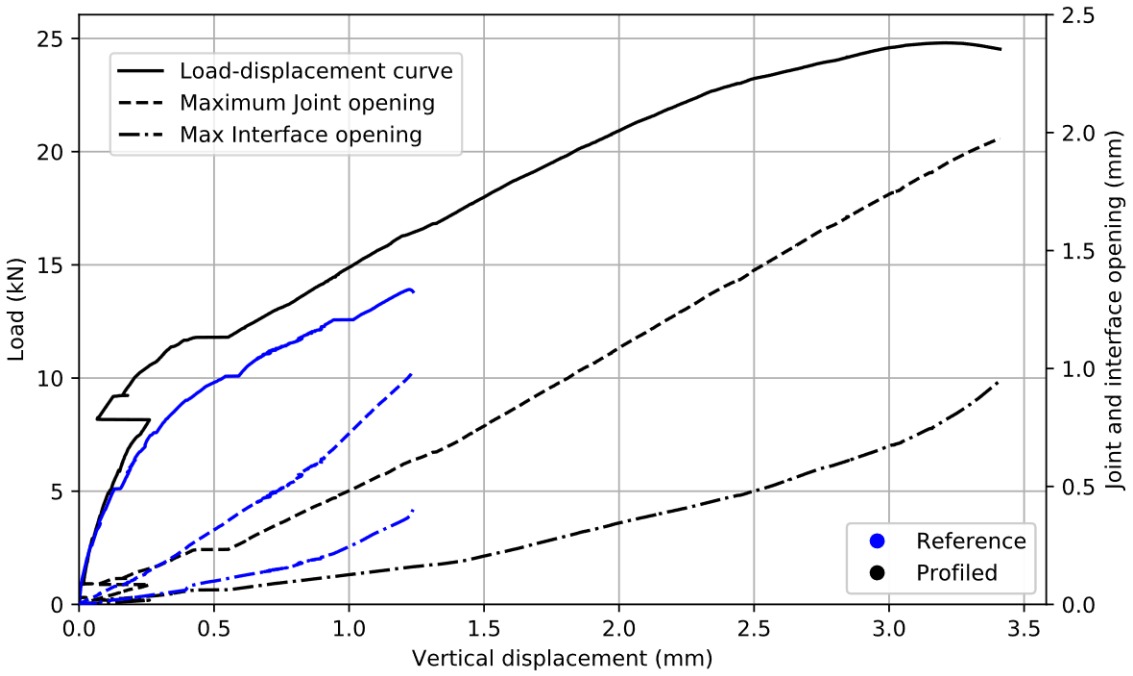

Figure 3-52: Sample 2 – Load-displacement graph with maximum interface and joint opening

The capacity of this sample is significantly higher than the reference sample with a smooth interface as a result of the increased tensile and shear capacity of the tooth-shaped interface. The sample failed due to a combination of interface delamination and a horizontal crack through the concrete. The stress in the coupling reinforcement at failure is

$$\sigma_s = \frac{M_{failure}}{A_s * \left(d - \frac{1}{3}x\right)} = 406MPa < f_y \tag{3.29}$$

The results of the load capacity and displacements of this hybrid SHCC-Concrete beam at failure are tabulated (see Table 3-7).

Property	Value	Unit
Load capacity	24.8	kN
Maximum Displacement	3.41	mm
Maximum Interface opening	0.95	mm
Maximum Joint opening	2.1	mm
Maximum Steel stress	406	MPa

Table 3-7: Sample 2 - Test results at failure

In Figure 3-53, the damage of the beam is shown at the failure side of the constant bending moment region. In the damage pattern, it can be seen that the horizontal crack goes through the concrete. As this crack progresses, the crack also goes through one tooth-shaped shape. As this horizontal crack reaches the end of the coupling reinforcement, a large vertical crack appears leading to the failure of the hybrid SHCC-concrete beam. The reason the joint opening is skewed is a result of the rotation of the plastic joint during casting.

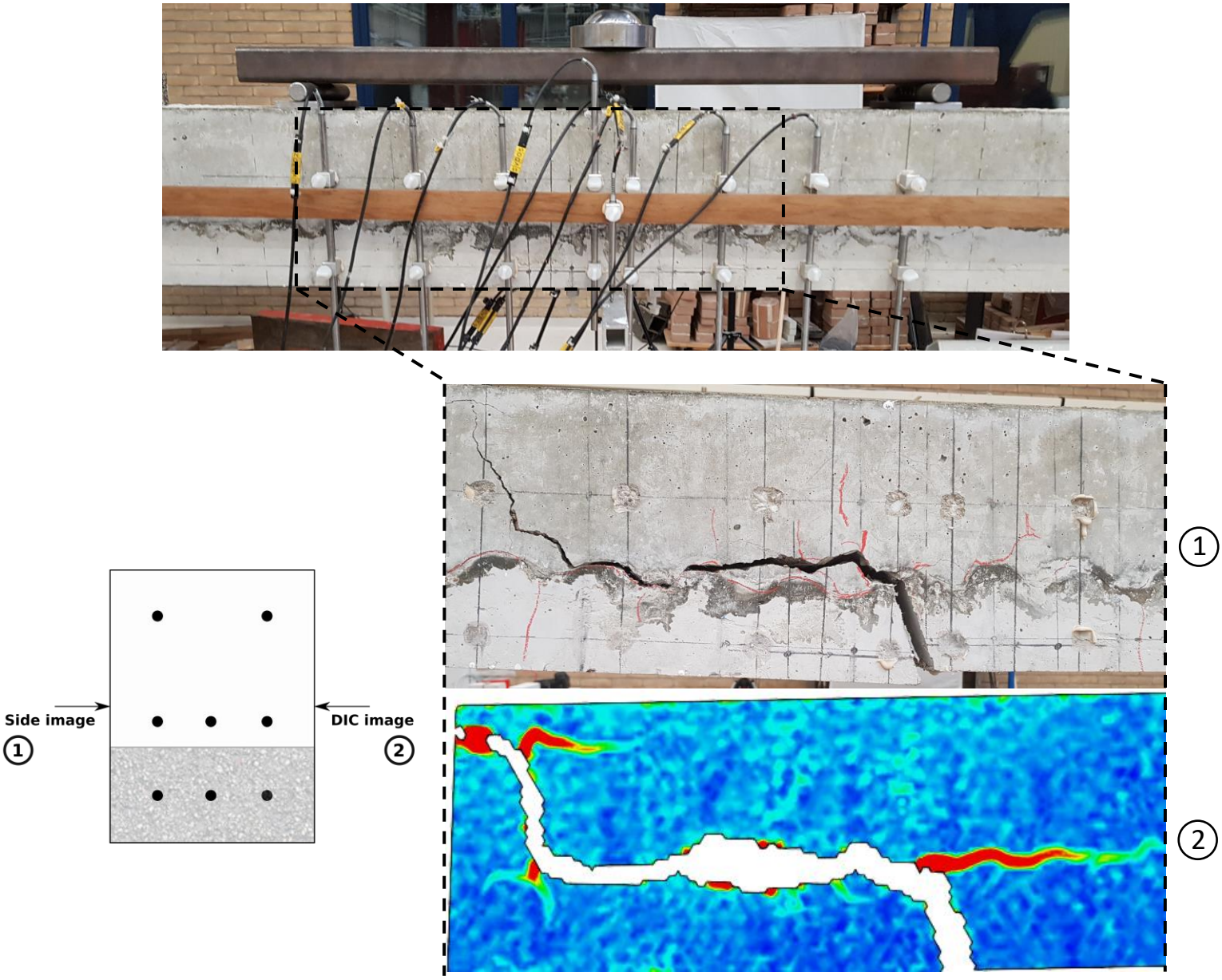

Figure 3-53: Damage of Sample 2 on the LVDT (1) and DIC (2) sides

The propagation of the cracks through the interface and concrete is shown using Digital Image Correlation results (see Figure 3-55 – Figure 3-63) . This is done in a step-by-step method of the corresponding loading points depicted in Figure 3-54. The area of interest is the constant bending moment region which has been investigated in GOM Correlate by specifying a surface component (see Figure 3-55).

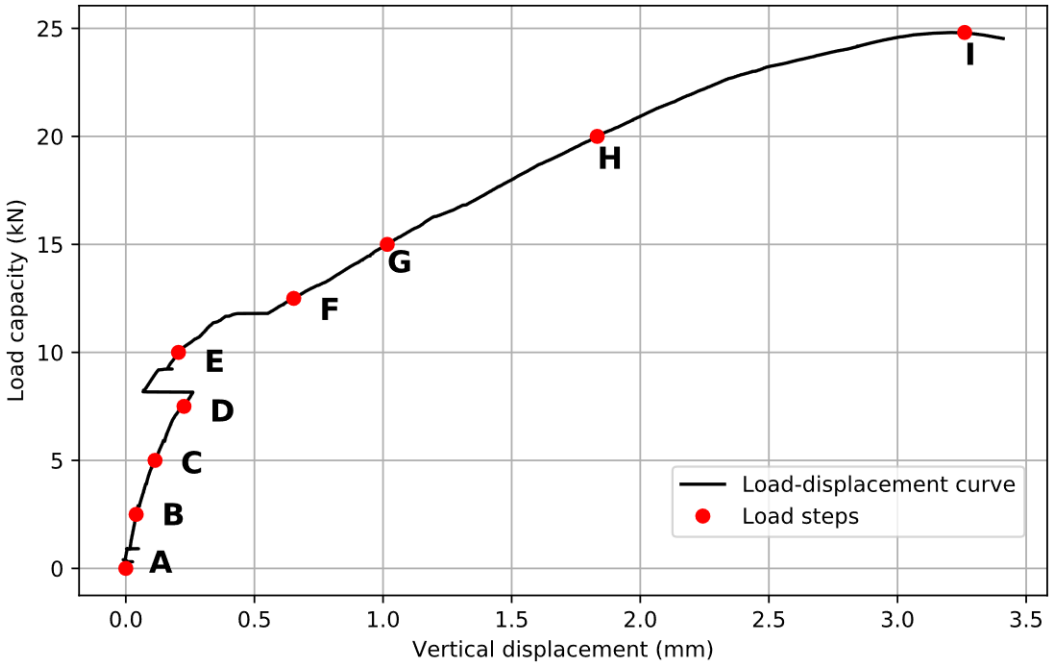

Figure 3-54: Sample 2 – Load-displacement graph with load steps for DIC images

All the DIC results for the corresponding loading points are shown in Figure 3-55 – Figure 3-63. Furthermore, also a comparative study is done for the critical sections (see Figure 3-55) of the interface and joint opening between the experimental and DIC results (see Figure 3-55 – Figure 3-63). These sections are the vertical displacement at the location of LVDT 5 and LVDT 6 (see Figure 3-37) and the horizontal displacement of the joint at the bottom side of the beam corresponding to LVDT 9 (note: no DIC images have been made of the bottom of the beam, therefore section LVDT 9 has been placed at the lowest possible points).

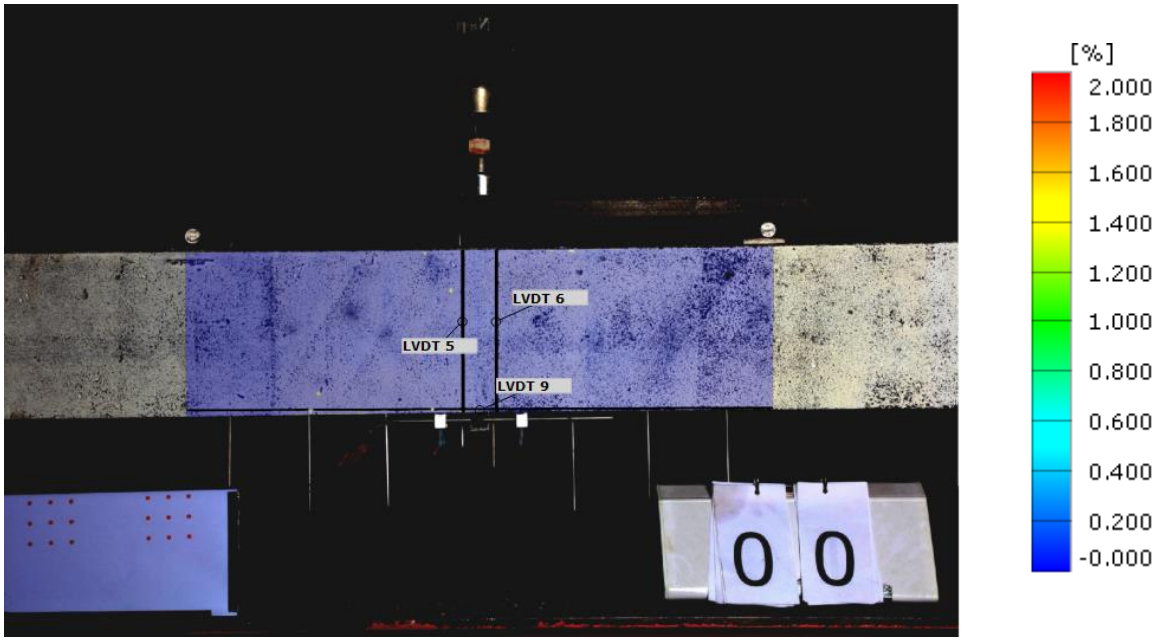

Figure 3-55: Load step A – 0 kN with surface component of constant bending moment region and LVDT sections

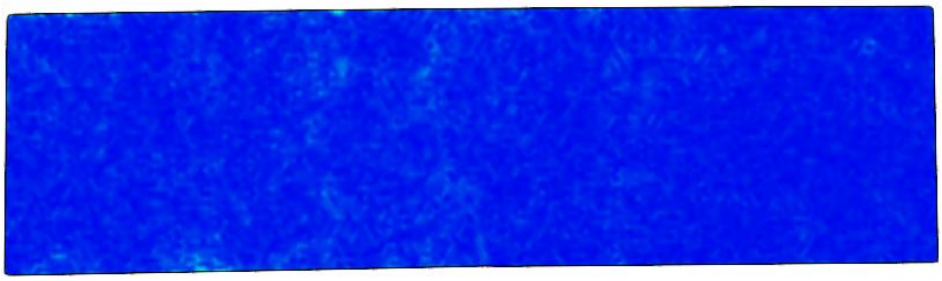

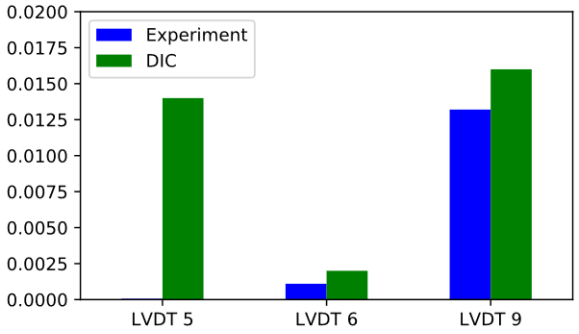

Figure 3-56: Load step B – 2.5 kN with comparison of DIC vs Experiments

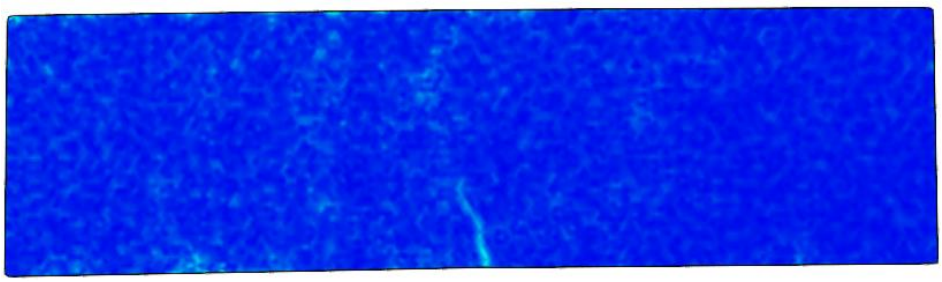

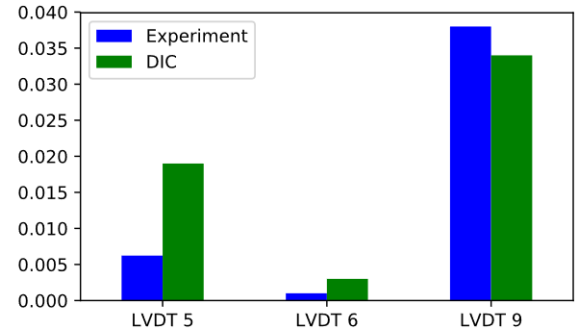

Figure 3-57: Load step C – 5kN with comparison of DIC vs Experiments

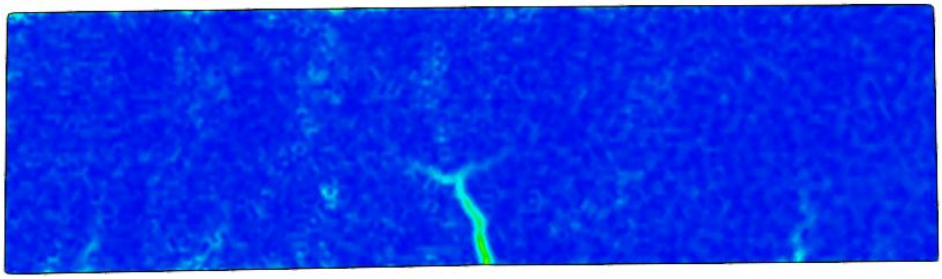

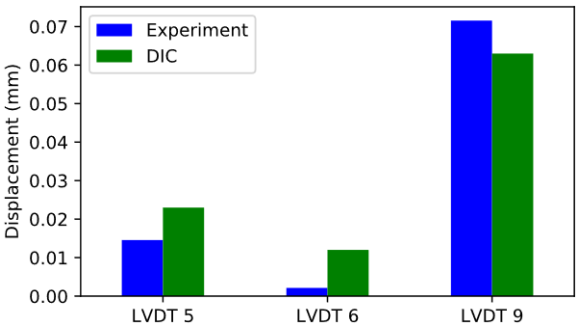

Figure 3-58: Load step D – 7.5 kN with comparison of DIC vs Experiments

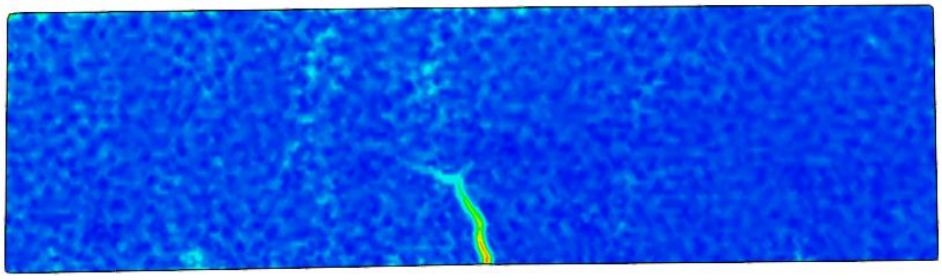

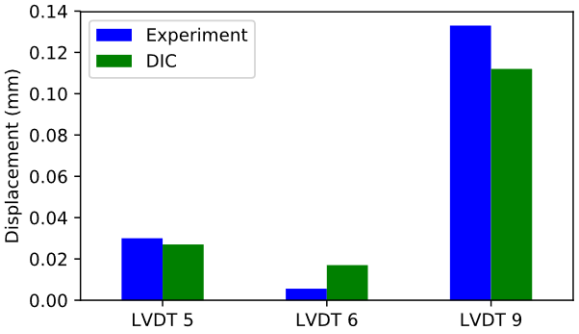

Figure 3-59: Load step E – 10 kN with comparison of DIC vs Experiments

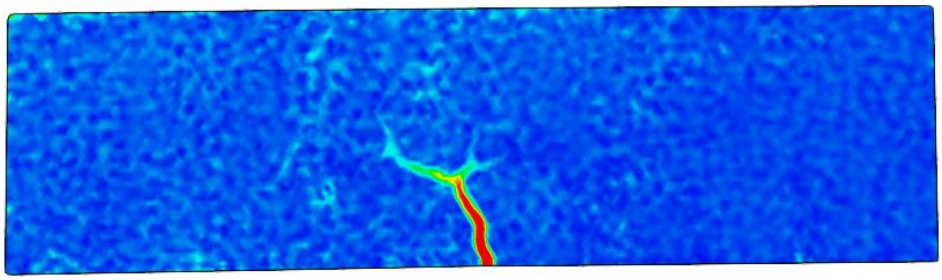

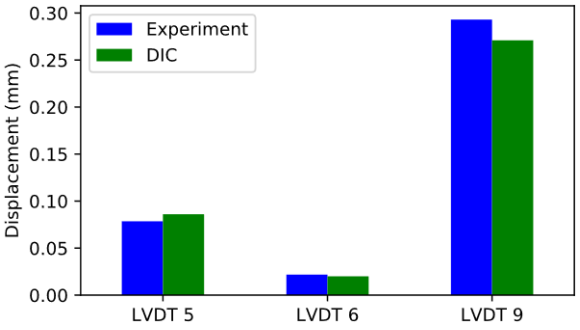

Figure 3-60: Load step F – 12.5 kN with comparison of DIC vs Experiments

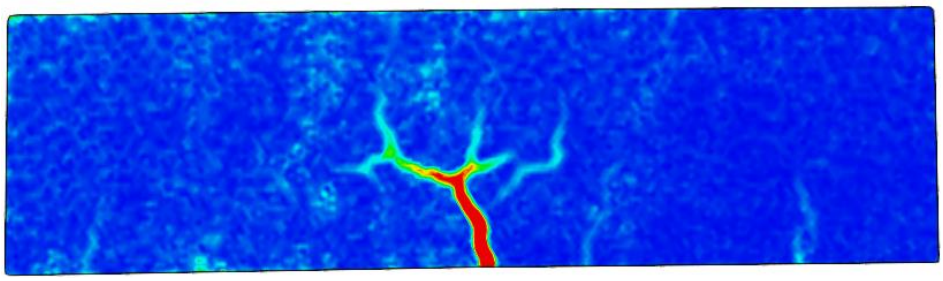

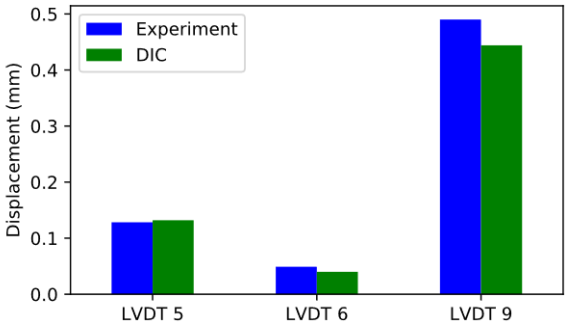

Figure 3-61: Load step G – 15 kN with comparison of DIC vs Experiments

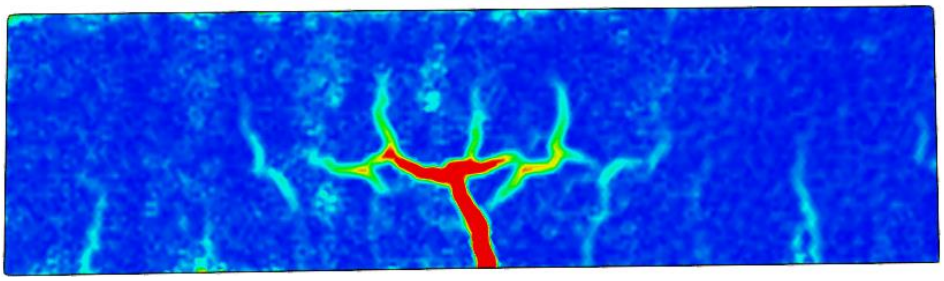

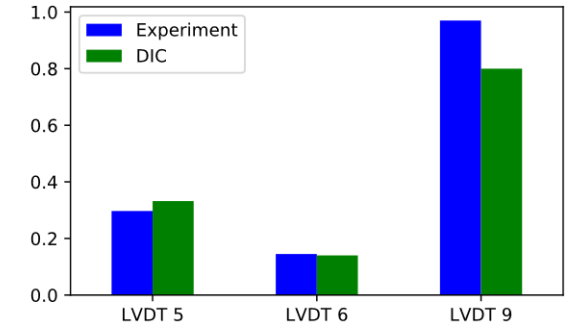

Figure 3-62: Load step H – 20 kN with comparison of DIC vs Experiments

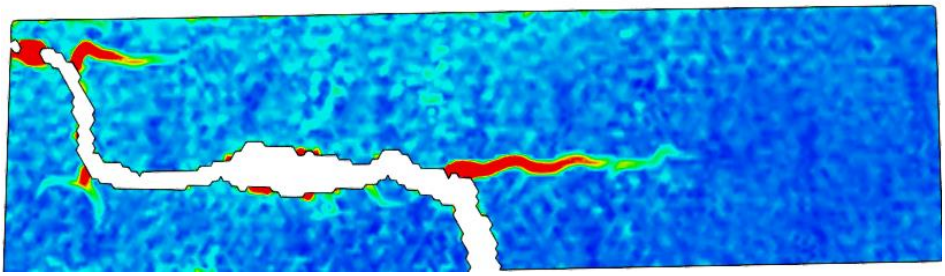

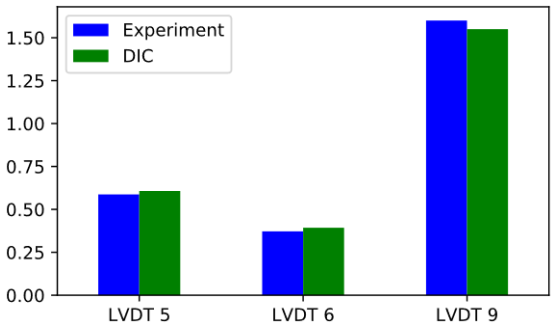

Figure 3-63: Load step I – Failure load with comparison of DIC vs Experiments at failure load

3.5.3 Sample 3 – Holed interface

For the sample with a holed interface, the vertical displacement at midspan, maximum interface opening and maximum joint opening versus the load is shown in Figure 3-64. As a comparison, also the results of the reference sample is shown.

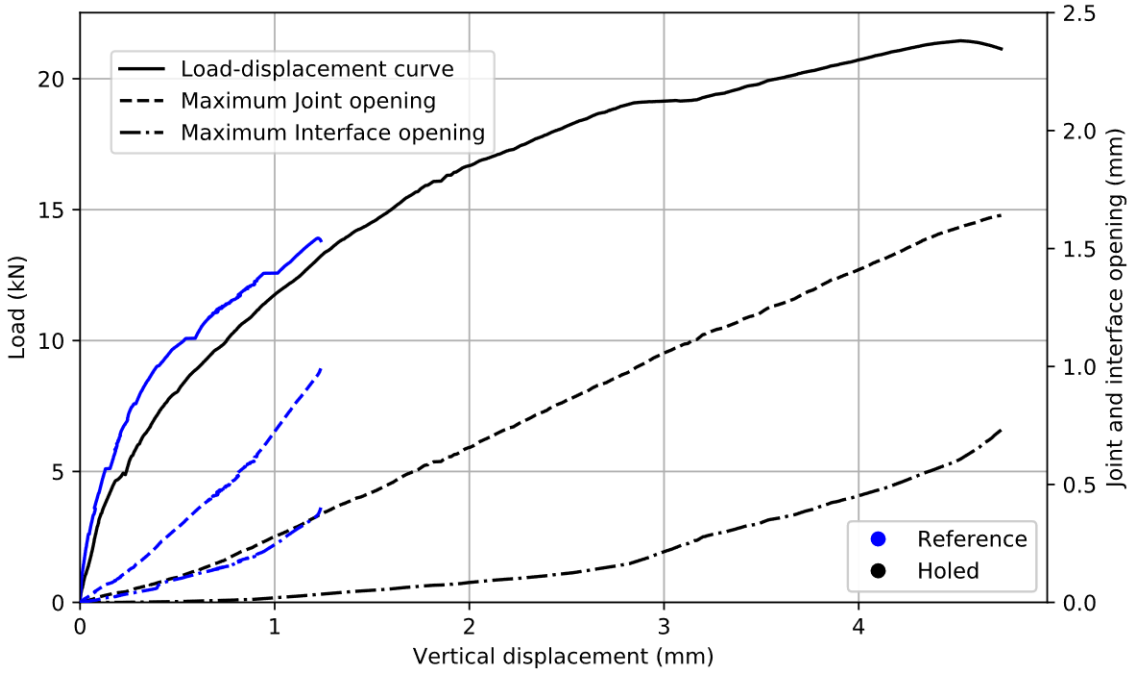

Figure 3-64: Sample 3 – Load-displacement graph with maximum interface and joint opening

The load capacity of this sample also increased significantly compared to a smooth interface due to the increased bond between the SHCC and concrete layers as a result of the applied holes in the SHCC. Nevertheless, this sample failed due to delamination of the interface prior to yielding of the coupling reinforcement

$$\sigma_s = \frac{M_{failure}}{A_s * \left(d - \frac{1}{3}x\right)} = 372MPa < f_y \tag{3.30}$$

The experimental results of this sample at failure are shown in Table 3-8.

Property	Value	Unit
Load capacity	21.5	kN
Maximum Displacement	4.73	mm
Maximum Interface opening	0.73	mm
Maximum Joint opening	1.68	mm
Maximum Steel stress	372	MPa

Table 3-8: Sample 3 – Test results at failure

The cracking pattern and delamination of the sample with a holed interface at failure can be seen in Figure 3-65 for both the LVDT and DIC side. In the cracking pattern of the DIC image, it can be seen that this delamination of the interface is along the length of the coupling reinforcement after which a large flexural crack appears resulting in the failure of the hybrid beam. Furthermore, several flexural cracks along the beam in the top concrete layer are visible at the location of the holes.

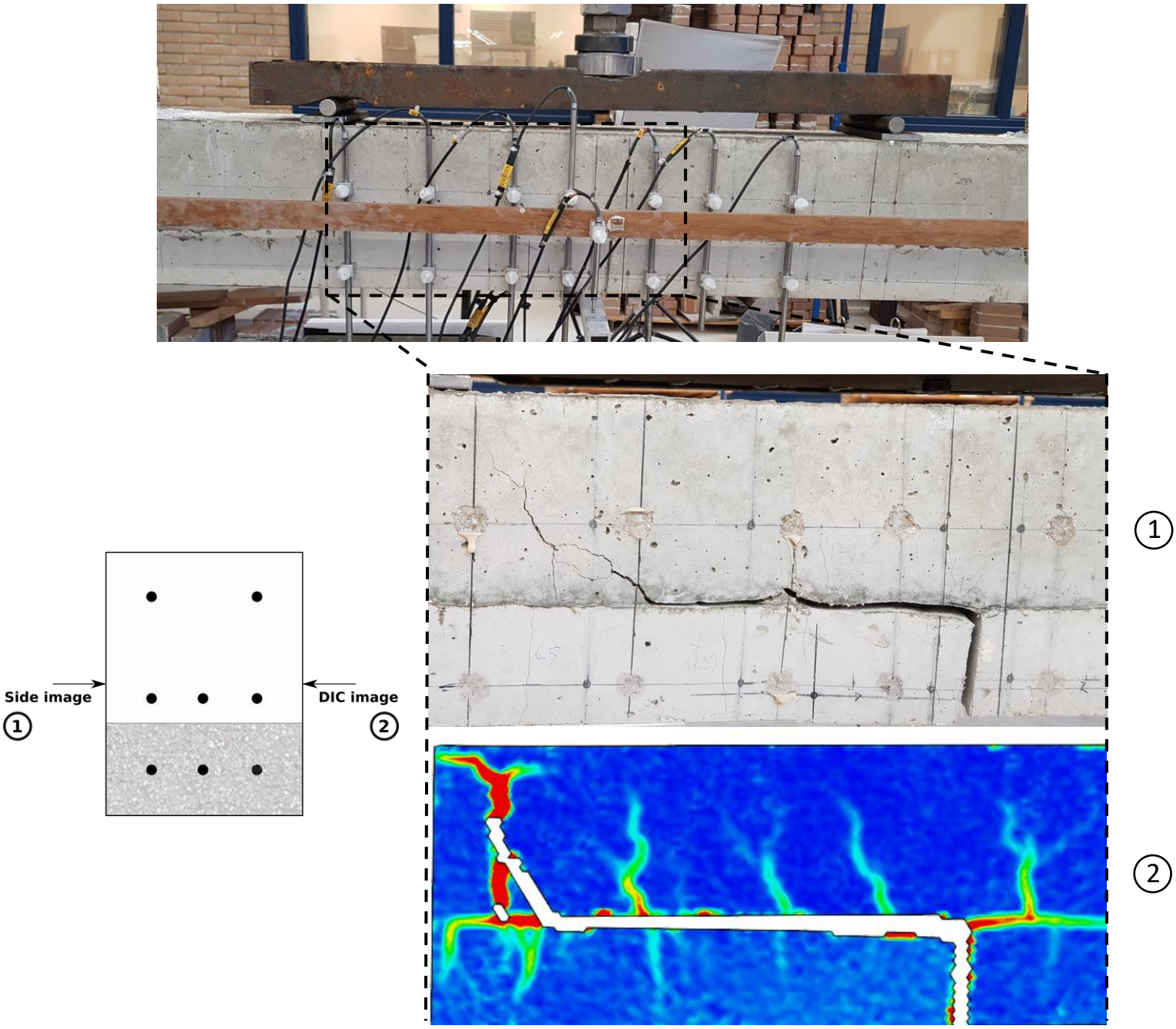

Figure 3-65: Damage of sample 3 on the LVDT (1) and DIC (2) sides

The step-by-step visualization of the cracking pattern of the sample with a holed interface is shown in Figure 3-67– Figure 3-75. These steps correspond to the loading points which are depicted in Figure 3-66.

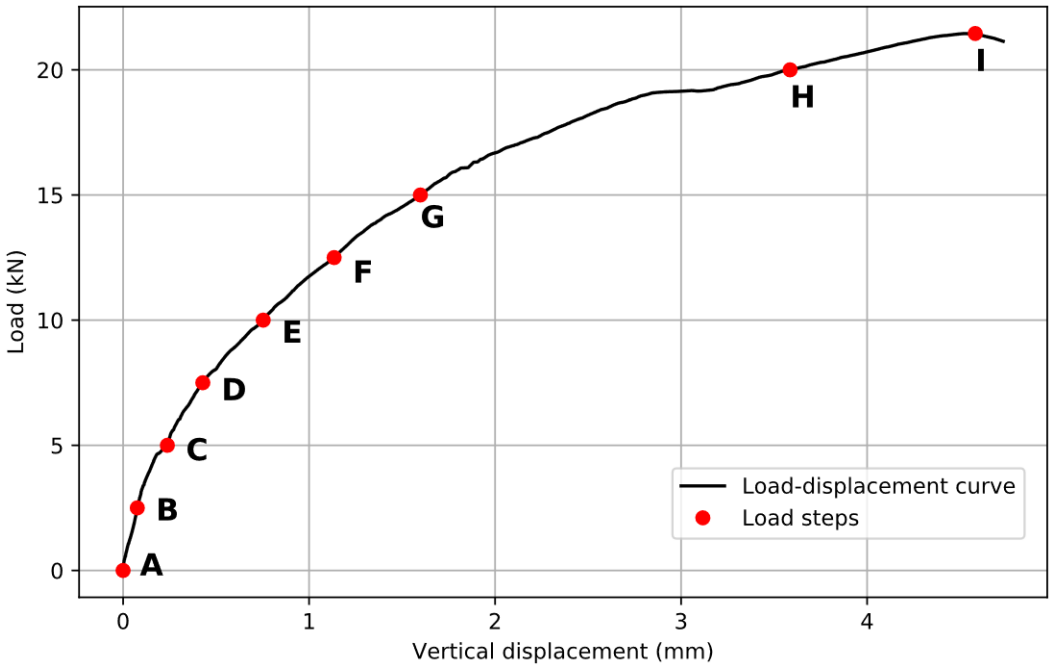

Figure 3-66: Sample 3 – Load-displacement graph with load steps for DIC images

In Figure 3-67, load step A is shown with the surface component of the constant bending moment region. The DIC images of the remaining load steps are based on this surface component. Next to this, also a comparison is made between the results of the LVDT and DIC of the interface and joint opening. These are also shown in Figure 3-68 – Figure 3-75. In order to obtain displacement from the DIC images, sections have been added in GOM Correlate at the same exact location of the LVDTs which are indicated in Figure 3-67 (note: no DIC images have been made of the bottom of the beam, therefore section LVDT 9 has been placed at the lowest possible points).

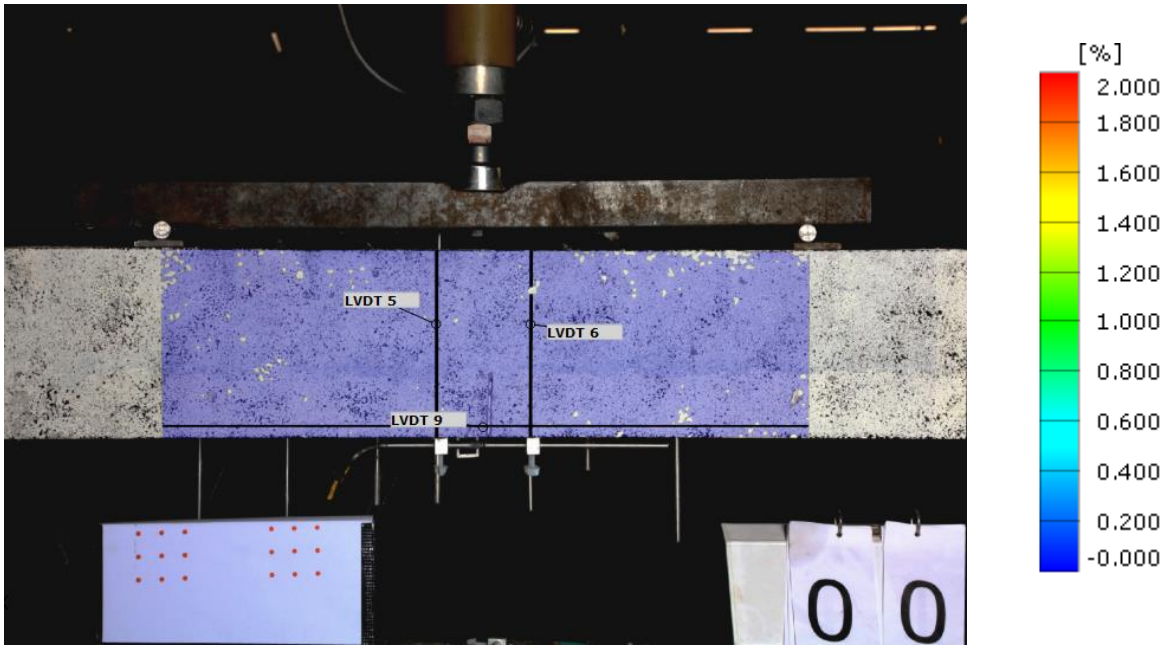

Figure 3-67: Load step A – 0 kN with surface component of constant bending moment region and LVDT sections

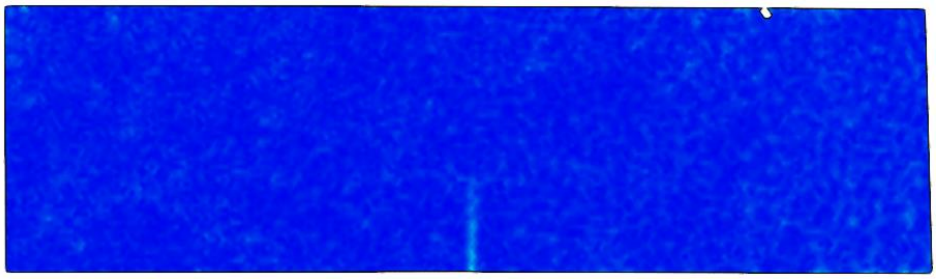

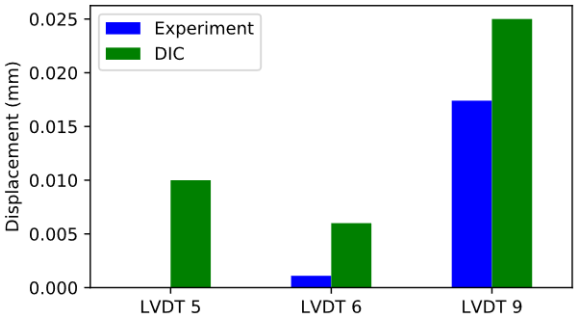

Figure 3-68: Load step B – 2.5 kN with comparison of DIC vs Experiments

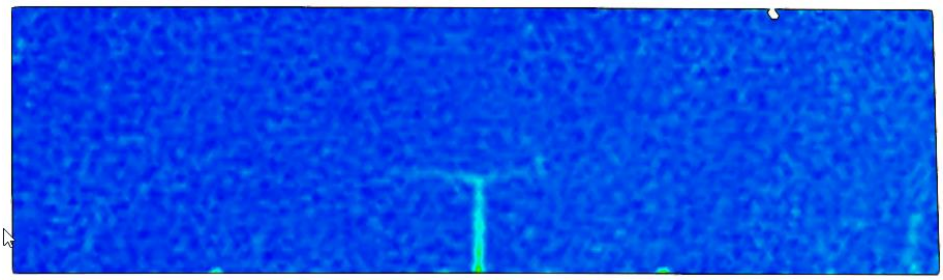

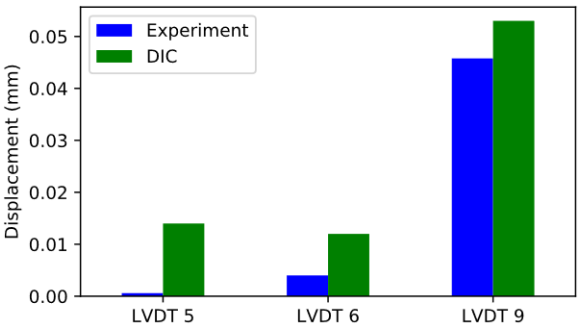

Figure 3-69: Load step C – 5kN with comparison of DIC vs Experiments

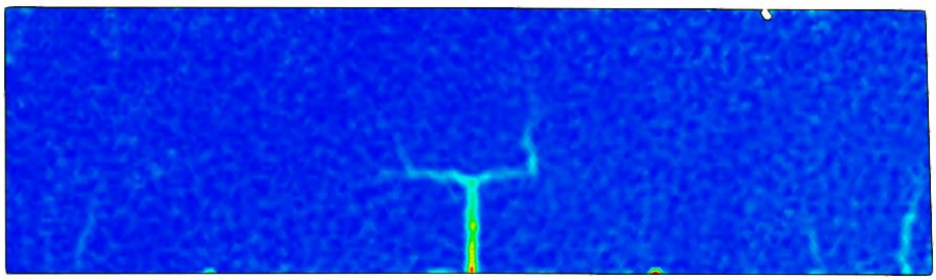

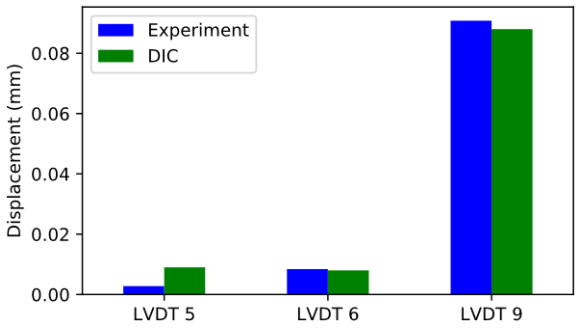

Figure 3-70: Load step D – 7.5 kN with comparison of DIC vs Experiments

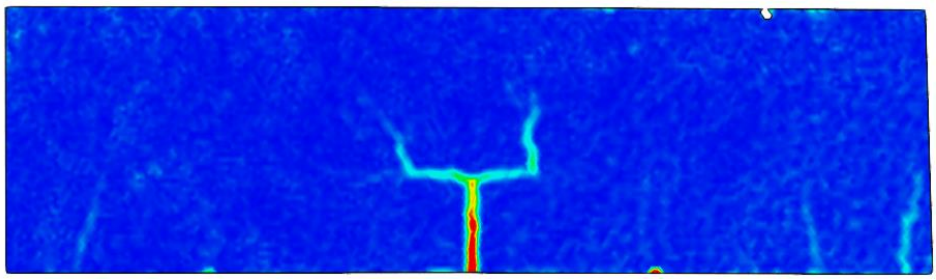

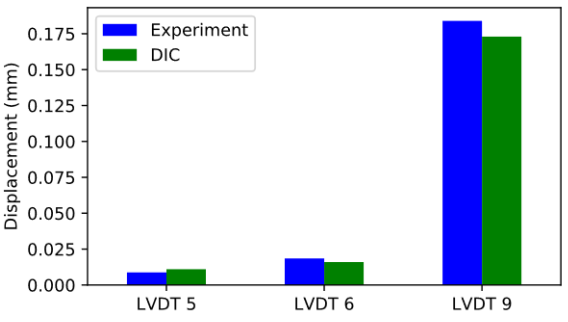

Figure 3-71: Load step E – 10 kN with comparison of DIC vs Experiments

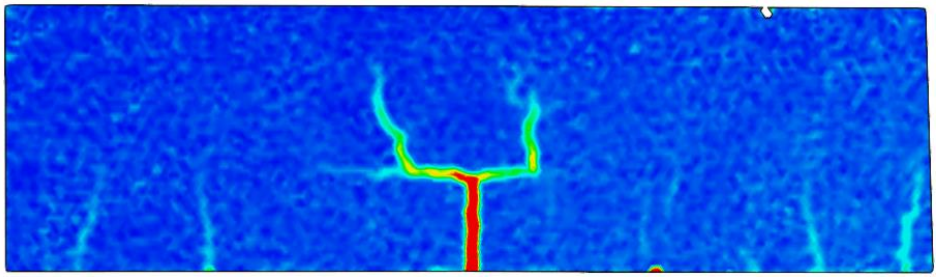

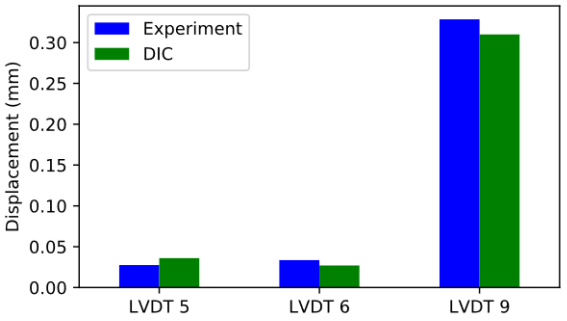

Figure 3-72: Load step F – 12.5 kN with comparison of DIC vs Experiments

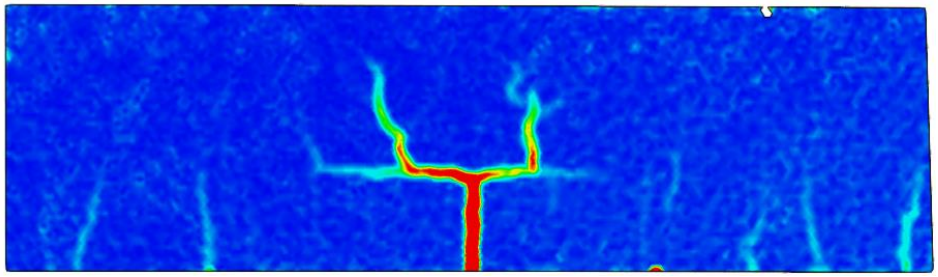

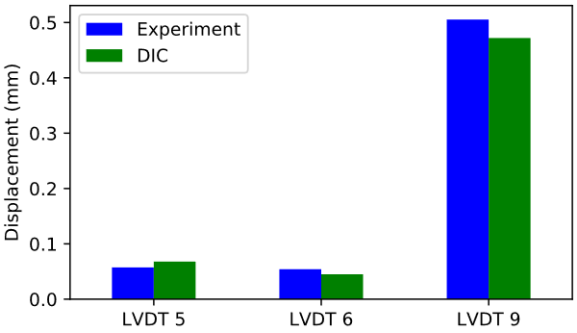

Figure 3-73: Load step G – 15 kN with comparison of DIC vs Experiments

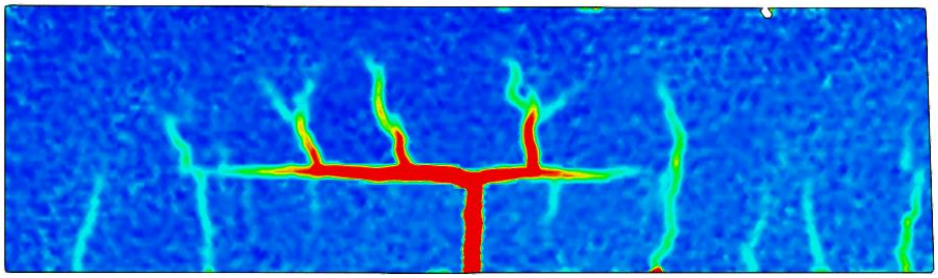

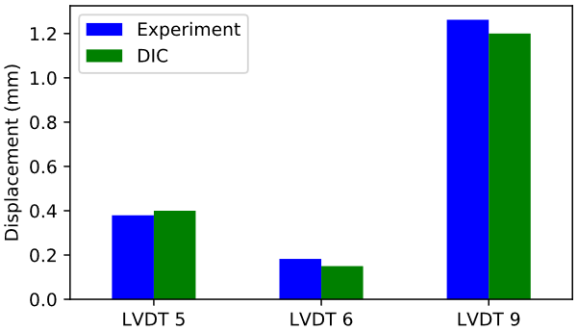

Figure 3-74: Load step H – 20 kN with comparison of DIC vs Experiments

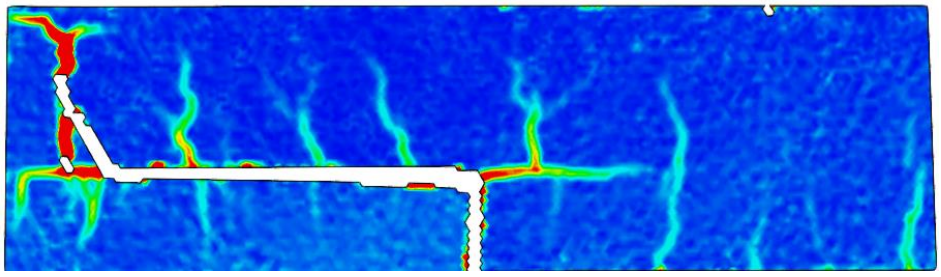

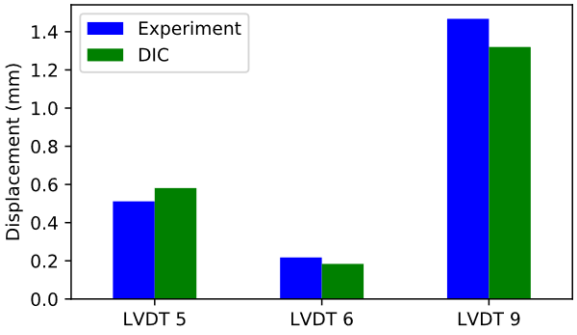

Figure 3-75: Load step I – Failure load with comparison of DIC vs Experiments at failure load

3.5.4 **Sample 4 – Epoxy and Sand**

Sample 4 consists of an interface with epoxy and coarse sand. The results from the four-point bending tests are shown in Figure 3-76 which consists of a load-displacement curve and two curves for the maximum interface and joint opening. Furthermore, also the reference sample is shown.

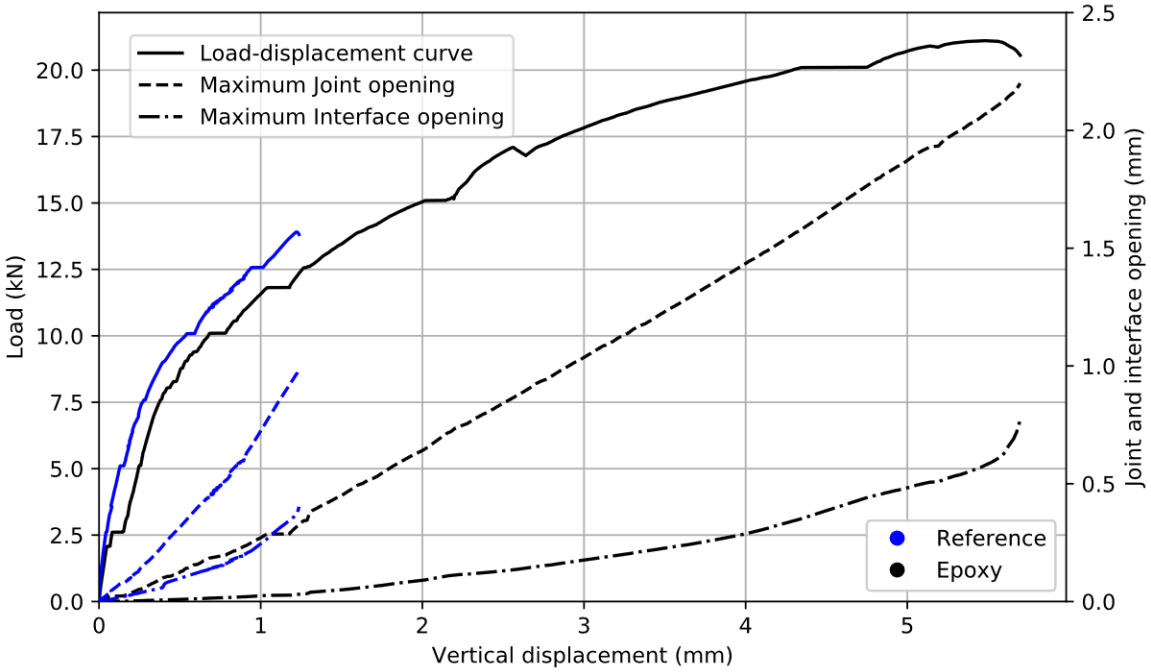

Figure 3-76: Sample 4 – Load-displacement graph with maximum interface and joint opening

By applying coarse sand on the interface, the bond between the SHCC and concrete is increased. As a result of this, a larger capacity is found. Furthermore, also the maximum interface opening remained minimal up until the failure load was being reached. As the load capacity is lower than the calculated yield capacity of the beam, the coupling reinforcement hasn't reached its yielding stress

$$\sigma_s = \frac{M_{failure}}{A_s * \left(d - \frac{1}{3}x\right)} = 366MPa < f_y \tag{3.31}$$

All the results of this sample at failure are shown in Table 3-9.

Property	Value	Unit
Load capacity	21.1	kN
Maximum Displacement	5.7	mm
Maximum Interface opening	0.77	mm
Maximum Joint opening	2.2	mm
Maximum Steel stress	366	MPa

Table 3-9: Sample 4 - Test results at failure

In Figure 3-77, an image is shown of the failure of the beam with a DIC image for comparison. Initially, the interface delaminated close to the joint. However, as this delamination progressed along the length of the coupling reinforcement, this crack started propagating through the concrete at the height of the coupling reinforcement. This crack propagated until the end of the coupling reinforcement where a large flexural crack appeared.

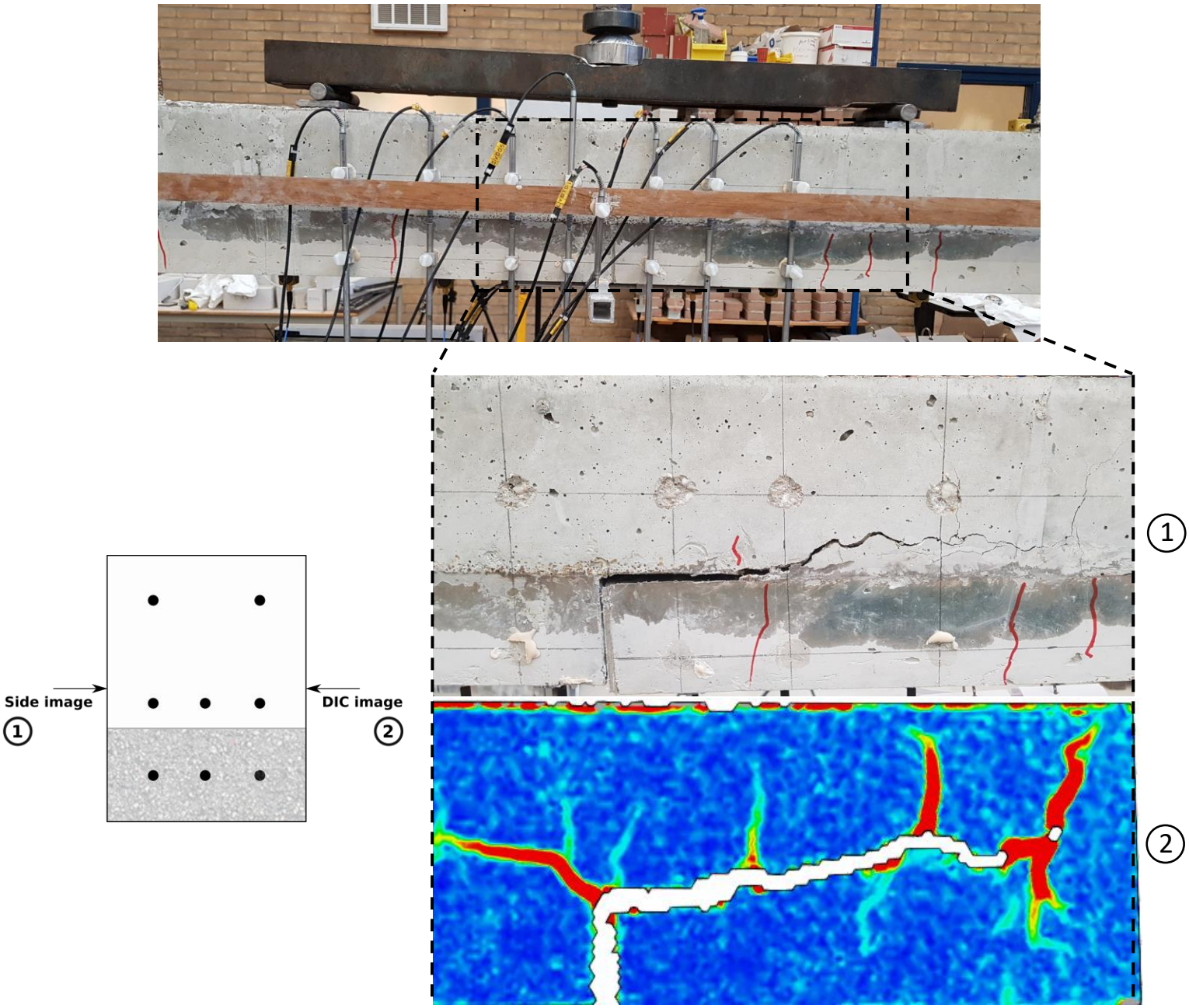

Figure 3-77: Damage of Sample 4 on the LVDT (1) and DIC (2) sides

The propagation of the cracks during the four-point bending tests is shown in Figure 3-79 – Figure 3-87. These images correspond to the loading points visualized in the load-displacement curve in Figure 3-78.

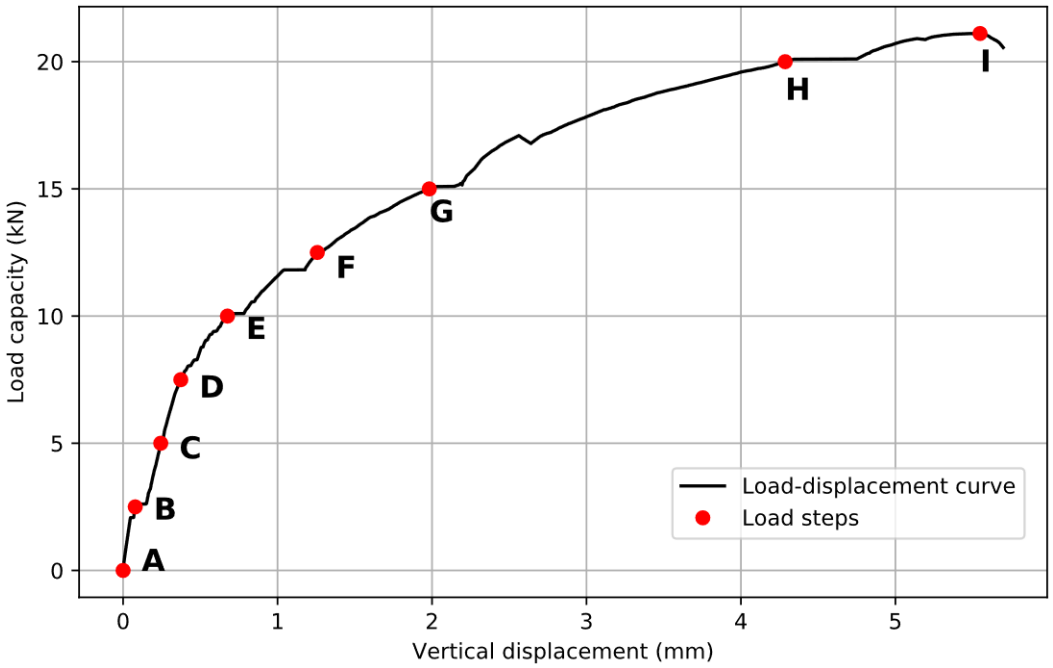

Figure 3-78: Sample 4 – Load-displacement graph with load steps for DIC images

The DIC images have been produced in GOM Correlate. The surface component on which the strains are generated is shown in Figure 3-79. Also, in this image, several sections are shown along which the displacements are generated to compare with the results of the LVDTs. These results are presented in a chart diagram in Figure 3-80Figure 3-79 – Figure 3-87 (note: no DIC images have been made of the bottom of the beam, therefore section LVDT 9 has been placed at the lowest possible points).

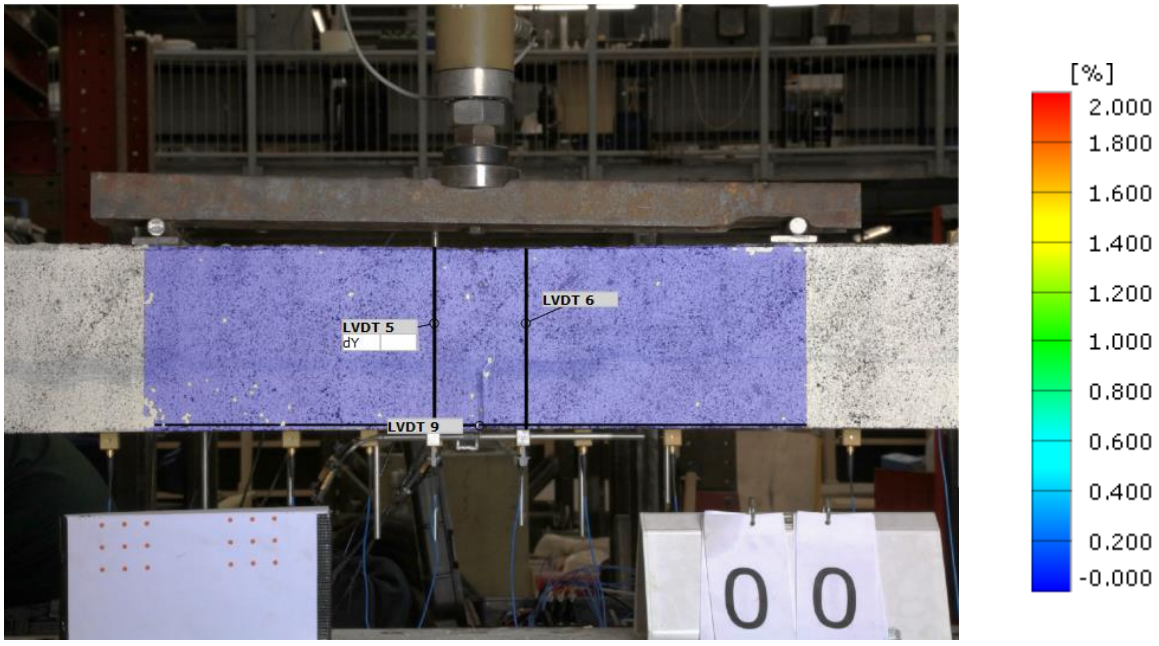

Figure 3-79: Load step A – 0 kN with surface component of constant bending moment region and LVDT sections

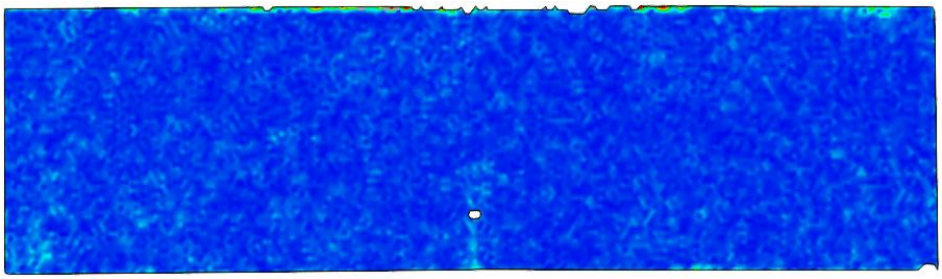

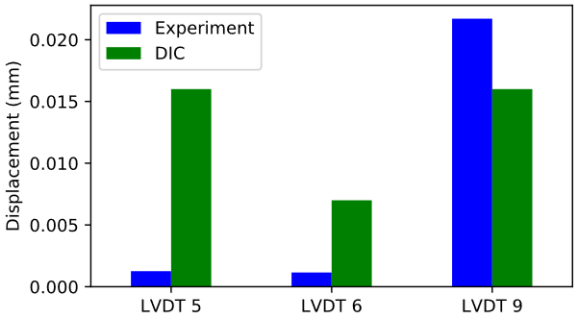

Figure 3-80: Load step B – 2.5 kN with comparison of DIC vs Experiments

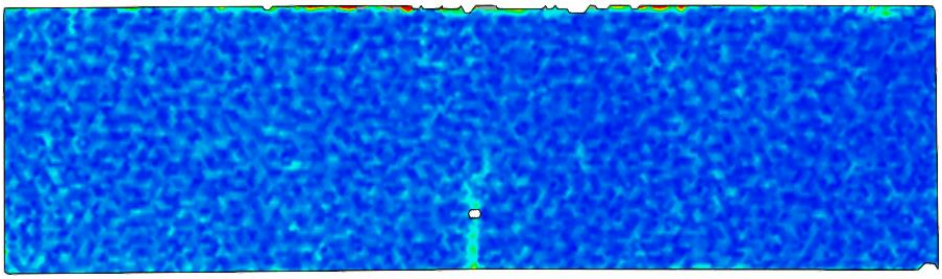

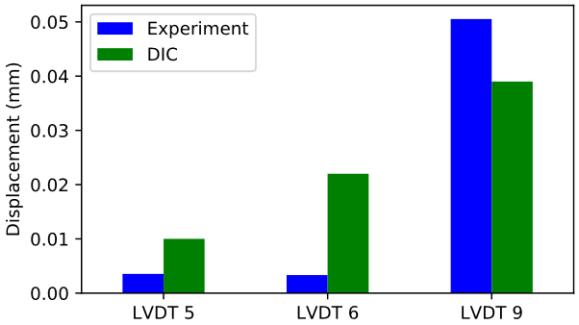

Figure 3-81: Load step C – 5kN with comparison of DIC vs Experiments

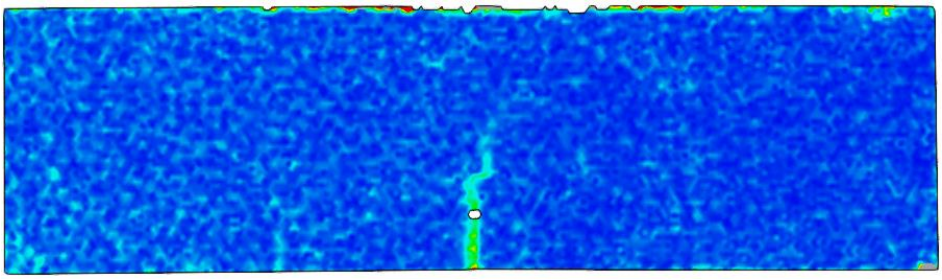

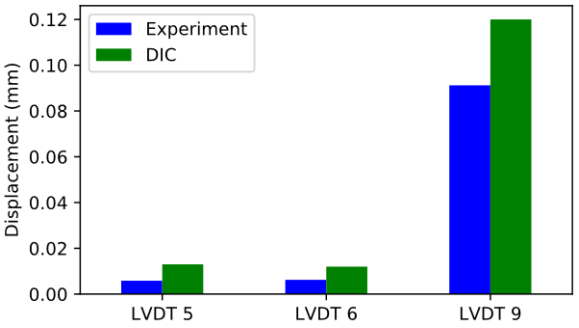

Figure 3-82: Load step D – 7.5 kN with comparison of DIC vs Experiments

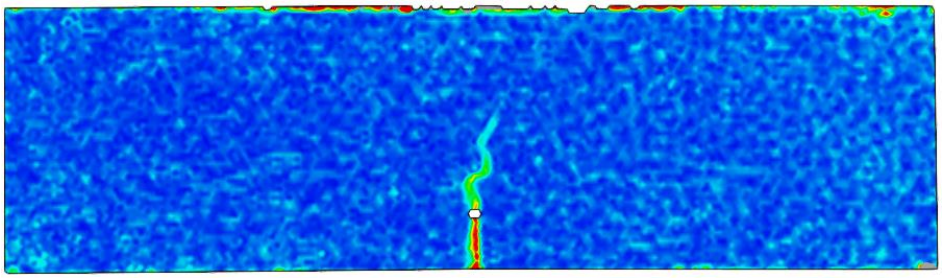

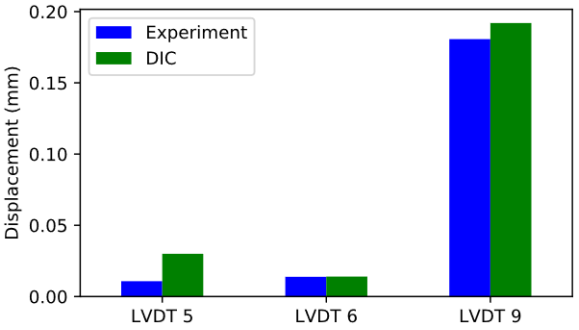

Figure 3-83: Load step E – 10 kN with comparison of DIC vs Experiments

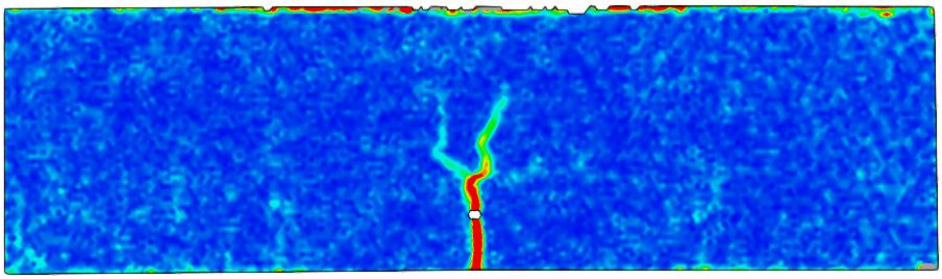

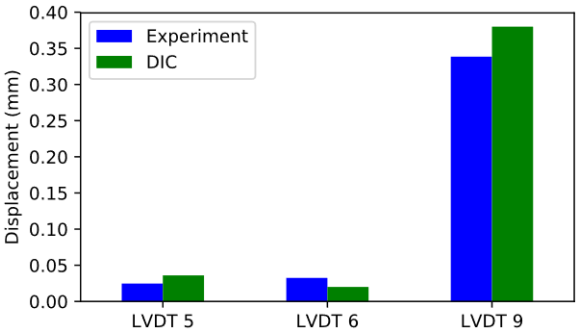

Figure 3-84: Load step F – 12.5 kN with comparison of DIC vs Experiments

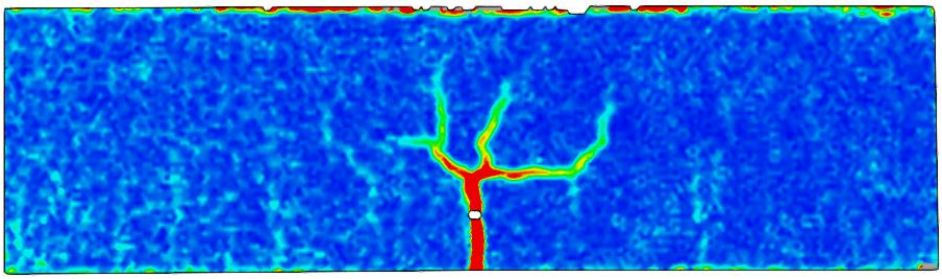

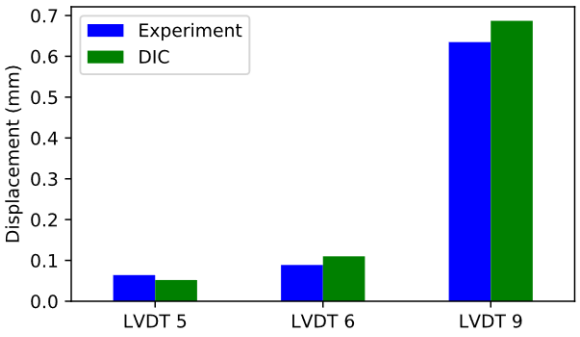

Figure 3-85: Load step G – 15 kN with comparison of DIC vs Experiments

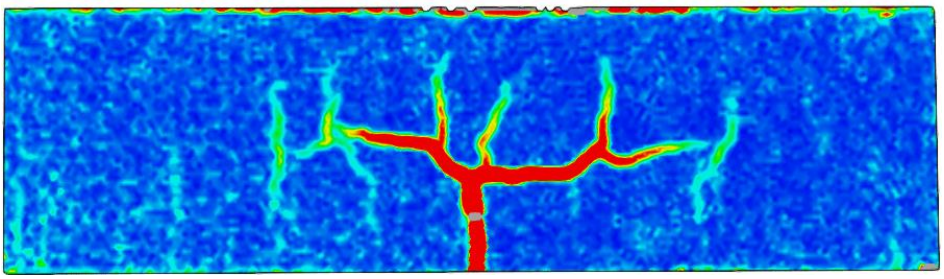

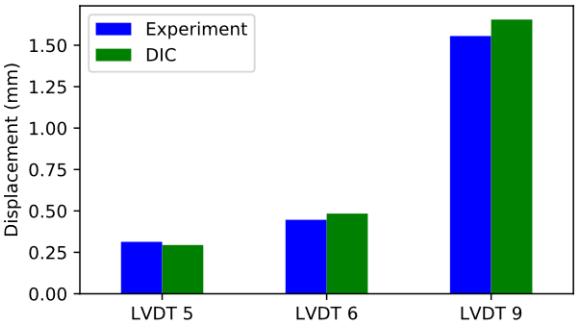

Figure 3-86: Load step H – 20 kN with comparison of DIC vs Experiments

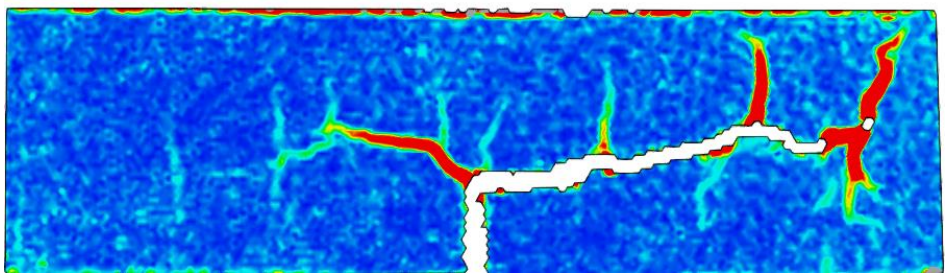

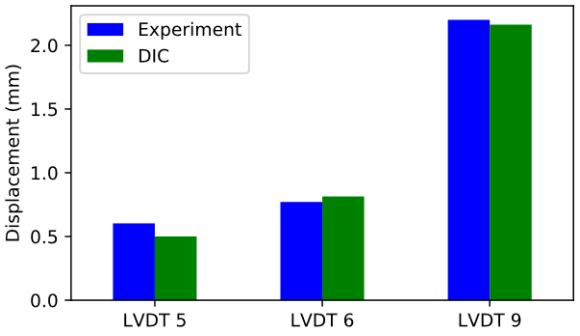

Figure 3-87: Load step I – Failure load with comparison of DIC vs Experiments at failure load

3.5.5 Sample 5 – Curing

For the sample with a different curing method, the vertical displacement, maximum interface opening and maximum joint opening are plotted against the load as is shown in Figure 3-88. Also the reference sample is shown in this figure.

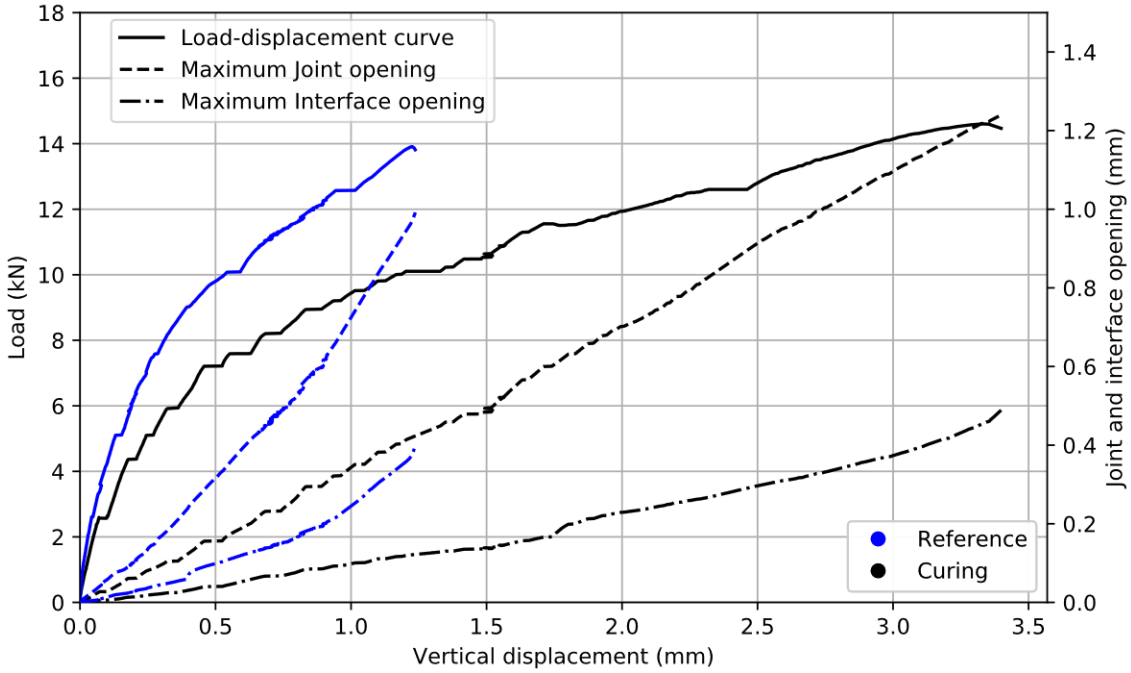

Figure 3-88: Sample 5 – Load-displacement graph with maximum interface and joint opening

The load capacity of this sample is similar to the result of the reference beam as both samples have a smooth interface. However, due to the curing of the sample in a humidity-controlled room, the stiffness of the samples reduced significantly. As a result of this, the deformation capacity of the beam increased with a factor 3 compared to the reference sample. Also, for this sample, no yielding of the coupling reinforcement is reached

$$\sigma_s = \frac{M_{failure}}{A_s * \left(d - \frac{1}{3}x\right)} = 253MPa < f_y \tag{3.32}$$

The results of this curing beam at failure are tabulated in Table 3-10.

Property	Value	Unit
Load capacity	14.6	kN
Maximum Displacement	3.4	mm
Maximum Interface opening	0.48	mm
Maximum Joint opening	1.24	mm
Maximum Steel stress	253	MPa

Table 3-10: Sample 5 – Test results at failure

The damage of the sample on both sides of the beam is shown in Figure 3-89. The damage pattern is similar to the result of the reference beam. The interface delaminated until the end of the coupling reinforcement. This delamination was already initiated before testing due to the interfacial shrinkage as can be seen by the cracks indicated with the red lines which occurred prior to testing (these cracks are not taken into account in the DIC analysis). No cracks appeared in the SHCC during testing. This indicates that there was no interaction between the SHCC and concrete top layer as a result of this delamination.

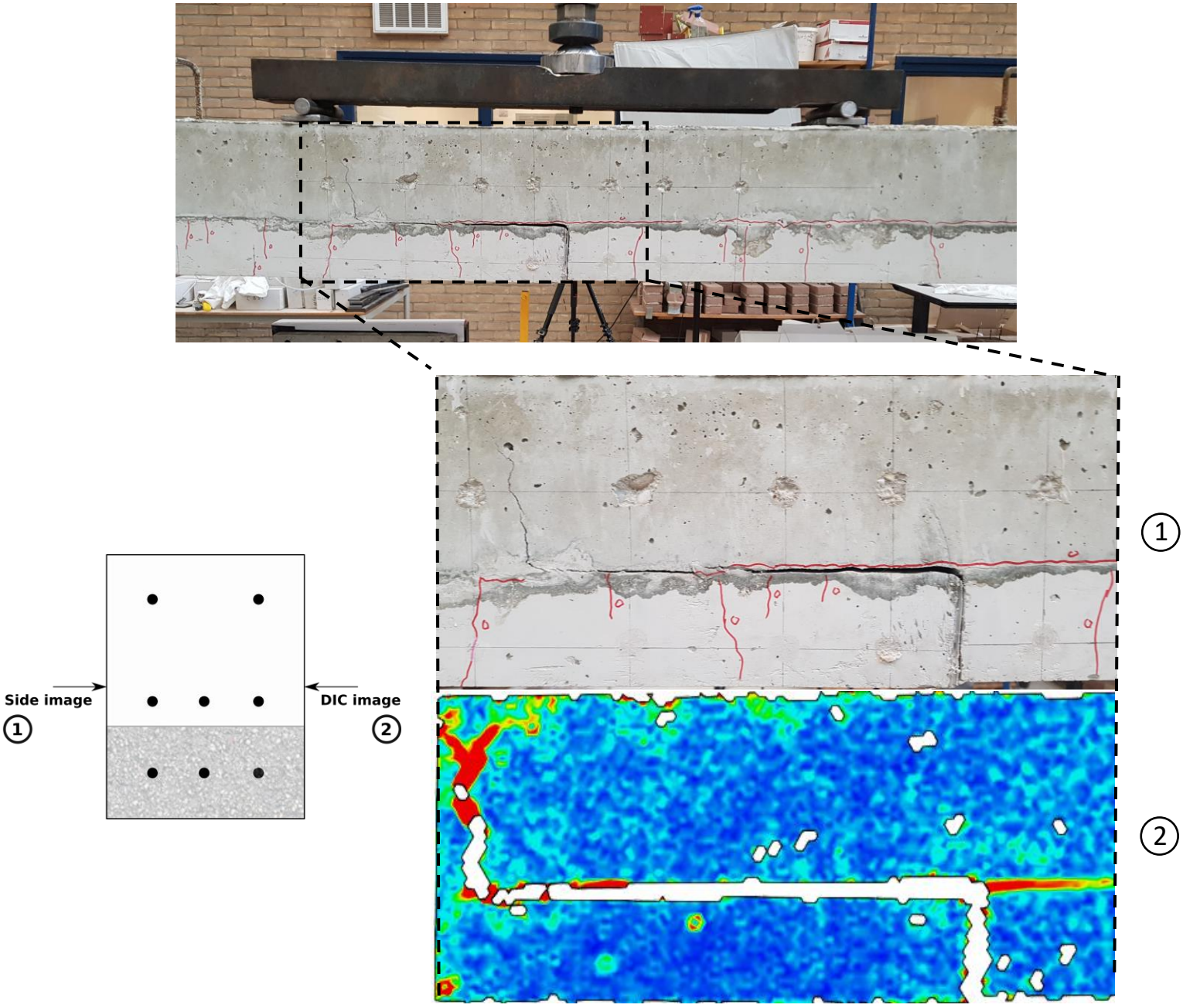

Figure 3-89: Damage of Sample 5 on the LVDT (1) and DIC (2) sides

A step-by-step visualization of the crack propagation in the constant bending moment region is shown in Figure 3-91 – Figure 3-99. These steps correspond to the points shown in the load-displacement curve in Figure 3-90.

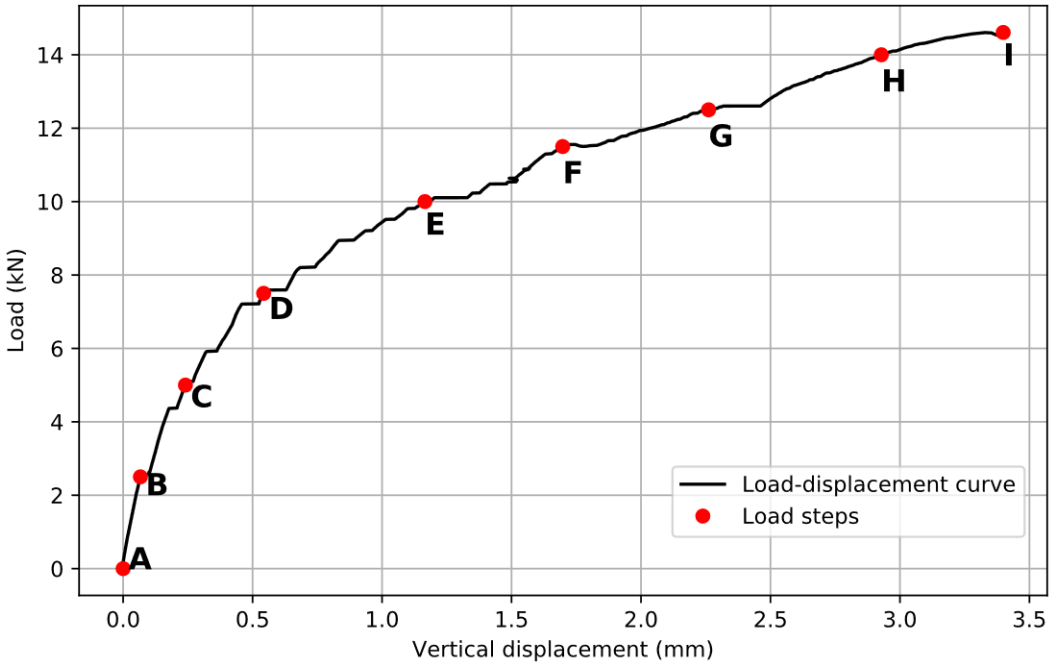

Figure 3-90: Sample 5 – Load-displacement graph with load steps for DIC images

The initial load step is shown in Figure 3-91. This step is the unloaded load step and therefore no strains are visible. The surface component of this sample is added in GOM Correlate as can be seen in the figure indicated by the blue surface component. For the remaining load steps, only this surface component is shown to visualize the crack propagation. Besides the DIC results, also a chart graph is shown comparing the experimental results of the LVDTs with results obtained from DIC in Figure 3-91 – Figure 3-99 (note that no DIC images have been made of the bottom of the beam, therefore section LVDT 9 has been placed at the lowest possible points).

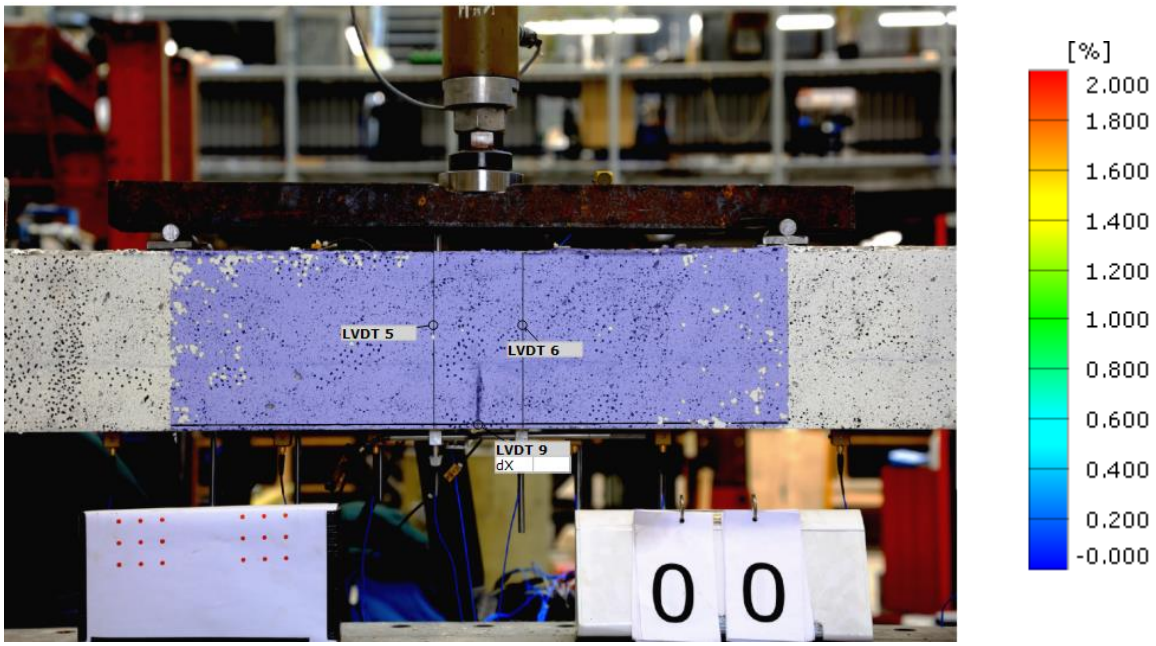

Figure 3-91: Load step A – 0 kN with surface component of constant bending moment region and LVDT sections

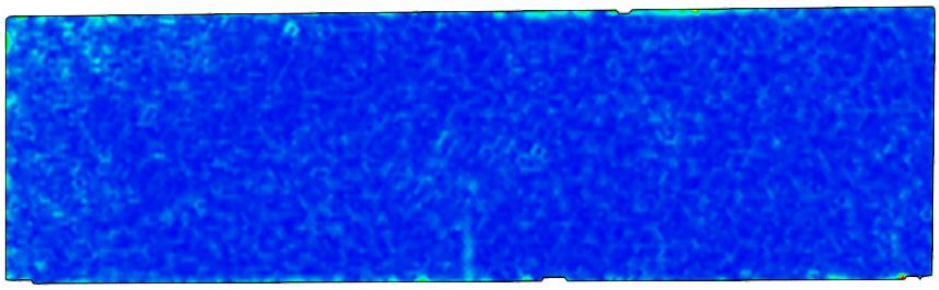

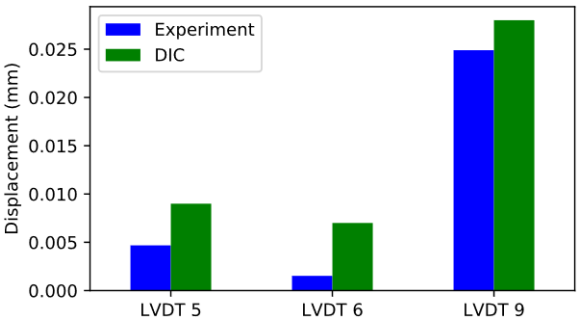

Figure 3-92: Load step B – 2.5 kN with comparison of DIC vs Experiments

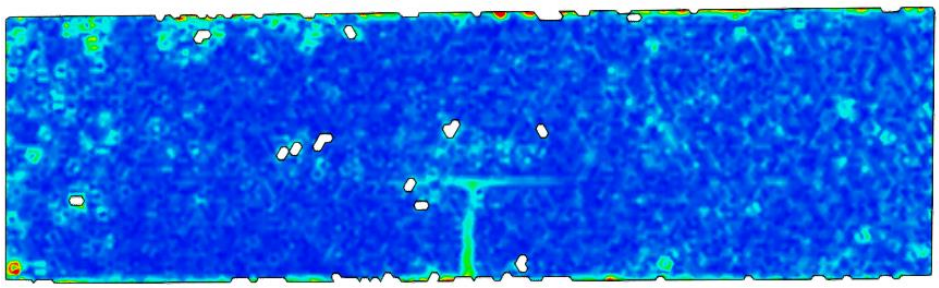

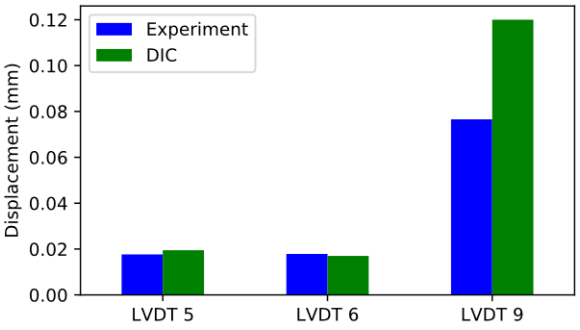

Figure 3-93: Load step C – 5kN with comparison of DIC vs Experiments

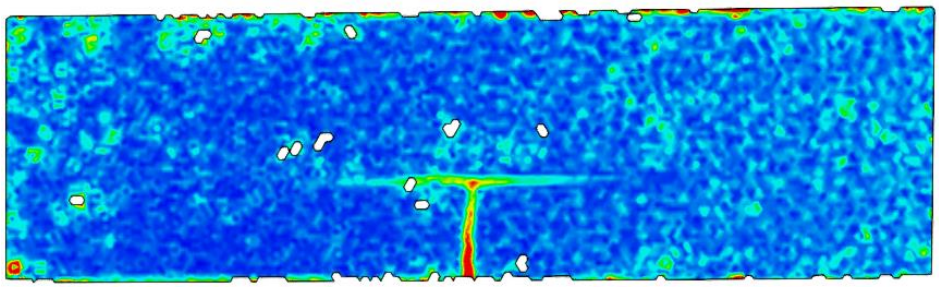

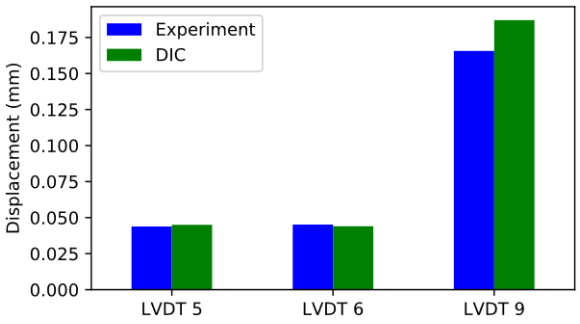

Figure 3-94: Load step D – 7.5 kN with comparison of DIC vs Experiments

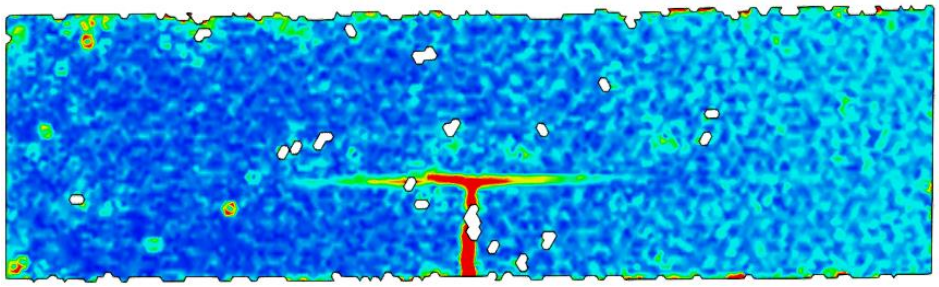

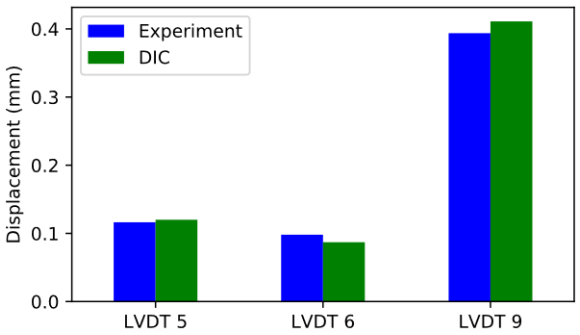

Figure 3-95: Load step E – 10 kN with comparison of DIC vs Experiments

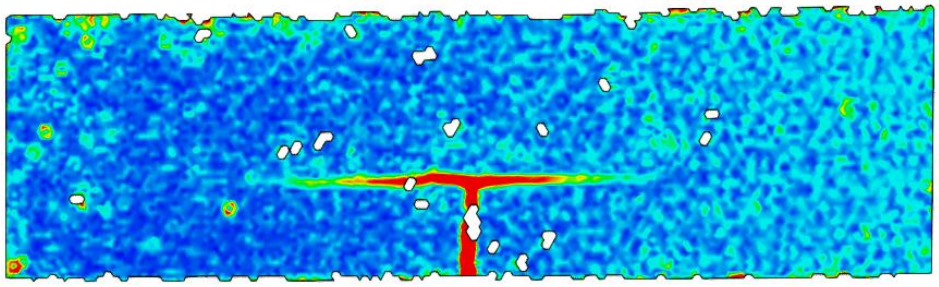

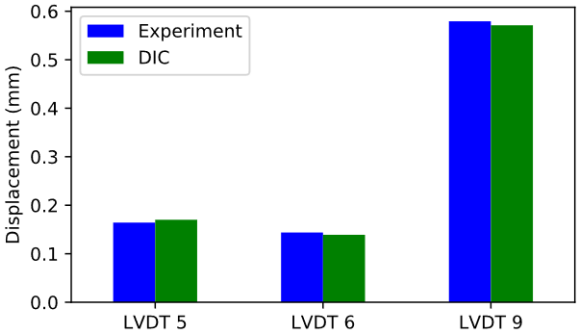

Figure 3-96: Load step F – 11.5 kN with comparison of DIC vs Experiments

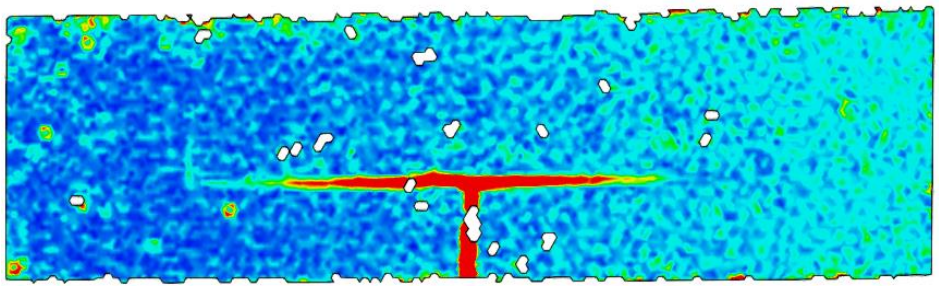

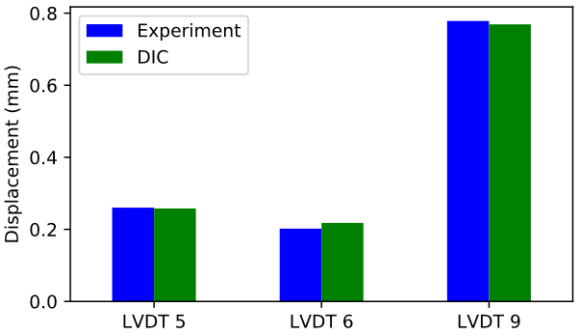

Figure 3-97: Load step G – 12.5 kN with comparison of DIC vs Experiments

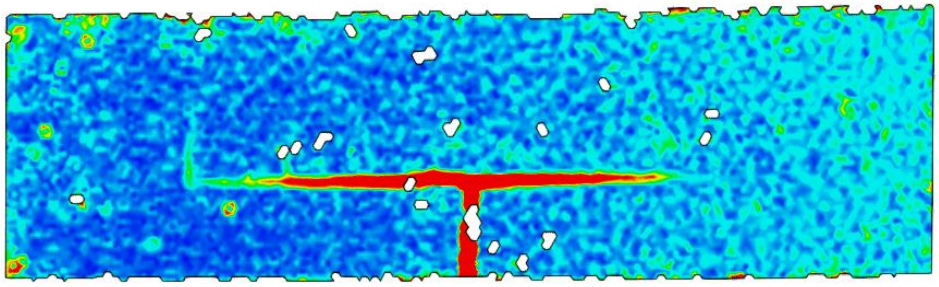

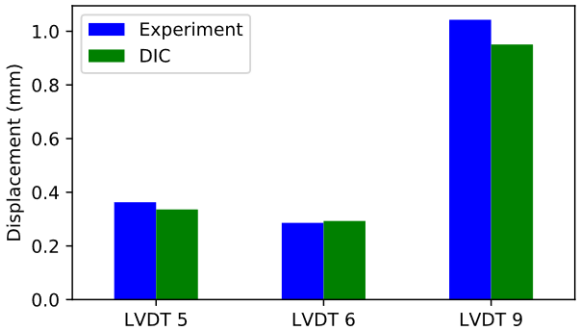

Figure 3-98: Load step H – 14 kN with comparison of DIC vs Experiments

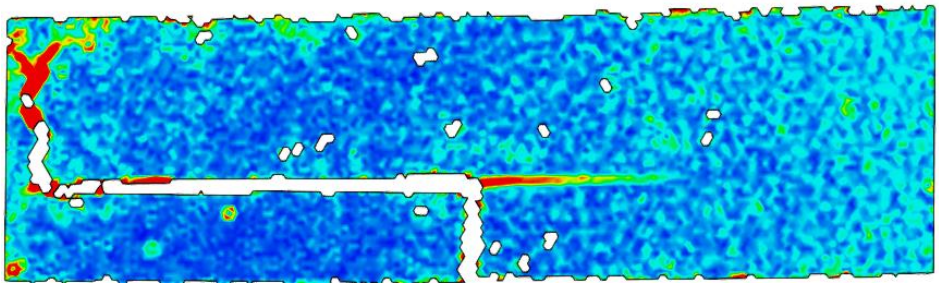

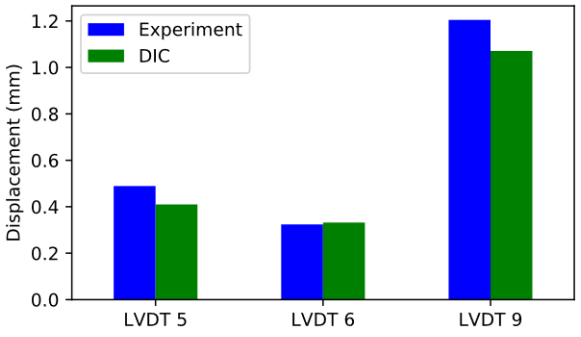

Figure 3-99: Load step I – Failure load with comparison of DIC vs Experiments at failure

3.5.6 **Sample 6 – No cover**

The results of the sample with the coupling reinforcement directly placed on top of the SHCC layer are shown in Figure 3-100. In this figure, the load is plotted against the vertical displacement and maximum joint and interface opening. The reference sample which has a coupling reinforcement cover of 10 mm is also shown in Figure 3-100.

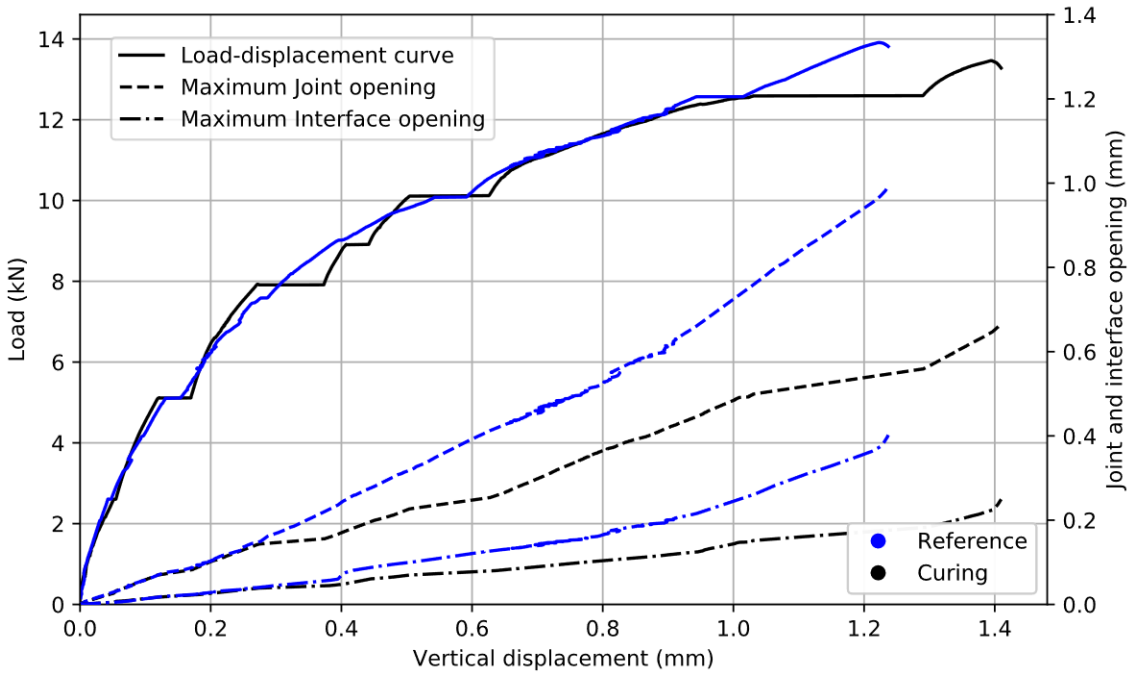

Figure 3-100: Sample 6 – Load-displacement graph with maximum interface and joint opening

The influence of placing the coupling reinforcement directly on top of the SHCC layer seems to not influence the global behavior of this hybrid SHCC-Concrete system. The load capacity and deformation capacity are similar to the reference case. The stress in the coupling reinforcement is reduced due to a higher effective height

$$\sigma_s = \frac{M_{failure}}{A_s * \left(d - \frac{1}{3}x\right)} = 201MPa < f_y \tag{3.33}$$

In Table 3-11, the results at failure of this sample are shown. Comparing these values to the reference sample, the interface opening and joint opening are significantly lower.

Property	Value	Unit
Load capacity	13.5	kN
Maximum Displacement	1.41	mm
Maximum Interface opening	0.28	mm
Maximum Joint opening	0.66	mm
Maximum Steel stress	201	MPa

Table 3-11: Sample 6 - Test results at failure

In Figure 3-101, the loading set-up is shown with a zoomed section of the location which failed. Furthermore, also the DIC result is shown at failure which has been mirrored to correspond to the failure location of the side image. The damage of this sample is similar to the result of the other two samples with a smooth interface (Sample 1 and Sample 5). Delamination of the interface caused the failure of the sample.

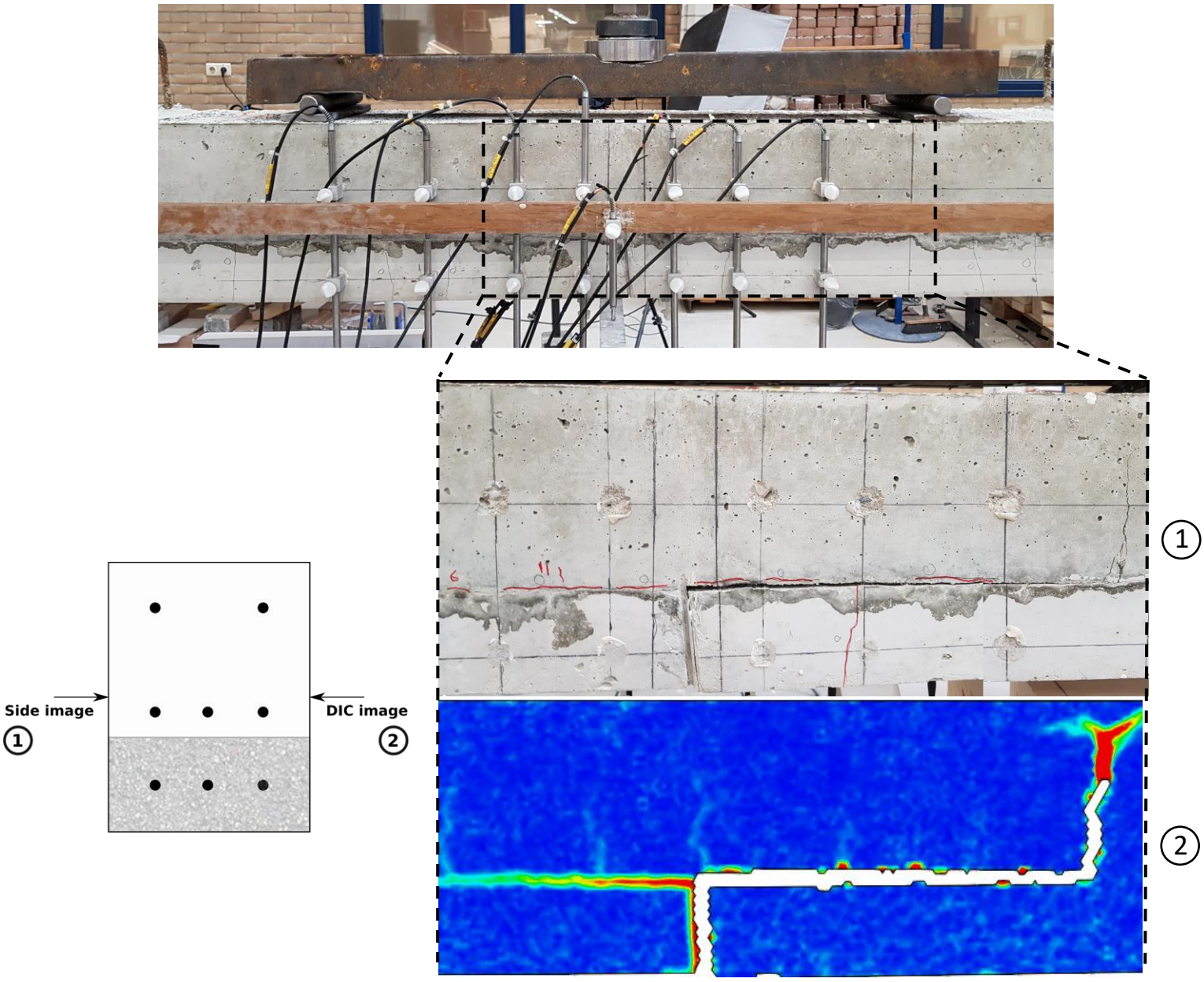

Figure 3-101: Damage of Sample 6 on the LVDT (1) and DIC (2) sides

The crack propagation of the sample is shown in Figure 3-103 – Figure 3-111 for the corresponding points depicted in the load-displacement curve in Figure 3-102.

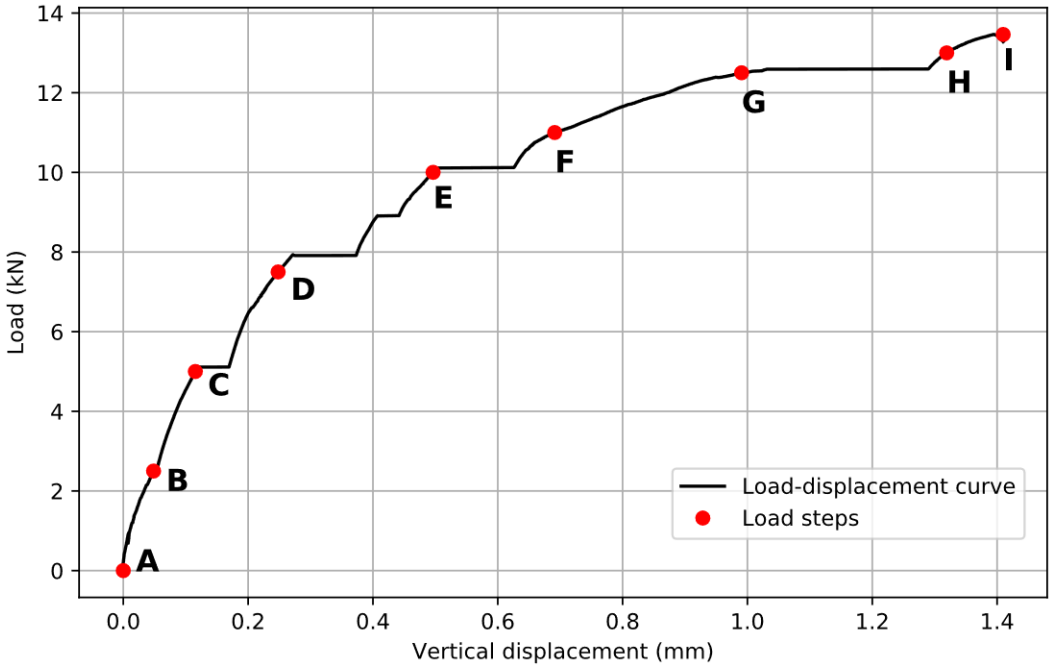

Figure 3-102: Sample 6 – Load-displacement graph with load steps for DIC images

The area of interest is the constant bending moment region which has been marked using a surface component in GOM Correlate as can be seen in Figure 3-103. Subsequently, this surface component is used to follow the damage of the sample. Furthermore, also a comparative study is done by comparing the LVDTs results during testing with the results obtained from the DIC analysis. In order to obtain values of the interface and joint opening, sections have been added (see Figure 3-103) from which the openings can be determined. In Figure 3-103 – Figure 3-111, the comparative study is shown in a bar chart beside the DIC images.

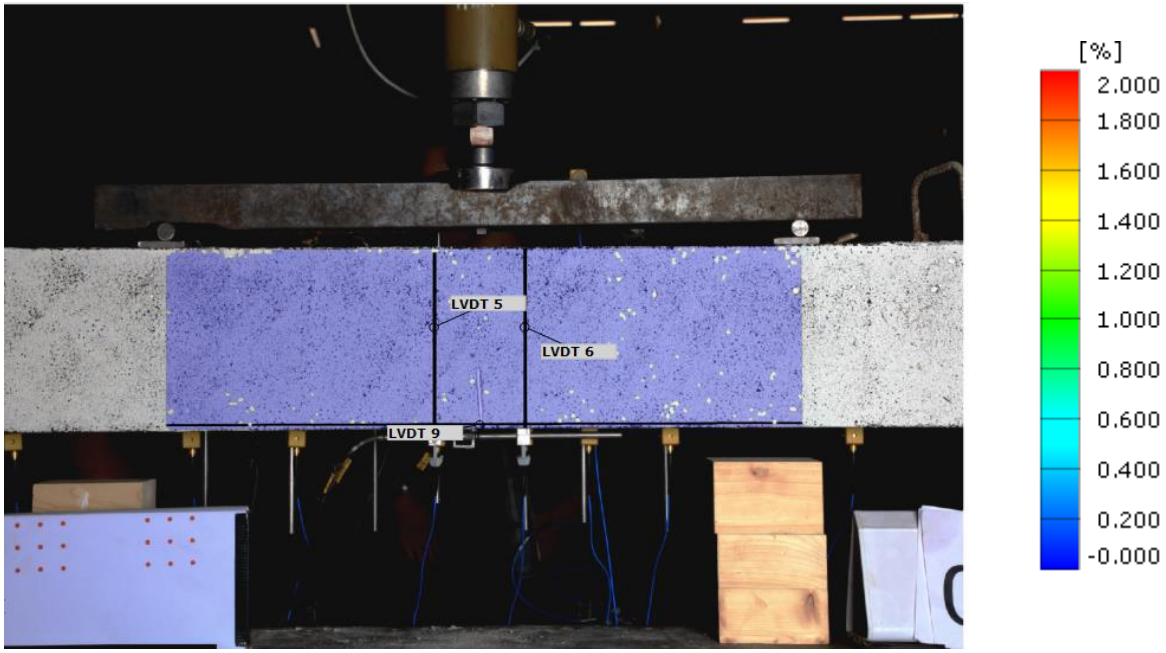

Figure 3-103: Load step A – 0 kN with surface component of constant bending moment region and LVDT sections

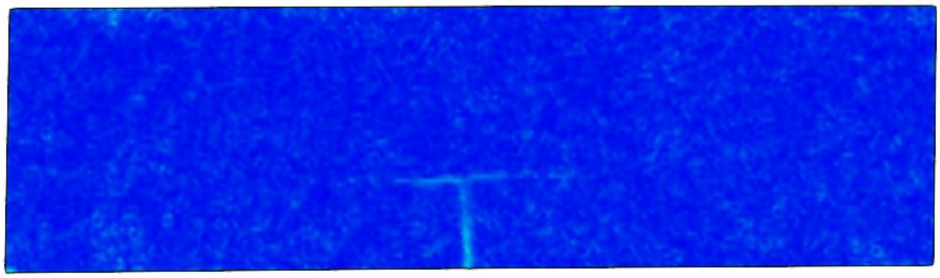

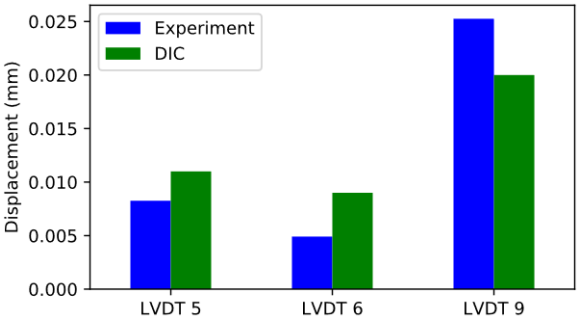

Figure 3-104: Load step B – 2.5 kN with comparison of DIC vs Experiments

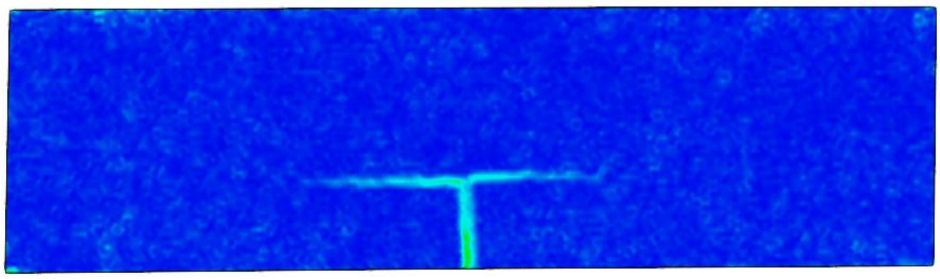

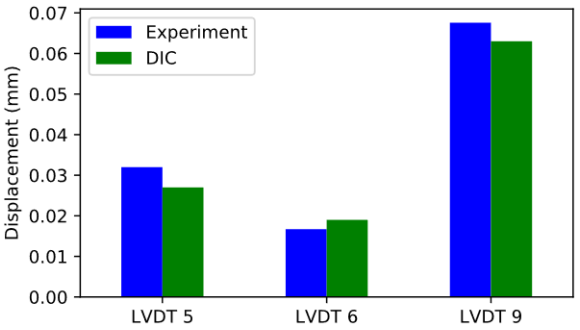

Figure 3-105: Load step C – 5kN with comparison of DIC vs Experiments

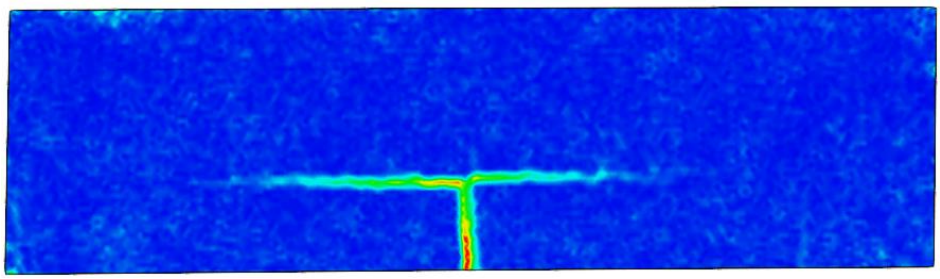

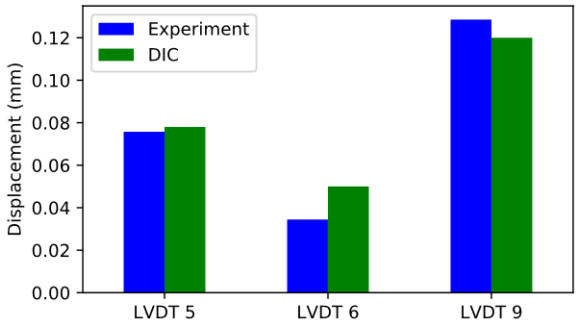

Figure 3-106: Load step D – 7.5 kN with comparison of DIC vs Experiments

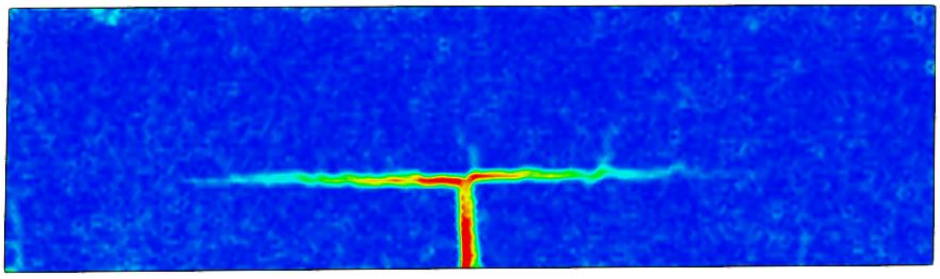

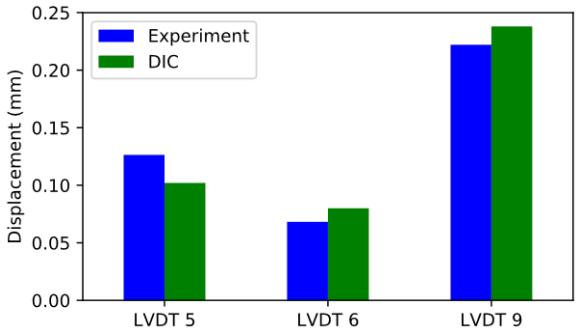

Figure 3-107: Load step E – 10 kN with comparison of DIC vs Experiments

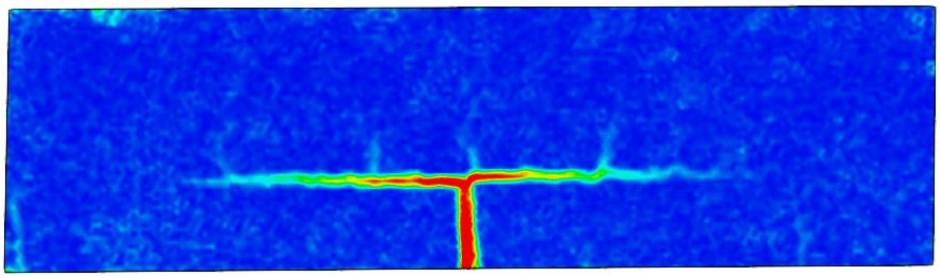

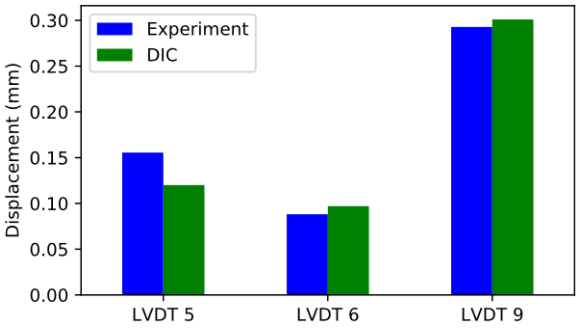

Figure 3-108: Load step F – 11 kN with comparison of DIC vs Experiments

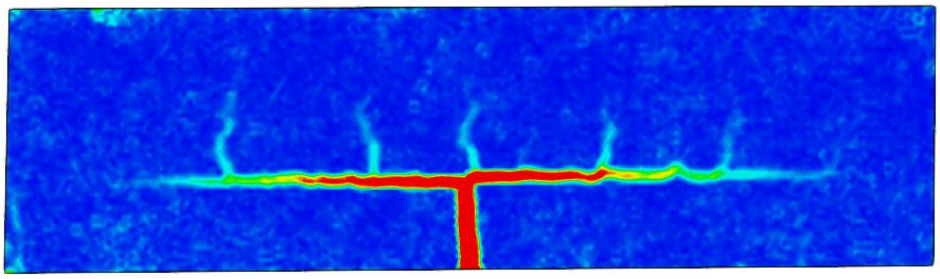

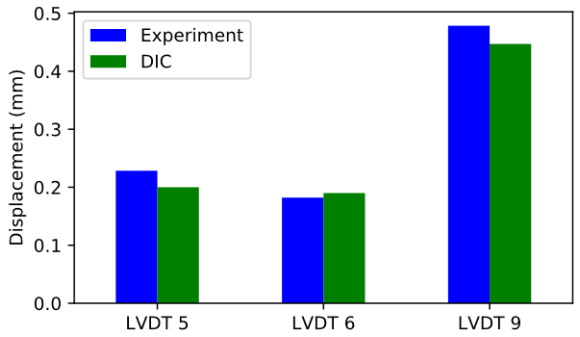

Figure 3-109: Load step G – 12.5 kN with comparison of DIC vs Experiments

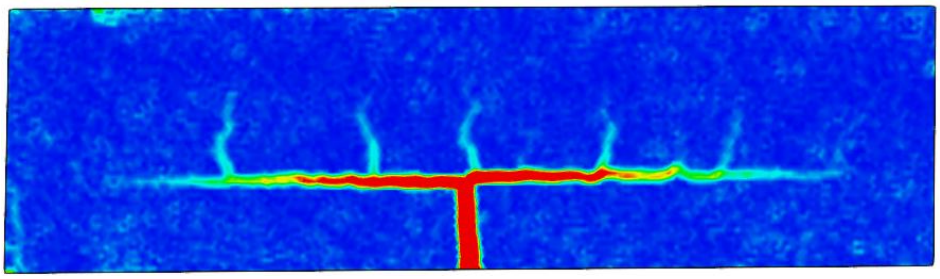

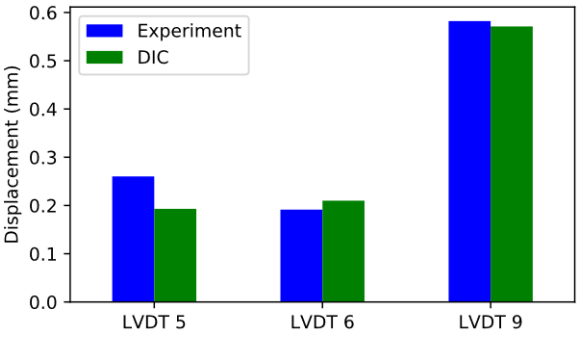

Figure 3-110: Load step H – 13 kN with comparison of DIC vs Experiments

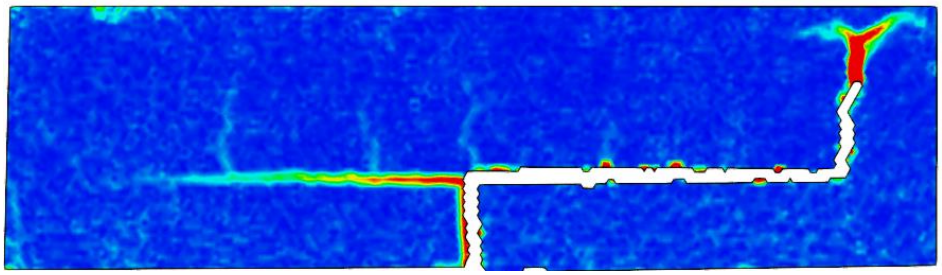

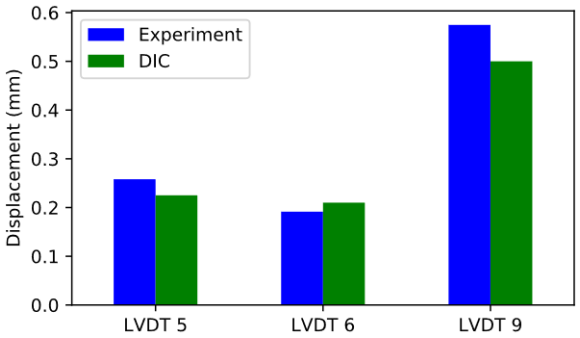

Figure 3-111: Load step I – Failure load with comparison of DIC vs Experiments at failure load

3.5.7 Sample 7 – Protruding reinforcement

The last sample consisted of stirrups nearby the joint. The roughness of the beam is kept smooth similarly to samples 1, 4 and 5. Figure 3-112 shows the vertical displacement at midspan, maximum joint opening and maximum interface opening against the load on the beam during testing. The curing sample is also shown in this figure (note that sample 7 has also been cured outside the mould, therefore sample 5 is used as the reference sample).

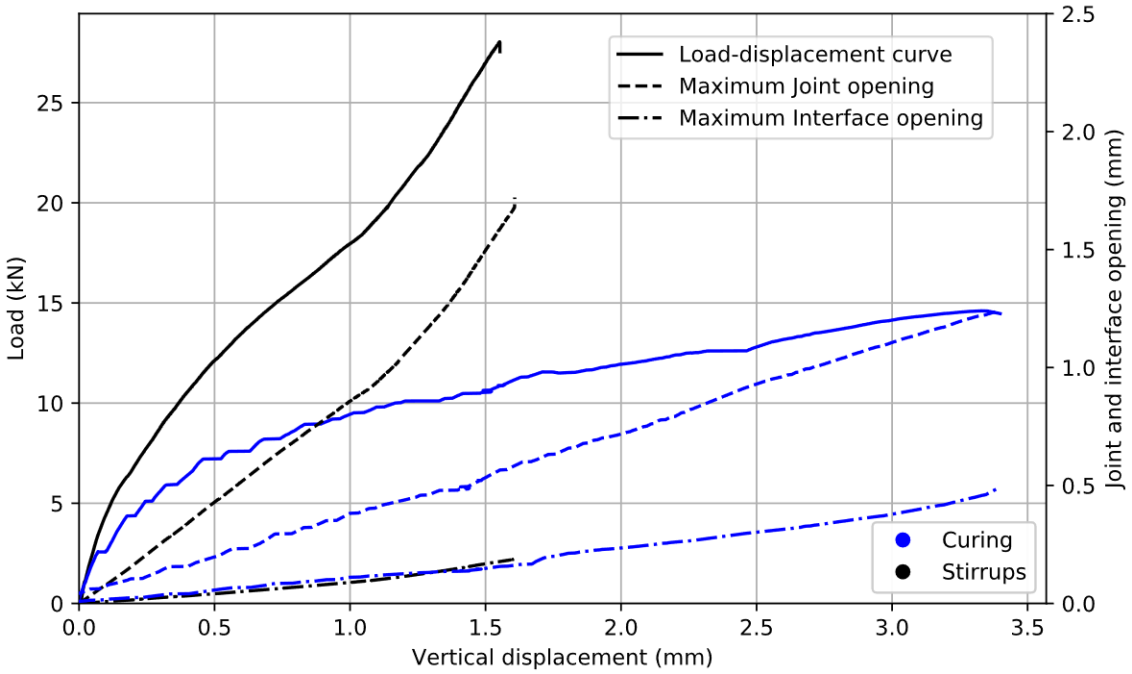

Figure 3-112: Sample 7 – Load-displacement graph with maximum interface and joint opening

The load capacity of the beam increased significantly as a result of the stirrups transferring the perpendicular tensile forces along the height of the beam. This larger capacity did however not result in yielding of the specimen. This is calculated taking into account the effective height of the coupling reinforcement with respect to the neutral axis of the compression zone

$$\sigma_s = \frac{M_{failure}}{A_s * \left(d - \frac{1}{3}x\right)} = 488MPa < f_y \tag{3.34}$$

The maximum load, displacement and stresses in the bar at failure are tabulated in Table 3-12.

Property	Value	Unit
Load capacity	28.17	kN
Maximum Displacement	1.68	mm
Maximum Interface opening	0.19	mm
Maximum Joint opening	1.72	mm
Maximum Steel stress	488	MPa

Table 3-12: Sample 7 - Test results at failure

The damage of the sample at failure is shown in Figure 3-113 of both sides of the beam (side image and DIC image). The opening of the interface up until the end of the coupling reinforcement did also occur for this sample. However, the opening of the interface is not clearly visible in the side image as the stirrups are holding the different layers together. The DIC image shows more clearly the delamination and cracking of the sample.

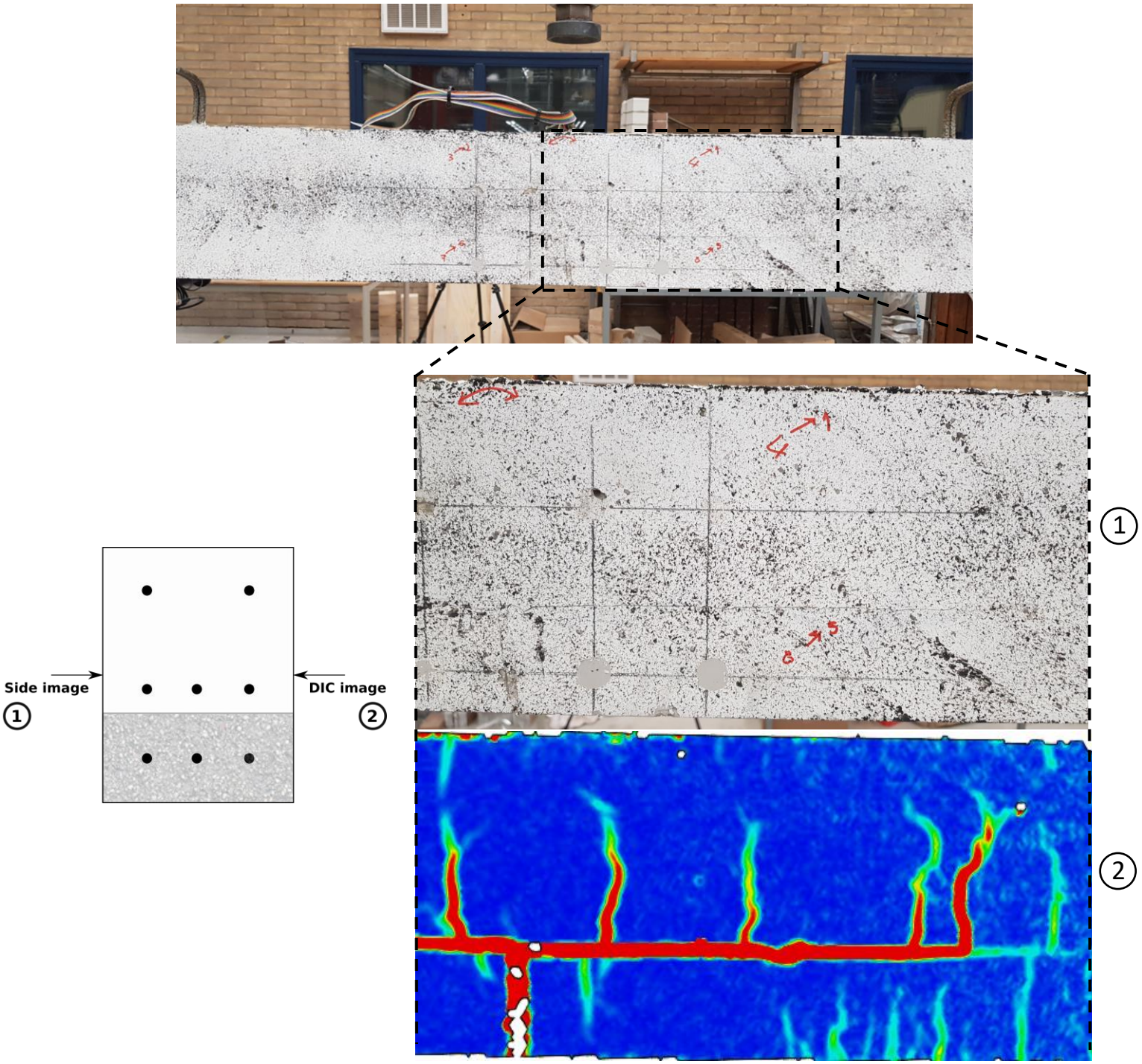

Figure 3-113: Damage of Sample 7 on the LVDT (1) and DIC (2) sides

The crack propagation of this sample is shown for several load steps in Figure 3-115 – Figure 3-123. These load steps are visualized in the load-displacement graph in Figure 3-114.

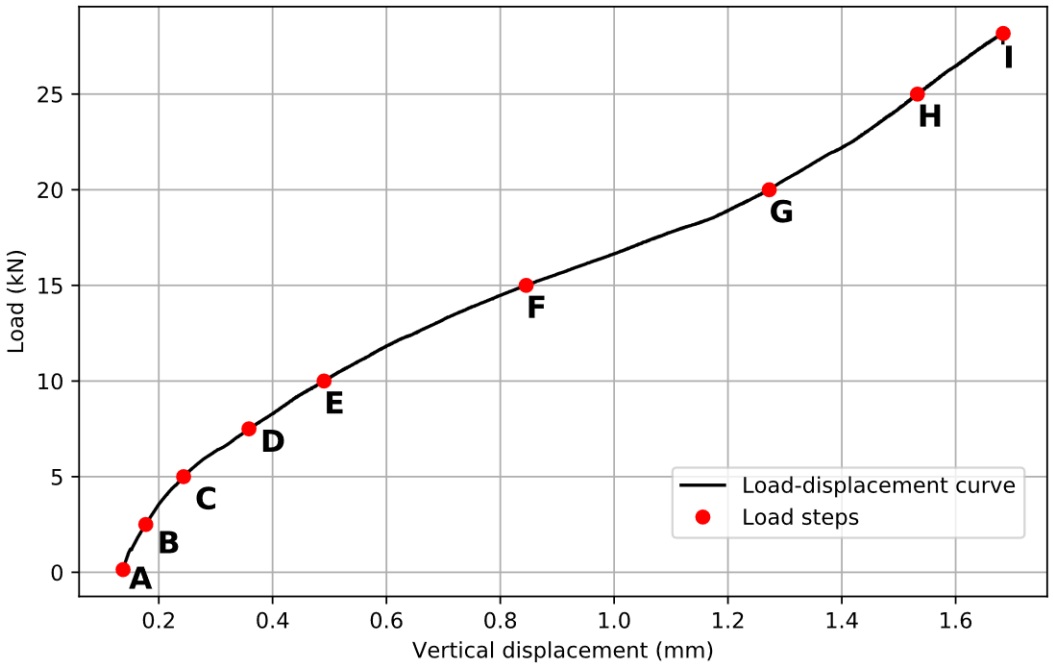

Figure 3-114: Sample 7 – Load-displacement graph with load steps for DIC images

The surface component over which the displacement field is determined can be seen in Figure 3-115. Furthermore, also several points are shown for the determination of the interface and joint opening. These will be compared to the results of the LVDTs 5, 6 and 10. The relative difference between the points corresponds to the interface and joint opening. The results of this analysis is shown in Figure 3-116 – Figure 3-123 together with the images showing the equivalent Von Mises strain distribution.

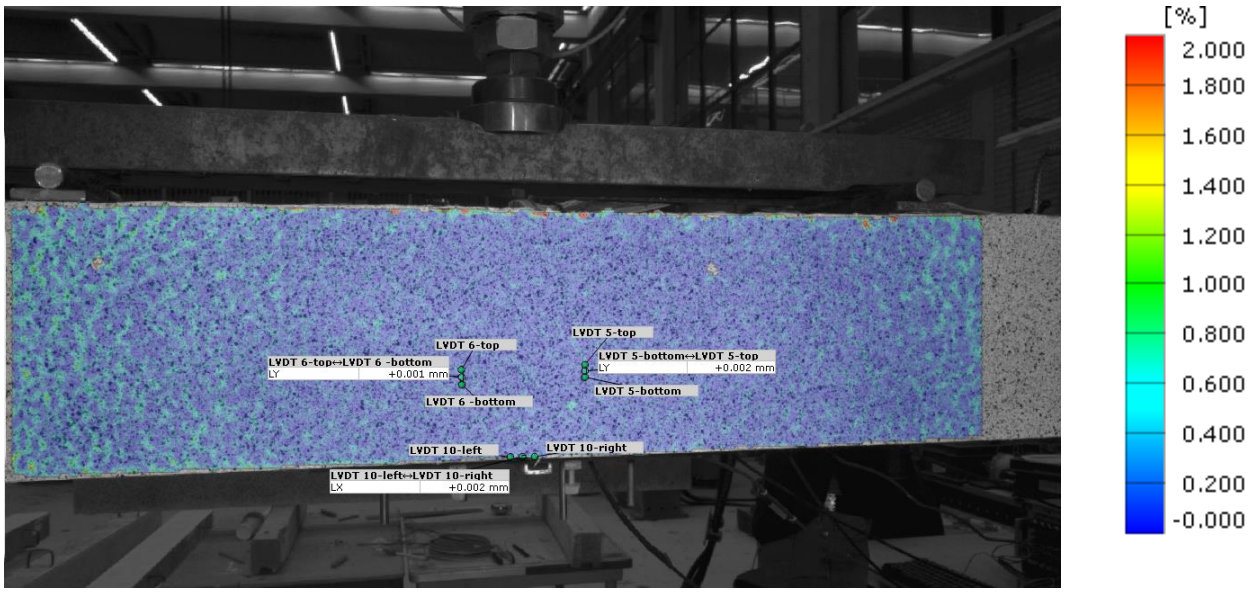

Figure 3-115: Load step A – 0 kN with surface component of constant bending moment region and LVDT sections

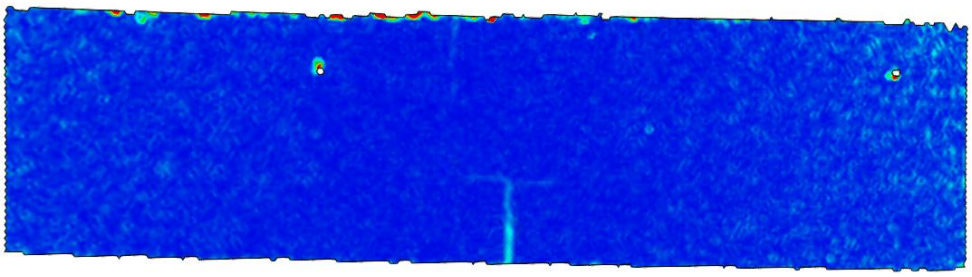

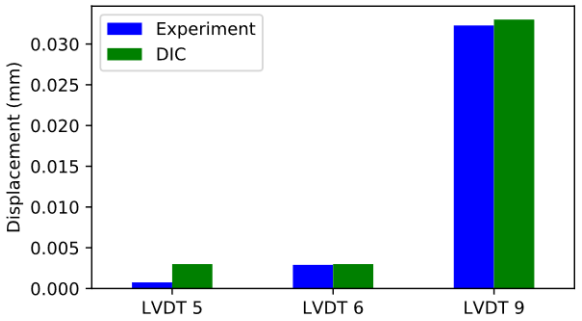

Figure 3-116: Load step B – 2.5 kN with comparison of DIC vs Experiments

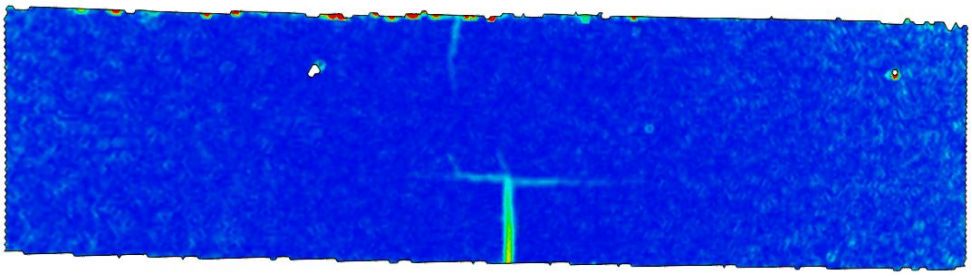

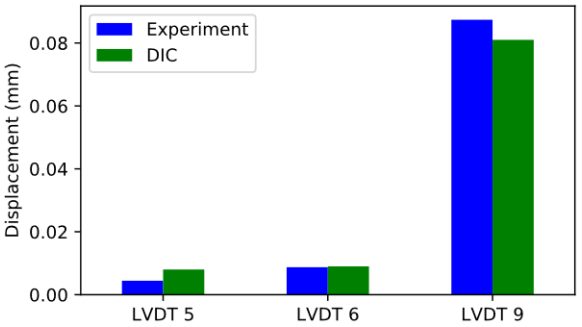

Figure 3-117: Load step C – 5 kN with comparison of DIC vs Experiments

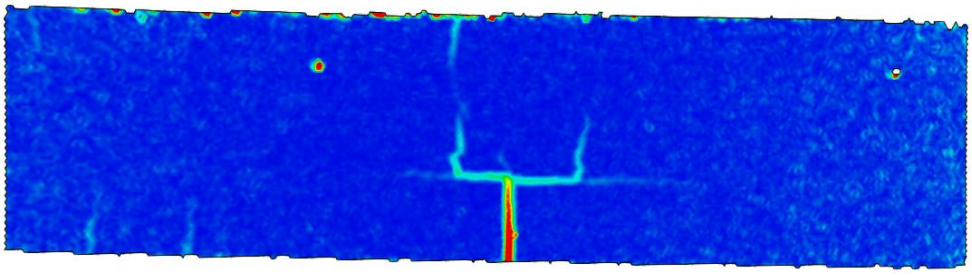

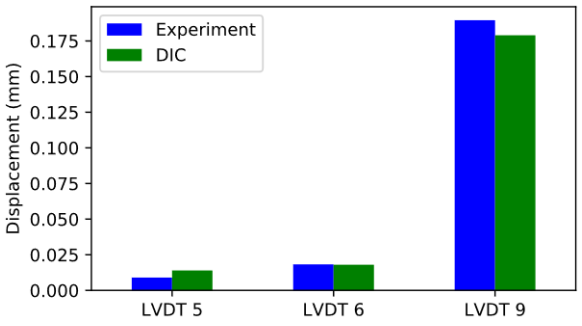

Figure 3-118: Load step D – 7.5 kN with comparison of DIC vs Experiments

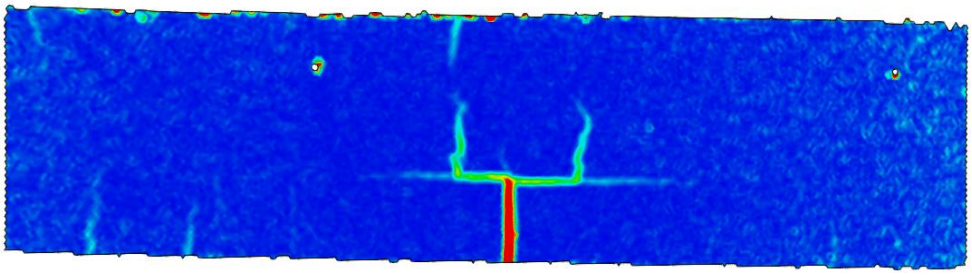

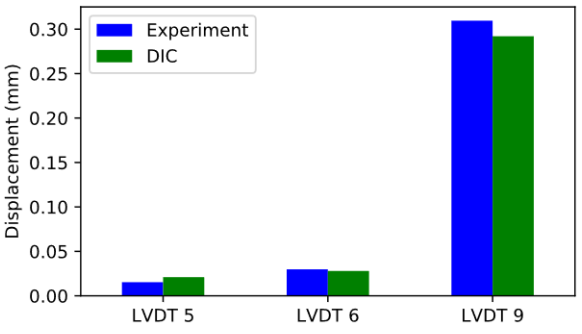

Figure 3-119: Load step E – 10 kN with comparison of DIC vs Experiments

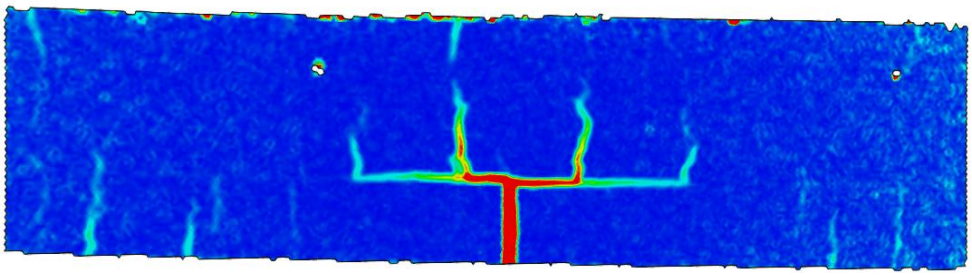

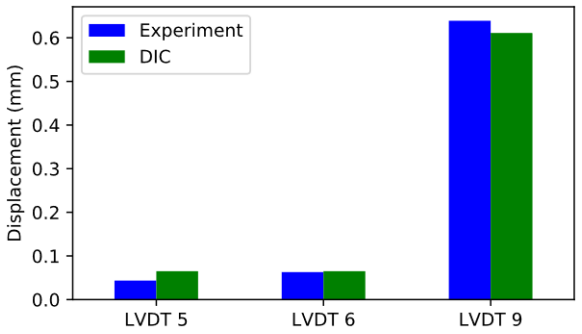

Figure 3-120: Load step F – 15 kN with comparison of DIC vs Experiments

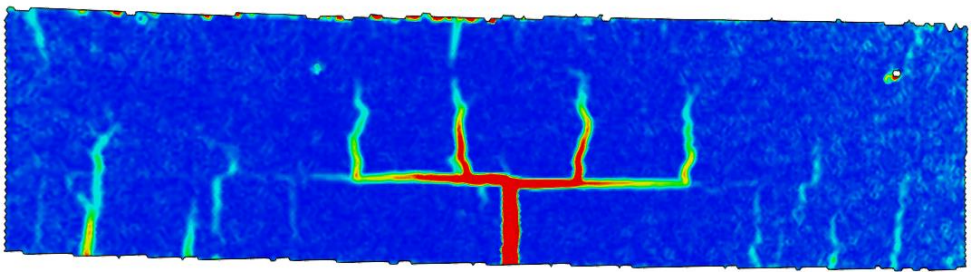

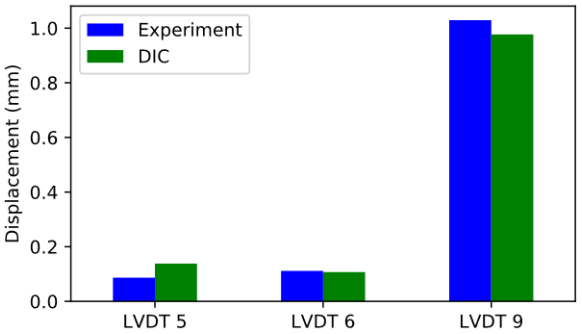

Figure 3-121: Load step G – 20 kN with comparison of DIC vs Experiments

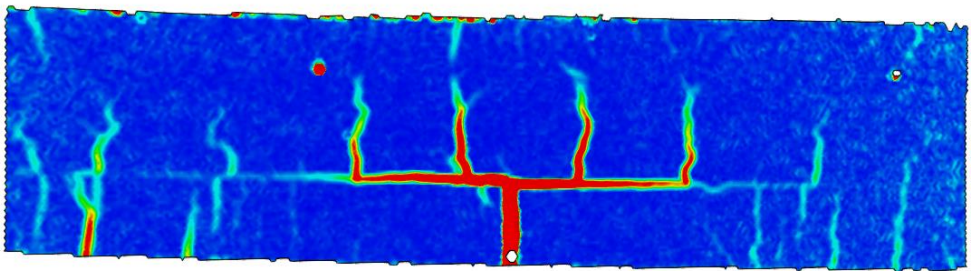

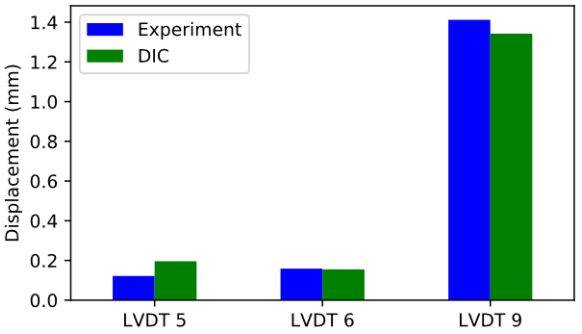

Figure 3-122: Load step H – 25 kN with comparison of DIC vs Experiments

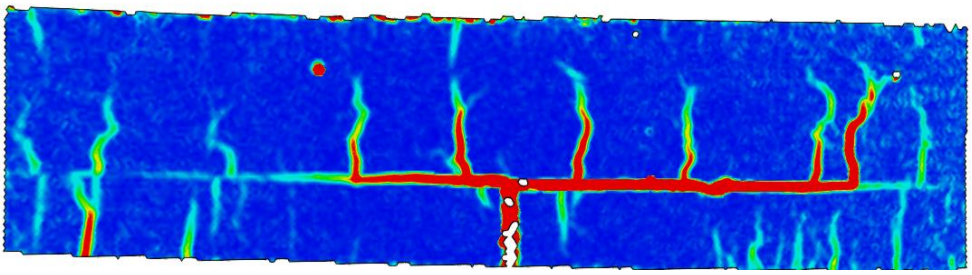

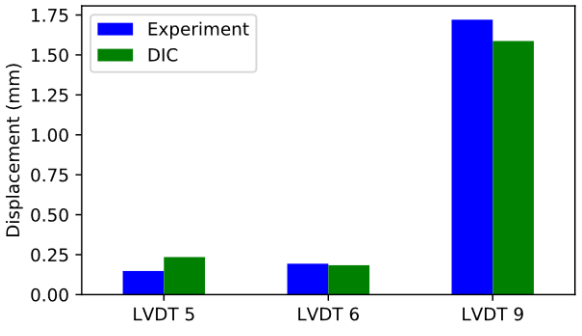

Figure 3-123: Load step I – Failure load with comparison of DIC vs Experiments at failure load

3.6 Discussion

3.6.1 Comparison of results

This research aimed to investigate the interfacial behavior of hybrid SHCC-Concrete beams by changing the interface roughness, reinforcement configuration and curing method. The first sample with a different interface roughness was the sample with a profiled interface. In Figure 3-124 and Figure 3-125 the experimental results of the sample with a profiled interface have been plotted against the results of the reference beam. The influence of the profiled interface is significant as the capacity of the beam increased from 13.9 kN to 25 kN.

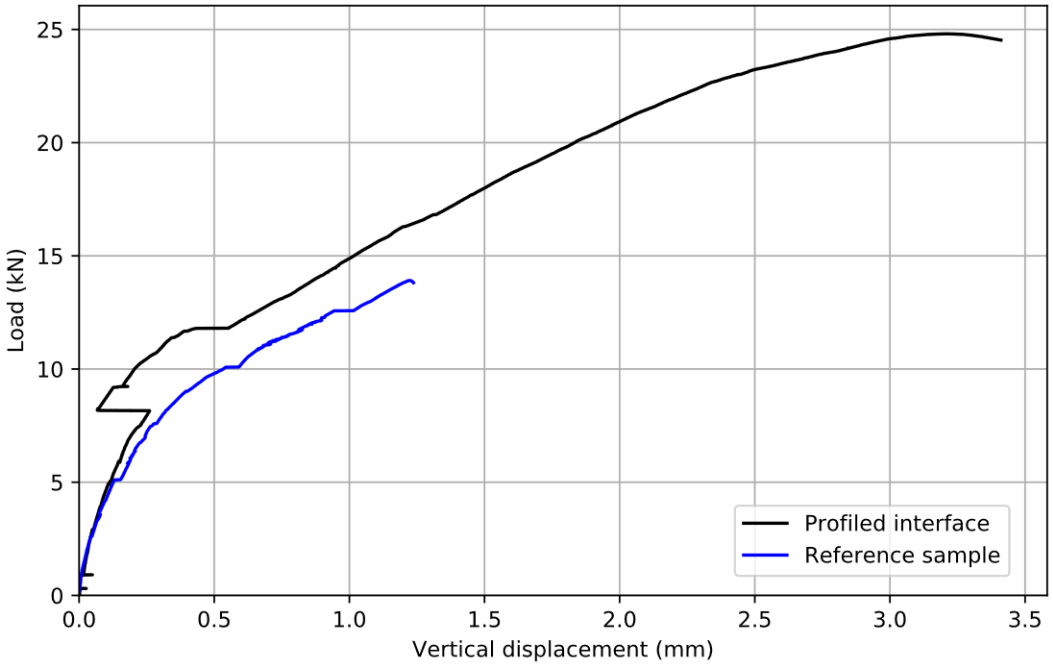

Figure 3-124: Comparison between the load-displacement graph of the reference and profiled sample

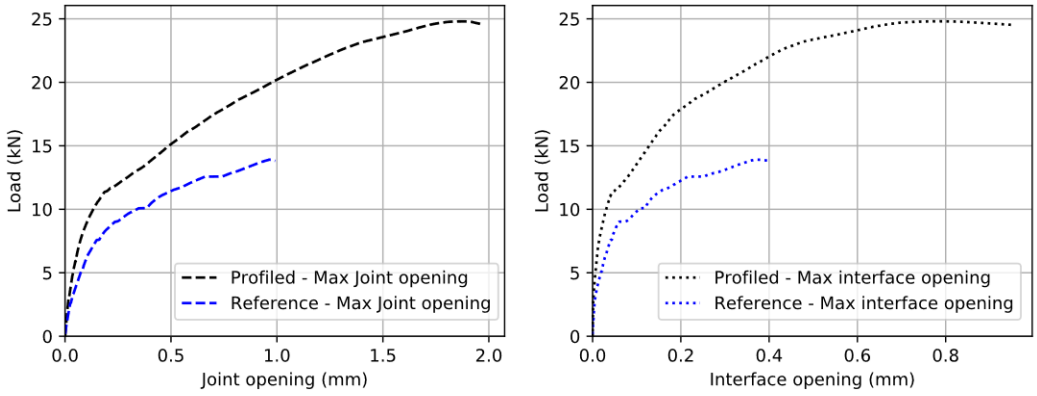

Figure 3-125: Comparison between the maximum joint and interface opening of the reference and profiled sample

The opening of the interface and joint is better controlled due to the increased bond between the SHCC and concrete layer. This increased bond can be visualized by the strains in x-direction at a load step before the failure of the beams (see Figure 3-126 and Figure 3-127). In these figures, several cracks are visible in the SHCC layer of the sample with a profiled interface which indicates a good bond at the interface. The

cracks in the reference sample are only visible in the concrete top layer as a result of the delamination of the interface. Due to this delamination, the SHCC layer is barely contributing to the resistance of the beam.

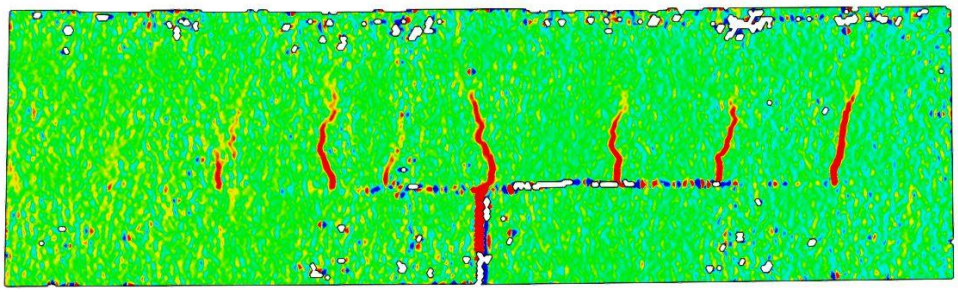

Figure 3-126: Reference sample – Strains in x-direction at a load step before failure

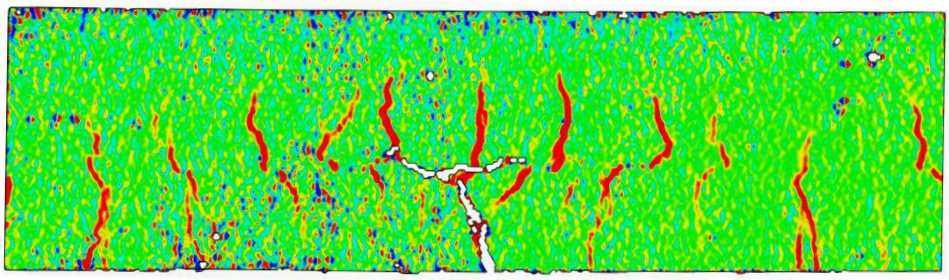

Figure 3-127: Profiled interface – Strains in x-direction at a load step before failure

The delamination of the interface can also be shown using the DIC results by visualizing the strains in y-direction (see Figure 3-128 and Figure 3-129). The delamination of the smooth interface at a load of 10 kN is already significant. Contrary to this, the profiled interface has barely delaminated at a load of 10 kN caused by this increased bond resulting from the mechanical interlocking of this tooth-shaped profile.

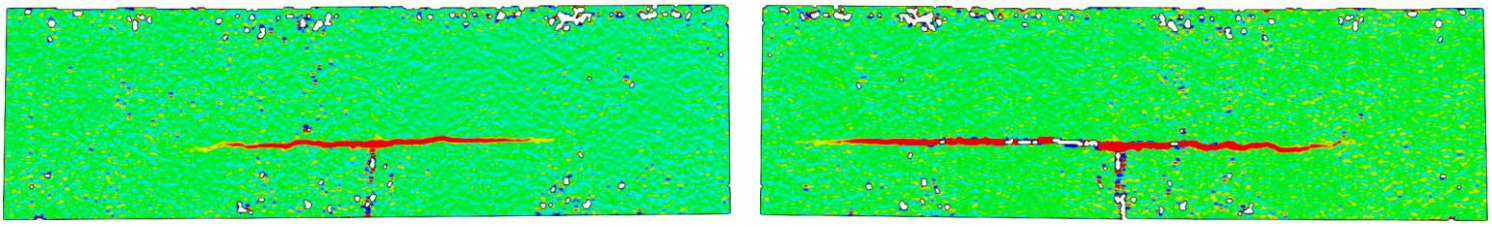

(a) (b)

Figure 3-128: Reference sample – Strains in y-direction for (a) load step at 10 kN; (b) load step before failure

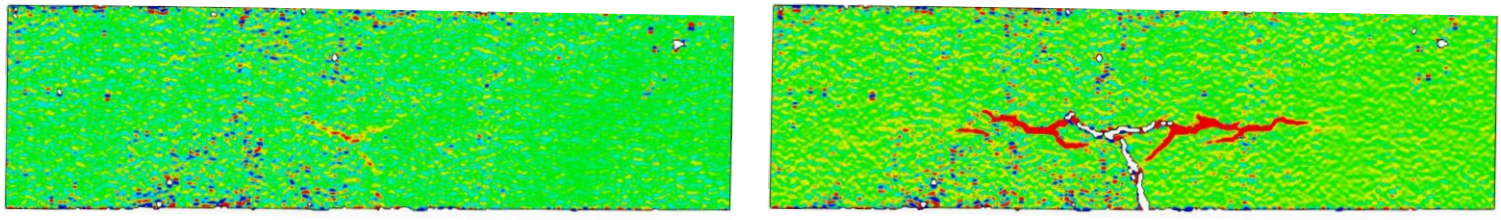

(a) (b)

Figure 3-129: Profiled interface – Strains in y-direction for (a) load step at 10 kN; (b) load step before failure

The sample with the profiled interface has also been cut into two pieces halfway along the width. This is done to see the crack propagation inside the beam (see Figure 3-130). From the surface cracks of the DIC results, the cracks went both through the crack and interface. However, from Figure 3-130, it can be seen that the crack only goes through the concrete at the level of the coupling reinforcement (see paragraph 3.6.2). This shows that the failure mechanism of the sample is a 3D problem. The reinforcement didn't yield as the load capacity is lower than the yielding capacity based on the analytical calculation in paragraph 3.1.2.

Figure 3-130: Crack propagation of the sample with a profiled interface

The holed interface is based on the same principle as the profiled interface. By already inserting holes in the SHCC layer before the concrete is cast, the mechanical interlocking between the SHCC and concrete will result in a higher capacity. The idea of this is to increase the interface tensile and shear capacity to achieve a better interface bond.

In Figure 3-131 and Figure 3-132, the results of the samples with a profiled and holed interface are shown. From this figure, it can be observed that the load capacity of the profiled interface is larger than the holed interface (24.8 kN vs 21.5 kN). However, the deformation capacity of the holed interface is larger. This difference in deformation capacity is most likely due to a higher mode I (tension) fracture energy of the interface with holes [10]. Furthermore, also the opening of the interface is larger for the profiled interface sample. This large difference is caused by the placement of the LVDT, as for the sample with a profiled interface, the LVDT was placed closer to the joint (20mm instead of 50mm from the middle joint).

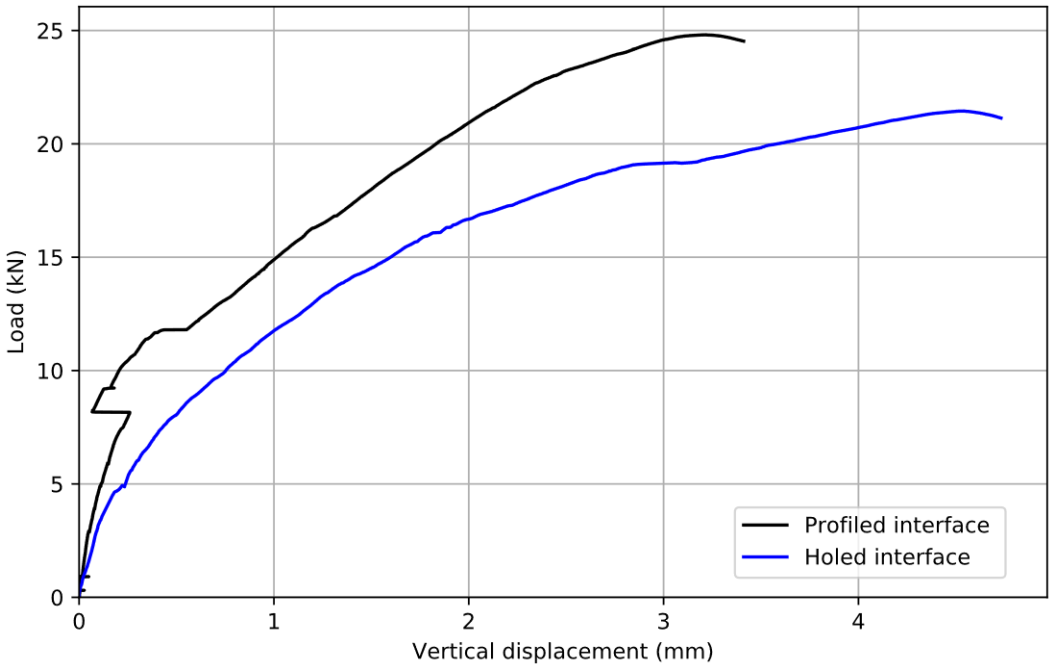

Figure 3-131: Comparison between the load-displacement graph of the samples with a profiled and holed interface

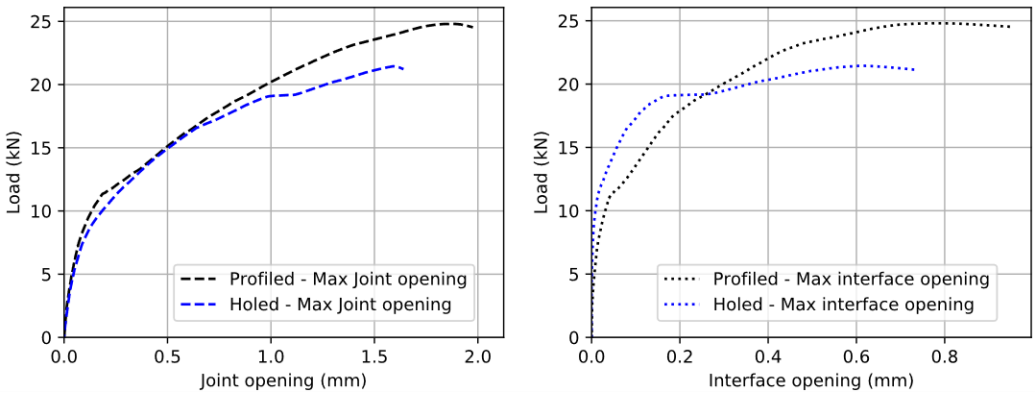

Figure 3-132: Comparison between the maximum joint and interface opening of the samples with a profiled and holed interface

In Figure 3-133, the strains in x-direction are shown at a load step before the failure of the beam for the sample with holes. Similarly, to the profiled interface shown in Figure 3-127, several cracks are visible in the SHCC beam as a result of the increased SHCC-concrete bond.

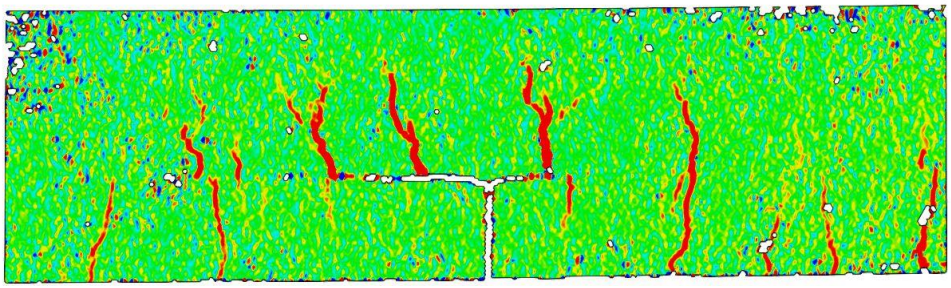

Figure 3-133: Holed interface – Strains in x-direction at a load step before failure

One of the samples which is similar to the reference sample has the coupling reinforcement directly placed on top of the SHCC layer (sample 6). The results of both these samples are shown together in Figure 3-134 and Figure 3-135. The load-displacement curve and interface opening are roughly similar indicating that the influence of directly placing the coupling reinforcement on the SHCC is negligible on the capacity of these systems. However, as the capacity is significantly lower than the yield capacity of these beams, the influence of the cover might have an effect when the stresses in the reinforcement become higher.

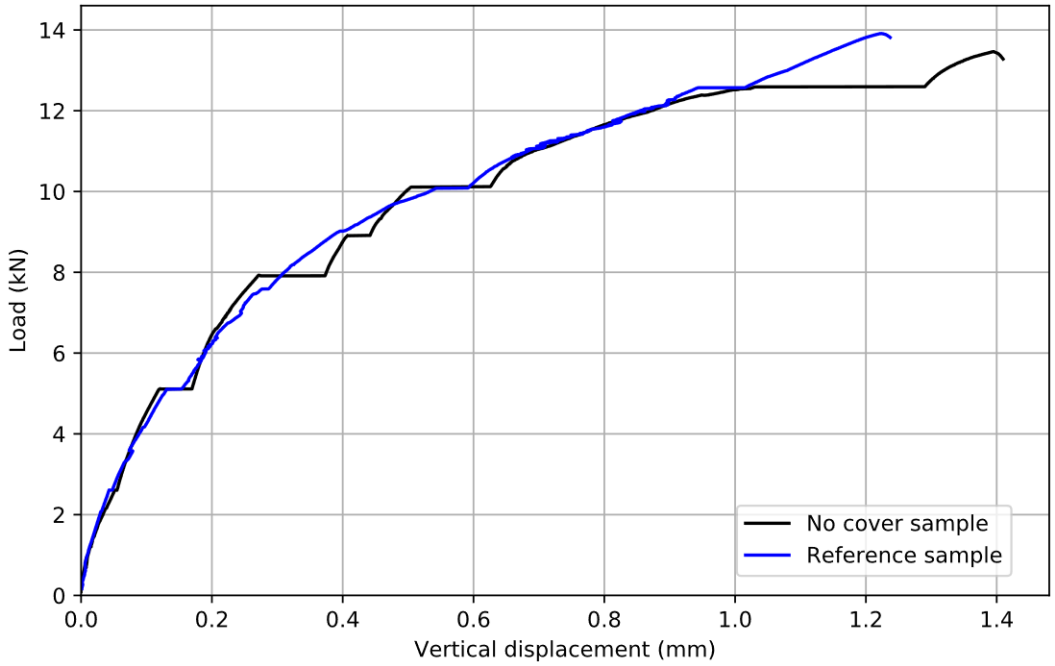

Figure 3-134: Comparison between load-displacement results of reference and no cover sample

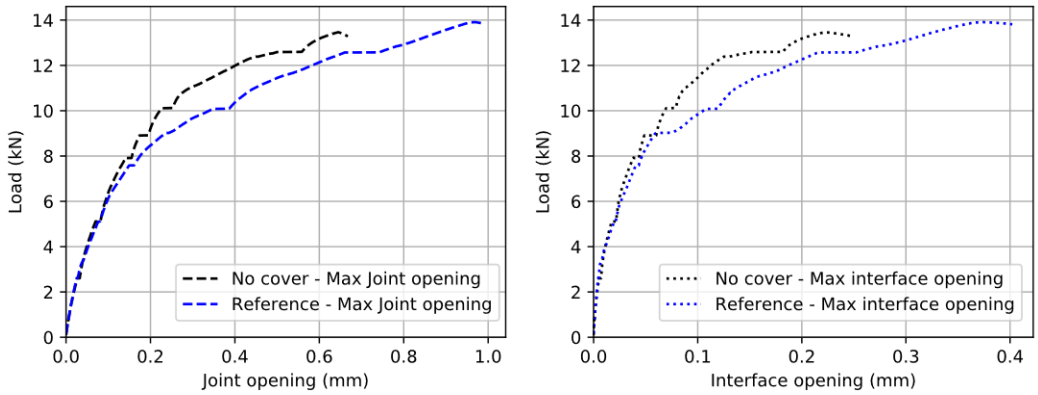

Figure 3-135: Comparison between maximum joint and interface opening of reference and no cover sample

The joint opening of both samples is however different. Up to a load of 6 kN, the opening of the joint is similar for both cases. For higher loads, the opening of the joint in the reference sample is larger compared to the 'No cover' sample. This is due to the fact that the stresses in the coupling reinforcement are higher for the reference sample. For this reference sample, the effective height between the coupling reinforcement and neutral axis of the compressive zone is lower, resulting in a higher stress in the coupling reinforcement. The same trend can be seen for the interface opening, which can be explained based on the eccentricity of the reinforcement bars (see paragraph 3.1.4.2). Besides the fact that the stress in the

coupling reinforcement is higher, also the effective height between the tensile reinforcement bars is higher resulting in larger perpendicular stresses at the interface.

The last sample consisted of a smooth interface with two stirrups placed nearby the joint to take up the tensile forces. A comparison between the reference sample and the sample with the stirrup is shown in Figure 3-136 and Figure 3-137. Initially, the behavior of both samples was similar until the delamination of the interface started at roughly 5 kN. The reference sample lost its stiffness as this delamination progresses through the interface up until the end of the coupling reinforcement, resulting in the failure of the beam. This process is prevented for the sample with the stirrups. After the bond between the SHCC and concrete is broken, the stirrups are taking up the tensile forces which results in a larger bearing capacity. The same can be seen in the figure with the interface opening. The stirrups result in a significant reduction of the interface opening as they prevent the opening of the interface at the location of the stirrup.

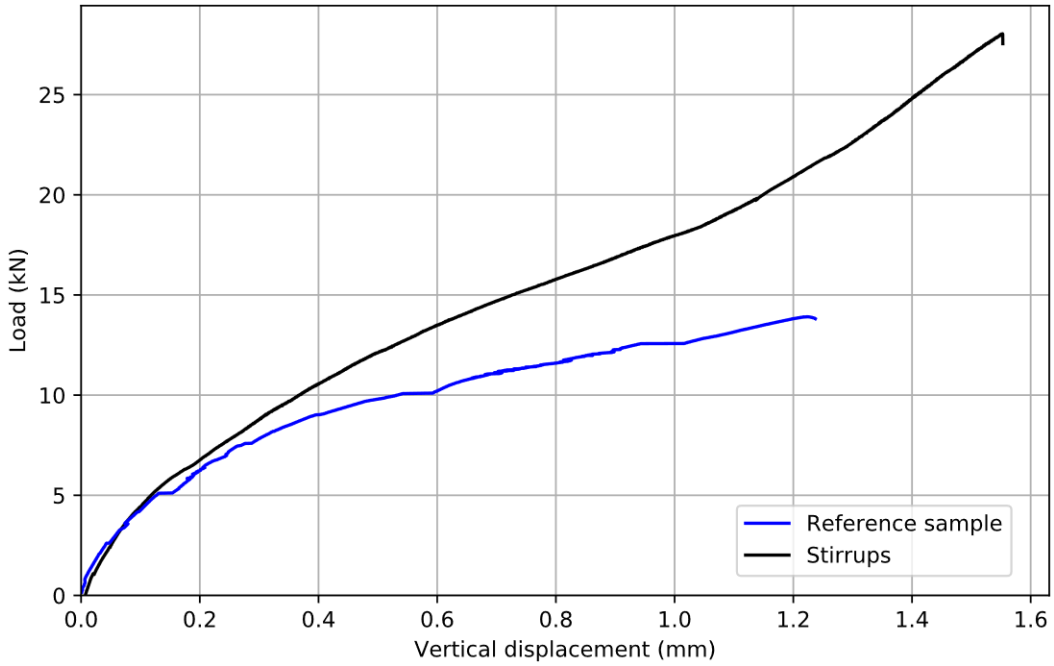

Figure 3-136: Comparison between load-displacement results of reference and stirrup sample

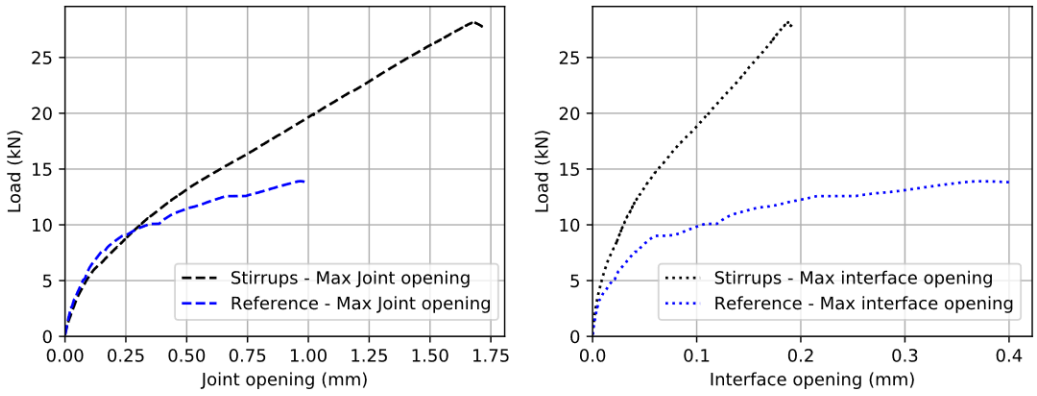

Figure 3-137: Comparison between maximum joint and interface opening of reference and stirrup sample

The strains in the stirrups have also been measured during the experiment with strain gauges. The placement of each strain gauge is different. In Figure 3-138, the placements of these gauges are shown with a number (the number within the parentheses is the gauge on the other leg of the stirrup).

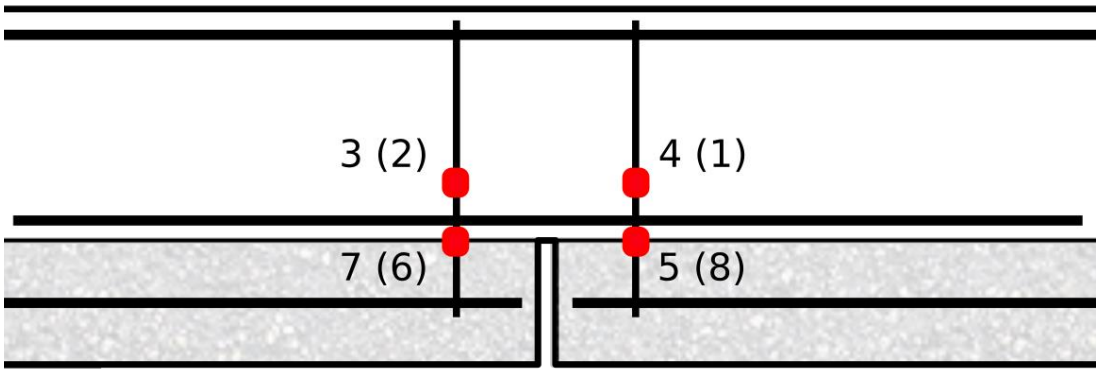

Figure 3-138: Numbering of strain gauges

Based on these strain measurements, the stresses in each of the eight strain gauges are determined which is visualized in Figure 3-141. In this graph, a large jump of the strain, thus also the stress, is happening for strain gauges 5 and 8. The load at which this happens corresponds to the failure load of the beam as a result of interface delamination (see Figure 3-113). Furthermore, also fracture of the concrete occurred at the location of the stirrup (see Figure 3-139).

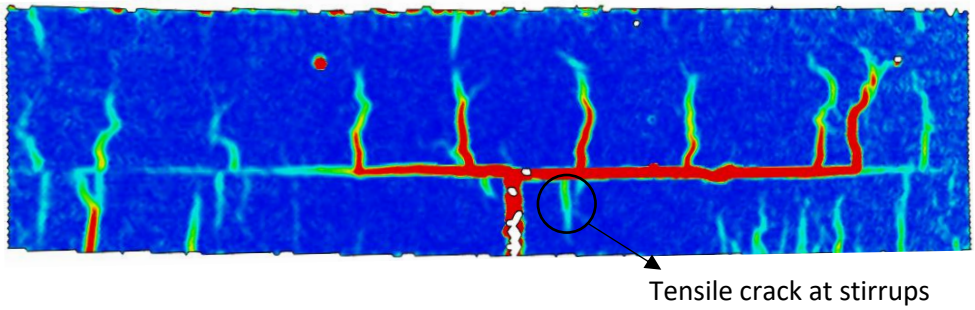

Figure 3-139: Concrete fracture at the stirrups

As the interface is weak, the delamination kept progressing through the interface while the stirrups were trying to prevent this. However, even for this case, the interface behind the stirrups delaminated up until the end of the coupling reinforcement where a flexural crack appeared. The opening of the interface is however controlled due to the stirrups. The final failure is a result of the interface delamination. This resulted in a load-capacity drop of the sample to roughly 20 kN as the stirrups were still holding the two separate concrete layers together. The test was stopped after this, however most likely pull-out failure of the stirrup would have occurred if the testing procedure was continued.

The concrete fracture at the stirrups is also a result of the interface delamination. Initially, the interface delaminated at the midspan joint, however the rotational restraint of the stirrup prevents this opening from further progressing. This rotational restraint will introduce tensile stresses at the top part of the SHCC at the location of the stirrup leading to tensile crack (see Figure 3-140).

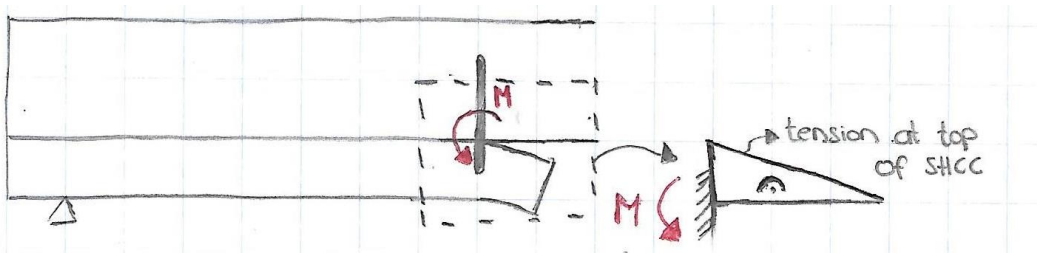

Figure 3-140: Rotational restraint at stirrup resulting in tensile cracks

The results of this sample show that the detailing of these hybrid SHCC-concrete beams is an important aspect. Even with the use of protruding reinforcement, delamination failure isn't prevented. Therefore, a combination of increasing the bond at the interface to prevent the delamination and use of stirrups to prevent the horizontal cracking in the concrete is something that has to be investigated.

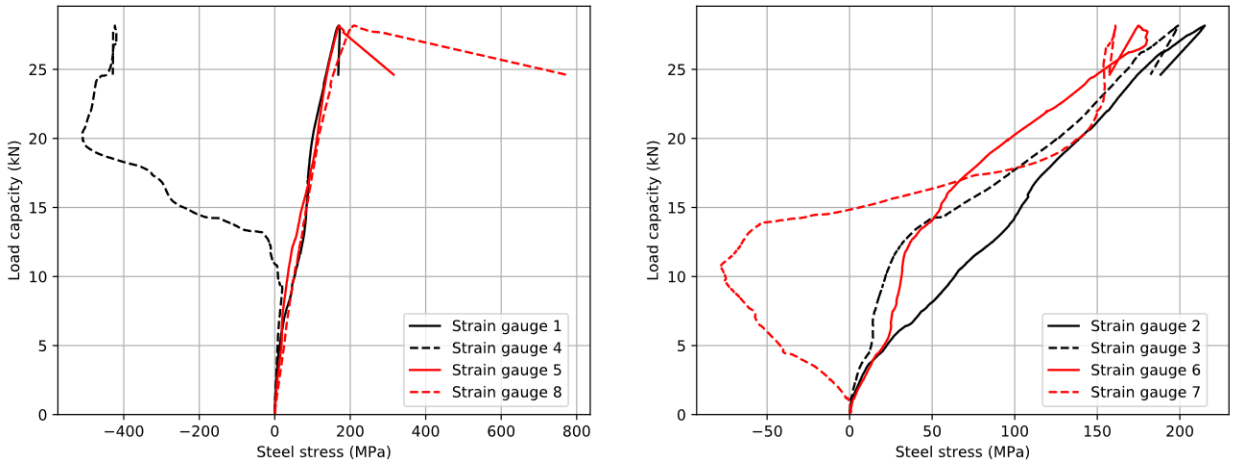

Figure 3-141: Load capacity against the steel stresses in the stirrups

3.6.2 Strut-and-Tie model

The failure modes of the samples at the interface and at the level of the coupling reinforcement is due to the perpendicular stresses resulting from the transfer of forces at the lap splice. A Strut-and-Tie model will be used to visualize this stress distribution through the hybrid SHCC-concrete beam (see Figure 3-142).

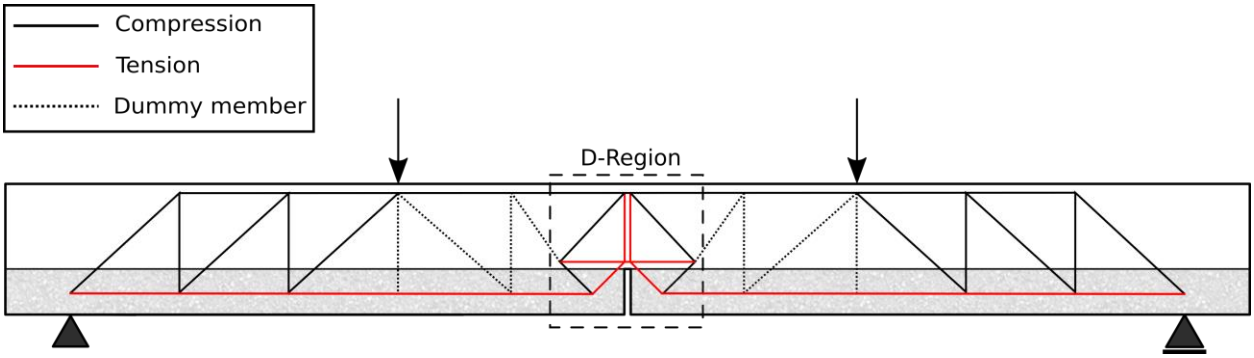

Figure 3-142: Strut-and-tie model

The critical region that gives rise to these failure modes is the disturbed region (D-Region) at the location of the middle joint. At this middle joint, the stress distribution of the lower tensile tie is disturbed resulting

in the redirection of the stresses to the coupling reinforcement. This will introduce perpendicular tensile stresses at the interface that can cause delamination (e.g. failure mode reference beam). This delamination will initiate at the joint. If the tensile strength of the interface is exceeded, the interface will open causing a shift of the D-Region away from the joint (see Figure 3-143). This mechanism keeps happening until the end of the coupling reinforcement is reached.

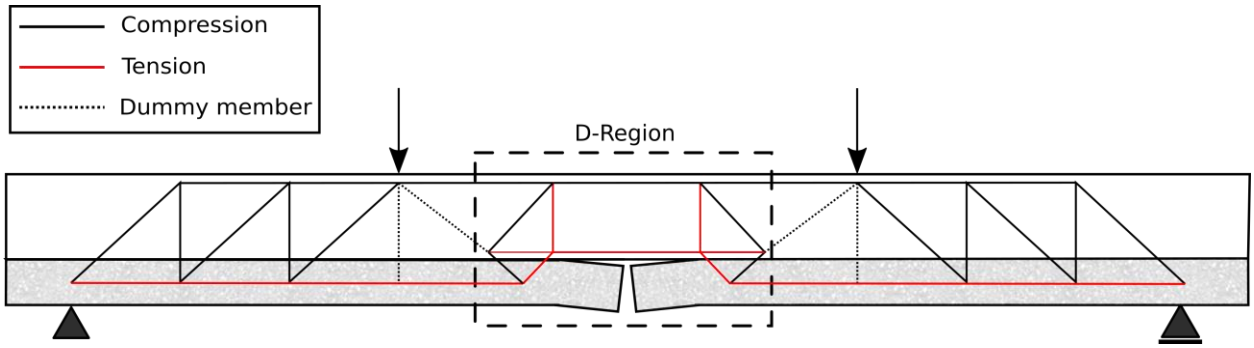

Figure 3-143: Shift of the D-Region in the Strut-and-tie model due to delamination

Based on this strut-and-tie model, it is assumed that the stresses along this vertical tie are constant. However, in reality, these stresses will be nonlinear with a localization of the stresses at the level of the coupling reinforcement (as this area is not influenced by the stresses due to the compressive struts). Note however that initially the largest stress will be located on the interface at the joint due to a stress concentration.

In order to verify this model, a simple FE model has been made to check the perpendicular stresses along the height of the tie. In this model, a composite beam with a middle joint assuming a perfect bond at the interface has been modelled. The perpendicular stresses in the concrete along the height of the beam will be shown at two locations. These locations are at the joint and at a distance of 10 mm away from the joint. The stress distributions for these two locations are plotted in Figure 3-144.

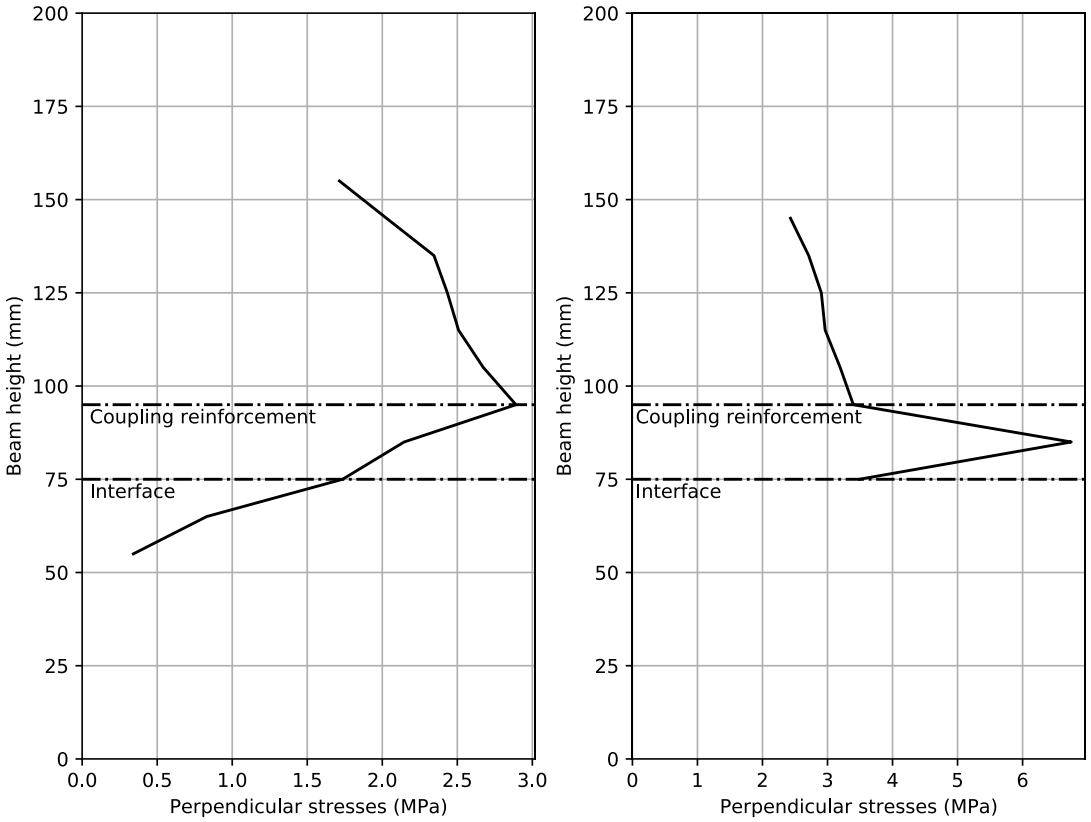

Figure 3-144: FEA – Perpendicular stresses at a section 10 mm away from the joint (left) and at the joint (right)

According to this FE model, the largest stress is indeed found at the location of the coupling reinforcement. The stresses at the interface are still large which will result in the delamination of the beams with a weak interface. In the right graph (the location of the joint), a singularity of the stresses happened resulting in stresses which are significantly higher than the concrete tensile strength (limitation of the FE model).

The stresses in the stirrups ($\emptyset 6$) and coupling reinforcement ($3x\emptyset 8$) are calculated based on the Strut-and-Tie model and the simple FE model assuming perfect bond (stirrups in the FE model are placed 5 mm away from the joint). For several load steps, these stresses are shown in Table 3-13 and Table 3-14.

Total load		FEA	STM	Unit
5	kN	14.58	63.1	MPa
10	kN	39.3	126.2	MPa
15	kN	104.3	189.4	MPa
20	kN	201.15	252.7	MPa
25	kN	277.9	315.8	MPa
30	kN	343.4	378.9	MPa
35	kN	395.7	442	MPa

Table 3-13: Comparison of stresses in stirrups

Total load		FEA	STM	Unit
5	kN	17.5	78.9	MPa
10	kN	52.12	157.9	MPa
15	kN	131.5	236.8	MPa
20	kN	283.34	315.7	MPa
25	kN	377	394.7	MPa
30	kN	456	473.7	MPa
35	kN	547	552.6	MPa

Table 3-14: Comparison of stresses in coupling reinforcement

The results show a good correspondence between the FE results and the Strut-and-Tie model. For the earlier load steps, the difference between the two models can be explained by the fact that initially the stresses are taken up by the concrete up until the tensile strength of concrete is reached.

Another comparison is made between the stresses in the stirrups according to the strain gauges which were used for sample 7. In Figure 3-145, the stresses based on strain gauge 1 are shown together with the stresses in the STM. The stresses in the STM are considerably larger than the stresses from the experiments. This is caused by two reasons. Firstly, the contribution of the concrete and interface isn't taken into account in the STM at the early load steps prior to cracking. Secondly, the location of the stirrups influences the results massively. During the experiment, the stirrups were placed 50 mm away from the joint. The interface opening at this location is smaller than the interface opening at midspan. This will result in a lower stress in the stirrups.

Based on the interface opening of the reference sample (both samples have a smooth interface), an extrapolation is done to determine the interface opening at the joint. Based on this, a factor of roughly 2 is determined between the opening at the stirrup (=LVDT 6) and joint (see Figure 3-146). Assuming this factor also between the opening of LVDT 5 and the midspan opening, the modified stress for the STM is calculated. In Figure 3-145, the comparison based on the modified stirrup stresses is shown. A good correspondence between the stresses is now obtained. Note however that assuming this factor 2 isn't entirely correct as the distance between LVDT 5 and 6 is larger than the distance between LVDT 5 and the midspan opening. Furthermore, also the rate of the interface opening increases as you get closer to the joint.

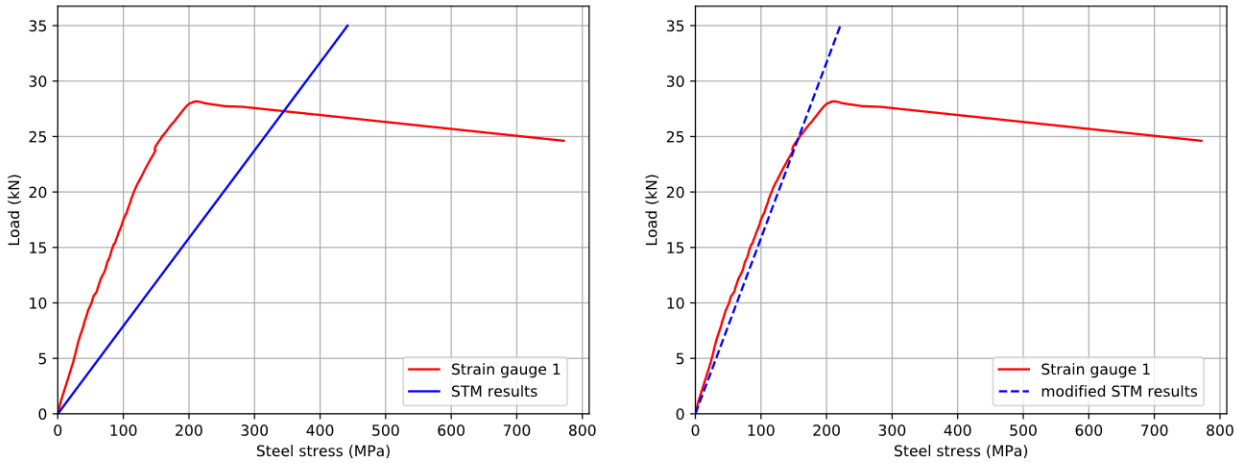

Figure 3-145: Stresses in the stirrups according to STM and strain gauges during the experiments

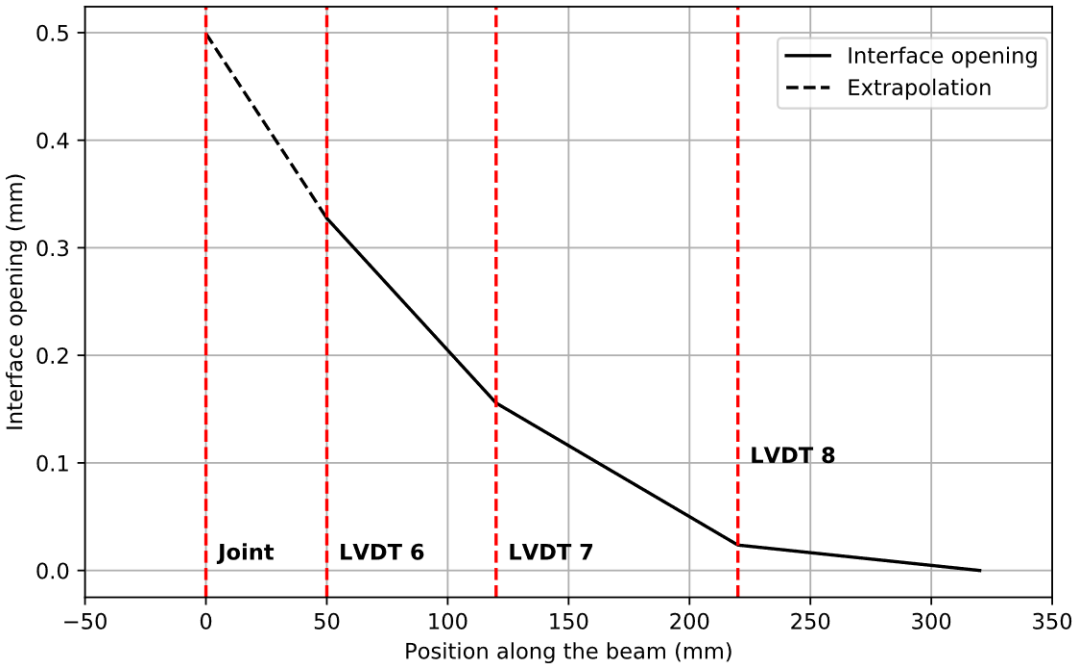

Figure 3-146: Extrapolation of the interface opening at the joint

The failure of the beam due to cracks at the coupling reinforcement was already shown for the sample with the profiled interface. Also, the sample with epoxy and sand failed in this manner (see Figure 3-147). In this figure, a longitudinal section of the failed sample is shown. Initially, the interface delaminated at the joint due to the stress concentration. However, as the interface has an increased bond, this crack transferred to the coupling reinforcement caused by the larger perpendicular stresses at that location.

Figure 3-147: Crack propagation of the sample with epoxy and sand at the interface

3.6.3 Drying shrinkage

One of the samples was exposed to drying outside the mould in a humidity-controlled room. The comparison of the experimental results between this sample and the reference sample is shown in Figure 3-148 and Figure 3-149. The stiffness reduction of the curing sample is visible in the load-displacement graph. This is caused by shrinkage cracks in the SHCC and interface as can be seen in Figure 3-150. The load capacity remained however similar, which indicates that the damage at the interface is mainly surface cracks due to the restraint of the reinforcement.

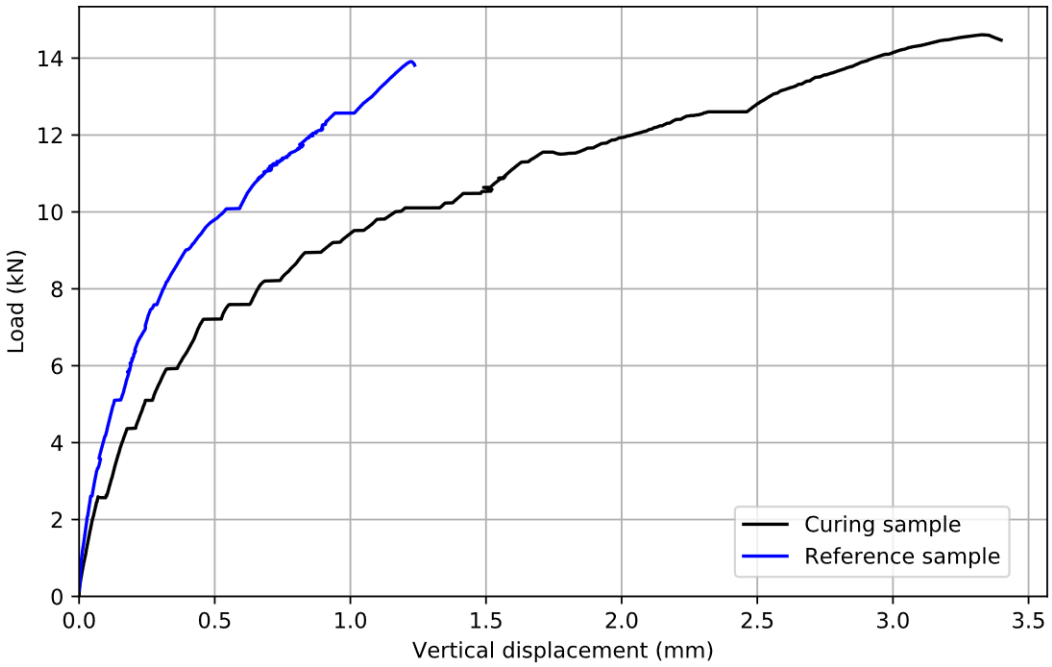

Figure 3-148: Comparison between load-displacement results of reference and curing sample

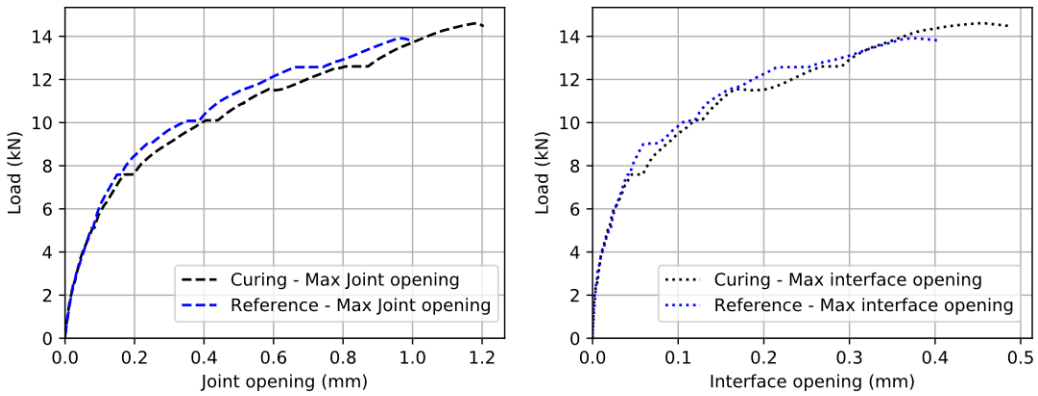

Figure 3-149: Comparison between maximum joint and interface opening of reference and curing sample

The interface and joint opening are similar for both samples (see Figure 3-149). The effective height of the coupling reinforcement is identical in both samples which means that the steel stress is also identical. Note however that the vertical displacement is not similar at similar same load steps. This shows that the vertical displacement of the hybrid SHCC-concrete has barely any influence on the joint opening.

Figure 3-150: Shrinkage cracks in the SHCC layer (left) and at the interface (right)

These shrinkage cracks at the interface can be explained using a simple model assuming linear elastic behavior. From the literature study, it was already said that the shrinkage of SHCC is significantly larger than the shrinkage of concrete [5]. As a result of this, the SHCC layer wants to shrink more than the concrete top layer. However, this is restricted at the interface by the composite action of the hybrid SHCC-concrete beam.

In this simple model, a pair of tensile forces are applied at the neutral axis of the SHCC layer up until the axial deformation is equal to the shrinkage of the SHCC.

$$N_{tensile} = E_{SHCC} * A_{SHCC} * \epsilon_{sh} \tag{3.35}$$

However, as we have a composite beam, this deformation of the SHCC layer is restricted by a compressive force with equal magnitude. As we now take into account the composite action of the hybrid beam, an eccentricity (y) of this compressive force (distance from the neutral axis of the SHCC layer to the neutral axis of the hybrid system) will also result in a bending moment. These equations are shown below with a graph of the stress distribution along the height of the beam in Figure 3-151 (no values of the stresses are shown as information regarding the differential shrinkage strain is required). The summation of these three components will give the stress distribution along the whole height of the beam.

$$\sigma_t = \frac{N_{tensile}}{A_{SHCC}} \qquad 0 \leq x \leq 70$$

$$\sigma_c = \begin{cases} \dfrac{-N_{tensile} * E_{SHCC}}{E_{SHCC} * A_{SHCC} + E_C * A_C} & 0 \leq x \leq 70 \\ \dfrac{-N_{tensile} * E_C}{E_{SHCC} * A_{SHCC} + E_C * A_C} & 70 \leq x \leq 200 \end{cases}$$

$$\sigma_M = \begin{cases} \dfrac{(N_{tensile} * y) * E_{SHCC} * (x - N.A)}{E_{SHCC} * I_{SHCC} + E_C * I_C} & 0 \le x \le 70 \\ \dfrac{(N_{tensile} * y) * E_C * (N.A - x)}{E_{SHCC} * I_{SHCC} + E_C * I_C} & 70 \le x \le 200 \end{cases}$$

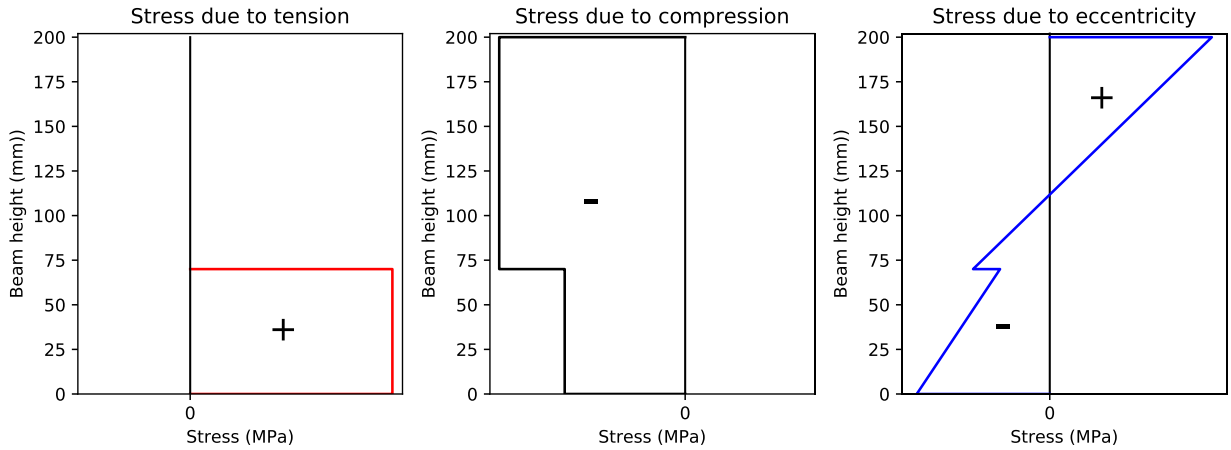

Figure 3-151: Stresses in the hybrid SHCC-concrete beam due to shrinkage

Due to this eccentric force, the hybrid SHCC-Concrete beam will bend. However, the stiffnesses of the SHCC and concrete aren't identical which will result in different curvatures ($\frac{M}{E_i I_i}$). As a result of this difference in curvature, perpendicular stresses at the interface will occur. These perpendicular stresses will lead to cracks at the interface when the interface tensile strength is exceeded.

3.6.4 **Summary**

In Figure 3-152 and Figure 3-153, the experimental results are shown for the samples with different interface roughnesses. These are the samples with a smooth interface, profiled interface, holed interface and the interface with epoxy and sand. The influence of increasing the roughness resulted in a larger bearing capacity and reduced interface and joint opening. The profiled interface showed the most promising result as it has the largest bearing capacity and lowest joint opening. Note that for the interface opening of the profiled interface, the LVDT was placed closer to the joint compared to the other samples. Thus, the interface opening is larger compared to the other samples as is shown in Figure 3-153. For all these samples, failure prior to yielding of the coupling reinforcement occurred.

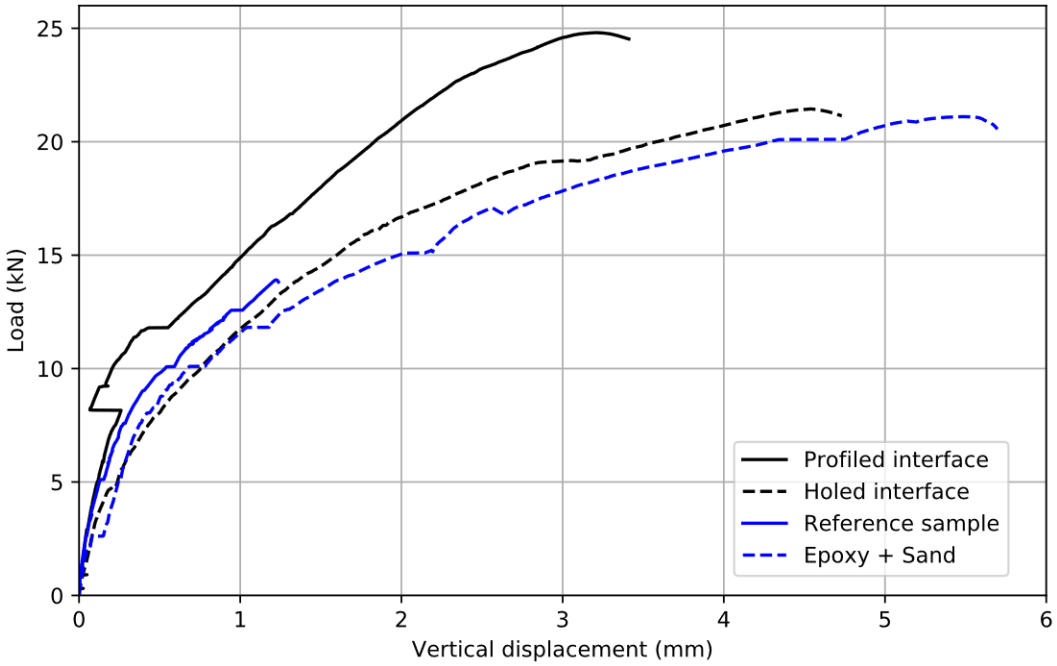

Figure 3-152: Load-displacement curves of samples with different interface roughness

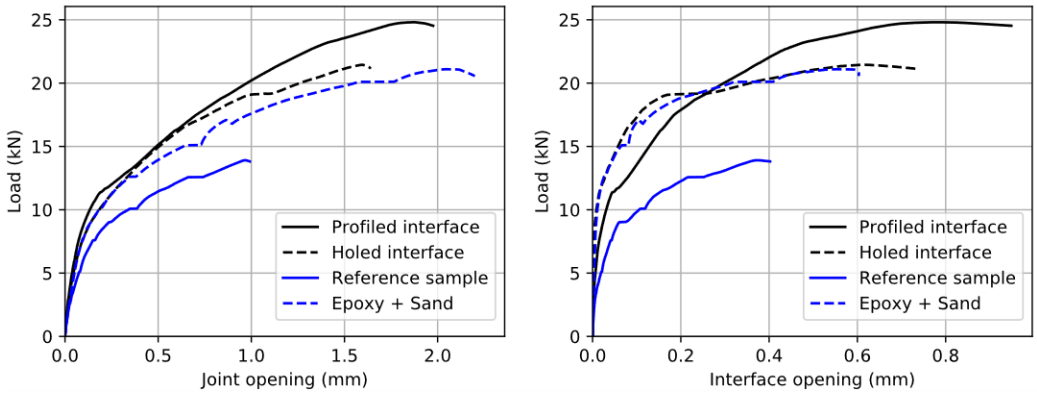

Figure 3-153: Joint and interface opening of samples with different interface roughness

The remaining samples have a smooth interface where the reinforcement cover, curing method and influence of the protruding reinforcement has been investigated. These results are shown together in Figure 3-154 and Figure 3-155. The effect of protruding reinforcement on the bearing capacity and interface opening is significant. The other parameters didn't seem to have an effect on the joint and interface opening. However, the curing sample has a lower stiffness due to the shrinkage cracks prior to testing which resulted in a larger midspan deflection. Also, for these samples yielding of the coupling reinforcement didn't occur due to delamination of the interface. The sample with stirrups didn't prevent the delamination, but did prevent the horizontal cracking at the coupling reinforcement. Therefore, the combination of increasing the roughness of the interface and protruding reinforcement at the joint is of interest to benefit from the strain hardening behavior of the SHCC.

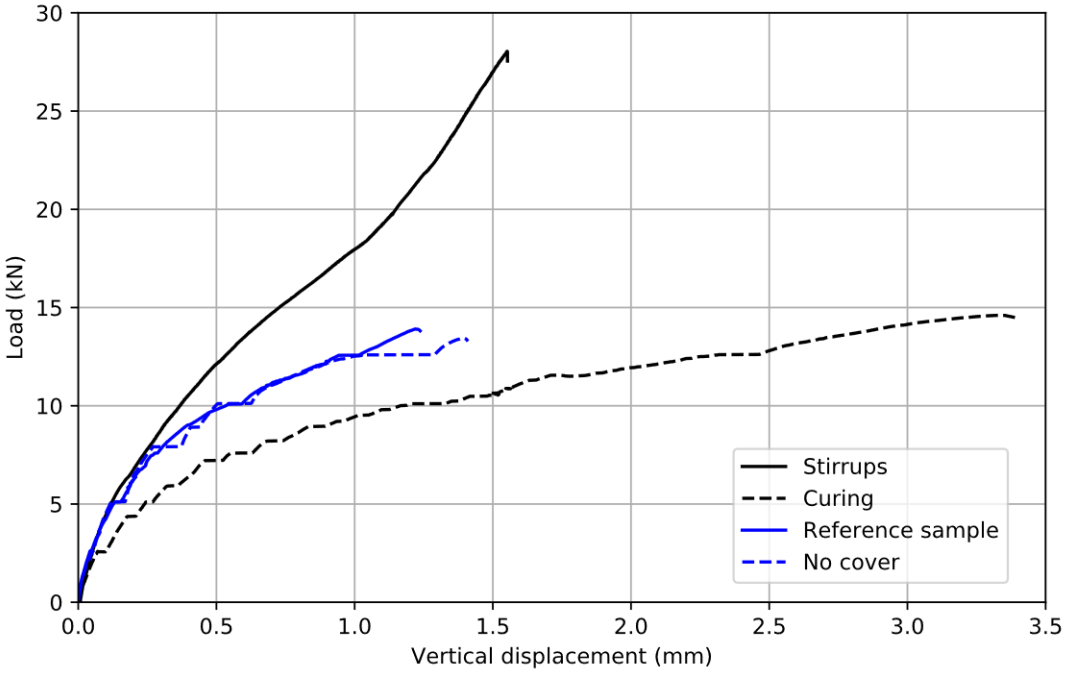

Figure 3-154:Load-displacement curve of samples with a smooth interface

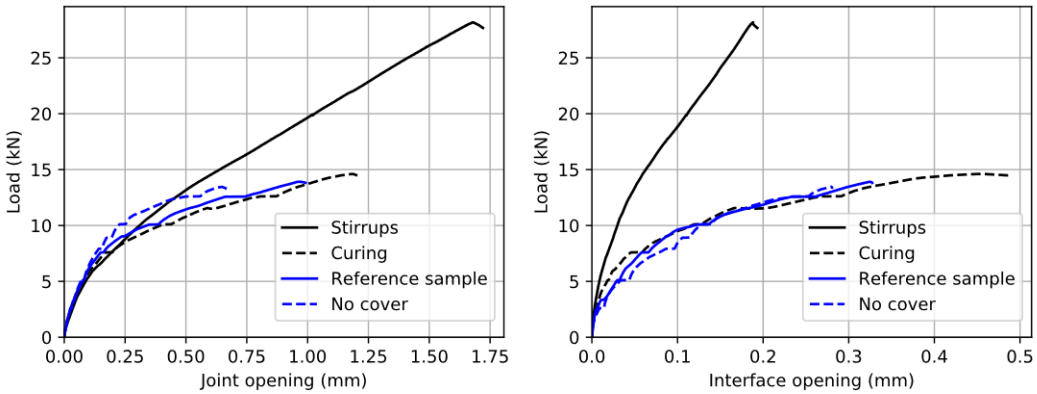

Figure 3-155: Joint and interface opening of samples with a smooth interface

4 Numerical model

4.1 Geometry

All models are made in a 2D-plane using regular plane stress element. The dimensions correspond to the experimental set-up which has a total length of 1900 mm, span of 1700 mm, width of 150 mm and a total height of 200 mm. The height of the beam is divided into two parts of 70 mm and 130 mm corresponding to the SHCC and conventional concrete layer.

4.1.1 Models

The FE models, corresponding to the dimensions given in paragraph 4.1, are shown in Figure 4-1 – Figure 4-3. In the first model, the interface between the SHCC and concrete layer is modelled as a perfect bond. The 2nd model is modelled by applying one interface along the whole length of the beam to represent a smooth interface. The 3rd model has a profiled interface which is based on the dimensions of the tooth-shaped interface. The last model is similar to model 2, however, stirrups are added at the joint to take up the tensile stresses (Figure 4-4).

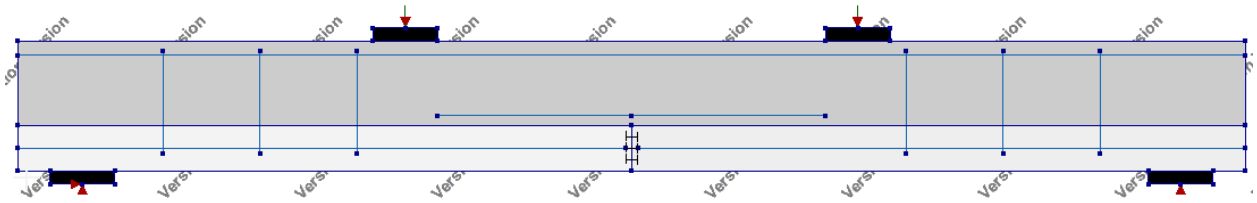

Figure 4-1: FE Model – Perfect bond at interface

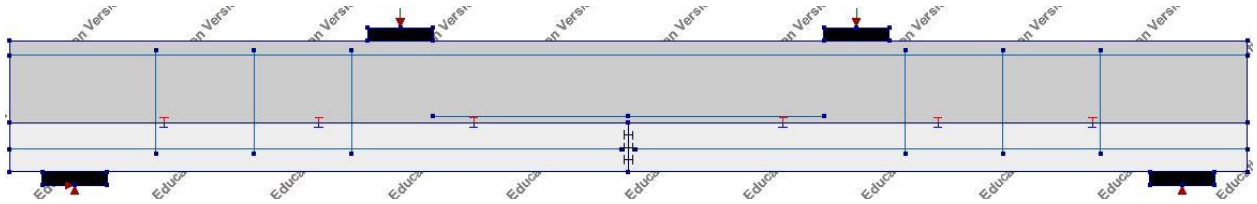

Figure 4-2: FE Model – Smooth interface

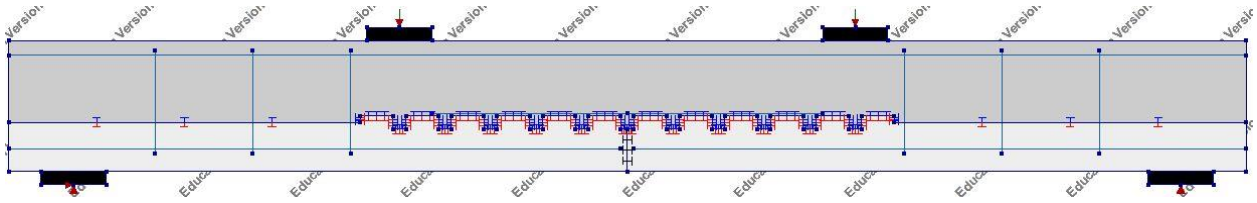

Figure 4-3: FE Model – Profiled interface

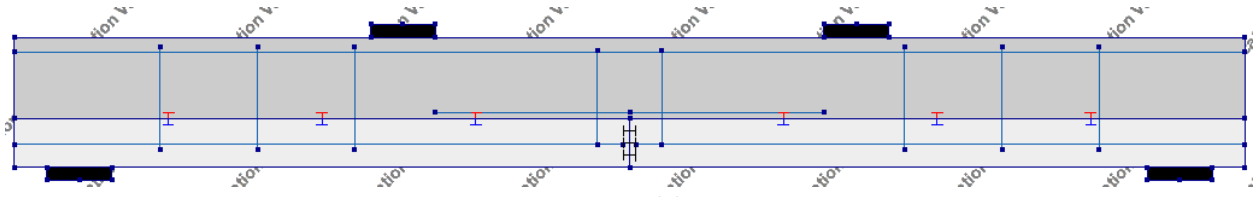

Figure 4-4: FE Model – Stirrups

4.2 Materials

In this subchapter, the constitutive models for the materials are elaborated. Obtaining accurate models for the SHCC and concrete material, based on experiments and literature, is essential in order to acquire meaningful results. Furthermore, also the reinforcement steel has to be modelled properly as it important in the mechanical behavior of the hybrid SHCC-concrete beams.

4.2.1 Concrete

The concrete properties used in the FE model are based on experiments and literature. The compression strength is calculated based on compression tests with concrete cubes. In total 16 cubes were tested resulting in an average compressive strength of 50 MPa (see Appendix A). This corresponds to a characteristic strength of 32 MPa which can be classified as concrete class C30/37. The young's modulus is also based on compressive tests on concrete samples with a shape of a prism. Based on these experiments an average Young's modulus of 35500 MPa was determined. The concrete mean strength can be obtained using equation 4.1.

$$f_{cm} = f_{ck} + 8 \tag{4.1}$$

Based on the recommendations in the Nonlinear FEA guidelines for concrete structures [25], a non-linear Hordijk tension softening curve is used for the tension behavior (see Figure 4-5). For the compressive behavior, a parabolic compression curve is used as is shown in Figure 4-6.

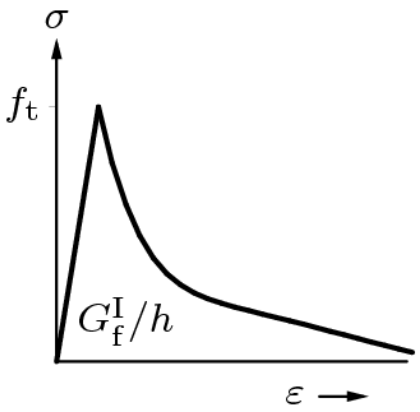

Figure 4-5: Hordijk tension softening curve

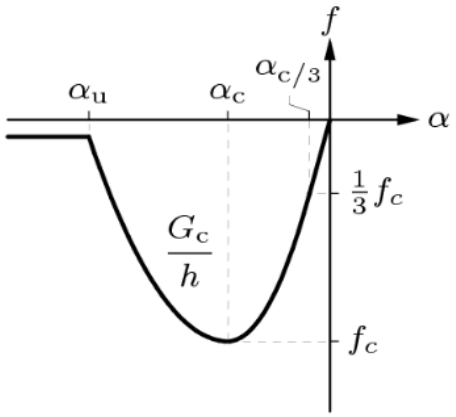

Figure 4-6: Parabolic compression curve

The fracture energy of the tension and compression curve are calculated based on the Nonlinear FEA guidelines for concrete structures using equations 4.2 and 4.3 [25].

$$G_f = 73 * {f_{cm}}^{0.18} \tag{4.2}$$

$$G_c = 250 * G_f \tag{4.3}$$

All the required parameters for the concrete FE model are shown in Table 4-1.

Property		Value	Unit
Material Class		Concrete and masonry	
Material model		Total strain-based crack model	–
Young's modulus	E_c	35500	MPa
Poisson's ratio	ν	0.2	–
Crack orientation		Rotating	–
Tensile curve		Hordijk	–
Tensile strength	f_{ct}	2.90	MPa
Tensile fracture energy	G_f	0.141	N/mm
Crack bandwidth specification		Rots	–
Compression curve		Parabolic	–
Compression strength	f_c	40	MPa
Compression fracture energy	G_c	35.4	N/mm

Table 4-1: Concrete properties

4.2.2 SHCC

The material properties of SHCC are shown in Table 4-2. Based on these properties, a user-defined tensile curve has been implemented in the finite element model to represent the behavior of the SHCC (see Figure 4-7). The compression curve for the SHCC material has been assumed ideal as is shown in Figure 4-8. The compressive strength and Young's modulus of the SHCC have been determined by means of compressive cube tests (see Appendix A).

Property		Value	Unit
Material Class		Concrete and masonry	
Material model		Total strain-based crack model	–
Young's modulus	E_{SHCC}	23000	MPa
Poisson's ratio	ν	0.2	–
Crack orientation		Rotating	–
Tensile curve		Fib fiber reinforced concrete	–
Tensile strength	f_{ct}	2.56	MPa
Ultimate tensile strength	f_{uct}	3.5	MPa
Compression curve		Ideal	–
Compression strength	f_c	40	MPa

Table 4-2: SHCC Properties

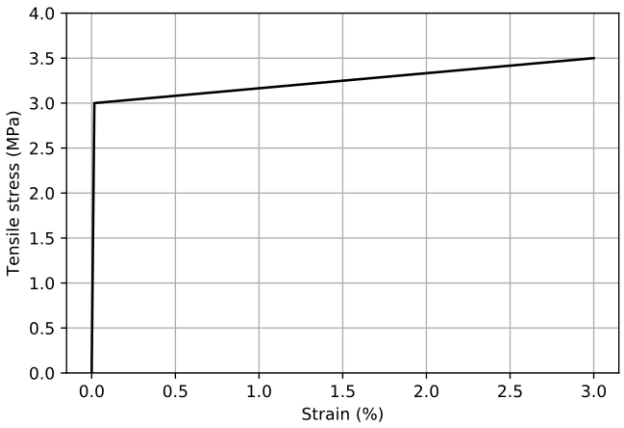

Figure 4-7: SHCC Tensile behavior

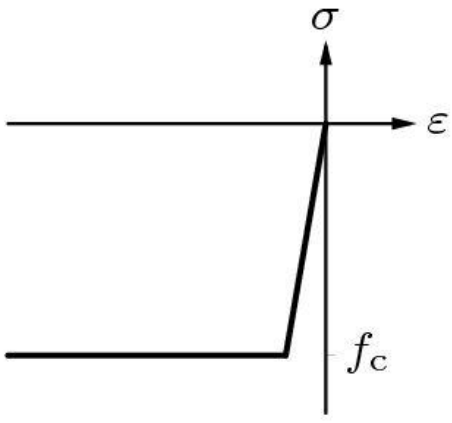

Figure 4-8: SHCC Compression curve

4.2.3 **Reinforcement steel**

Ribbed reinforcement type B500 has been used in the experiments. Therefore, the material properties of this type of steel are used in the model. Von Mises plasticity has been applied to add the hardening effect of the reinforcement steel. All the model properties are shown in Table 4-3. The stress-strain diagram of the reinforcement steel is shown in Figure 4-9.

Property		Value	Unit
Material Class		Reinforcements	
Material model		Von Mises plasticity	–
Young's modulus	E_s	210000	MPa
Poisson's ratio	ν	0.3	–
Plastic hardening		Total strain-yield stress	–
Hardening hypothesis		Strain hardening	–
Hardening type		Isotropic hardening	–
Yield strength	f_y	550	MPa
Fracture strength	f_u	650	MPa

Table 4-3: Reinforcement steel properties

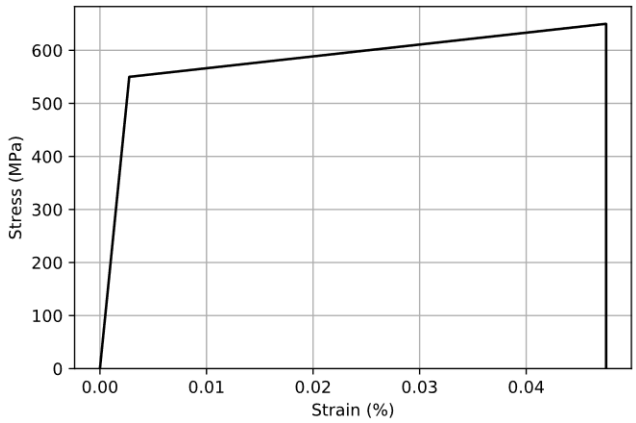

Figure 4-9: Reinforcement stress-strain diagram

4.3 Loads

The experiments were done using a four-point bending configuration set-up. Similarly, based on the testing configuration, this has been implemented in the model. Two steel plates have been added at the top of the beam at the same location of the load points during the experiments. The load has been applied by applying a prescribed deformation. As a result of this, the loading points have to be also supported in the same direction the loads are applied (see paragraph 4.4).

4.4 Supports

The beams are supported at a distance of 100 mm from the edges of the beam. Steel plates are added to distributes the forces through the beam in order not to get singularities. The left support is restrained in the vertical and horizontal direction. The right support of the beam is only restrained in vertical direction. Furthermore, also supports are added at the load points so that a displacement-controlled analysis can be executed. If no supports are added, the loading points are free to move and no forces are generated. All the information regarding the supports is shown in Table 4-4.

Property	Restraint direction
Left support	Vertical and horizontal
Right support	Vertical
Left loading support	Vertical
Right loading support	Vertical

Table 4-4: Support restrains

4.5 Joint

The joint between the two SHCC layers has been added in the FE model, by applying a connection between the edges of the SHCC layers (see Figure 4-10). The connection type has been set as 'No connection' so that it is not able to transfer forces.

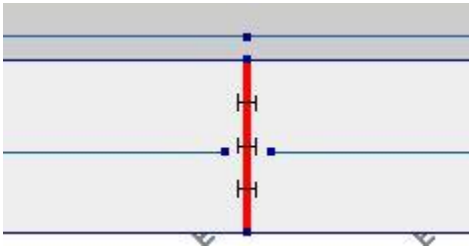

Figure 4-10: No connection edge between the SHCC Layers

4.6 Interface

The interface between the concrete and SHCC is an important aspect of the analysis. The interface is modelled using a Coulomb friction model with a tensile strength cut-off as is shown in Figure 4-11.

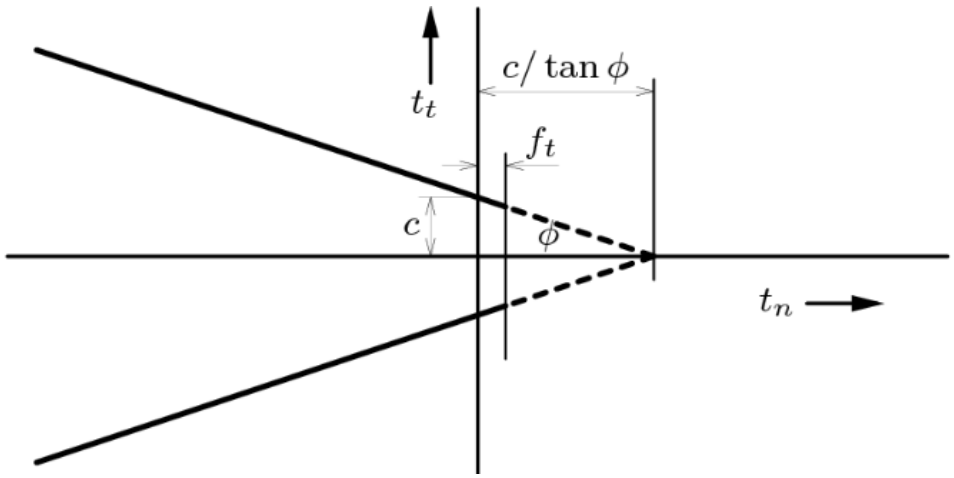

Figure 4-11: Coulomb friction model [26]

The (initial) parameters for the Coulomb friction modes are shown in Table 4-5. Initial values of the interface stiffness are based on the following expressions [27].

$$D_{11} = \frac{E_{\text{concrete}}}{\text{element size}} * 10 \left({}^{N}/_{mm^3} \right) \tag{4.4}$$

$$D_{22} = D_{11} \tag{4.5}$$

The interface tensile strength depends on the interface preparations and is therefore different for each model. The cohesion of the interface is assumed to be twice the interface tensile strength [27]. The value of the friction angle is based on the FIB Model Code [28]. In this code the friction angle depends on the interface roughness which is defined as a smooth interface ($\mu = 0.5 - 0.7$), rough interface ($\mu = 0.7 - 1$) and very rough interface ($\mu = 1 - 1.4$).

Property		Value	Unit
Connection type		Interface	–
Element class		Structural Line Interfaces	–
Class		Interface elements	–
Material model		Coulomb friction	–
Linear material type		2D Line interface	–
Normal stiffness	D_{11}	35500	N/mm^3
Shear stiffness	D_{22}	35500	N/mm^3
Cohesion		$2 * f_t$	MPa
Friction angle		Dependent on model	rad
Dilatancy angle		–	rad
Interface opening model		Gapping model	–
Tensile strength	f_t	Dependent on model	MPa
Model for gap appearance		Brittle	–

Table 4-5: Interface properties

Based on the different models, the values of the stiffnesses, friction angle and dilatancy angle will be adjusted by calibrating using the experimental results. The dilatancy angle describes the volume increase

at the interface due to plastic shearing. The normal uplift of the interface can be expressed in terms of the dilatancy angle and shear-slip at the interface [26].

$$u_p = \int \tan(\psi)\ d\left|\Delta v_p\right| \tag{4.6}$$

- u_p = Normal uplift at the interface
- ψ = Dilatancy angle
- Δv_p = shear-slip at the interface

4.7 Mesh

For all models, a mesh is generated using quadratic elements with a size of 10 mm. In Figure 4-12, a mesh is shown for model 2. Each element consists of 4 corner nodes and 4 intermediate nodes. The interface elements are based on two boundary lines with a total of 6 nodes [26]. All the elements used in the FE model are shown in Table 4-6.

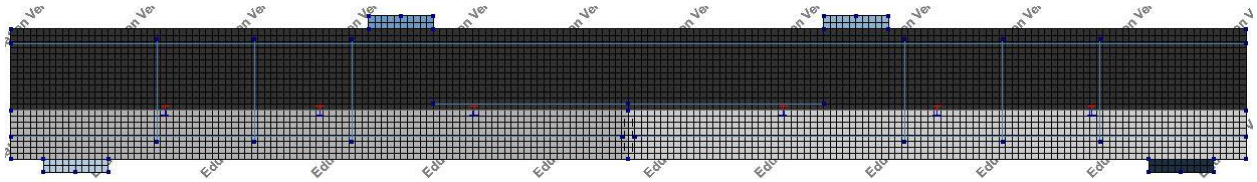

Figure 4-12: Example of mesh for model 1

Property	Element type
Concrete	CQ16M
SHCC	CQ16M
Steel plates	CQ16M
Joint	CL12I
Interface	CL12I
Reinforcement steel	Embedded reinforcement

Table 4-6: Element types

4.8 Analysis method

The analysis method is based on a load-displacement controlled analysis with physically nonlinear effect. The number of load steps is 100 with a prescribed deformation of 0.04 mm per load step. The maximum allowable number of iterations is 100 using an energy norm with a convergence tolerance of 0.001. The iterative method is based on a regular Newton-Raphson method. In Table 4-7 all these inputs are shown.

Property	Value
Command	Structural nonlinear
Nonlinear effects	Physical
Load steps	100
Iterative method	Newton-Raphson
Line search	Off
Maximum iterations	100
Convergence norm	Energy
Convergence tolerance	0.001

Table 4-7: Analysis method

5 Numerical analysis

5.1 Model 1 – Perfect bond

The first model is based on a perfect bond at the interface between the SHCC and concrete layer. This model is made to verify the analytical calculations of paragraph 3.1.2 and will be used as a starting model for the models with a Coulomb-friction model at the interface.

The load-displacement curve of the model with a perfect bond at the interface is shown in Figure 5-1. The load capacity of the beam at failure is 23.8 kN.

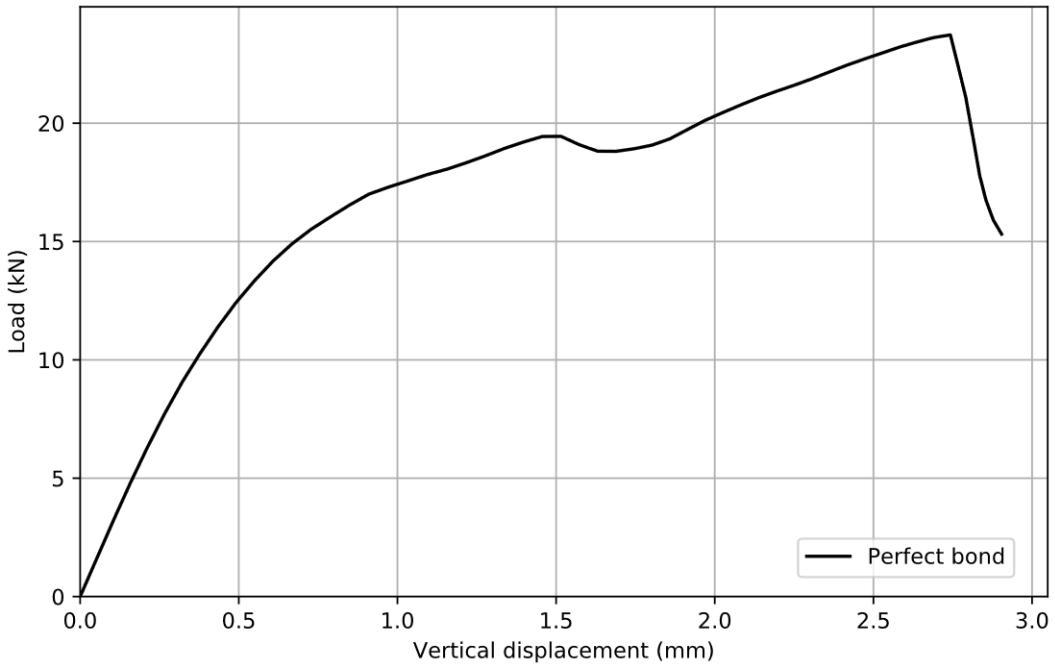

Figure 5-1: Load-displacement curve of model with perfect bond

Comparing this load-capacity with the capacity based on the analytical calculation (see Table 5-1), the result from the FEA model is significantly lower than the expected capacity calculated based on the analytical calculation.

Property	Value	Unit
Yielding	34.88	kN
Flexural failure	38	kN

Table 5-1: Load capacity at yielding and flexural failure

In order to understand the underlying reason for this lower capacity, the failure mode of the beam will be looked at based on the principal crack width (see Figure 5-2). In this figure, the large horizontal crack going through coupling reinforcement is detrimental to the failure of the beam. This failure mode corresponds to the Strut-and-Tie model explained in paragraph 3.6.2.

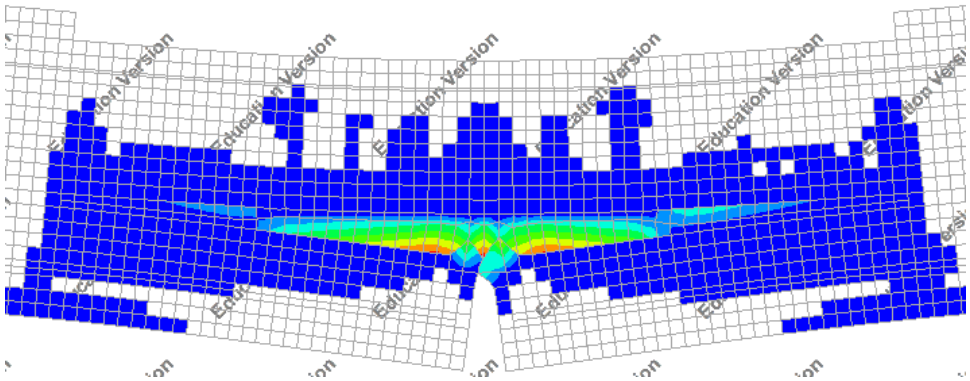

Figure 5-2: Principal cracking of the constant bending moment region with perfect bond at the interface

In order to verify the analytical calculation, the large horizontal crack at the reinforcement has been prevented by using protruding reinforcement according to the Strut-and-Tie model (see Figure 5-3). The load-displacement curve of this modified model is shown in Figure 5-4.

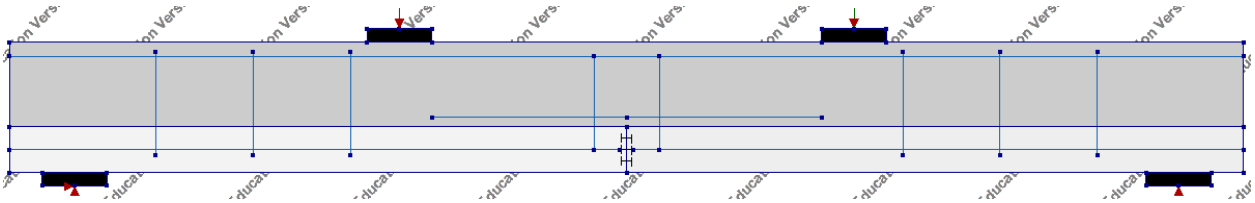

Figure 5-3: Modified perfect bond model with stirrup according to STM model

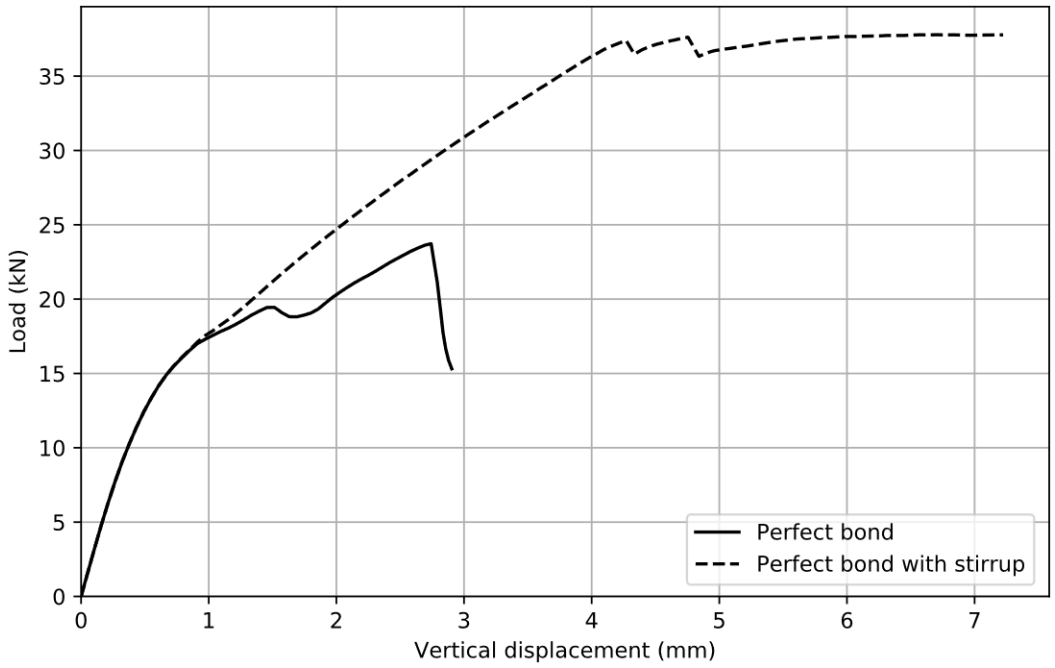

Figure 5-4: Load-displacement curve of the modified model with perfect bond

In Table 5-2, the load capacities at yielding and failure are again compared between the analytical calculation and the FEA results of the modified model. For this modified model, the loads at yielding and failure are in correspondence. This result supports the stress distribution according to the Strut-and-Tie model around the joint.

Property	Value	Unit
Yielding - FEA	35.57	kN
Yielding - Analytical	34.88	kN
Flexural failure – FEA	37.78	kN
Flexural failure- Analytical	38	kN

Table 5-2: Comparison of capacities of FEA and analytical

In order to confirm the distribution of the stresses along the vertical tie of the STM model, the stresses along the stirrups are shown in Figure 5-5. In this figure, it can be seen that the stresses are localized around the interface with the largest stress at the level of the coupling reinforcement. This corresponds to the results of the simple model in Figure 3-144. Furthermore, also the stress in the coupling reinforcement is shown which indeed shows yielding of the coupling reinforcement (Figure 5-6).

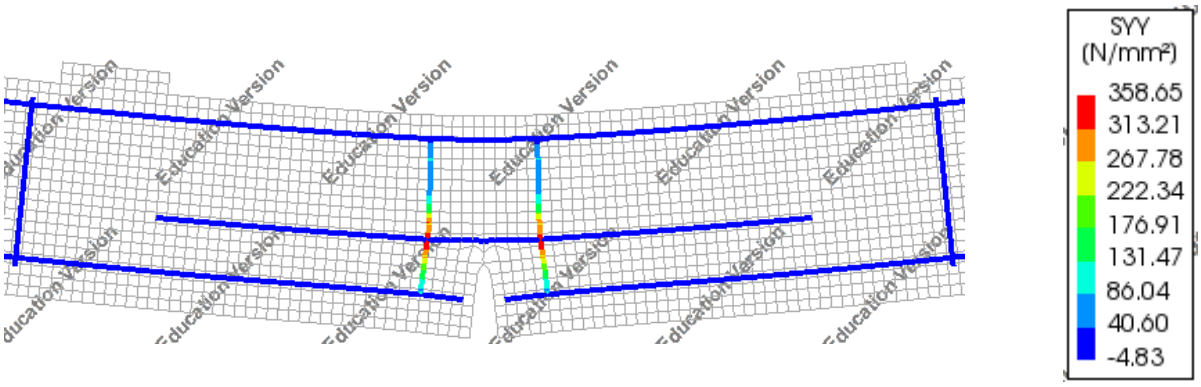

Figure 5-5: Stresses in the stirrups

Figure 5-6: Stress in the coupling reinforcement

5.2 Model 2 – Smooth interface

The second model is based on the reference beam with a smooth interface. The load-displacement, interface opening and joint opening results have been analyzed in the model. The interface opening has been obtained using the 'Interface Relative Displacement' output option. The joint opening is taken as the displacement in x-direction of the lowest node at the joint.

The initial values shown in Table 4-5 didn't lead to satisfactory results. Therefore, a calibration was done based on the experimental results. The adjusted parameters are shown in Table 5-3. The dilation angle describes the volume increase (displacement perpendicular to the interface) at the interface due to plastic shearing. In case this volume increase is restrained, a larger capacity will be obtained.

Property		Value	Unit
Normal stiffness	D_{11}	1200	N/mm^3
Shear stiffness	D_{22}	1200	N/mm^3
Cohesion		1.1	MPa
Friction angle		0.85	rad
Dilatancy angle		0 (1)	rad
Tensile strength	f_t	0.55	MPa

Table 5-3: Smooth interface – Calibrated interface properties

In Figure 5-7 the experimental result is shown together with the FEA results with and without dilatancy. The load capacity of the FE result without dilatancy is significantly underestimated as a result of early interface delamination failure. The FE result with dilatancy shows good correspondence with the experimental result.

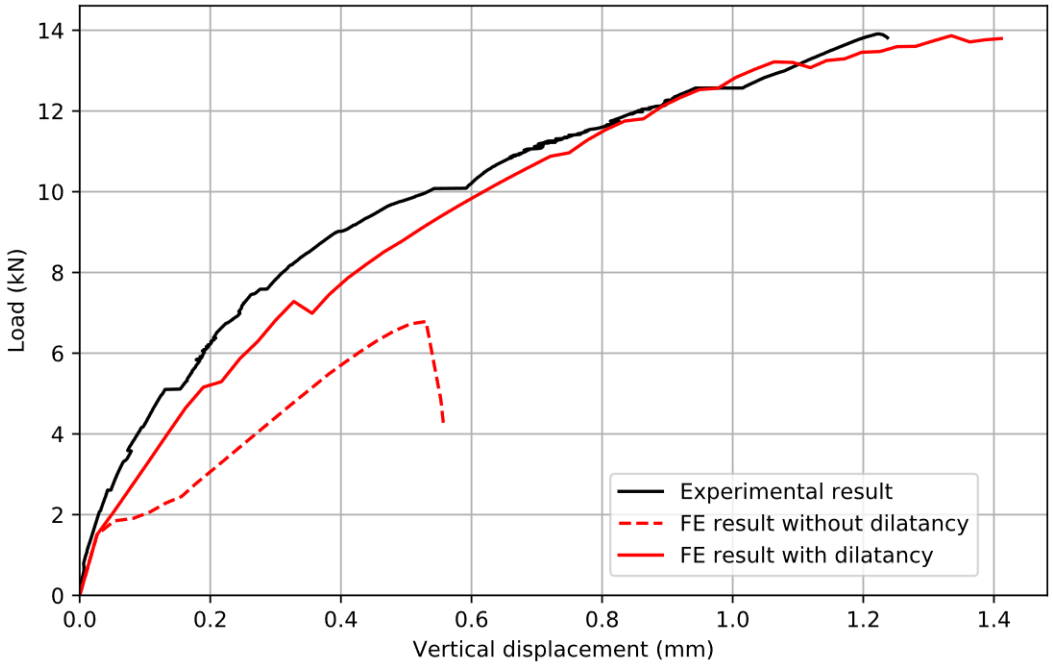

Figure 5-7: Load-displacement curve – Comparison experimental result and FE results

In order to understand the influence of dilatancy, the failure mode will be compared at two interface nodes (see Figure 5-8). These are the nodes at the midspan joint (Node A) and at a location of 75 mm from the joint (Node B).

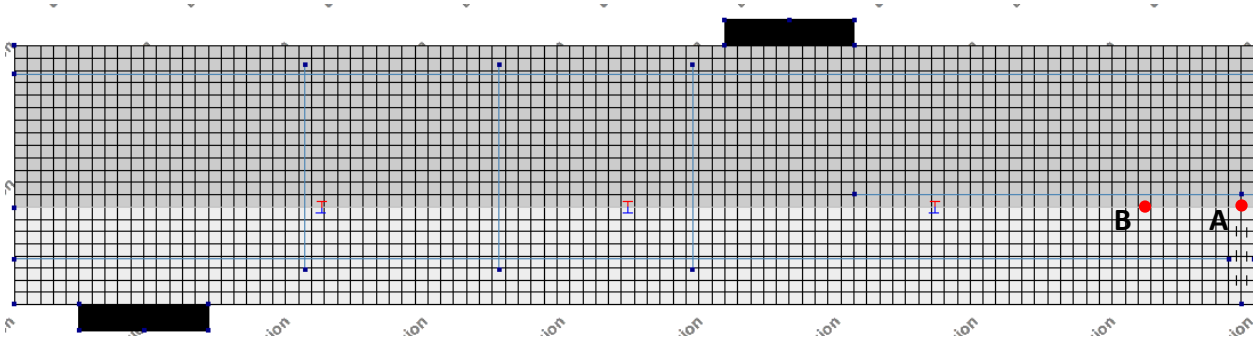

Figure 5-8: Smooth interface – Location of nodes for comparison of failure envelopes

In Figure 5-9 and Figure 5-10, the stress combinations for both FE analyses are shown. The result of node A is identical for the analyses with and without dilatancy (no restraint of the interface opening). The failure of this node occurs as a result of reaching the interface tensile strength (vertical cut-off line). The failure envelope of node B is however different. In case no dilatancy is used, the sample also fails due to the exceedance of the interface tensile strength. However, no intermediate points are visible, meaning that the progression of the interface delamination occurs fast. As a result of this, a low bearing capacity of this model is obtained as was shown in Figure 5-7. For the result with dilatancy, a different stress combination envelope is achieved. As a result of the larger restraint of the interface opening, the effect of shear at the interface will become more important. This is also seen in Figure 5-10 as the failure of node B occurs by reaching the Mohr-Coulomb failure envelope.

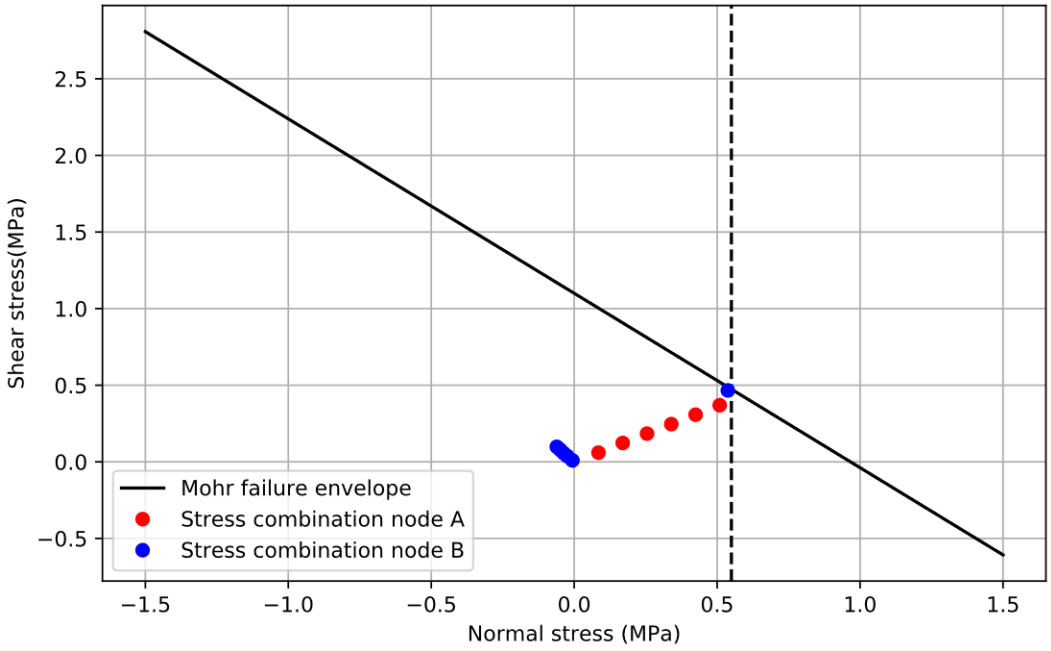

Figure 5-9: Failure modes of nodes A and B without dilation

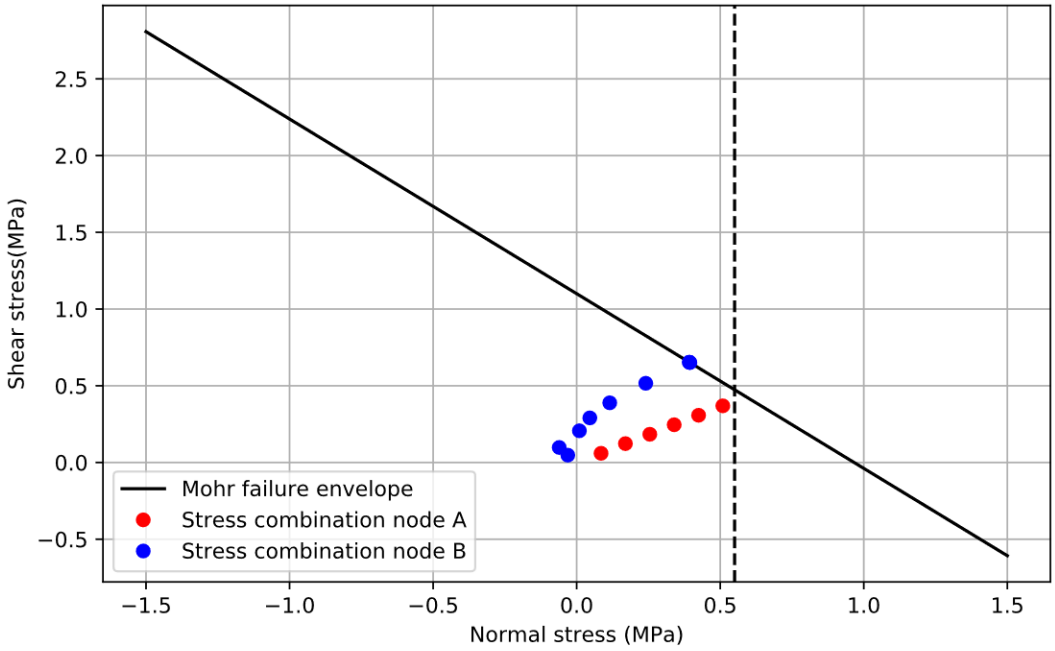

Figure 5-10: Failure modes of nodes A and B with dilation

Based on these results, it is chosen to further elaborate the model including dilation. The FEA results with a dilatancy angle are shown together with the experimental results in Figure 5-11 and Figure 5-12. The load-displacement curve of the FE model corresponds well to the experimental results. However, the finite element model isn't able to predict the opening of the interface and joint well.

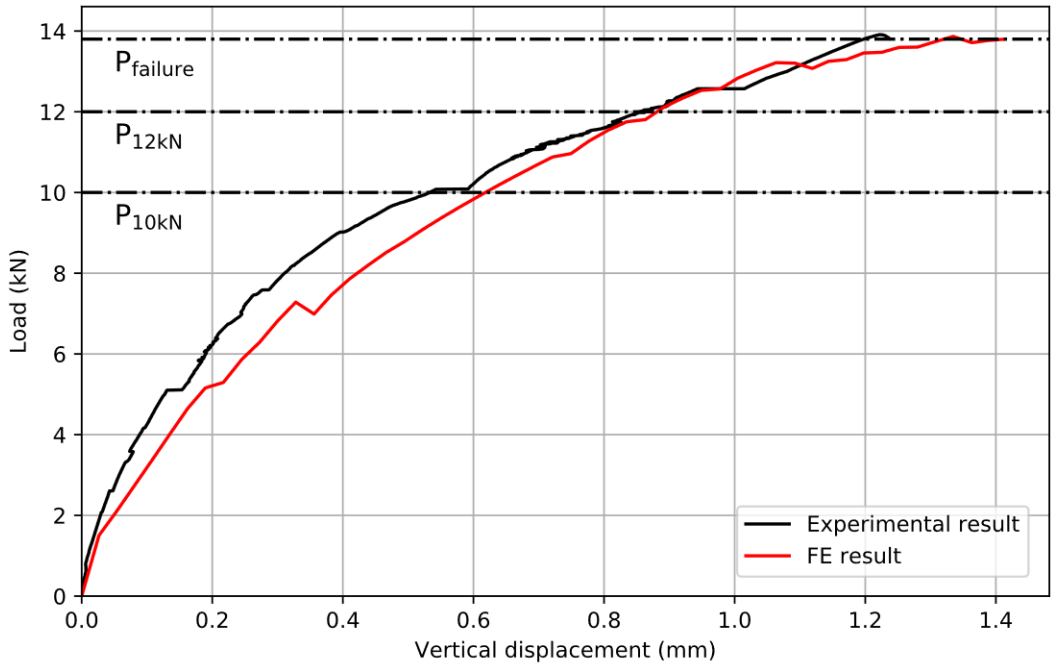

Figure 5-11: Load-displacement curve – Comparison FE and experimental results (Reference sample)

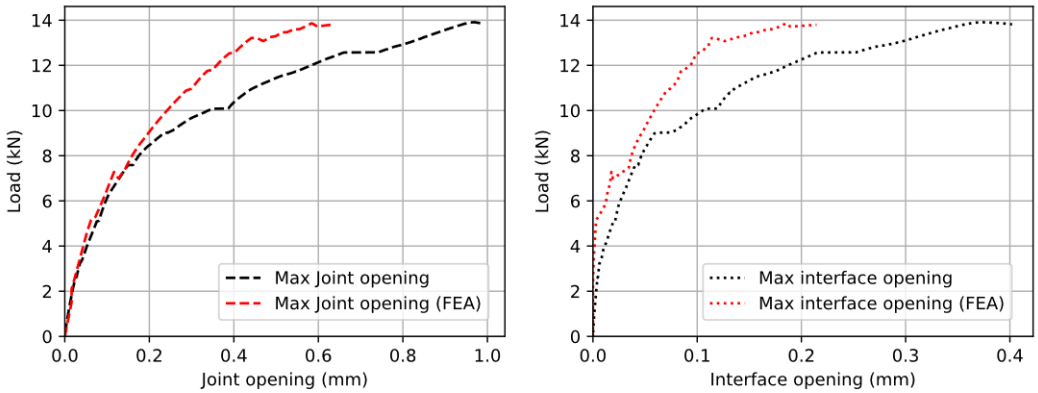

Figure 5-12: Maximum joint and interface opening – Comparison FE and experimental results (Reference sample)

The strain in x-direction of the FE model and experimental result will be compared at three different load steps (see Figure 5-11). In Figure 5-13 and Figure 5-14, a comparison between the numerical and experimental damage in the constant bending moment region is shown for the corresponding load steps. The delamination of the interface which was seen during the experiments can also be seen at the interface in the FE model based on the gap opening criteria. When the tensile strength of the interface is exceeded, the interface opens up (the FE results show normalized interface openings). As a result of this, there is no bond between the SHCC and concrete which is confirmed in both results as there are no cracks in the SHCC layer.

Furthermore, also the failure mechanism is similar between the experimental and FE results. After the interface delamination reaches the end of the coupling reinforcement, a large flexural crack appears resulting in the failure of the beam. The cracks in x-directions between the experimental and FE results are however different. The experimental result shows a greater number of cracks in the concrete top layer. Furthermore, the crack spacing and width are respectively smaller and larger in the FE results.

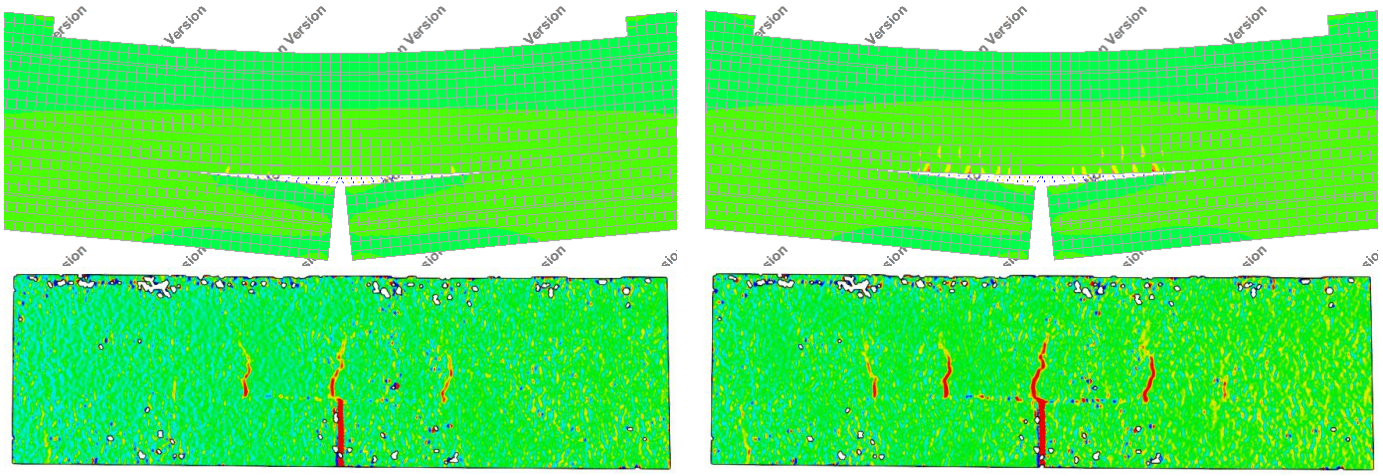

Figure 5-13: Smooth interface – Damage in experimental and numerical analysis for P = 10 kN (left) and P=12 kN (right)

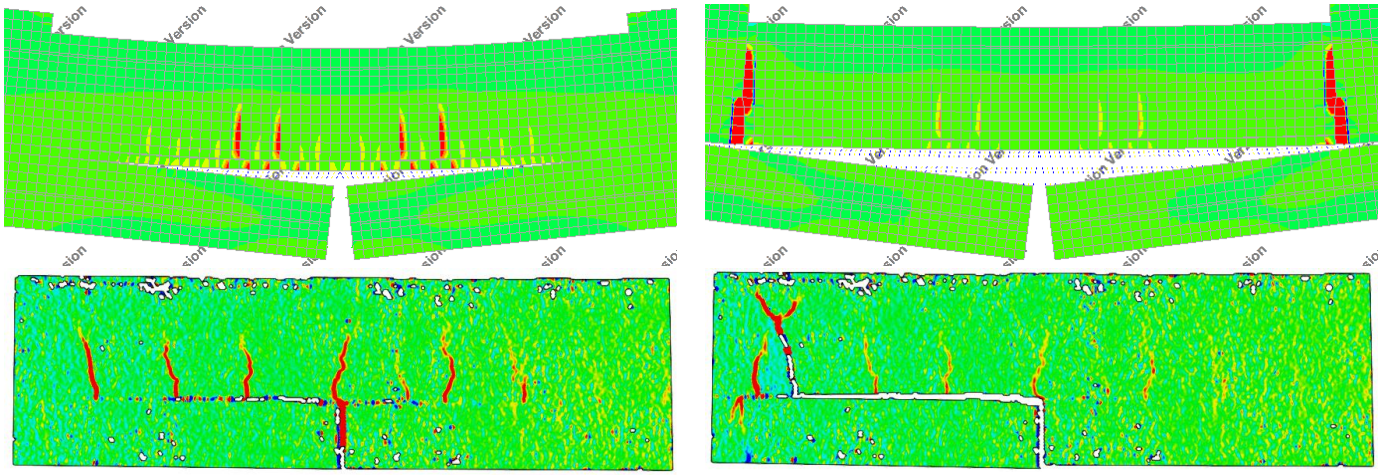

Figure 5-14: Smooth interface – Damage in experimental and numerical analysis for step before and after the failure load

The stress distribution along the interface is shown in Figure 5-15 for the first load step. The stress distribution along the interface is non-linear. However, the stresses correspond to the theory of the reinforcement eccentricity as is shown in Figure 5-16. As a result of this eccentricity, an internal moment will occur resulting in tensile stresses at the joint.

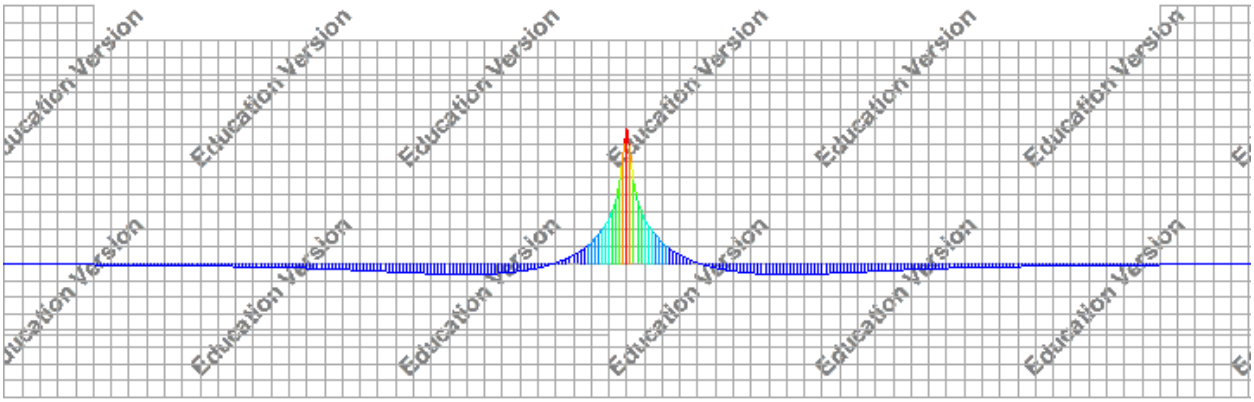

Figure 5-15: Stress distribution along the interface at the first load-step

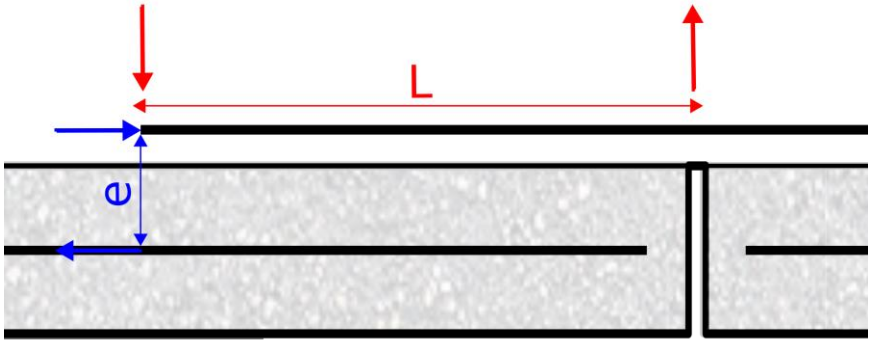

Figure 5-16: Internal moment due to reinforcement eccentricity

These results show that the Coulomb-friction model predicts the bearing capacity and failure mode well compared to the experimental results. However, the flexural cracks in the concrete top layers differ between the FE and experimental results. Based on this FE result, it is recommended to use an interface tensile strength of 0.55 MPa and shear strength of 1.1 MPa for the modelling of a smooth interface. The friction angle should be taken as 0.85 rad. In Table 5-4, the recommended values based on this analysis are shown. Furthermore, also the recommended values of the Eurocode and FIB model code are shown for smooth interfaces.

Property		Smooth interface	Eurocode	FIB model code	Unit
Interface model		Coulomb friction	–	Shear friction	MPa
Tensile strength	f_t	0.5	–	–	MPa
Cohesion	c	1	1.05	0.6	MPa
Friction angle	φ	0.85	0.6	$0.5-0.7$	Rad
Dilatancy angle	ψ	1	–	–	Rad
Normal stiffness	D_{11}	1200	–	–	N/mm^3
Shear stiffness	D_{22}	1200	–	–	N/mm^3

Table 5-4: Comparison between calibration values of FE analysis and values recommended by Eurocode and FIB code

Based on this table, a larger friction angle should be taken for a smooth interface compared to the recommended values of the FIB model code and Eurocode. The calibrated cohesion does correspond well with the Eurocode value. The value given in the FIB Model code is however nearly twice as low compared to the recommended value based on this analysis. An important aspect which has to be taken into account is that the Eurocode and FIB model code values aren't based on an interface friction model with an interface tensile cut-off.

5.3 Model 3 – Interface with epoxy and sand

The third model is based on the experimental sample with epoxy and sand on the interface. This model is based on a smooth interface similar to model of paragraph 5.2. The friction angle, interface tensile strength and stiffness will be modified to replicate the increased bond of this epoxy and sand interface. In order to obtain these increased interface bond values, a sensitivity study is done. In Figure 5-17, the influence of the interface tensile strength on the bearing capacity is shown without dilatancy (friction angle and interface stiffness are taken as the values from model 2). Furthermore, also the experimental result and the FE result with perfect bond are shown. From this result, the influence of the interface tensile strength at low values (0.5 and 1 MPA) results in a low load capacity. For an interface tensile strength of 2 MPa, the bearing capacity has increased significantly. However, increasing this tensile strength even more to 3 MPa doesn't converge further to the situation with perfect bond. Comparing these results to the experimental results, the load capacity is well predicted by having an ITS of 2-3 MPa. However, the deformation capacity is significantly lower than the results of the experiment.

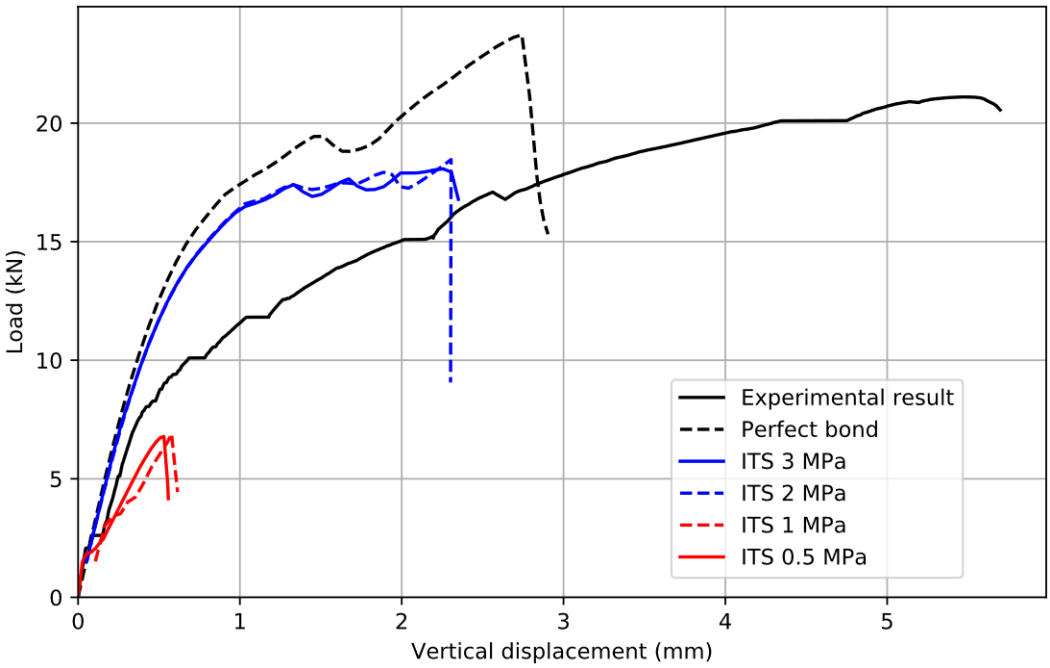

Figure 5-17: Influence of interface tensile strength (ITS)

The failure mode for these different models with varying interface tensile strength are also analyzed and are shown in Table 5-5. In this table, it can be seen that the failure of the models with an ITS of 0.5 MPa and 1 MPa occurred due to reaching the interface tensile strength which resulted in delamination of the interface. For the models with an ITS of 2 MPa and 3 MPa, the failure occurred due to a horizontal crack at the level of the coupling reinforcement. Therefore, barely any difference is seen between the results of the models with an ITS of 2 MPa and 3 MPa in terms of bearing capacity.

Interface tensile strength (ITS)	Failure mode
0.5	Delamination
1	Delamination
2	Concrete top layer
3	Concrete top layer

Table 5-5: Failure modes of the ITS sensitivity analysis

Besides the interface tensile strength, also the influence of the stiffness of the interface has been analyzed on the load capacity and displacement capacity. The interface tensile strength is taken as 2 MPa for this sensitivity analysis. The result is shown in Figure 5-18 (the stiffness in normal and shear direction are equal). Increasing the interface stiffness both in normal and shear direction with a factor 10 doesn't show any influence on the bearing capacity and displacement capacity. Similar results are also found by a reduction of the stiffness with a factor 10.

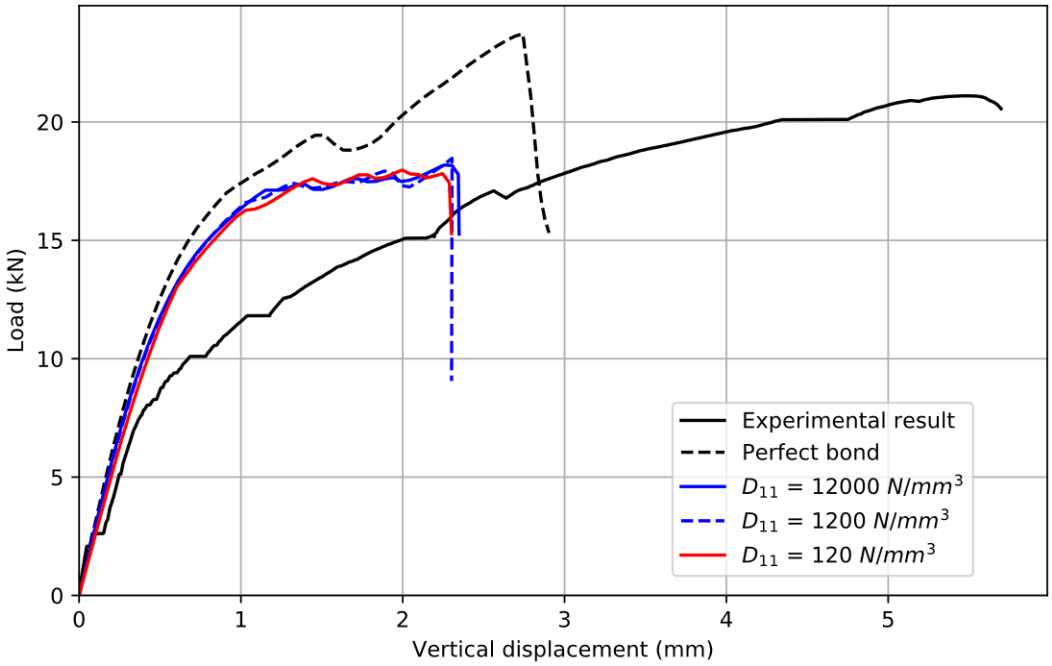

Figure 5-18: Influence interface stiffness

Based on these sensitivity analyses, it is concluded that the FE model isn't able to predict the behavior of the experimental result with epoxy and sand on the interface, based on the Coulomb friction interface model with an interface tensile cut-off. The displacement capacity is underestimated by the FE model. Therefore, it is chosen to not further elaborate on this model.

5.4 Model 4 — Profiled interface

The mesh of the model for the sample with a profiled interface was shown in Figure 4-3 (simplified as the slopes have been modelled as straight lines). Similar interface parameters of the model with a smooth interface of paragraph 5.2 are used in this model for the profiled interface (see Figure 5-19). This way the mechanical interlocking of the tooth-shaped dents will be analyzed in order to obtain a similar behavior compared to the experimental result.

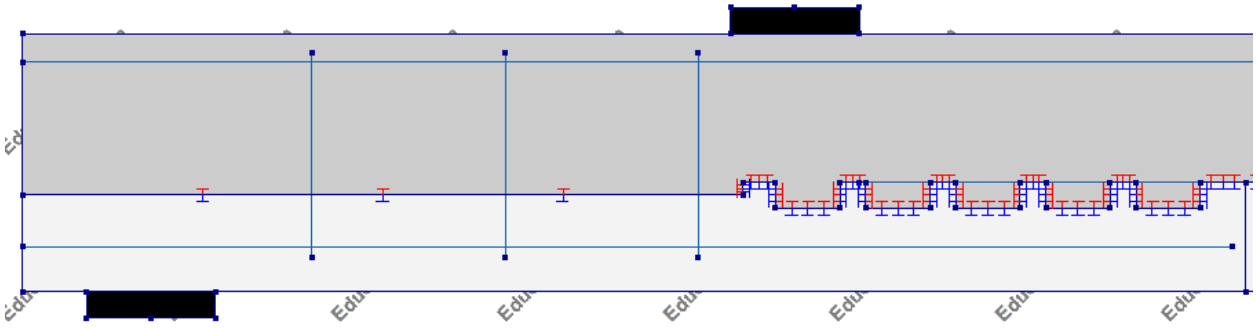

Figure 5-19: Interface following the tooth-shaped dents (only one half of the beam is shown)

In Table 5-6 the values of the interface are shown. As mentioned before, these values are similar to the parameters shown in Table 5-3.

Property		Value	Unit
Normal stiffness	D_{11}	1200	N/mm^3
Shear stiffness	D_{22}	1200	N/mm^3
Cohesion		1.2	MPa
Friction angle		0.85	rad
Dilatancy angle		0(1)	rad
Tensile strength	f_t	0.6	MPa

Table 5-6: Profiled interface – Calibrated interface properties

Similarly, to the model with a smooth interface, a comparison is made between the FE results with and without dilatancy (see Figure 5-20). Also, for this case, the dilatancy results in a higher capacity which corresponds better to the experimental results. However, compared to the results of the model with a smooth interface, the influence of the dilatancy angle on the bearing capacity is less significant. This can be explained by the fact that the mechanical locking of the profiled interface already helps at preventing the interface delamination as a result of the interlocking shear mechanism. Thus, the analysis of this model will be continued using the dilatancy angle.

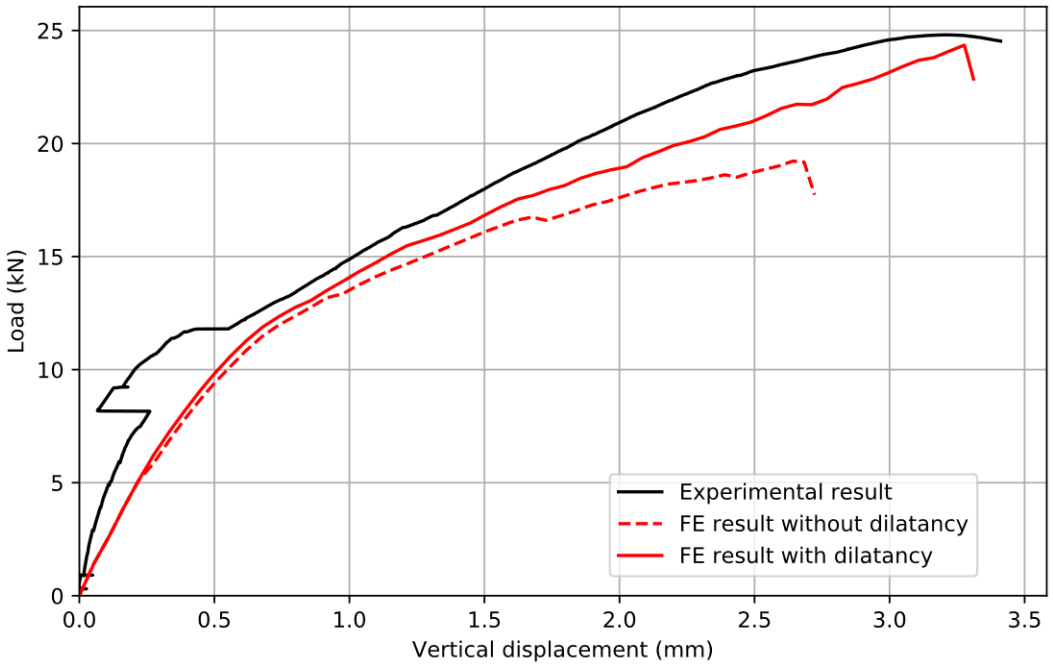

Figure 5-20: Profiled interface – Effect of dilatancy

Figure 5-21 shows the load-displacement curve of both the experimental and numerical results of the profiled sample for the case with dilatancy. The initial response of the finite element corresponds well with the experimental response. However, as the load increases the response starts to differ. This is most likely because initially the response is based on a bonded interface. As the load increases the top parts of the profiled interface start to delaminate while at the dents the concrete cracks at the reinforcement level (see Figure 5-26). The flat parts of the profiled interface did however not delaminate during the experiments (see Figure 3-130).

In Figure 5-22, the interface and joint opening are compared. The results of the joint opening do correspond well with the experimental results. The interface opening initially has a stiffer response, but as the load increases the results become similar. These results show that the way the interface has been modelled is promising.

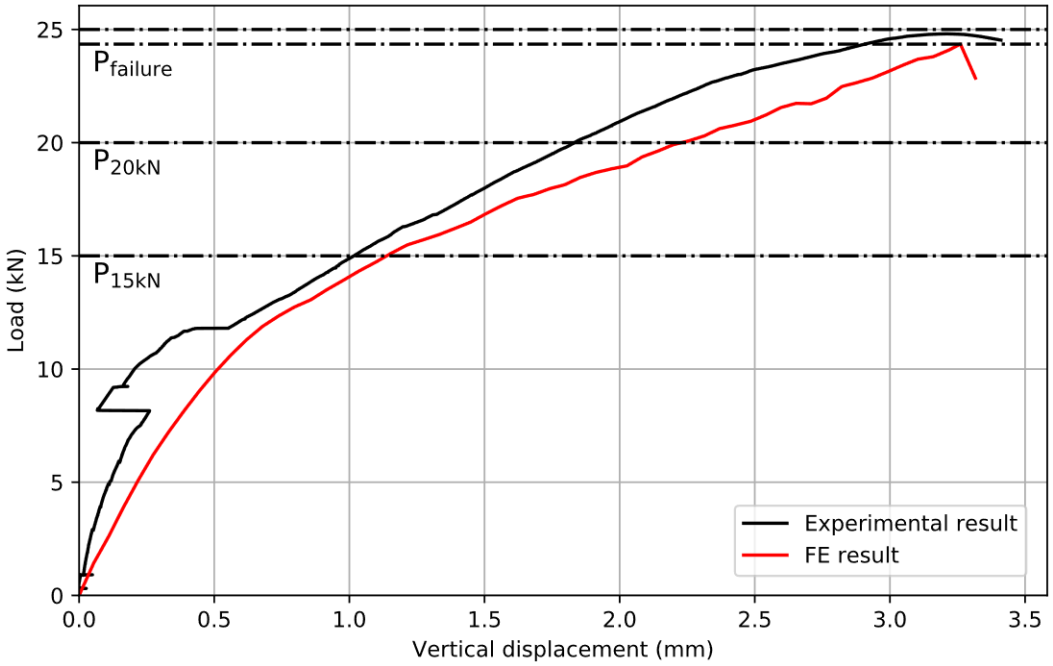

Figure 5-21: Load-displacement curve – Comparison FE and experimental results (Profiled sample)

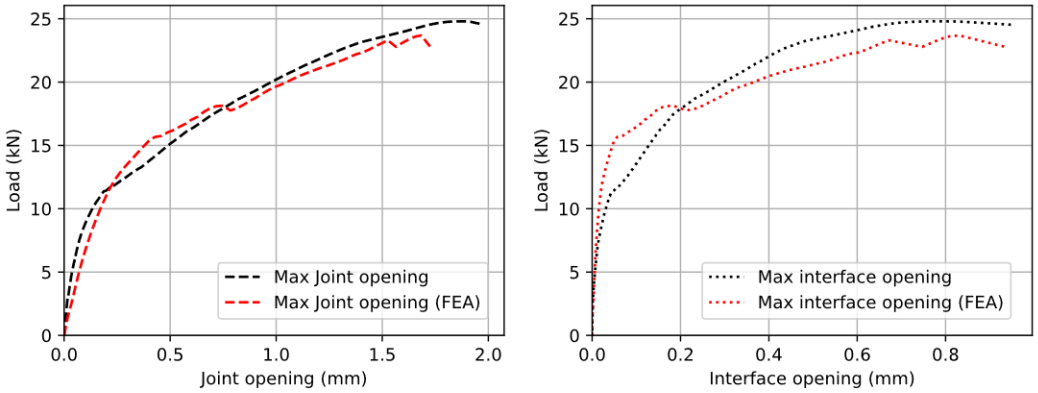

Figure 5-22: Maximum joint and interface opening – Comparison FE and experimental results (Profiled interface)

Figure 5-23 and Figure 5-24 show the strain in x-direction for various load steps shown in Figure 5-21. The strain distribution in the concrete top layer is similar between the experimental and numerical analysis. Furthermore, due to the mechanical interlocking between the SHCC and concrete layers, several cracks are shown in the SHCC layer in both analyses. The flexural cracks in the SHCC aren't visible in the FE results. This is caused by the limiting material models to replicate the multiple cracking behavior of the SHCC. However, a user-defined stress and strain relationship have been given as input for the SHCC (see Figure 4-7). Therefore, even if the material model isn't able to replace the multiple cracking behavior, the crack strains should be visible. These cracking strains are shown in Figure 5-25. In this figure, we can see the

large horizontal crack strain and flexural strain in the concrete top layer. Furthermore, the crack strains in the SHCC are also shown despite the fact that they are not visible in Figure 5-23 and Figure 5-24.

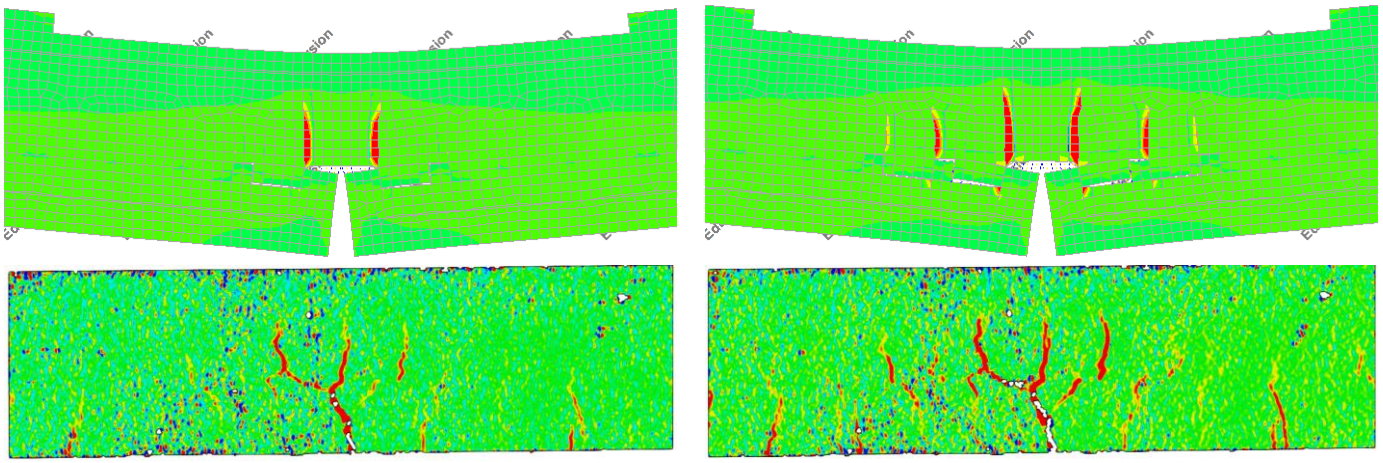

Figure 5-23:Profiled interface – Damage in experimental and numerical analysis for P = 15 kN (left) and P=20 kN (right)

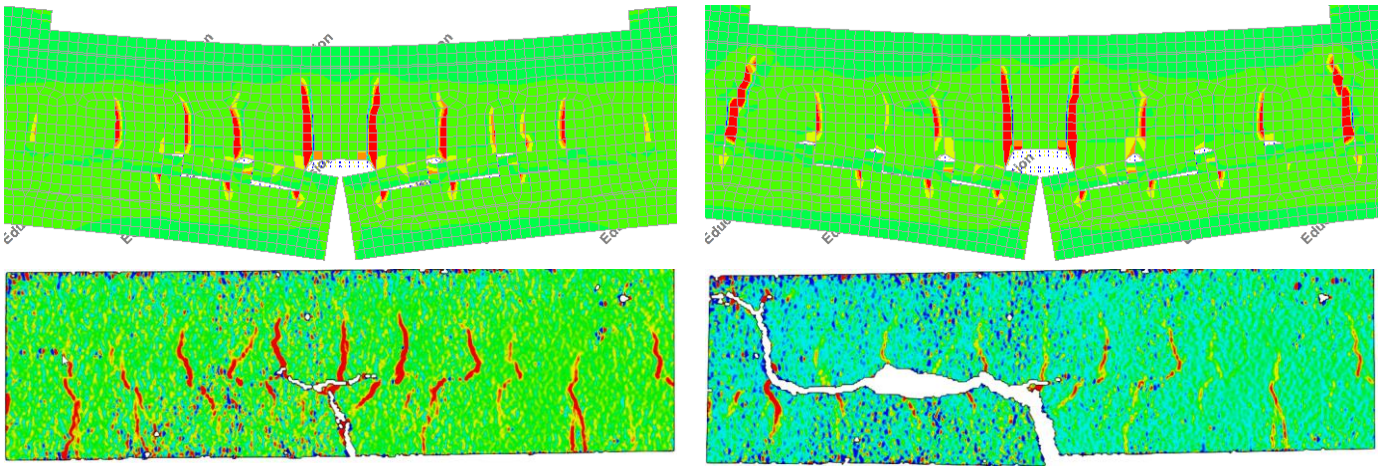

Figure 5-24: Profiled interface – Damage in experimental and numerical analysis for step before and after the failure load

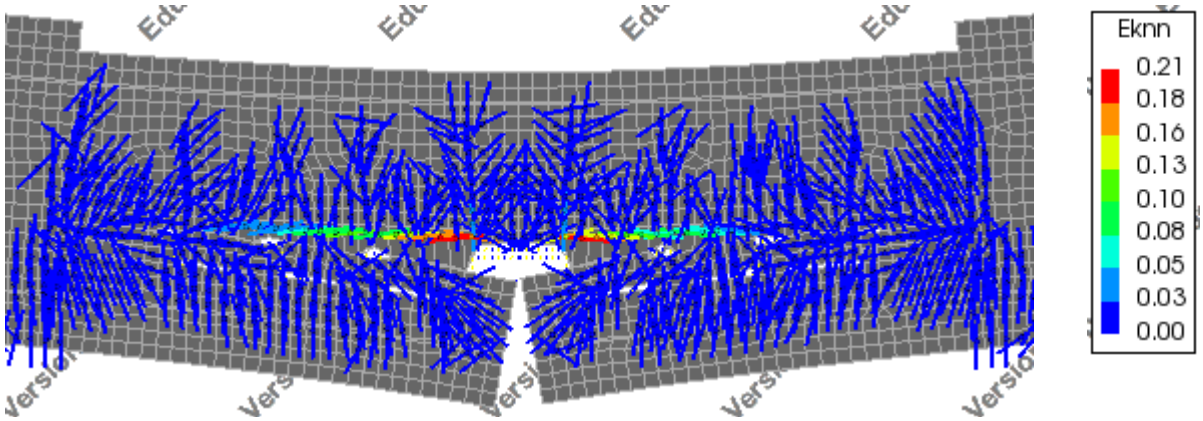

Figure 5-25: Crack strains in the constant bending moment region

In Figure 5-26 the delamination at the interface is shown. As a result of the mechanical interlocking of the profiled interface, delamination of the dents doesn't occur. Instead, a large horizontal crack starts to propagate as the tensile capacity of the concrete is exceeded.

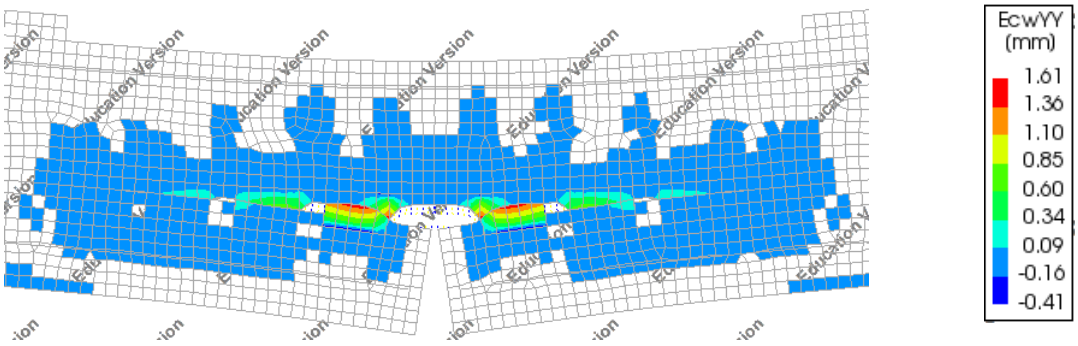

Figure 5-26: Delamination and cracking at the interface

The reason for this large crack in y-direction was explained in paragraph 3.6.2 using a strut-and-tie model (STM). In Figure 5-27, the STM is again shown for the beam with a smooth interface (the same principle is valid for a rough interface). In this vertical tension tie at the joint, the largest stress is found at the level of the coupling reinforcement.

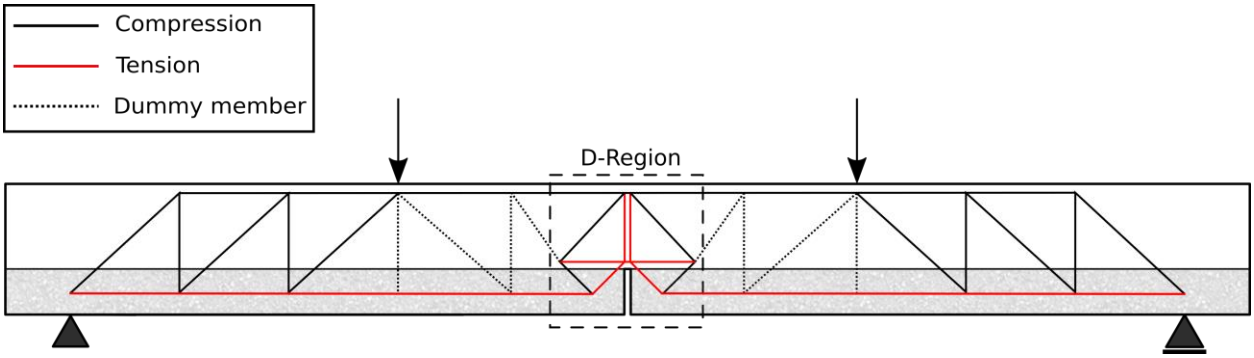

Figure 5-27: Strut-and-tie model of the stress distribution in the beam

This STM is validated for this model by looking at the in-plane principal components of the stresses during the finite element analysis (see Figure 5-28). In this figure, the transfer of the forces from the bottom reinforcement to the coupling reinforcement by vertical tensile stresses is clearly seen at the joint. As a result of this, large horizontal cracks appear as the concrete strength is exceeded. This force transfer mechanism is shifted as the interface delaminates which results in the crack propagations until the end of the coupling reinforcement is reached.

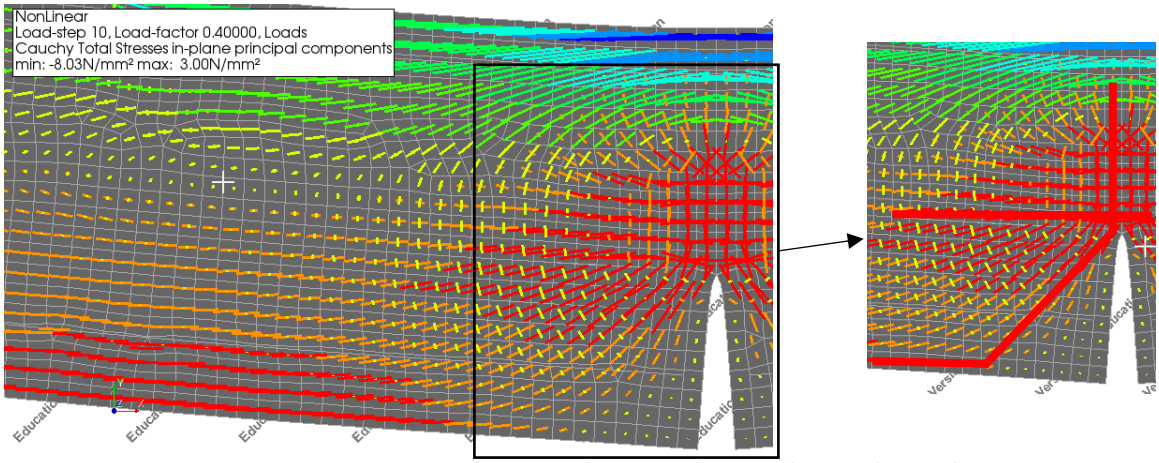

Figure 5-28: Stress trajectories at the joint with a zoomed section showing the tensile trajectories

In order to better understand the way the stresses are distributed along this vertical tensile tie for the profiled sample, the position of the coupling reinforcement is shifted upwards. The horizontal crack for this case is shown in Figure 5-29. The crack is again located at the level of the coupling reinforcement. This shows that the localization of stresses is at the level of the coupling reinforcement.

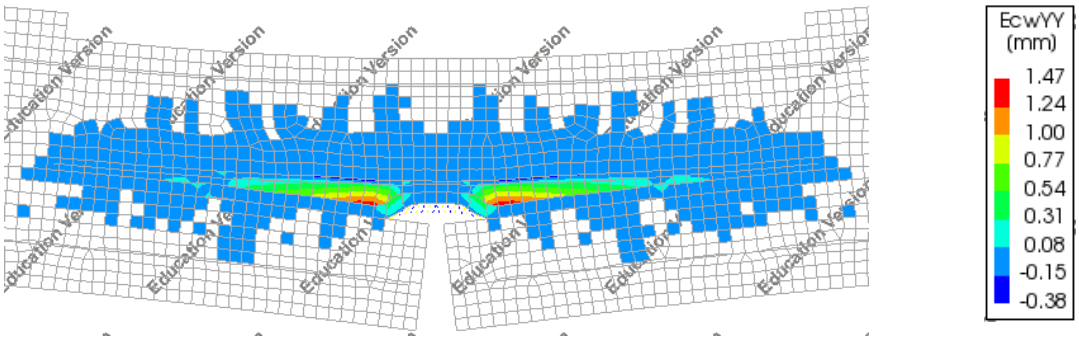

Figure 5-29: Delamination and cracking at the interface with different position of the coupling reinforcement

At several interface nodes, the stress combination will be analyzed with respect to the Mohr-Coulomb failure envelope. These nodes are the interface node at the joint and the bottom corner nodes of the first profiled shape (see Figure 5-30). For nodes B and C, the stresses on both the horizontal and vertical parts will be analyzed.

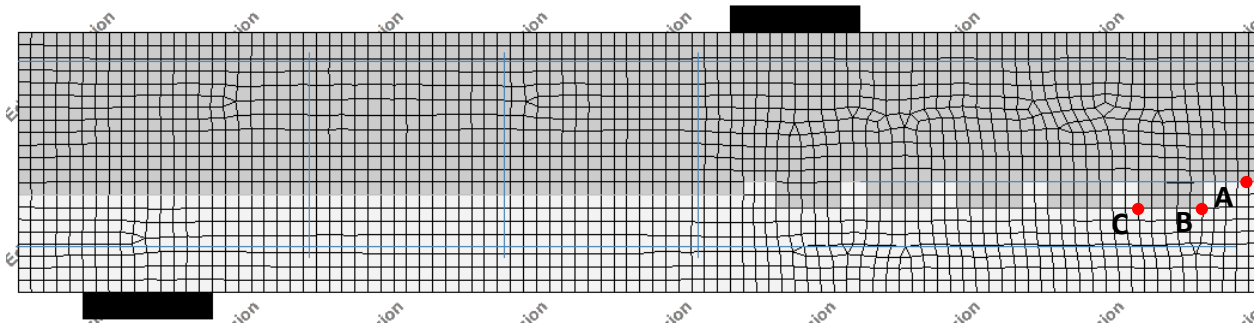

Figure 5-30: Profiled interface – Locations of nodes for analyzing the failure modes

In Figure 5-32, the tensile and shear stress combination for the three interface nodes are shown (at the horizontal part of the dent). Node A fails due to the exceedance of the interface tensile strength (vertical cut-off line). A similar failure mode happens for node B as it delaminates (small opening) as a result of the perpendicular tensile stresses at the interface. Node C initially also had a tensile stress due to the eccentricity of the reinforcement bars. However, the mechanical interlocking of the profiled interface prevented the progression of this initial delamination at the midspan joint. This mechanical interlocking effect attributed to the compressive and shear stresses at node C.

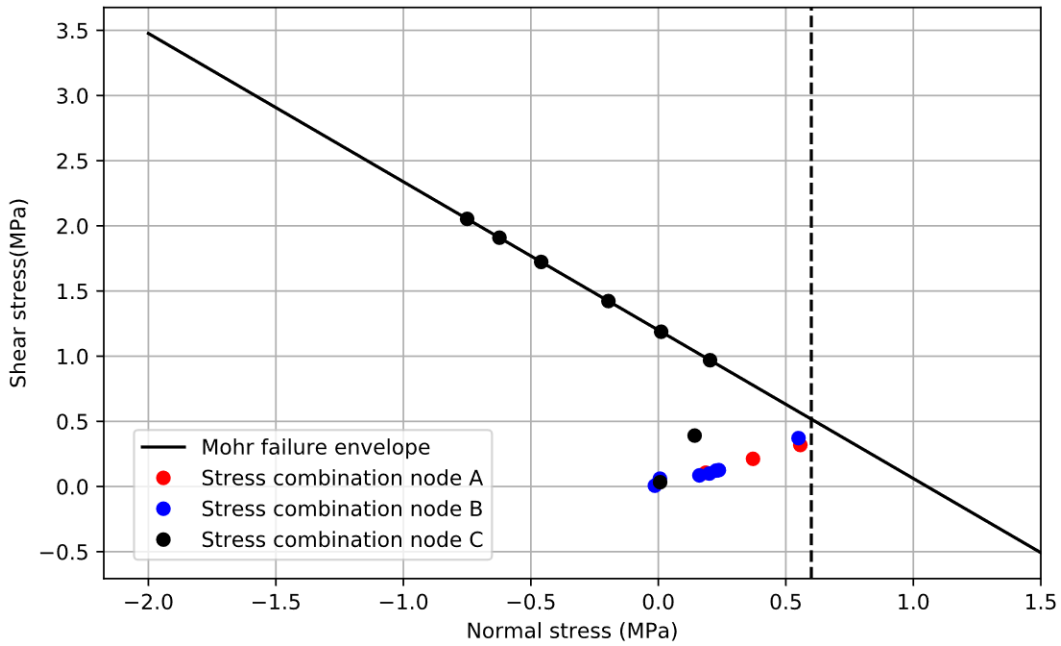

Figure 5-31: Failure modes of nodes A, B and C on the horizontal parts

The effect of the mechanical interlocking can be analyzed by looking at the normal and shear stresses for nodes B and C at the vertical part of the dents (see Figure 5-32). As a result of the mechanical interlocking, normal stresses occur opposite to the direction of the shear stresses at the smooth interface of node A. This is seen in the stress combination for node B. For this node, the failure happens by reaching the Mohr-Coulomb failure envelope at a large shear stress. For node C, an opposite stress state to node B has to happen. This is seen in Figure 5-32, as in this case tensile stresses occur instead of compressive stresses. The failure of this node occurred by reaching the interface tensile strength.

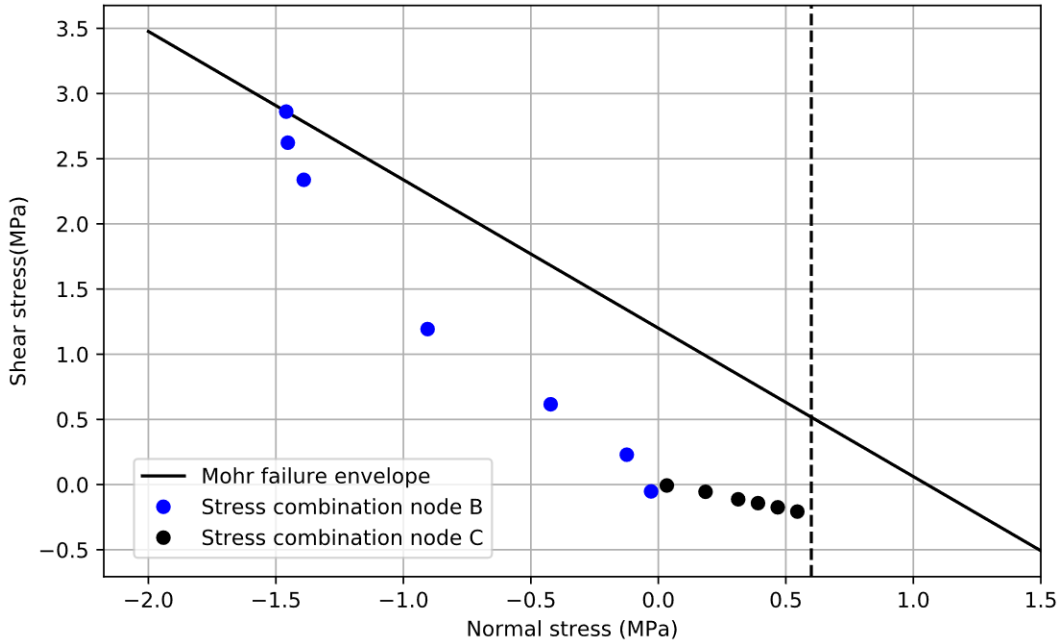

Figure 5-32: Failure modes of nodes B and C on the vertical part

While these results show good correspondence with the experimental results, the modelling can become quite time-consuming for larger structures or 3D models. Therefore, a model with a smooth interface is made to replicate the interfacial behavior of the profiled interface. While the mechanical interlocking at the interface can't be modelled, the interface tensile and shear strength can be adjusted to correspond to the experimental results.

In Figure 5-33, a comparison is shown between the experimental result and two FE models. One FE model consists of a Coulomb friction interface with an interface tensile strength (ITS) equal to the concrete strength. This choice is based on the experimental result as no delamination occurred. The other model is based on a perfect bond at the interface, identical to the model of paragraph 5.1. Based on the load-displacement graphs, a better correspondence between the experimental and numerical result is found in case the interface is modelled as perfect bond. The load capacity is however slightly lower.

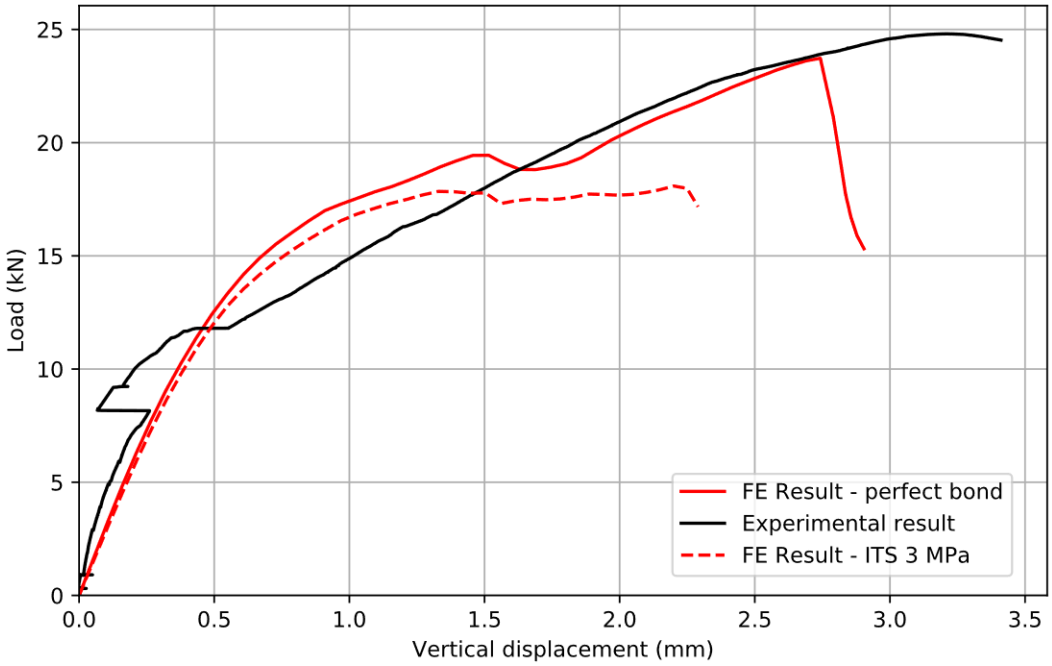

Figure 5-33: Comparison experimental result with models with smooth interface

For the FE model with perfect bond, the strains in x-direction and y-direction is shown for the load-step before failure in Figure 5-34. Comparing this result with the results shown in Figure 5-24, the flexural crack at midspan is now also visible (as there is no delamination at the joint). This also occurred during the experiment. The failure of this sample happened due to the horizontal crack along the coupling reinforcement which is supported by the concrete strain in y-direction.

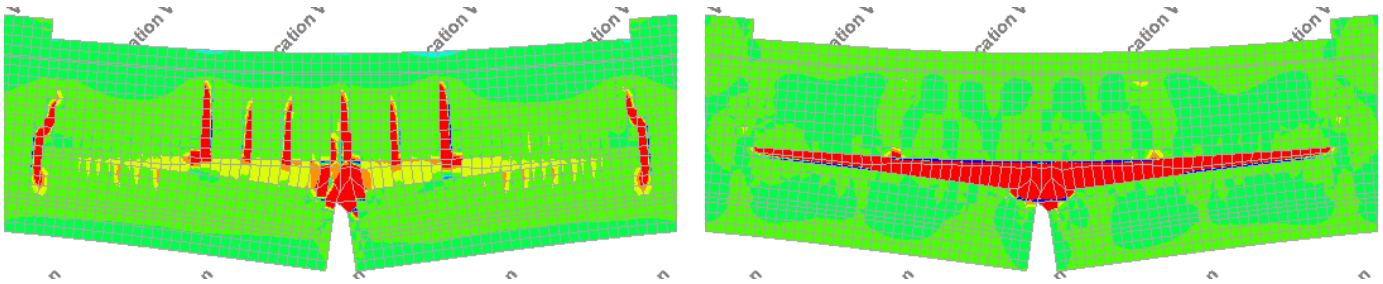

Figure 5-34: Concrete strain in x-direction (left) and y-direction (right) before failure

5.5 Model 5 – Protruding reinforcement

The influence of protruding reinforcement nearby the joint for a model with a weak interface is investigated. The location of the stirrups corresponds to the experimental study where the stirrups were placed at a distance 50 mm from the joint. However, for the experimental analysis, the sample was damaged prior to testing as it was cured outside the mould in a humidity-controlled room. Therefore, the point of this study is to analyze the failure mechanism to help understand the experimental result. The interface properties are based on the results of model 2 (see Table 5-7).

Property		Value	Unit
Normal stiffness	D_{11}	1200	N/mm^3
Shear stiffness	D_{22}	1200	N/mm^3
Cohesion		1.2	MPa
Friction angle		0.85	rad
Dilatancy angle		0 (1)	rad
Tensile strength	f_t	0.6	MPa

Table 5-7: Calibrated interface properties

In Figure 5-35 and Figure 5-36, the results are shown for both the FE and experimental results. The capacity of both results is roughly the same. However, the stiffness of the FE results is lower than the experimental results. Furthermore, also the deformation capacity of the results is significantly different. The interface opening and joint opening are however similar. This is because the interface and joint opening are independent on the deformation capacity of the sample. As was mentioned before, the point of this study is not to obtain similar result between the experiment and numerical analysis, but to investigate the damage of the sample.

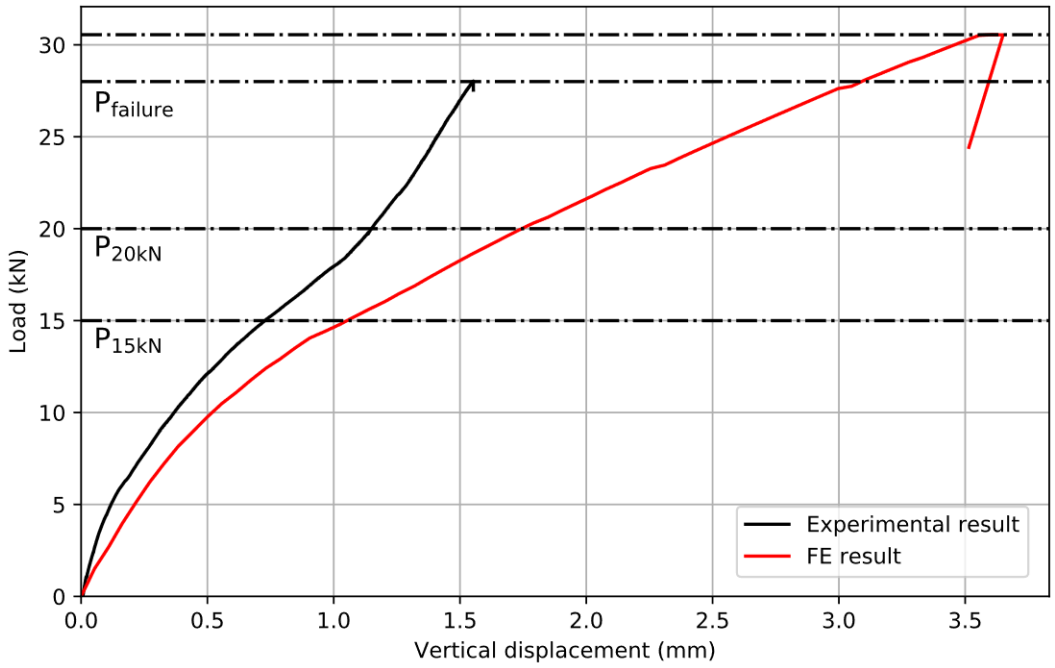

Figure 5-35: Load-displacement curve – Comparison FE and experimental results (Stirrup sample)

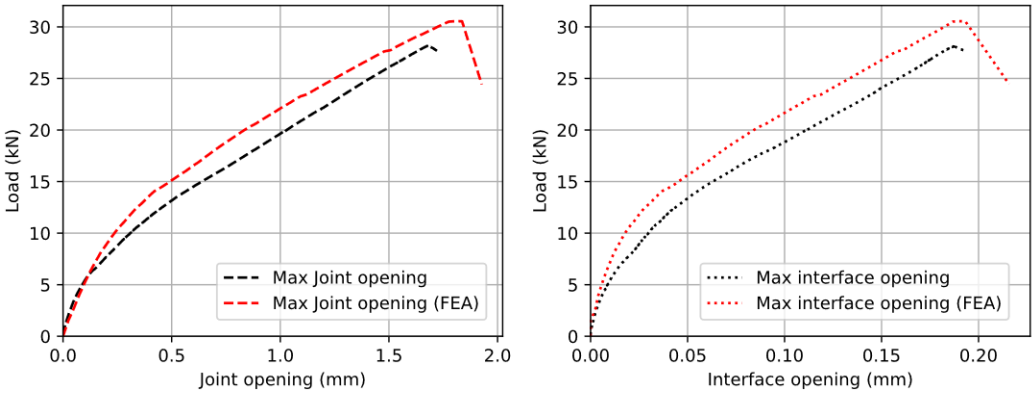

Figure 5-36: Maximum joint and interface opening – Comparison FE and experimental results (Stirrup sample)

The failure of this model was caused by the delamination of the interface. As a result of this delamination, also tensile cracks occurred at the location of the stirrup on the top part of the SHCC. This was also seen during the experiment as a large vertical crack occurred at the end of the coupling reinforcement due to delamination of the interface. Furthermore, also the concrete surrounding the stirrups cracked at the top part of the SHCC. This was seen in the DIC results and strain measurement of the strain gauges. A large strain jump occurred in the strain gauge while in the DIC result the tensile strain in the concrete is visible. This exact failure mode also happens in the FE model as is shown in Figure 5-37 and Figure 5-38.

In these figures, the concrete strain in x-direction is shown based on the experimental DIC result and FE result. These images correspond to the load steps in Figure 5-35. The flexural crack at the end of the coupling reinforcement and fracture around the stirrup at the top part of the SHCC layer are similar for both results. Furthermore, also the number of flexural cracks in the concrete top layer corresponds which each other (the crack spacing isn't similar). However, the flexural cracks in the SHCC aren't visible in the FE analysis which was also the case for the profiled interface model. This is caused by the limited material models in DIANA FEA to replicate the strain-hardening behavior of SHCC.

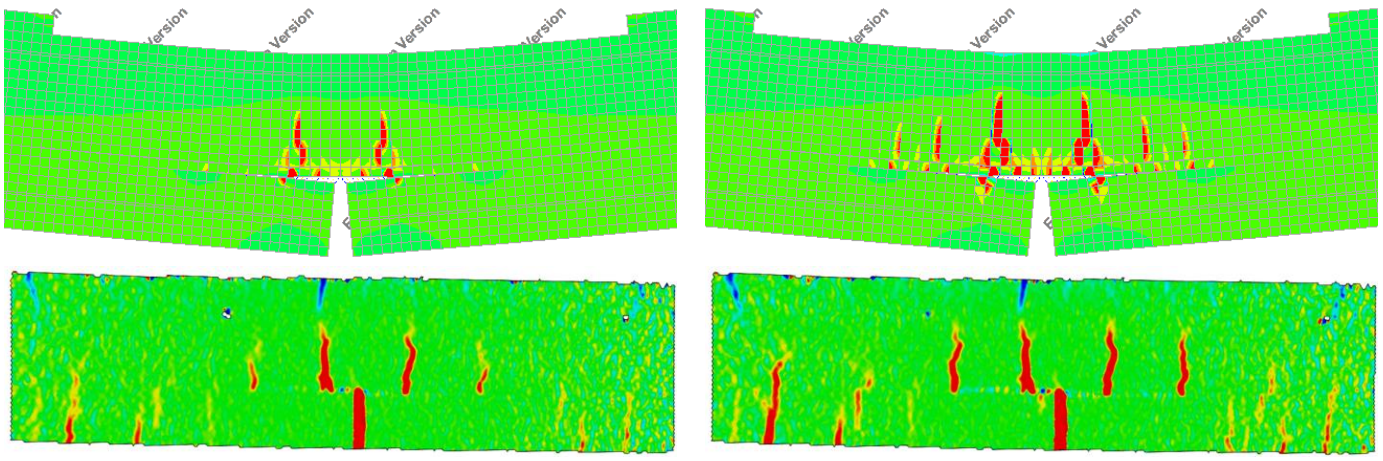

Figure 5-37: Stirrups – Damage in experimental and numerical analysis for P = 15 kN (left) and P= 20 kN (right)

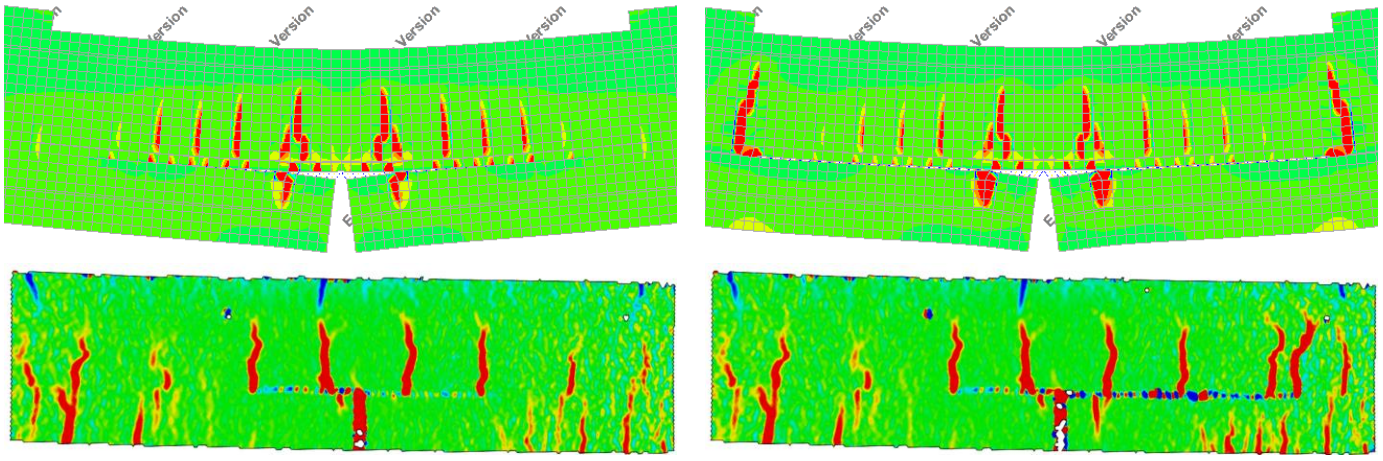

Figure 5-38: Stirrups – Damage in experimental and numerical analysis for step before and after the failure load

This failure of the concrete at the top part of the SHCC at the location of the stirrup is a result of the rotational restraint. This was already discussed in paragraph 3.6.1. The principal stress trajectories will be analyzed to see whether it supports this theory (see Figure 5-39). In this figure, the stress trajectories at the bottom of the SHCC layer are shown. However, at the location of the stirrup, the stresses are redirected to the top layer of the SHCC layer as a result of the rotation restraint of the protruding reinforcement (red lines in the zoomed section). Furthermore, also the compressive strains are visible due to the dowel action (black line in zoomed section). This dowel action introduces compressive support action as is shown in Figure 5-40.

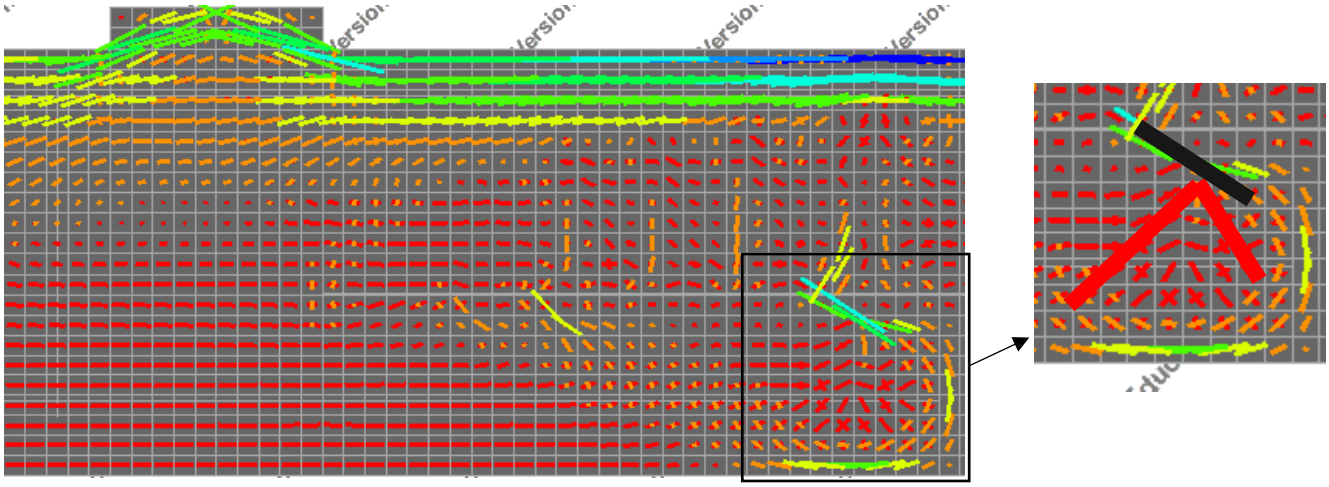

Figure 5-39: Stress trajectories before failure of the model

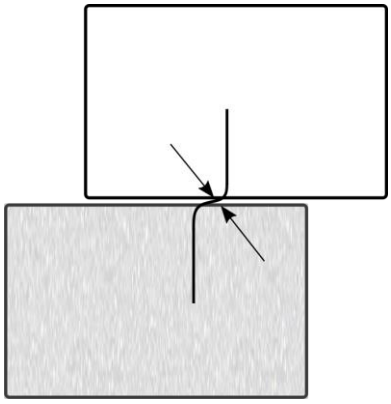

Figure 5-40: Compressive forces due to dowel action

The stress combinations will also be analyzed at several interface nodes. These are located at the midspan joint, protruding reinforcement and at a distance of 200 mm away from the joint (see Figure 5-41).

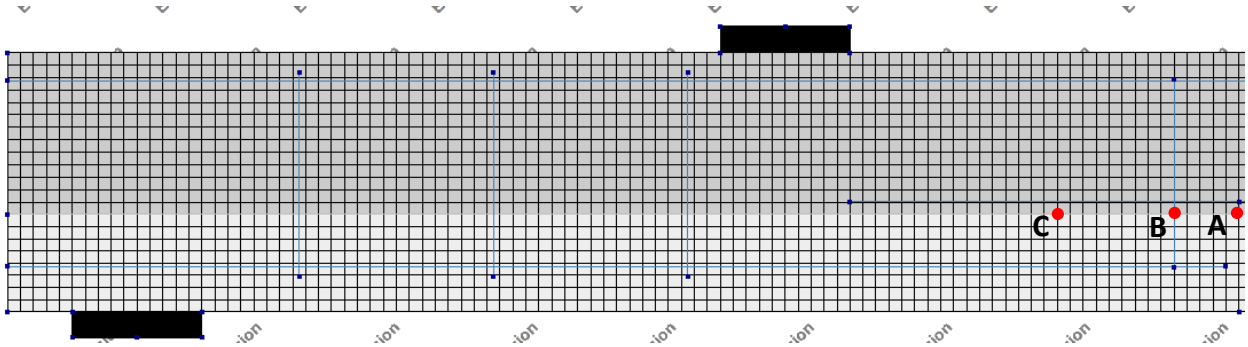

Figure 5-41: Protruding reinforcement – Location of nodes for analyzing stress combination

The stress combination of the FE analysis for the corresponding interface nodes is shown in Figure 5-42. Node A has a similar failure mode compared to model 2 and model 4. This node failed in tension as a result of the reinforcement eccentricity. Node B is at the location of the protruding reinforcement. Therefore, no interface stresses are visible as the stirrup is taking these stresses and preventing the opening of the interface. Node C is located close to the end of the coupling reinforcement. Initially, node C is in compression by the reinforcement eccentricity stress distribution along the interface. However, as the interface delamination progressed along this interface, tensile stresses started to occur at this location. Eventually, this node also failed due to reaching the interface tensile strength.

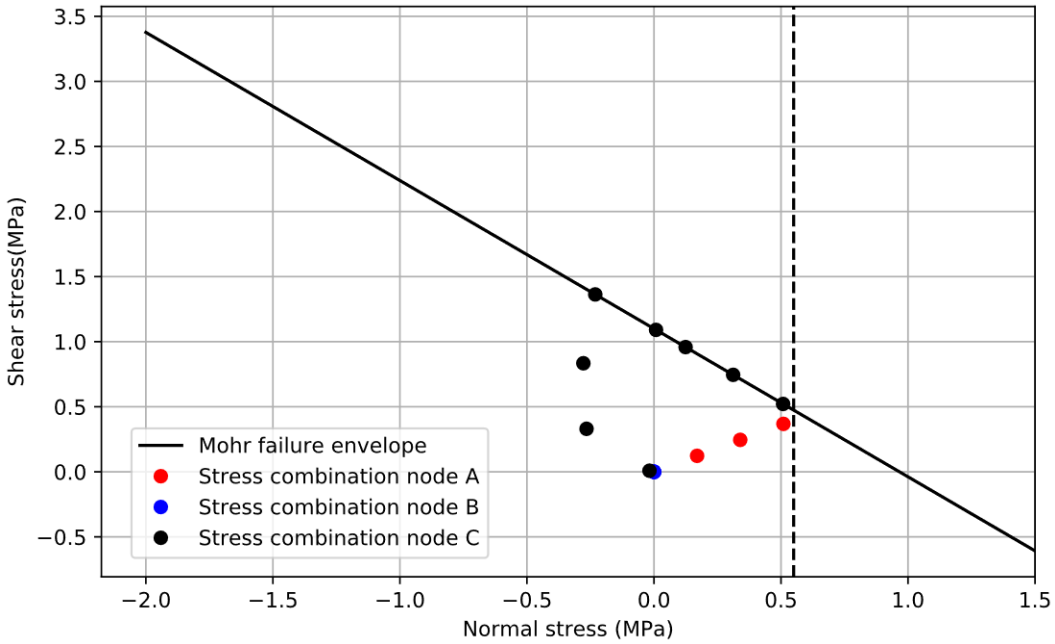

Figure 5-42: Stress combination for nodes A, B and C

A final analysis is done to see whether yielding can be obtained by increasing the interface tensile and shear strength of the interface. The tensile strength and cohesion are increased to 2 MPa and 4 MPa respectively while the remaining parameters are kept similar to the values in Table 5-7.

The load-displacement graph is shown in Figure 5-43. In this figure, also the result of the model with a weak interface is shown. The model with an increased tensile strength shows increased capacity resulting in yielding of the coupling reinforcement. As a result of this, the deformation capacity of the beam increases significantly. The failure mode is based on a flexural failure as is shown in Figure 5-44. Also, the principal crack-width of the sample with a weak interface is shown in Figure 5-44. In this figure, the delamination is visible with a vertical crack at the end of the coupling reinforcement. This resulted also in a concrete fracture around the stirrups. These results show that in order to achieve yielding of these hybrid systems, the bond of the interface has to be increased to prevent delamination. Furthermore, stirrups are needed to prevent horizontal cracking in the top concrete layer.

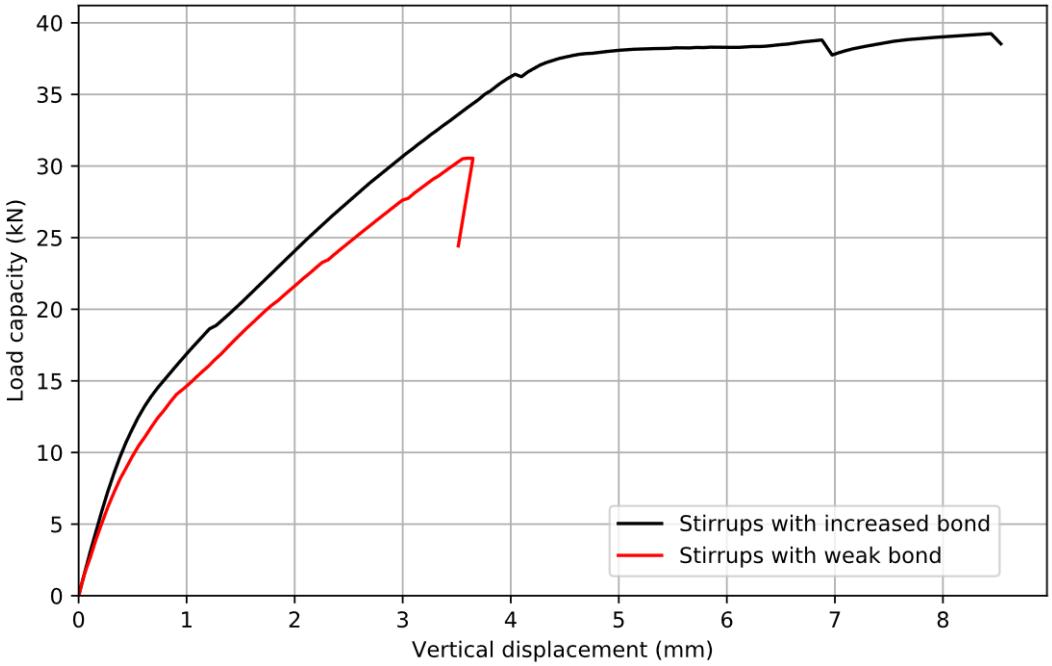

Figure 5-43: Comparison of model 5 with weak and strong bond

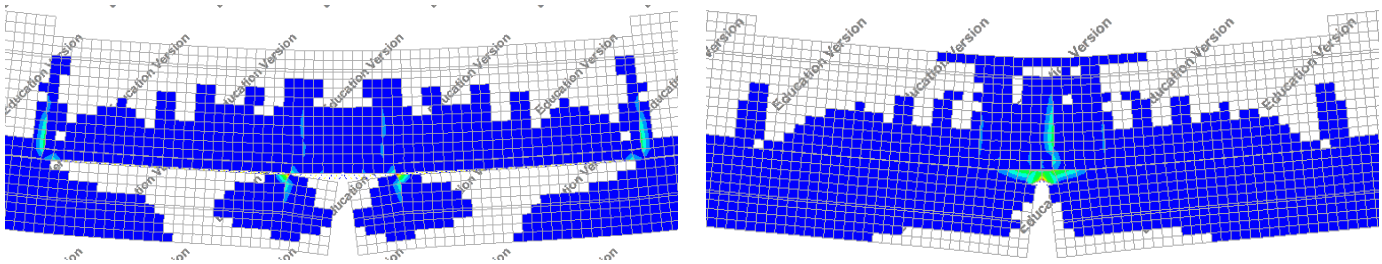

Figure 5-44: Principal cracking of the model with a weak (left) and strong interface (right)

6 Conclusions and Recommendations

6.1 Conclusions

As was mentioned in paragraph 1.2, the objective of this study was to investigate the interfacial behavior of hybrid SHCC-concrete beams for several governing parameters. This is done by investigating the effect of the interface roughness, reinforcement cover, curing method and protruding reinforcement on the interfacial behavior of these hybrid beams. Four-point bending tests are performed to obtain a constant-bending moment region. In this region, the crack propagation, interface opening and joint opening are studied for various load steps.

The reference sample consisted of a smooth interface between the SHCC and concrete layers. This sample exhibited weak interfacial behavior. As a result of this weak bond at the interface, no cracks were visible in the SHCC layer. This is attributed to the early debonding of the interface which prevented the composite action of this hybrid SHCC-concrete beam. The failure of the samples was caused by the delamination of the interface until the end of the coupling reinforcement. At this location, a large flexural crack appeared as there is no reinforcement available. The load capacity of this beam was 13.9 kN which is roughly $\frac{1}{3}$ of the expected capacity of this hybrid system in case a flexural failure occurs.

The influence of the interface roughness has been investigated for three samples. These are the samples with a profiled interface, holed interface and an interface with epoxy and (rough) sand. From the test results, it is observed that for these samples the load-bearing capacity increased significantly. However, the load capacities were still lower than the calculated capacity based on yielding of the coupling reinforcement.

How does the profile at the contact area influence the interface behavior and how is this reflected in the cracking pattern? The profiled interface sample has an increased interfacial behavior due to the mechanical interlocking in the constant bending moment region. As a result of this mechanical interlocking, shear stresses occur at the interface. Consequently, the delamination failure of the sample was prevented. Crack propagation from the SHCC to the concrete layer is observed. The failure of the sample was caused by a large horizontal crack at the level of the reinforcement. This can be explained by the perpendicular tensile stresses generated based on the transfer of forces from the tensile reinforcement in the SHCC to the coupling reinforcement.

The sample with holes also showed an improved interfacial behavior resulting from the mechanical interlocking at the holes. This was observed during the test by several flexural cracks in the SHCC and concrete top layer at the location of these holes. The load capacity of this sample was however lower than the sample with the profiled interface. The failure mechanism of the beam was also similar to the samples with a smooth interface as also for this sample delamination was the decisive failure mode with concrete cracking at the location of the holes.

For one sample, instead of modifying the roughness of the SHCC when it is still in a wet state, the roughness of the SHCC has been increased in its hardened state. This is done by applying epoxy and sand on the SHCC before casting the concrete top layer. As a result of the increased roughness at the interface, the bond between the SHCC and concrete is improved. This is shown in terms of an increased bearing capacity and a reduction of the interface opening. Furthermore, also the crack propagation of the samples shows the improved composite action of the SHCC and concrete (cracks in the SHCC). The failure mode of

this sample was caused by a horizontal crack at the coupling reinforcement as a result of the perpendicular tensile stresses.

Besides the influence of the interface roughness, also several samples have been investigated with a smooth interface. This is done to determine the influence of the reinforcement cover, curing method and protruding reinforcement on the interfacial behavior of these hybrid SHCC-concrete beams.

How does the cover of the coupling reinforcement influence the interfacial behavior? The influence of the cover of the coupling reinforcement was investigated for one sample. The coupling reinforcement was directly placed on top of the SHCC layer to investigate the effect of the concrete-steel bond on the interfacial behavior. The results showed that having the coupling reinforcement directly on top of the SHCC layer had no significant effect. Identical to the sample with a smooth interface, the failure occurred due to the delamination of the interface. However, an important aspect that should be taken into account is that the stresses in the coupling reinforcement were relatively low compared to the steel stresses which would occur in case yielding of the samples would have occurred.

What is the influence of the curing method on the interfacial behavior? For one sample a different curing method was done to investigate the effect of shrinkage. Instead of letting the samples dry in the mould covered by plastic sheets, the sample was placed in a humidity-controlled room (RH 50%). Several shrinkage cracks were visible in the SHCC layer and at the interface before testing the samples. As a result of this, the stiffness of the sample reduced which was measured by the LVDTs in terms of the reduced initial slope of the load-displacement curve. The load capacity of the beam did however remain the same which indicates that the visible damage was mainly surface cracks. This is attributed to the restraint of the reinforcement in the SHCC layer.

How does protruding reinforcement at the joint influence the interfacial behavior? The influence of protruding reinforcement through the interface has been investigated for one sample. Two stirrups were placed on each side of the joint at a distance of 50 mm to take up the perpendicular tensile forces. The experimental results showed an increased bearing capacity and reduced interface opening. The failure mode was caused by the delamination of the interface (note that the sample was also damaged prior to testing as it was placed in a humidity-controlled room). As a result of this delamination, also concrete fracture at the location of the stirrups occurred. The result showed that the influence of stirrups for this configuration doesn't prevent delamination, but only prevent the fast progression of the interface failure. Also, for this sample no yielding of the coupling reinforcement occurred.

One of the research questions stated that inverse modelling would be done to determine the interface tensile and shear strength for future modelling purposes of these hybrid SHCC-concrete beams. The inverse modelling has been done for two samples. These are the sample with a smooth interface and the sample with a profiled interface. The sample with epoxy and sand at the interface has also been modelled, however the Coulomb friction model with an interface tensile strength cut-off didn't lead to satisfactory results.

What are the tensile and shear capacity of the concrete-to-concrete interface based on inverse modelling? The first model which was based on a sample from the experimental analysis was the FE model with a smooth interface (model 2). The FE result shows good correspondence with the experimental result in terms of bearing capacity and displacement capacity when dilation was included for the interface. Furthermore, also the failure mode corresponds with each other as in both cases delamination of the interface occurred up until the end of the coupling reinforcement. However, the

interface and joint opening are out of range compared to the one measured with LVDTs during the experiment. Furthermore, also the flexural cracking in the SHCC and concrete differ between the FE analysis and experimental analysis. It seems that the Coulomb friction model isn't sufficient to replicate the crack propagation in the concrete and SHCC for samples where brittle interface failure is decisive. Based on this model, an interface tensile strength and shear strength of 0.5 MPa and 1 MPa are recommended for the modelling of smooth interfaces to replicate the global behavior. The friction angle should be taken as 0.85.

The third model was based on the sample with a profiled interface. This interface was modelled based on the dimension of the tooth-shaped profile to simulate the mechanical interlocking of the system. As a result of this mechanical interlocking, large shear stresses occurred at the interface preventing the delamination. The load against the displacement, joint opening and interface opening are well predicted by the FE model. However, the initial stiffness of the system is lower which can be attributed to the limiting material models in DIANA to replicate the strain hardening behavior effect of the SHCC. This is also seen in the cracking pattern in the SHCC as the crack propagation in the SHCC differs from the experimental results. As the modelling of these tooth-shaped profiles can be quite time-consuming, an additional model with a smooth interface was made to replicate the global behavior of the beam. Based on this model, an interface with perfect bond is recommended for the modelling of a beam with a profiled interface.

These results show that the detailing of the systems at the joint is critical for the behavior of the beam. The influence of the cover of the reinforcement didn't seem to affect the global behavior of the beam. Increasing the roughness of the interface results in a larger capacity as the delamination of the interface is prevented. However, as a result of the transfer of forces at the lap splice, perpendicular tensile stresses appear which are localized at the reinforcement level. For one sample, stirrups are placed to take up these perpendicular tensile stresses. However, failure of the interface still occurred due to the combination of tensile and shear stresses. Based on the FE model, yielding of the coupling reinforcement can be obtained by both increasing the interface roughness and including protruding reinforcement at the joint. From the numerical analysis, the following interface characteristics are recommended for future modelling purposes (see Table 6-1). The recommendations of the profiled interface are based on a smooth interface with perfect bond.

Property		Smooth interface	Profiled interface	Unit
Interface model		Coulomb friction	Perfect bond	MPa
Tensile strength	f_t	0.5	–	MPa
Cohesion	c	1	–	MPa
Friction angle	φ	0.85	–	Rad
Dilatancy angle	ψ	1	–	Rad
Normal stiffness	D_{11}	1200	–	N/mm^3
Shear stiffness	D_{22}	1200	–	N/mm^3

Table 6-1: Recommended interface parameters based on inverse modelling

6.2 Recommendations

Based on the results of this study, the following recommendations are made for future research possibilities to further investigate the interfacial behavior of hybrid SHCC-concrete beams.

1. For one sample, a different curing method has been chosen to investigate the effect of shrinkage on the interfacial behavior. The results showed no significant effect on the bearing capacity of the beam as a result of the restraint of the reinforcement for the reinforcement percentage used in this research. A more thorough study has to be done to investigate the effect of shrinkage on the interfacial behavior. Furthermore, also other long-term effects such as creep should be taken into account.
2. Based on the results of this study, it was concluded that the interface failure is dominated by the perpendicular tensile stresses at the interface. However, when a rough interface is applied or protruding reinforcement through the interface is used, the shear stress at the interface becomes more prominent. Therefore, future research regarding the stress distribution along the interface to better understand the failure mode has to be done. A possibility is to work on an analytical model to determine the capacity of this interface. A thorough study has to be done regarding the nonlinear stress distribution of the interface. As a starting model, the smooth interface can be modelled as discrete springs both for tension and shear.
3. In the last finite element model, yielding of the sample was achieved by increasing the interface bond and placing protruding reinforcement through the interface. The experimental research can be continued by investigating samples in which the roughness of the interface is improved including protruding reinforcement to prevent the failure of the concrete top layer.

7 Bibliography

[1] Z. Huang, "Flexural behavior of reinforced concrete beams with a layer of SHCC in the tension zone," Master Thesis , Technische Universiteit Delft, 2017.

[2] H. Borsje and G.G.A Dieteren, "Onderzoek naar de technische oorzaak van de gedeeltelijke instorting van de in aanbouw zijnde parkeergarage P1 Eindhoven Airport," TNO, 2017.

[3] V. C.Li, "ENGINEERED CEMENTITIOUS COMPOSITES (ECC) – TAILORED COMPOSITES THROUGH MICROMECHANICAL MODELING," University of Michigan, 1997.

[4] S. Wang and V. C.Li, "Engineered Cementitious Composites with High-Volume Fly Ash," ACI Materials Journal, 2007.

[5] S.-J. Jang, J.-H. Kim, S.-W. Kim, W.-S. Park and H.-D. Yun, "The Effect of Shrinkage-Compensation on the Performance of Strain-Hardening Cement Composite (SHCC)," MDPI, 2018.

[6] M.Lukovic, "INFLUENCE OF INTERFACE AND STRAIN HARDENING CEMENTITIOUS COMPOSITE (SHCC) PROPERTIES ON THE PERFORMANCE OF CONCRETE REPAIRS," Ph.D., Technische Universiteit Delft, 2016.

[7] S. Yin and S. Xu, "Flexural Behavior of Reinforced Concrete Beams with TRC Tension Zone Cover," Journal of Materials in Civil Engineering, 2014.

[8] A. Haroon, K.R. Ramsundar, G. Velrajkumar and M. Arun, "An Overview of Interface Behaviour between Concrete to Concrete," International Journal of Advanced Structures and Geotechnical Engineering, 2014.

[9] M.E. Mohamad and I.S. Ibrahim, "INTERFACE SHEAR STRENGTH OF CONCRETE-TO-CONCRETE BOND WITH AND WITHOUT PROJECTING STEEL," Jurnal Teknologi, 2015.

[10] G.A.P.G. van Zijl and H. Stander, "SHCC repair overlays for RC: Interfacial bond characterization and modelling," Master Thesis, University of Stellenbosch, 2009.

[11] T. Kanakubo, "Study on Size Effect in Bond Splitting Behavior of ECC," Bond in Concrete 2012 – Bond in New Materials and under Severe Conditions, 2012.

[12] M.E. Mohamad, I.S. Ibrahim, R. Abdullah, A.B. Abd. Rahman, A.B.H. Kueh and J. Usman, "Friction and cohesion coefficients of composite concrete-to-concrete bond," Cement & Concrete Composites 56, 2014.

[13] C. Yu, K.Y. Leung and Q. Cao, "Behavior of concrete members constructed with SHCC/GFRP permanent formwork," Fracture Mechanics of Concrete and Concrete Structures, Hong Kong University of Science and Technology, 2010.

[14] H.J. Yang, J.S. Kim, S.H. Kim and H.D. Yun, "Flexural Performance of Reinforced Concrete Beams with a Layer of Expansive Strain-hardening Cement-based Composite(SHCC)," Chungnam National University, 2011.

[15] M. Li and V. C.Li, "Behavior of ECC/Concrete Layer Repair System Under Drying Shrinkage Conditions," Advanced Civil Engineering Materials Research Laboratory, The University of Michigan, 2011.

[16] C.R. Braam, J.J. Meester, L.T.H. Esink, W.A.P. de vos and S.N.M. Wijte, "Bezwijken parkeergarage Eindhoven airport," Adviesbureau Hageman, 2017.

[17] J.D. Kovach, "Horizontal shear capacity of composite concrete beams without interface ties," Theses, Lehigh University, 2008.

[18] Karin Lundgren, Johan Helgesson and Rasmus Sylven, "Joints in lattice girder structures," CHALMERS UNIVERSITY OF TECHNOLOGY, 2013.

[19] J. Stehle, B.L. Karihaloo and A. Kanellopoulos, "Performance of joints in reinforced concrete slabs for two-way spanning action," ICE Proceedings Structures and Buildings, 2010.

[20] NEN, "Eurocode 2: Design of concrete structures - Part 1-1: General rules and rules for buildings," 2004.

[21] Y. Yang, J. de Uijl, J. Walraven, "Critical shear displacement theory: on the way to extending the scope of shear design and assessment for members without shear reinforcement," Structural concrete, 2016.

[22] J.P. Grant, "Non-Contact Lap Splices in Dissimilar Concretes," Master thesis, Virginia Polytechnic Institute and State University, 2015.

[23] C.R. Braam, "CT3150 - Concrete structures 2," TU Delft, 2013.

[24] B. Mobasher, "Digital Image Correlation," ScienceDirect, 2016.

[25] M.A.N. Hendriks, A. de Boer and B. Belletti, "Guidelines for Nonlinear Finite Element Analysis of Concrete Structures," Rijkswaterstaat, 2017.

[26] TNO DIANA, "User's Manual 10.3," 2019.

[27] D. Pryl and J.Červenka, "ATENA Program Documentation Part 11," Červenka Consulting s.r.o., 2018.

[28] "Model Code 2010 Volume 1," fib, 2012.

[29] NEN, "NEN-EN 13747+A2 - Precast concrete products - Floor plates for floor systems," 2010.

[30] B.B. Casal, "Connections Between Concrete Layers with Different Ages," Universidade Técnica de Lisboa .

[31] M.Eriksen and M. Kolstad, "Investigation of Cracking Behavior in Reinforced Concrete Panels with Bond-slip Reinforcement," Master thesis, 2016.

[32] S.H. Tung, M.H. Shih and W.P. Sung, "Development of digital image correlation method to analyse crack variations of masonry wall," Sadhana Vol. 33, 2008.

[33] P. Moga and C. Pondichi, "CONCRETE SHRINKAGE EFFECT ON THE COMPOSITE," Technical University of Cluj-Napoca, 2014.

A Cube compression test results

Batch 1-1 – Concrete cube compression tests

Cube number	Age	Dimensions		Force		Stress	
1	49	15 x15x15	cm^3	1152.6	kN	51.33	MPa
2	49	15 x15x15	cm^3	1168.6	kN	51.94	MPa
3	49	15 x15x15	cm^3	1195.2	kN	53.13	MPa
4	49	15 x15x15	cm^3	1090	kN	48.44	MPa
5	49	15 x15x15	cm^3	1002.7	kN	44.56	MPa
6	49	15 x15x15	cm^3	1166.6	kN	51.85	MPa
7	49	15 x15x15	cm^3	1067.4	kN	47.44	MPa
8	49	15 x15x15	cm^3	1200.7	kN	53.36	MPa

Table A-1: Batch 1 Concrete cube compression test results

Batch 1-2 – Concrete cube compression tests

Cube number	Age	Dimensions		Force		Stress	
1	49	15 x15x15	cm^3	1159.6	kN	51.54	MPa
2	49	15 x15x15	cm^3	1066.5	kN	47.4	MPa
3	49	15 x15x15	cm^3	1130.1	kN	50.23	MPa
4	49	15 x15x15	cm^3	1132.8	kN	50.35	MPa
5	49	15 x15x15	cm^3	1056.4	kN	46.95	MPa
6	49	15 x15x15	cm^3	1129.9	kN	50.22	MPa
7	49	15 x15x15	cm^3	1189.2	kN	52.85	MPa
8	49	15 x15x15	cm^3	1081.3	kN	48.3	MPa

Table A-2: Batch 1 Concrete cube compression test results continued

SHCC cube compression tests

Cube number	Age	Dimensions		Force		Stress	
1	51	15 x15x15	cm^3	1173.8	kN	52.17	MPa
2	51	15 x15x15	cm^3	1157	kN	49.59	MPa
3	51	15 x15x15	cm^3	1131.5	kN	50.30	MPa
4	51	15 x15x15	cm^3	1160	kN	51.40	MPa

Table A-3: SHCC cube compression test results

B Casting and testing dates

Casting dates

Material	Casting date
SHCC	$16-07-2019$
Concrete	$18-07-2019$

Table B-1: Casting dates

Demoulding dates

Beam sample	Demoulding date
1	$30-08-2019$
2	$27-08-2019$
3	$28-08-2019$
4	$24-07-2019$
5	$20-08-2019$
6	$02-09-2019$
7	$04-11-2019$

Table B-2: Demoulding dates

Testing dates

Beam sample	Testing date
1	$06-09-2019$
2	$30-08-2019$
3	$02-09-2019$
4	$09-09-2019$
5	$03-09-2019$
6	$09-09-2019$
7	$06-12-2019$

Table B-3: Testing dates

C Influence of shear reinforcement

An extra numerical study is done to investigate the effect of shear reinforcement on the interfacial behavior in the constant bending moment region. This appendix will only show the result of this study. In chapter 4, the FE model is explained thoroughly. In Figure C-1, the FE result is shown for the model without shear reinforcement. In this figure, the results of the models with a perfect bond and a Coulomb friction model at the interface is shown. For the Coulomb friction model, the interface tensile strength (ITS) is varied.

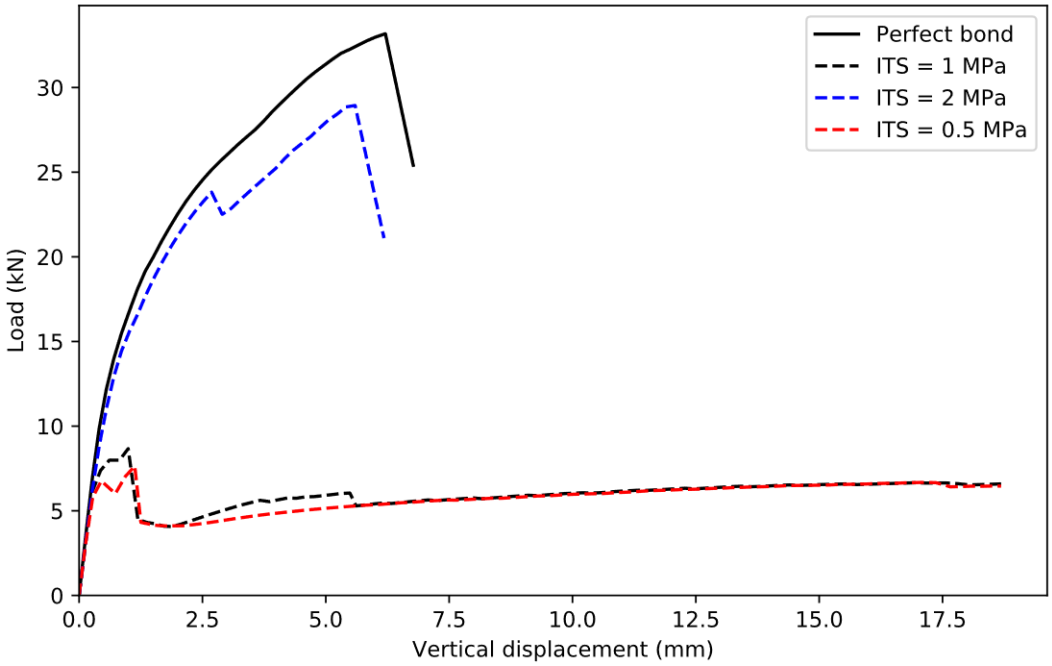

Figure C-1: FE result without shear reinforcement

The same study with having shear reinforcement in the shear region according to Huang's study [1] (see Figure C-2).

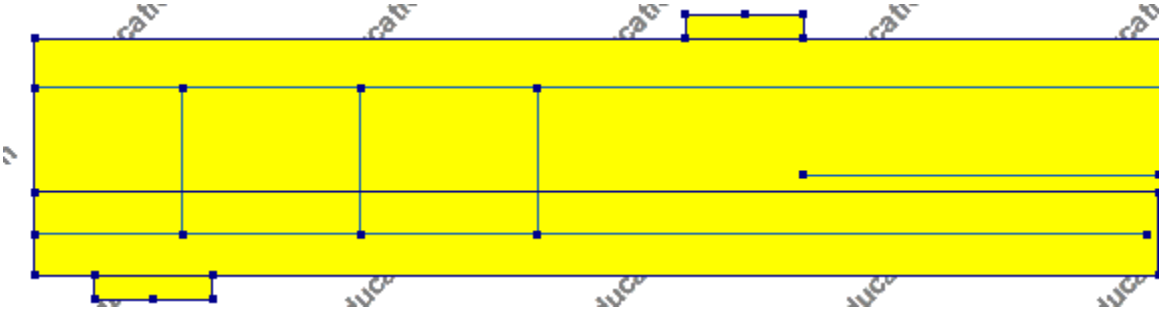

Figure C-2: Model with shear reinforcement

The result is shown in Figure C-3. When comparing this result to the result of Figure C-1, an identical load-displacement curve can be seen for all the different results. This shows that having shear reinforcement in the shear region doesn't influence the interfacial behavior in the constant bending moment region.

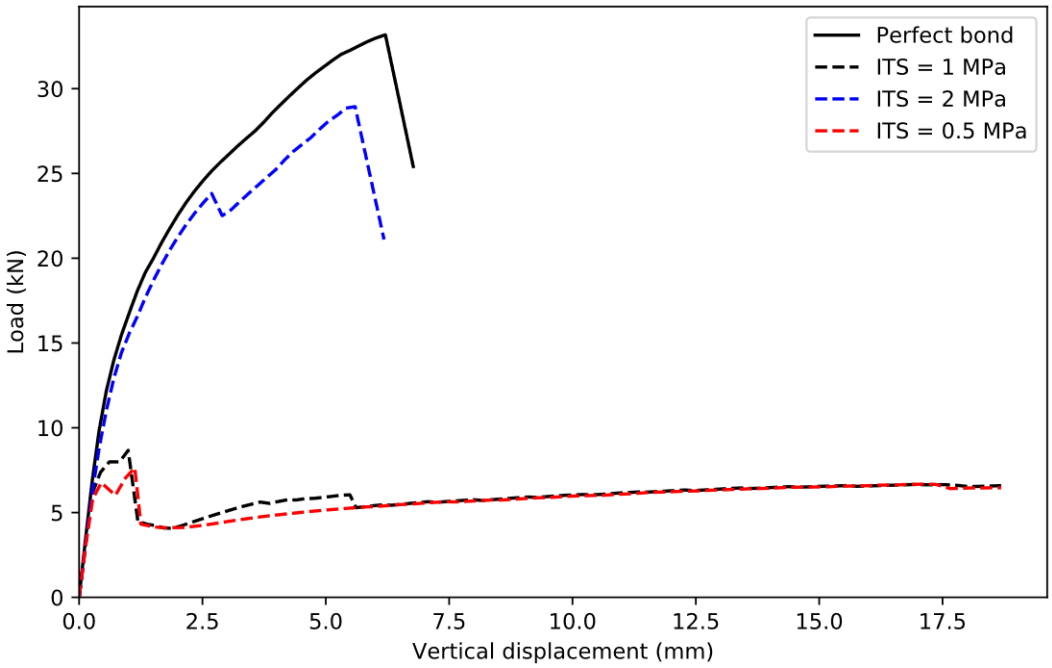

Figure C-3: FE result with shear reinforcement